Preparation and Optimisation of Transparent Conducting Patterns Using Inkjet Printing

By

Zhaoting Xiong

A Doctoral Thesis

submitted in partial fulfilment of the requirements

for the award of

Doctor of Philosophy of Loughborough University

September 2013

Abstract

Transparent conducting patterns (TCPs) are critical components that are required to be integrated into photovoltaic (PV) cells for energy harvesting. Among the manufacturing processes that are available for the deposition of TCPs onto various substrates, inkjet printing which can be categorised as an additive dispensing process has demonstrated its competitiveness by offering numerous advantages, including non-contact, high resolution, high printing speed, low cost and low material consumption. However, the present bottlenecks to be overcome for further take-up of inkjet printing technology imperatively demand the understanding of materials behaviour involved in the ink formulation and printing process. This thesis is dedicated to the elaboration of fundamental aspects of technical challenges that have been encountered in the uses of inkjet printing technology for the generation of TCPs, thereby optimisation of functional properties of the printed patterns can be achievable through the modification of inks and optimum parameters used in the printing process.

In this study, the methods of adjusting the relevant properties of deionized water by adding certain additives (e.g. surfactants) were firstly developed to obtain the desirable properties viable for inkjetting, thereby a water-based solution or suspension containing the functional materials can be prepared and modified as an ink suitable for use in specific inkjet printheads. To elaborate the characteristics of inks during jetting, the effect of ink properties (e.g. viscosity and surface tension) on the formation of droplets during the inkjet printing process were then analysed through numerical simulation using FLUENT software package. Experimental trials were then exercised for the successful deposition of basic patterns including dots, tracks and films. Applying the above stated approaches, this thesis has primarily focused on the ink formulation and printing experiments to understand the materials behaviour in the deposition of TCPs based on three types of transparent conducting materials that have been commonly used in the production of TCPs.

Deposition of PEDOT:PSS thin films: the electric conductivity of inkjet printed PEDOT:PSS thin films has been optimised through annealing processes and conductors doping. It has been found that drastic improvements of the electric conductivity of the deposited thin films can be achieved through solvent annealing by adding glycerol as

the co-solvent. However, thermal annealing of the thin films after inkjet printing was found to be inefficient for improving the electric conductivity of PEDOT:PSS. Interestingly, doping silver nanoparticles in the PEDOT:PSS ink can increase in the electric conductivity of PEDOT:PSS thin film, but this increase has inevitably resulted in a reduction in the optical transparency.

Deposition of ITO patterns: Laser assisted inkjet (LIJ) technology has been for the first time applied for the deposition of ITO (Indium-Tin Oxide) patterns onto glass substrates. The location of *in-situ* laser radiation around the position of ink droplet landing has been altered as such an optimised location can be determined to obtain uniform ITO tracks with potential refined resolution of the track width. With the laser being focused on the identified optimum location, the effect of laser power on the morphology of tracks and the subsequent influence on the conductivity were then investigated. The experimental results have also revealed that the critical thickness (cracks are induced and emerged when the thickness of prints is greater than this value) of inkjet printed ITO tracks is larger than that for the films. This has been explained and discussed with the assistance of a mathematic model to elaborate the effect of the dimensions of the deposited structures.

An in-situ synthesis of semi-transparent silver thin films: A novel process which is able to fabricate semi-transparent and conductive silver thin films *in-situ* has been developed in this work. This process utilised a unique approach to integration of conductive silver networks using a layer of precursor materials which can be pre-deposited on the substrate by inkjet printing. The printed layer was then cured to enable *in-situ* synthesis of a thin film of silver network microstructure. The experimental investigation indicated that such microstructure of silver thin films is determined by the amount of ink materials deposited by inkjet printing; as such a conductive semi-transparent silver thin film can be formed under the certain printing resolution.

Key words: Transparent conducting pattern, inkjet printing, thin film, conductivity, transparency.

Publications

1. Z. Xiong and C. Liu, Optimization of inkjet printed PEDOT: PSS thin films through annealing processes. Organic Electronics, 2012, Vol. 13(9), pp.1532-1540.
2. Z. Xiong, C. Dong, H. Cai, C. Liu, and X. Zhang. Composite Inks of Poly(3,4-ethylenedioxythiophene)/Poly(styrenesulfonate)/Silver Nanoparticles and Electric/Optical Properties of Inkjet-Printed Thin Films. Materials Chemistry and Physics, 2013, Vol. 141(1), pp.416-422.
3. Z. Xiong, C. Liu, and X. Zhang. Inkjet printing of silver nano particles doped PEDOT: PSS thin film. in Electronic Packaging Technology and High Density Packaging (ICEPT-HDP), 2012 13th International Conference on. 2012. IEEE.
4. Z. Xiong and C. Liu. The application of inkjet direct writing in solar cell fabrication: An overview. in Electronic Packaging Technology and High Density Packaging (ICEPT-HDP), 2011 12th International Conference on. 2011. IEEE.
5. Z. Xiong and C. Liu. Effect of substrates surface condition on the morphology of silver patterns formed by inkjet printing. in Microelectronics and Packaging Conference (EMPC), 2011 18th European. 2011. IEEE.

Acknowledgements

This research is financially supported by the Marie Curie International Research Staff Exchange Scheme Project within the 7th European Community Framework Programme, No. PIRSES-GA-2010-269113, entitled “Micro-Multi-Material Manufacture to Enable Multifunctional Miniaturised Devices (M6)”.

I would like to take this opportunity to express my sincerest thanks to my supervisor, Prof. Changqing Liu, for his support and patient guidance in my study. I would also like to thank Prof. Xianglin Zhang from Huazhong University of Science and Technology, Dr. Masahiro Aoyagi and Dr. Jun Akedo from National Institute of Advanced Industrial Science and Technology, for their care and guidance during my stays in China and Japan.

I am grateful to the technical support that I have received from Mr. Andy Sandaver, Mr. Chunfa Dong, Mr. Hao Cai, Mr. Shunsuke Nemoto and Mr. Hiroki Tsuda.

Finally, I would like to thank all my friends and colleagues for their company and help during my stays in UK, China and Japan, which encouraged me to overcome the difficulties and finish the PhD study.

Table of Contents

Abstract ..... **I**

Publications ..... **III**

Acknowledgements ..... **IV**

Table of Contents ..... **V**

List of Abbreviations ..... **IX**

List of Figures ..... **XII**

List of Tables ..... **XVIII**

Chapter 1 Introduction ..... **- 1 -**

1.1 Background ..... - 1 -

1.1.1 Transparent conducting patterns (TCPs) ..... - 1 -

1.1.2 Inkjet technology ..... - 3 -

1.2 Problem statements and research motivation ..... - 4 -

1.3 Research aims and objectives ..... - 6 -

1.4 Statement of the main contributions to knowledge ..... - 7 -

1.5 Thesis structure ..... - 7 -

Chapter 2 Inkjet Technology ..... **- 10 -**

2.1 Classification ..... - 10 -

2.2 Inkjet inks ..... - 12 -

2.3 DOD deposition mechanism ..... - 15 -

2.3.1 Ejection phase ..... - 15 -

2.3.2 Droplet flight phase ..... - 16 -

2.3.3 Impact phase ..... - 17 -

2.4 Optimisation of feature size ..... - 17 -

2.4.1 Reduction of droplet size ..... - 17 -

2.4.2 Control of spreading ..... - 18 -

Chapter 3 Experimental Methods ..... **- 19 -**

3.1 Inkjet printers ..... - 19 -
3.1.1 Principle of inkjet printer ..... - 19 -
3.1.2 Jetlab®4 inkjet printer ..... - 20 -
3.1.3 Fanjet IIA-1501 inkjet printer ..... - 23 -
3.1.4 Laser assisted inkjet (LIJ) printer ..... - 24 -
3.2 Materials ..... - 26 -
3.2.1 Inks & precursors ..... - 26 -
3.2.2 Additives ..... - 27 -
3.2.3 Substrates ..... - 28 -
3.3 Characterization and analysis ..... - 29 -
3.3.1 Measurement of conductivity ..... - 29 -
3.3.2 Transparency ..... - 31 -
3.3.3 Surface profile ..... - 31 -
3.3.4 AFM ..... - 32 -
3.3.5 SEM ..... - 32 -
3.3.6 TEM ..... - 33 -
3.3.7 XRD ..... - 33 -
3.3.8 Viscosity ..... - 33 -
3.3.9 Surface tension ..... - 34 -
Chapter 4 Ink Formulation and Pattern Printing ..... - 35 -
4.1 Ink formulation ..... - 36 -
4.1.1 Introduction ..... - 36 -
4.1.2 Properties optimisation ..... - 36 -
4.1.3 Prevention of nozzle blocking ..... - 40 -
4.2 Simulation of droplet formation ..... - 41 -
4.2.1 Simulation procedures ..... - 41 -
4.2.2 Simulation and verification ..... - 44 -

4.2.4 Failure analysis ..... - 53 -
4.3 Initial pattern printing ..... - 56 -
4.3.1 Methodology ..... - 56 -
4.3.2 Dot printing ..... - 58 -
4.3.3 Track printing ..... - 64 -
4.3.4 Film printing ..... - 67 -
4.4 Conclusions ..... - 69 -
Chapter 5 Inkjet Printing of PEDOT:PSS Thin Film and Optimisation ..... - 71 -
5.1 Introduction ..... - 72 -
5.1.1 Introduction of PEDOT:PSS ..... - 72 -
5.1.2 Inkjet printing of PEDOT:PSS thin film ..... - 74 -
5.1.3 Optimisation of PEDOT:PSS ..... - 75 -
5.2 Solvent & thermal annealing ..... - 77 -
5.2.1 Solvent annealing ..... - 77 -
5.2.2 Thermal annealing ..... - 83 -
5.3 Conductor doped PEDOT:PSS ..... - 88 -
5.3.1 Silver nanoparticle (Ag NPs) doped PEDOT:PSS ..... - 88 -
5.3.2 Effect of substrate temperature ..... - 99 -
5.4 Conclusion ..... - 103 -
Chapter 6 Laser Assisted Inkjet Printing of Indium Tin Oxide ..... - 105 -
6.1 Introduction ..... - 106 -
6.1.1 Indium tin oxide (ITO) ..... - 106 -
6.1.2 Laser assisted inkjet (LIJ) process ..... - 107 -
6.2 Experimental procedures ..... - 108 -
6.3 ITO thin film printing ..... - 109 -
6.3.1 Morphology ..... - 109 -
6.3.2 Conductivity ..... - 112 -

6.3.3 Transmittance ..... - 113 -
6.4 ITO track printing ..... - 114 -
6.4.1 Effect of laser position ..... - 114 -
6.4.2 Effect of laser power ..... - 118 -
6.4.3 Critical thickness of track ..... - 124 -
6.5 Conclusion ..... - 129 -
Chapter 7 Self-assembly Synthesis of Silver Thin Film *via* Inkjet Printing .... - 131 -
7.1 Introduction ..... - 132 -
7.2 Experimental procedures ..... - 133 -
7.2.1 Ink formulation ..... - 133 -
7.2.2 Thin film deposition ..... - 134 -
7.3 Effect of printing resolution ..... - 135 -
7.3.1 Morphology ..... - 135 -
7.3.2 Conductivity ..... - 138 -
7.3.3 Transparency ..... - 139 -
7.4 Conclusion ..... - 140 -
Chapter 8 Conclusions and Future Work ..... - 141 -
8.1 Main conclusions ..... - 141 -
8.2 Recommendation for future work ..... - 146 -
References ..... - 149 -
Appendix ..... - 168 -

List of Abbreviations

3D	3 Dimensional
AFM	Atomic Force Microscope
ACN	Acetonitrile
AZO	Aluminium doped Zinc Oxide
BHJ	Bulk Heterojunction
CCD	Charge-Coupled Device
CIJ	Continuous Ink Jet
CNT	Carbon Nanotube
DI	Deionized
DMS	Dimethyl Sulphate
DMSO	Methyl Sulfoxide
DOD	Drop On Demand
EB	Electronic Beam
FTO	Fluorine doped Tin Oxide
HDI	High Density Interconnect
HOMO	Highest Occupied Molecular Orbital
IC	Integrated Circuit
IPA	Iso-Propyl Alcohol
ITO	Indium-Tin Oxide
LED	Light Emitting Diode

LIJ	Laser-assisted Ink Jet
MOD	Metal Organic Decomposition
NMP	1-Methy1-2-Pyrrolidinone
NP	Nano Particle
OLED	Organic Light Emitting Diode
OPV	Organic Photovoltaic Device
P3HT	Poly(3-hexylthiophene-2,5-diyl)
PCB	Printed Circuit Board
PCE	Power Conversion Efficiency
PEDOT	Poly(3,4-ethylenedioxythiophene)
PI	Polyimide
POETE	Polyoxyethylene(12) tridecyl ether
PSS	Poly(styrenesulfonate)
PV	Photovoltaic
PVD	Physical Vapour Deposition
PVP	Poly(vinylpyrrolidone)
RMS	Root Mean Squared
SAM	Self-Assembled Monolayer
SDBS	Sodium Dodecyl Benzene Sulfonate
SDS	Sodium Dodecyl Sulphate
SEM	Scanning Electron Microscope

TCO	Transparent Conducting Oxide
TCP	Transparent Conducting Pattern
TEM	Transmission Electron Microscope
THF	Tetrahydrofuran
UDF	User-Defined Function
UV	Ultra Violet
UV-Vis	Ultraviolet-visible spectroscopy
VBI	Viscosity Blending Index
vol.%	Volume Percentage
VOF	Volume of Fluid
wt.%	Weight Percentage
XRD	X-Ray Diffraction

List of Figures

Figure 1.1 Applications of TCPs with different resistivity ..... - 1 -
Figure 1.2 SEM micrographs of (A) CNT film, (B) silver nanowire network, (C) Au nanowire grating and (D) AFM of graphene flakes ..... - 3 -
Figure 1.3 Schematic illustration of drop on demand inkjet printing..... - 3 -
Figure 1.4 Applications of inkjet technology and market size (after ref. [26])..... - 4 -
Figure 1.5 Feature size of different printing methods ..... - 6 -
Figure 1.6 An overview of the thesis structure..... - 8 -
Figure 2.1 Classification of inkjet technology (after) ..... - 11 -
Figure 2.2 Schematic of CIJ (a) and DOD (b)..... - 11 -
Figure 2.3 Schematic of thermal inkjet (a) and piezo inkjet (b) (after ref.[50])..... - 12 -
Figure 2.4 Sequence of series images taken during the DOD drop formation..... - 16 -
Figure 2.5 Simulated liquid droplet during flight ..... - 16 -
Figure 3.1 Schematic diagram of principle of DOD inkjet printer..... - 20 -
Figure 3.2 Microfab Jetlab® 4 inkjet printer..... - 21 -
Figure 3.3 Schematic illustration of dispensing printhead of jetlab® 4 printer ..... - 22 -
Figure 3.4 Waveform of jetlab® 4 printer..... - 22 -
Figure 3.5 Fanjet IIA-1501 inkjet system (a) and partial enlarged detail (b)..... - 23 -
Figure 3.6 Exploded view of Nova-Q JA128/80 AQ ..... - 24 -
Figure 3.7 Laser assisted inkjet printer at AIST, Japan..... - 25 -
Figure 3.8 Patterns for conductivity measurement of tracks..... - 29 -
Figure 3.9 Schematic structure of four-point probe measurement of sheet resistance- 31 -
Figure 4.1 Components of self-developed water based inkjet ink and their properties that can affect characteristics of inks..... - 36 -
Figure 4.2 Theoretical prediction of the viscosities of water mixed with glycerol compared with experimental data obtained at 20 °C..... - 37 -
Figure 4.3 Viscosities of five mixtures of water and glycerol at temperatures from 10 °C to 35 °C ..... - 38 -
Figure 4.4 Surface tension of water and water mixed with different surfactants..... - 39 -
Figure 4.5 Surface tension of water mixed with ethanol..... - 39 -
Figure 4.6 Surface tension of 85 wt.% water + 15 wt.% ethanol mixed with glycerol obtained at 20 °C ..... - 40 -

Figure 4.7 Flow chart of the simulation procedure for droplet formation in inkjet printing ..... - 41 -
Figure 4.8 Geometrical model established by GAMBIT ..... - 42 -
Figure 4.9 Meshed model and partial enlarged detail of the orifice..... - 43 -
Figure 4.10 Typical variation predicted for the pressure in the orifice of the nozzle - 44 -
Figure 4.11 Simulation results of droplet formation from 8.0 μs to 132.4 μs from start of pressure pulse ..... - 45 -
Figure 4.12 Velocity cloud picture of the droplets obtained at 136 μs ..... - 46 -
Figure 4.13 Experimental (ink properties: 5 cps, 30 dynes/cm) (a) and simulation (ink properties: 1 cps, 40 ynes/cm) (b) results of formation of droplets in the inkjet process - 48 -
Figure 4.14 Simulation results for liquids A, B, C and D at 33.0 μs (a), 52.6 μs (b), 90.6 μs (c) and 118.4 μs (d) ..... - 50 -
Figure 4.15 Simulation results for liquid C, E, F and G at 33.0 μs (a), 47.2 μs (b), 76.6 μs (c), 84.4 μs (d), 90.6 μs (e) and 105.0 μs (f) ..... - 51 -
Figure 4.16 The predicted effect of surface tension on the droplet velocity and number of satellites..... - 52 -
Figure 4.17 The predicted effect of viscosity on the droplet velocity and number of satellites ..... - 53 -
Figure 4.18 Retraction captured with CCD camera as the order of time (from left to right) ..... - 54 -
Figure 4.19 Simulation of the jetting process with a reduced pressure pluse magnitude - 54 -
Figure 4.20 Model of sine-shaped meniscus ..... - 55 -
Figure 4.21 Simulation of the jetting process for sine-shaped meniscus ..... - 56 -
Figure 4.22 Pathway of nozzle in film printing..... - 57 -
Figure 4.23 PEDOT:PSS film printed on glass substrate..... - 58 -
Figure 4.24 Top views obtained by optical microscopy and cross-section profiles obtained by Zygo of droplets on glass substrates preheated at different temperatures (top to bottom is 20°C, 35°C, 50°C, 65°C and 80°C) ..... - 60 -
Figure 4.25 Optical top view of dots on (from left to right) glass, hydrophobic paper, FR4 and polyimide at 20°C ..... - 61 -
Figure 4.26 Diameters of dots printed on four substrates under different preheat temperatures (ambient temperature: 20°C) ..... - 61 -

Figure 4.27 Schematic model of droplet spreading process..... - 62 -
Figure 4.28 Printed silver tracks with different dot spacing values (from left to right: 170 μm, 125 μm, 110 μm, 100 μm, 80 μm, 70 μm, 60 μm and 50 μm. The average dot diameter is approximately 150 μm)..... - 64 -
Figure 4.29 Average dot diameters, track width of one layer on different substrates (move down)..... - 65 -
Figure 4.30 schematic illustration of droplet spreading ..... - 66 -
Figure 4.31 Width and thickness of tracks through multiple printing..... - 67 -
Figure 4.32 Relationship between the film thickness and the content of PEDOT: PSS in the ink ..... - 68 -
Figure 5.1 Chemical formula of PEDOT (top) and PSS (bottom) ..... - 72 -
Figure 5.2 Schematic structure of PEDOT:PSS (after ref. [92])..... - 73 -
Figure 5.3 Cross-sectional view of the schematic morphological model for PEDOT:PSS thin films derived from combined STM and X-AFM measurements ..... - 73 -
Figure 5.4 Viscosity distribution mapping of the mixture of glycerol, PEDOT: PSS and DI water ..... - 77 -
Figure 5.5 Surface roughness of PEDOT:PSS thin films vs. addition of glycerol (deposited at room temperature)..... - 78 -
Figure 5.6 AFM images on an area of 1 × 1 μm^2 of thin films prepared with pristine PEDOT:PSS and PEDOT:PSS doped with 5%, 10%, 20% and 35% glycerol..... - 79 -
Figure 5.7 Conductivity of PEDOT:PSS thin films vs. addition of glycerol ..... - 80 -
Figure 5.8 Thickness and surface roughness of PEDOT:PSS thin film under different baking conditions ..... - 81 -
Figure 5.9 AFM images (500 × 500 nm^2) and cross section profiles of PEDOT:PSS thin films baked at 100°C, 150°C and 200°C..... - 81 -
Figure 5.10 Conductivity of PEDOT:PSS thin film under different baking conditions .. - 82 -
Figure 5.11 Transmittance of glass substrate, pristine and glycerol doped PEDOT:PSS thin films with substrate ..... - 83 -
Figure 5.12 The appearance of PEDOT:PSS films after baking at different temperatures ..... - 84 -
Figure 5.13 Thickness and surface roughness of the PEDOT:PSS thin films baked at different temperatures..... - 85 -

Figure 5.14 AFM images and cross section profiles of PEDOT:PSS thin films: affect of thermal annealing ..... - 86 -
Figure 5.15 Phase images of PEDOT:PSS thin films due to thermal annealing..... - 86 -
Figure 5.16 Conductivity of the PEDOT:PSS thin films after baking at different temperatures ..... - 87 -
Figure 5.17 Transmittance of bare glass and PEDOT:PSS thin films with glass substrate after baking at different temperatures..... - 88 -
Figure 5.18 XRD patterns of silver lattice structure from the obtained Ag NPs for the ink formulation ..... - 91 -
Figure 5.19 TEM images of silver NPs before (a) and after (b) separation from PEDOT:PSS ..... - 92 -
Figure 5.20 B-splines of size distribution of the silver NPs of composites I, II, and III.. - 93 -
Figure 5.21 B-splines of size distribution of the silver NPs of composites V, III, and IV- 93 -
Figure 5.22 B-splines of size distribution of the silver NPs of composites III, VI, and VII ..... - 94 -
Figure 5.23 Conductivity of thin film prepared by ink-jetting the pristine PEDOT:PSS, Inks A-G and a-g, and the average size of the Ag NPs in them. ..... - 95 -
Figure 5.24 Schematic illustration of the proposed structure of the films formed by ink-jet printing of Ag NPs doped PEDOT:PSS ..... - 96 -
Figure 5.25 UV-Vis spectrum of thin films printed with pristine PEDOT:PSS, Inks E, C, D and c..... - 97 -
Figure 5.26 AFM height images of thin films printed with pristine PEDOT:PSS (a), Ink D (b) and Ink d (c) with a vertical scale of 50 nm..... - 98 -
Figure 5.27 SEM images of pristine PEDOT:PSS thin film (a) and Ag-PEDOT:PSS thin film (b) ..... - 99 -
Figure 5.28 Pristine PEDOT:PSS thin films printed on glass substrate preheated to 20°C (a) and 80°C (c), and Ag NP doped PEDOT:PSS thin films printed on glass substrate preheated to 20°C (b) and 80°C (d)..... - 100 -
Figure 5.29 Surface profile of the y direction of Ag-PEDOT:PSS thin film printed on 20°C and 80°C substrates ..... - 101 -
Figure 5.30 Conductivity of thin films prepared with pristine and Ag NP doped PEDOT:PSS vs. preheating temperature ..... - 102 -

Figure 5.31 Conductivity of pristine PEDOT:PSS and Ag-PEDOT:PSS thin films after baking at 200 °C ..... - 102 -
Figure 6.1 Schematic illustration of laser assisted inkjet process ..... - 107 -
Figure 6.2 Thickness vs. deposited amount of ink per unit area of the films printed with MOD ITO ink and ITO nanoparticle ink..... - 109 -
Figure 6.3 Cracks on the films printed with MOD ITO ink (a) and ITO nanoparticle ink (b) ..... - 110 -
Figure 6.4 Height image ((a) and (c)) and phase image ((b) and (d)) of ITO films printed with MOD ITO ink under dot matrix of 250×20 ((a) and (b)) and 250×100 ((c) and (d)) ..... - 111 -
Figure 6.5 Height image ((a) and (c)) and phase image ((b) and (d)) of ITO films printed with ITO nanoparticle ink under dot matrix of 250×20 ((a) and (b)) and 250×100 ((c) and (d)) ..... - 112 -
Figure 6.6 Sheet resistance of the films printed with MOD ITO ink and ITO nanoparticle ink at different thicknesses ..... - 113 -
Figure 6.7 Transmittance of glass substrate and ITO films..... - 114 -
Figure 6.8 Position of laser radiations (yellow dots) in the inkjet printing and the corresponding top view of the obtained tracks..... - 115 -
Figure 6.9 Cross sectional profile of tracks printed with laser applied at A, B, C and without laser ..... - 116 -
Figure 6.10 Schematic illustration of Marangoni effect..... - 117 -
Figure 6.11 Cross sectional profile of tracks printed with laser applied at D, E, F, and G ..... - 117 -
Figure 6.12 Cross sectional profile of track printed with laser radiation applied at point H ..... - 118 -
Figure 6.13 Optical top view of ITO tracks printed with MOD ITO ink under different laser powers..... - 119 -
Figure 6.14 Width of tracks printed with MOD ITO ink vs. laser power ..... - 119 -
Figure 6.15 Cross sectional profile of ITO tracks printed with MOD ITO ink under different laser power..... - 120 -
Figure 6.16 Conductivity measurements of tracks printed with MOD ITO ink vs. laser power ..... - 121 -
Figure 6.17 Optical top view of ITO tracks printed with ITO nanoparticle ink under different laser power..... - 122 -

Figure 6.18 Width of tracks printed with ITO nanoparticle ink vs. laser power..... - 122 -
Figure 6.19 Cross sectional profile of ITO tracks printed with ITO nanoparticle ink under different laser power..... - 123 -
Figure 6.20 Conductivity of tracks printed with ITO nanoparticle ink vs. laser power... - 124 -
Figure 6.21 Schematic illustration of microstructures of initial ink material deposited (a), sintered under a free flow condition (b), and sintered under a constrained condition (c)..... - 125 -
Figure 6.22 SEM image of initial cracks on ITO thin film ..... - 126 -
Figure 6.23 Schematic drawing of pulling forces between particles and at the interfaces- 126 -
Figure 6.24 Schematic drawing of force F(x,y,z) exerted in the ITO track and film due to sintering..... - 127 -
Figure 7.1 Fine metal grids with a track width of 5 μm..... - 132 -
Figure 7.2 Appearances of pristine composite solution (a) (d), SDBS doped composite solution (b) (e) and JC-601 doped composite solution (c) (f) right after formulating (a) (b) (c) and 24 hours after formulating (d) (e) (f)..... - 134 -
Figure 7.3 Dot array printed with self-developed ink ..... - 135 -
Figure 7.4 Optical observation of thin films printed under resolutions of 300 × 300 (a), 600 × 600 (b), 900 × 900 (c) and 1200 × 1200 (d) dpi after baking under 150 °C for 1 hour..... - 136 -
Figure 7.5 SEM images of top view (a) and cross section profile (b) of the thin films... - 137 -
Figure 7.6 Schematic illustration of the *in-situ* formation of silver grids ..... - 138 -
Figure 7.7 Measurement of sheet resistance of the printed silver thin films..... - 139 -
Figure 7.8 UV-Vis spectrum of printed silver thin films ..... - 140 -
Figure 8.1 Sheet resistivity and transmittance of reported inkjet printed thin films (coloured rectangular blocks) and thin films prepared in this study (coloured curves and dots)..... - 142 -

List of Tables

Table 2.1 Comparison of CIJ and DOD ..... **Error! Bookmark not defined.**
Table 2.2 The advantages, disadvantages and applications of four types of inks ..... - 13 -
Table 3.1 Properties of PEDOT:PSS solution from sigma-aldrich **Error! Bookmark not defined.**
Table 3.2 Properties of SunTronic U5603 silver ink from Sunjet **Error! Bookmark not defined.**
Table 3.3 Components and their concentration of MOD ITO ink ..... - 27 -
Table 3.4 Properties of ITO nanoparticle ink ..... - 27 -
Table 3.5 Chemicals utilized in ink formulation and the sources ..... - 28 -
Table 3.6 Substrates utilized in the printing and the sources ..... - 29 -
Table 3.7 Model and corresponding application of SEM employed in this study .... - 32 -
Table 4.1 Ink properties used in the simulation ..... - 49 -
Table 4.2 The numbers *Re*, *We*, *Oh* and *Z* for liquid A-G calculated based on the simulation results ..... - 53 -
Table 4.3 Contact angle and surface energy of the substrates used in this study ..... - 63 -
Table 5.1 Summary of research works of improving the conductivity of PEDOT:PSS by altering distribution ..... - 76 -
Table 5.2 Summary of research works in improving the conductivity of PEDOT:PSS by doping with additional conductors ..... - 77 -
Table 5.3 Preparation and reaction parameters of Ag-PEDOT:PSS composite solutions and mass of filtered Ag particles ..... - 89 -
Table 5.4 Contents of silver in Inks A-G and a-g ..... - 90 -
Table 6.1 Summary of research into preparation of ITO patterns using wet chemical deposition ..... - 106 -
Table 6.2 Properties of modified ITO inks and the diameter and velocity of the obtained droplets ..... - 108 -

Chapter 1 Introduction

1.1 Background

1.1.1 Transparent conducting patterns (TCPs)

Transparent conducting patterns (TCPs) are structural patterns that are both optically transparent and electrically conductive. Due to the material physics, the visible light transmittance and electric conductivity of a material can be inversely correlated with each other, i.e., more transparent materials tend to have lower conductivity [1]. This is particularly true for the case of solid thin films. To ensure the electrical conductivity of solid thin films, no energy gap should exist between the energy level occupied by electrons and the empty energy level in the material, but in such a case, light can be easily absorbed when passing through the thin film due to the internal photoelectric effect [2]. Therefore, it has been recognised that a compromise often exists between conductivity and transparency for TCPs [3]. As a critical electronic component, TCPs are ubiquitously used in solar cells, displays, touch screens, smart windows, flexible lighting, and electronic books. The resistivity of commonly used TCPs range from <10 Ω/sq to 10^6 Ω/sq, depending on the application [4] (Figure 0.1).

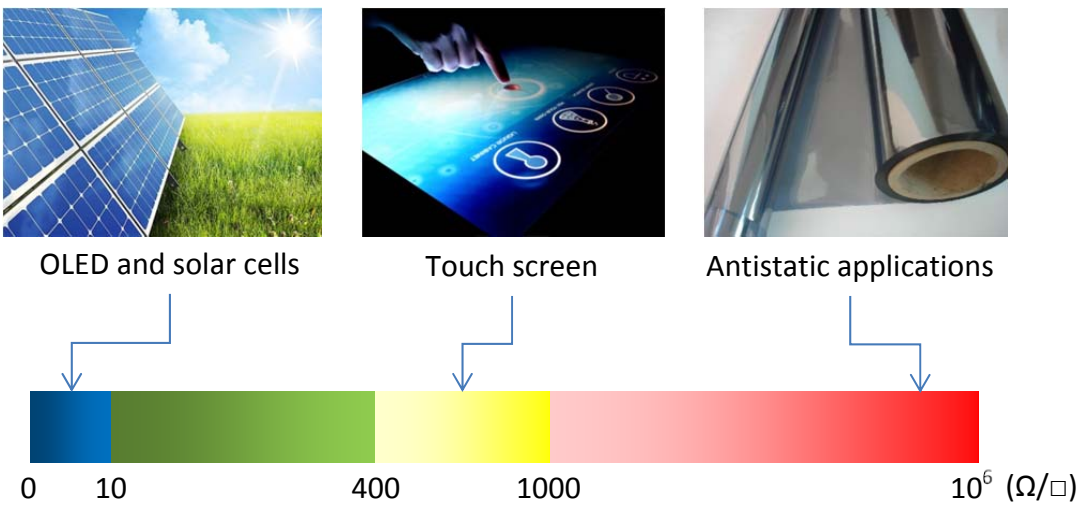

Figure 0.1 Applications of TCPs with different resistivity

At present, the most widely used TCPs are transparent conducting oxide (TCO) patterns. TCOs are doped metal oxides typically including indium tin oxide (ITO), fluorine

doped tin oxide (FTO) and doped zinc oxide (ZnO). The industry standard TCO is ITO which has a conductivity of 10^4 S/cm and a transmittance of larger than 80% [5]. However, ITO has the drawbacks of being expensive in materials and manufacturing. Therefore novel TCOs with multiple components such as aluminium doped zinc oxide (AZO), and indium doped cadmium oxide have been developed [6, 7]. Optimal combinations of different components have proved to be able to achieve high performance at a relatively low cost. TCO patterns can be fabricated by various methods including spray pyrolysis, electron beam evaporation, chemical vapour deposition, magnetron sputtering, radio frequency sputtering, molecular beam epitaxy, screen printing, pulsed laser deposition and sol-gel techniques [4, 8-11].

Conductive polymers gained prominence during the 1980s when a broad range of commonly available polymers were found to exhibit significant electrical conductivities *via* simple chemical doping mechanisms. The conducting polymers are mostly derivatives of polyacetylene, polyaniline, polypyrrole or polythiophenes [12]. Compared with TCOs, conducting polymers often have much lower conductivity (no higher than 3000 S/cm [13]), but higher transmittance (approx. 10% or less absorption in the visible spectrum [14]). Another advantage of conducting polymers is that they can be made into flexible patterns without losing much conductivity, which makes them useful in the development of flexible electronics. As conductive polymers are soluble in either water or organic solvents, the solution can be deposited in principle by all techniques that can be utilised for the deposition of waterborne coatings. The common deposition techniques for such materials include spin coating, drop casting, screen printing, doctor blading, inkjet printing and spraying [12].

Another important type of TCP is patterns made of emerging micro/nano structured materials. The development of new nanoscale materials has driven intensive research on the integration of optical, electrical, thermal, and mechanical properties in various forms. The new nanoscale materials can be made from individual separated functional components/elements and from continuous and percolated films. These include nanoscale forms of carbon such as carbon nanotubes (CNTs) and graphene, as well as nanostructured or microstructured metals, such as thin metal films, metal grids and metallic nanowires [15-18], shown in Figure 0.2.

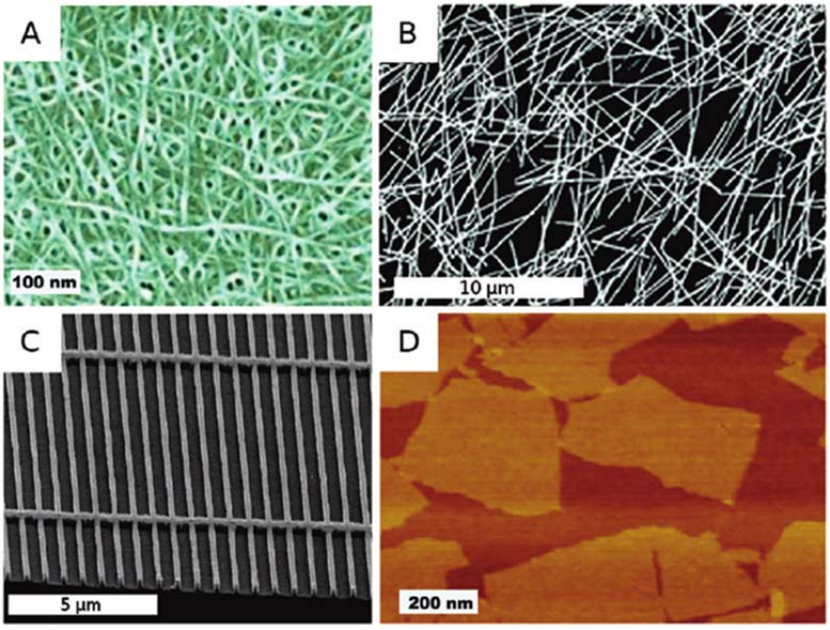

Figure 0.2 SEM micrographs of (A) CNT film, (B) silver nanowire network, (C) Au nanowire grating and (D) AFM of graphene flakes [15]

Due to the relatively small size of the nanoscale forms of highly conducting "wires" or "sheets", these materials can be dispersed in solvents to form suspensions which can be processed by low cost techniques, i.e. solution coating methods. The combination of less expensive raw material and low cost fabrication techniques has been very attractive for the continued research into these nano-materials and their potential applications.

1.1.2 Inkjet technology

Inkjet technology is a printing process in which droplets of ink are projected through sophisticated machinery onto a substrate material to form a predesigned and computer-determined pattern, as illustrated in Figure **0.3**.

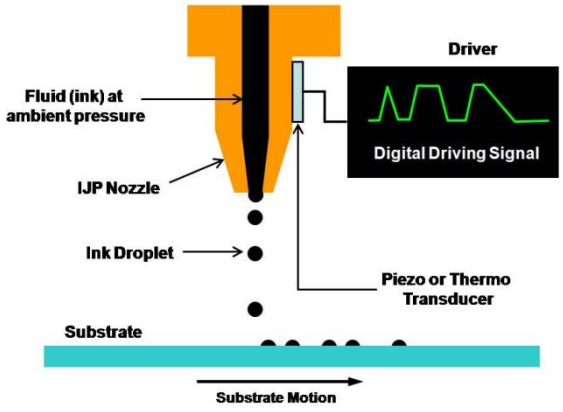

Figure 0.3 **Schematic illustration of drop on demand inkjet printing [19]**

Since the first inkjet printer was invented during the 1950s [20], inkjet technology has become a versatile printing method and been extensively utilised for various applications thanks to the continuous improvement in print quality and reduction of cost. As a precision micro dispensing (1-100 picoliters) tool, inkjet printing has numerous unique advantages compared with the conventional printing process, including no -contact with the substrate, high resolution, high printing speed, low cost and low material consumption. Therefore, the technology has been used in a wide range of applications in biomedical, electronic, photonic and sensors manufacturing [21] [22-25], as summarised in Figure 0.4.

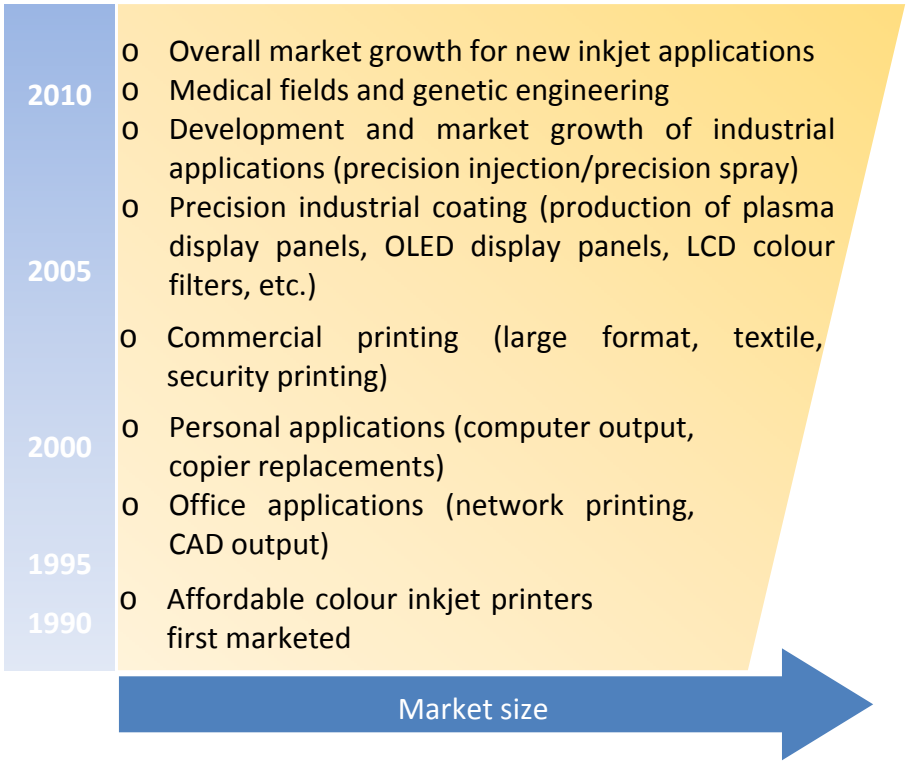

Figure 0.4 Applications of inkjet technology and market size (after ref. [26])

1.2 Problem statements and research motivation

Inkjet printing has been considered as an alternative in the fabrication of various types of TCPs in recent years. Numerous research and investigations have been primarily focused on this area using engineering materials including conductive polymers, TCOs, carbonaceous material and metals [27-34]. Some of the inkjet printed TCPs have been integrated into photovoltaic devices and exhibited acceptable performance [32, 35-39]. However, there have been several technical factors to overcome to further

commercialize such technology, which have included resolving the challenges in understanding the materials behaviour in ink formulation and printing process.

Firstly, except for metal inks, which have already been widely applied in inkjet printing, commercially available functional inks that can be deposited as TCPs are mostly designed for conventional fabricating approaches such as screen printing, spin coating, etc. Only limited types of functional inks designed for inkjet printing are provided by a few companies, for example, Orgacon™ PEDOT:PSS inkjet ink from AGFA [40] and ITO nanometal ink from ULVAC Technologies, Inc [41]. Nonetheless, the cost of such inks is often very high [42]. Moreover, the adjustments of the ink components are sometimes required in the processing of functional materials. For instance, Poly(3,4-ethylenedioxythiophene):poly(styrenesulfonic acid) (PEDOT:PSS), a prevalent conducting polymer, often requires modification by adding co-solvents or conductors to achieve better electric conductivity before it is integrated in devices. However, inkjet printing demands strict properties of the inks to be jetted, and as such the types of materials that can be deposited by inkjet printing are restricted. For this reason, so far only initial trials on preparation of TCPs using pristine functional material, i.e. without doping additives which can critically affect the functionality, have been carried out through inkjet printing in lab-scale studies. Therefore, further understanding as to how the characteristics of fluidic inks can be controlled so that stable droplets with good morphology can be obtained during the inkjet printing is essential, which can thereby extend the application of inkjet printing in the fabrication of functional TCPs.

There exists also another challenge in using inkjet printing, which is the control of feature size of ink deposition that ultimately determines the printing resolution for any viable application. As shown in Figure 0.5, the feature size of inkjet printing is normally higher than 10 μm, which is not competitive in the fabrication of integrated circuits (ICs). Theoretically, the attainable feature size of inkjet printing is governed by the droplet size generated through printing and the droplet interactions with the substrate surfaces [43]. Numerous methods and experimental trials have been implemented to reduce the feature size from these two aspects. Nonetheless, more effective approaches are still under investigations which may lead to future success.

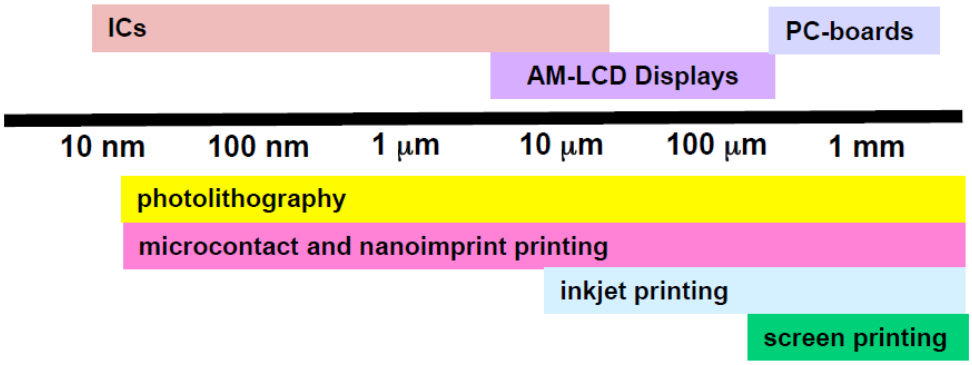

Figure 0.5 Feature size of different printing methods [44]

This work is initiated with a clear motivation to elaborate the fundamental aspects that are closely associated with the deposition of various patterns and thin films using inkjet printing techniques. This can allow the fabrication of various functional components or thin films such as conductive transparent films for photovoltaic applications.

1.3 Research aims and objectives

This PhD project has concentrated on various fundamental aspects encountered in the application of inkjet technology for printing TCPs. The work has involved ink formulation aiming to deliver functional inkjettable fluids which may be readily used for deposition of various patterns through inkjet printing, and the optimisation of inks and jetting process to enable robust printed patterns. The objectives that must be realised through various tasks have therefore been identified as follows:

1. To develop suitable methods for formulating inks with the functional properties as well as the characteristics suitable for inkjet process. This should be carried out by understanding the effect of the properties of inks on both the functional properties that can be achieved in the final deposited patterns and the effect on the formation of droplets in the process of inkjet printing.
2. To implement various inkjet printing trials to test the formulated inks for the generation of certain patterns including dots, tracks and films, and explore the application in both lab-scale experimental inkjet printers and commercial industrialised printers.
3. To optimise and enhance the electric conductivity of PEDOT:PSS thin films deposited by inkjet printing process, through incorporating conventional

enhancement approaches e.g. solvent annealing and doping with additional conductors, and to understand the mechanism of the improvements.

4. To investigate and evaluate the application of laser assisted inkjet (LIJ) technology in the printing of ITO inks, achieving the fabrication of fine crack-free ITO patterns using two types of inks that have been developed for inkjet printing.
5. To explore new approaches for the fabrication of TCPs through inkjet printing, in particular, *in-situ* approaches to the complex integration of multifunctional microstructures.

1.4 Statement of the main contributions to knowledge

1. The effect of relevant ink properties, including surface tension and viscosity on the formation of droplets from a commercial inkjet printhead was discussed. The results provide guidance for the formulation of inks for both lab-scale experiments and industrial production.
2. Two methods (solvent annealing and doping with conducting nano particulates) through which the electrical conductivity of PEDOT:PSS can be improved were proved to be compatible with inkjet printing. It was verified that inkjet printing is an applicable process to prepare PEDOT:PSS patterns with high functionality.
3. LIJ printing was for the first time applied in the preparation of ITO patterns. The printing parameters were optimised to achieve narrow ITO tracks with good morphology. It is found that LIJ is beneficial for the preparation of thick ITO patterns without inducing cracks.
4. A self-assembly synthesis method to fabricate semi-transparent silver thin film using inkjet printing was developed. The electrical and optical properties of the silver thin films prepared in the initial trials indicate that this method opens up a new processing route for the fabrication of metallic TCPs.

1.5 Thesis structure

This thesis contains eight chapters which can be divided into five sections, as shown in Figure 0.6, i) literature review; ii) methodology; iii) ink formulation and patterns printing; iv) printing of multi-functional patterns; and v) summary.

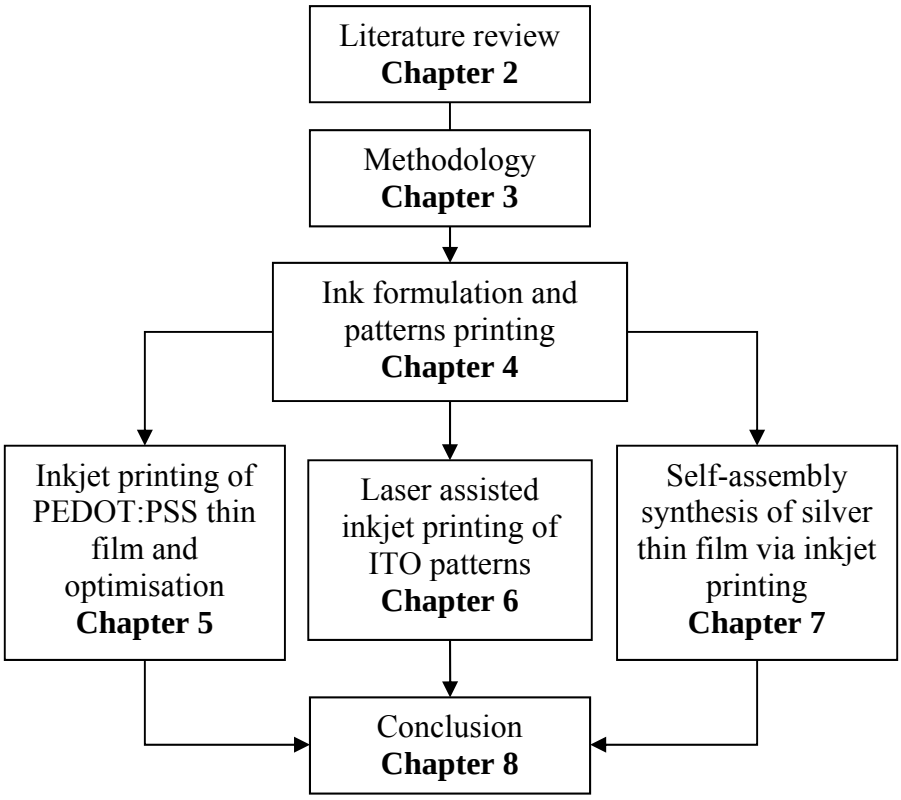

Figure 0.6 An overview of the thesis structure

The first section served as literature review (chapter 2) introduces inkjet printing including the principle and applications.

The second section (chapter 3) described the details of research methodology, technical approaches that are closely associated with the equipment and related tools used to prepare samples and characterisation, as well as the materials involved in this work.

The third section (chapter 4) provides a detailed investigation on the suitability of inkjet printing process, involving the formulation of inkjet inks and various process parameters used in the printing of patterns (i.e. dot, track and film) obtained through numerous printing trials. Simulation is also conducted to understand the effect of ink properties on the formation of droplets by considering the properties of inks and printing parameters.

The fourth section presents the main results of printing TCPs using three primary types of TCPs materials: PEDOT:PSS (chapter 5), ITO (Chapter 6) and silver (Chapter 7). Chapter 5 focuses on the preparation and optimisation of PEDOT:PSS thin films using inkjet process which includes the enhancement of electrical conductivity of the

deposited films through annealing treatments. In the printing of ITO described in chapter 6, simultaneous laser assistance for *in-situ* treatment of the inkjetted droplets is introduced which was merged with the inkjet system to achieve the fabrication of refined ITO patterns using two types of ITO inks prepared prior to the inkjet printing. In chapter 7, *in-situ* self-assembly synthesis of silver thin film that can serve as a transparent conducting thin film is described and the characteristics of the thin films obtained are compared with one another.

Finally, the major findings of the thesis, as well as some recommendations for future work, are summarised in the final section (chapter 8).

Chapter 2 Inkjet Technology

Inkjet is a non-contact dot-matrix printing technology in which droplets of ink are jetted from a small aperture directly to a specified position on a media to create an image. The first inkjet device was built by Elmqvist in 1951 [20]. After that, inkjet technology has been studied and improved frequently. In the 1970s, IBM [45] licensed the technology and adapted continuous inkjet technology (CIJ) for their computer printers. The first drop on demand (DOD) inkjet system was invented at the end of the 1970s and systems based on this technique were soon produced commercially [46, 47]. With the development of inkjet technology, the application of inkjet printers is no longer limited to imaging and marking. Inkjet has become a robust tool for the preparation of various patterns of functional materials.

Compared with other printing methods, inkjet printing has numerous unique benefits. There is no contact between the printhead and substrate during the printing, therefore it has the capability of printing on a wide range of substrates. The substrate can be rigid or flexible, rough or smooth; even 3D surfaces can be processed. The deposition of the droplets is accurate and data-driven, leading to high quality outputs. Additionally, inkjet is a low cost process with high material usage efficiency, with a possibility of customisation for mass production that has also been demonstrated [48]. However, one of the main challenges for inkjet technology is in the development of functional inks. Due to the specific rheological requirements for the inkjet inks, many inks are remaining in the experimental trial stage, instead of commercialization of production [49].

2.1 Classification [50, 51]

According to the principle of printing, inkjet technology can be broadly classified as continuous inkjet (CIJ) and drop on demand (DOD), with variants within each classification, as shown in Figure **0.1**.

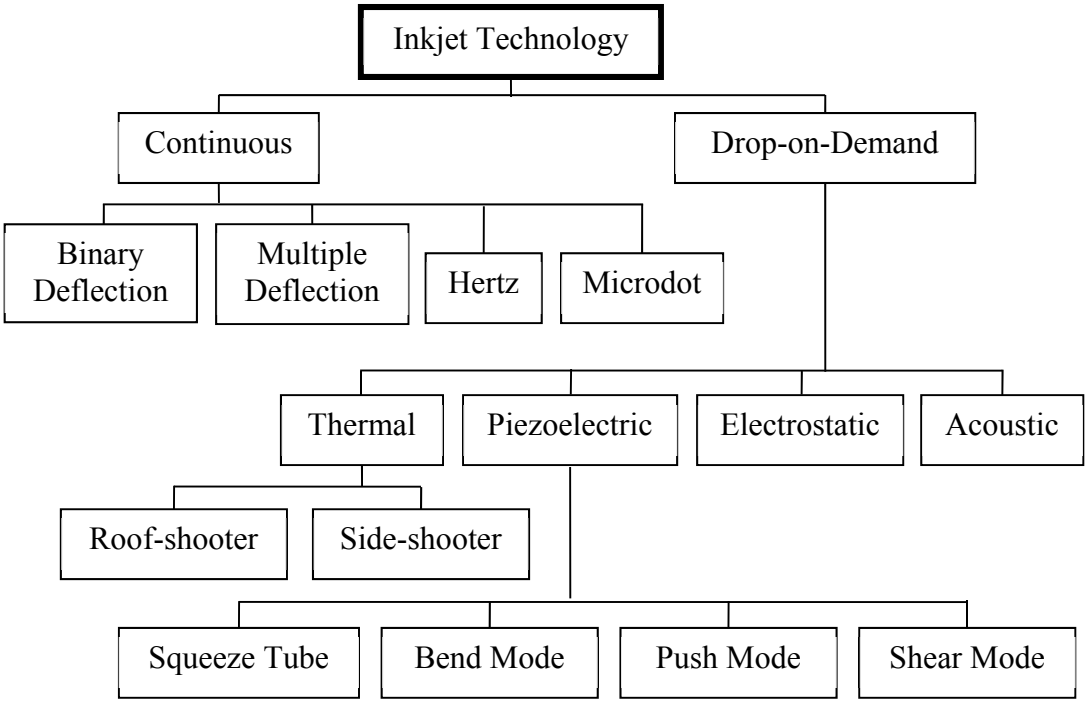

Figure 0.1 **Classification of inkjet technology (after [51])**

In CIJ, a pump directs liquid ink from a reservoir to microscopic nozzles creating a continuous stream of ink droplets by using high frequency vibration (typically 50 kHz to 175 kHz) to promote breakup of the jet by Rayleigh instability. The ink droplets are subjected to an electrostatic field to impart a charge. The charged drops are then either directly jetted to the substrate as printing drops or to a collection gutter for re-use after passing through a deflection field (Figure **0.2** (a)). In DOD mode, the drops are ejected as required (Figure **0.2** (b)). The drops are normally formed by a pressure pulse. The pressure pulse can be generated primarily using two methods, thermal and piezoelectric, which are the most common subcategories of DOD.

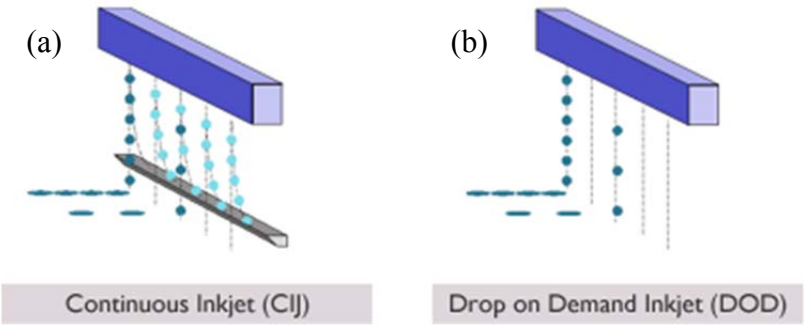

Figure 0.2 **Schematic of CIJ (a) and DOD (b) [50]**

In thermal inkjet configuration, the drops are formed by rapidly heating a resistive element in a small chamber which contains the ink of print. The high temperature (350-400 °C) causes the ink close to the heater to vaporize, creating a bubble which leads to a pressure pulse that forces the formation of drops through the nozzle (Figure 0.3 (a)). In piezoelectric inkjet configuration, the pressure pulse is caused by the distortion of a piezoelectric crystal when an electric field is applied (Figure 0.3 (b)).

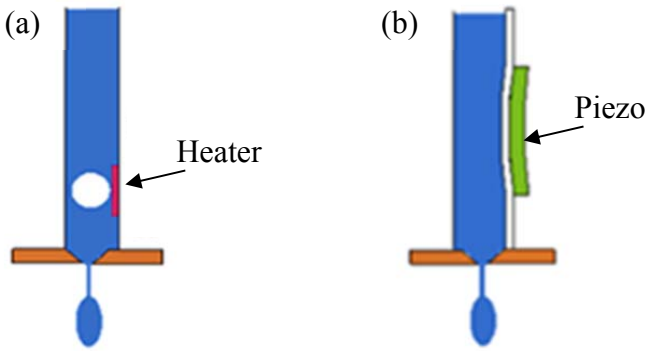

Figure 0.3 Schematic of thermal inkjet (a) and piezo inkjet (b) (after ref. [50])

The comparison of CIJ and DOD are summarized in Table 2.1. According to their advantages and disadvantages, CIJ and DOD are applied in different areas. The high drop ejection frequency of CIJ makes it suitable for high speed printing, such as labelling of packaging, while DOD is more suitable for applications requiring high precision.

Table 0.1 Comparison of CIJ and DOD

Type of inkjet		Printing speed	Resolution	Ink	Cost
CIJ		High	Low	Can be volatile Must be electrically chargeable	High maintenance
DOD	Thermal	Low	High	Special design required	Low cost for printhead
	Piezo	Low	High	Maximum ink development freedom	High cost for printhead

2.2 Inkjet inks

Four categories of inkjet inks which are primarily utilised commercially are phase-change, solvent based, water based and ultra violet (UV) curable inks. The advantages, disadvantages and applications of the four types of inks are summarized in Table 2.2.

Other types of inks such as oil-based and liquid toner are less prevalent therefore not listed. However, this classification is focussed on the conventional inks for image generation. Inks containing functional materials are mostly of the latter three forms.

Table 2.2 The advantages, disadvantages and applications of four types of inks [52]

	Advantages	Disadvantages	Applications
Phase-change	Very fast drying Environmentally friendly Good opacity High quality	Lack of durability Poor abrasion resistance	Barcodes on nonporous substrates
Solvent based	Good print quality Good image durability Wide range of compatible substrates Low cost Fast drying time	Environmental concerns Requirement for high maintenance	Choice for grand format and wide format
Water based	Relatively inexpensive Environmentally friendly	Requirement for porous or specially treated substrates	Desktop
UV curable	Very fast drying Environmentally friendly Wide range of compatible substrates High quality	Relatively expensive Requirement for special facilities	Wide format/flatbed sectors Niche applications

Ink properties including surface tension, viscosity, incorporated particle size, adhesion, cure rate and thixotropy need to be considered when formulating an inkjet ink [53]. Proper selection of these parameters is necessary to enable stable jetting of droplets with optimal morphology [54, 55]. Among these properties, viscosity, density and surface tension of the inks are of most concern as these parameters influence the drop formation mechanism and subsequent drop size under a given pulse wave. This study has concentrated on the viscosity and surface tension, because the inks adopted in this study are either solvent-based or water-based and the density of these inks is almost constant.

Several characteristic dimensionless numbers, i.e. *Re*, *We*, *Oh* and *Z,* have been utilized to represent the physical properties of inks. *Re* (Reynolds number) is the ratio of the inertial to viscous forces, while *We* (Weber number) describes the balance between inertial and capillary forces [56]. *Oh* (Ohnesorge number) is defined as the ratio between the square root of *We* and *Re*, and is a measure of the influence of the viscosity, which is independent of fluid velocity. *Z* is the inverse of *Oh*:

$$Re = \frac{\rho u a}{\eta} \tag{2.1}$$

$$We = \frac{\rho u^2 a}{\sigma} \tag{2.2}$$

$$\frac{Re}{We} = \frac{\sigma}{u\eta} \tag{2.3}$$

$$\frac{1}{Z} = Oh = \frac{(We)^{1/2}}{Re} = \frac{\eta}{(\sigma\rho a)^{1/2}} \tag{2.4}$$

Where ρ, u, a, σ and η are ink density, droplet velocity, characteristic length (the radius of the printing orifice), surface tension and viscosity, respectively.

The numbers mentioned above have been used to predict the possibility of droplet formation. Fromm [57] reported that droplets can be obtained when $Re/We > 2$. Reis et al. [58] regarded $1 < Oh^{-1} < 10$ to be the essential condition for a jettable ink. However, in Jang et al.'s study [59], the essential condition is demonstrated to be $4 < Oh^{-1} < 14$. When $Oh^{-1} < 4$, long-lived filaments may occur; when $Oh^{-1} > 14$, satellite droplets are likely to be generated. It has also been shown that low viscosity can make droplet ejection more fluent, but high surface tension may cause significant satellite droplets. However, a contradictory conclusion has been made by Ozkol et al. [60] who considered high viscosity and high surface tension can help to eliminate satellites. Xu et al. [61] suggested that *We* must be higher than a certain value to ensure the success of ejection, since a high value of *We* helps the drop elongation and initiates the necking of the drop. When $We > 9$, satellite droplets can be completely eliminated. Feng et al. [62] suggested a $Re < 5$ can avoid satellite droplets. The size of the droplets is also affected by the ink properties. Low viscosity and high surface tension is likely to result in big droplets [60, 63].

The contradictory conclusions are caused by the use of different printing nozzles, as each type of nozzle is more suitable for inks with certain properties. The study of effect of ink properties on the formation of droplets is beneficial for the formulation of proper ink to achieve good droplet morphology in inkjet process.

2.3 DOD deposition mechanism

The jetting process for inkjet printing can be divided into three phases: ejection phase, droplet flight phase and impact phase.

2.3.1 Ejection phase

The formation of droplets is critical in inkjet printing. Stable droplets with good morphology can ensure high quality output, while failures (i.e. deviation of the droplet trajectories from the nozzle direction and satellites) may significantly decrease the precision and resolution of printing. The ejection process can be described as follows [64]:

When a pressure pulse is generated in the chamber, ink in the nozzle is accelerated and pushed out of the orifice. As a result, a liquid column with a hemi-spherical head is formed (1-4 in Figure **0.4**). The liquid column is stretched due to the difference in axial velocity between the head of the column and the liquid at the exit of the nozzle. Affected by the negative pressure associated with the next pulse, a neck appears at the end of the liquid column during the stretching (6-9 in Figure **0.4**). Finally, the liquid column breaks from the orifice, and a droplet with long tail is obtained (10 in Figure **0.4**). As an identical velocity is not achieved for all parts of the droplet, the droplet may break into fragments, therefore satellite droplets can be formed (11-15 in Figure **0.4**). Satellite droplets can either merge with the primary drop (16-17 in Figure **0.4**) or become a permanent satellite droplet, which is determined by the relative velocities of the primary drop and satellite.

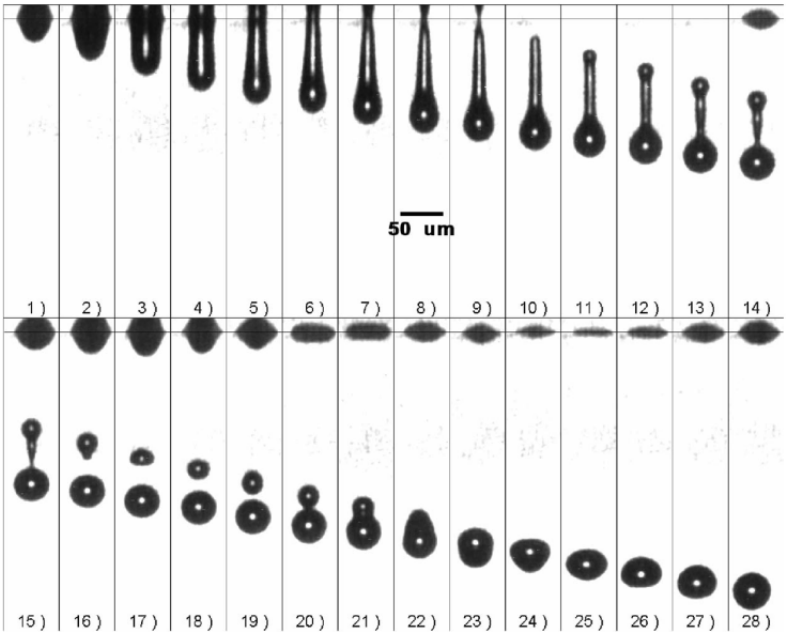

Figure 0.4 **Sequence of series images taken during the DOD drop formation [64]**

2.3.2 Droplet flight phase

In droplet flight, the droplet shape has been shown to be primarily determined by the competition between surface tension and inertia and its shape changes among a prolate spheroid, a sphere and an oblate spheroid if viscous effects within the liquid are not considered, as simulated in Figure **0.5** [65]. However, in a real situation, the viscous forces with the liquid can resist shearing flow within the liquid, which leads to the amplitude of oscillation diminishing and the shape of the droplet gradually become close to sphere, which can be clearly observed in Figure 2.4.

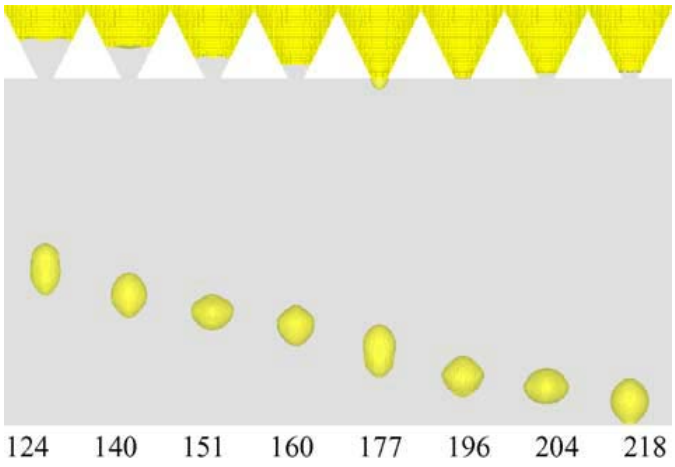

Figure 0.5 **Simulated liquid droplet during flight [65]**

2.3.3 Impact phase

The deposition mechanism during the impact phase can be divided into four stages. I) At the earliest stage of impact, the shape of the droplet resembles a truncated sphere. II) The interface between the droplet and substrate increases with increasing time, and a thin film bounded by a rim is formed. III) The drop begins to recede. And finally IV) the droplet spreads until it reaches equilibrium.

The impact phase can be affected by a number of parameters including impact velocity, drop diameter, liquid viscosity and surface tension, surface wettability and roughness. The different influencing parameters change in their importance during the four stages. The impact velocity and drop diameter affects the spreading process in stage I and the expansion speed of the drop in stage II. The impact velocity also plays an important role in the receding of the drop (stage III). The surface tension and viscosity of the liquid affects the deformation of the drop in stage II, stage III and stage IV. The surface wettability and roughness of the substrate always influence the spreading of the contact line, which engages stage I, stage II and stage IV. [66] [67][68]

2.4 Optimisation of feature size

The printing resolution is limited by the feature size (the size of a single dot), as patterns printed with inkjet technology are based on single dots. The feature size is determined by the drop diameter and the spreading process [43]. Correspondingly, the feature size can be reduced by diminishing the droplet diameter and suppressing the spreading of the droplets on the substrate.

2.4.1 Reduction of droplet size

Commercially available print heads can eject 1 pL drops that yield approximately 20 μm line widths on substrates pre-treated by surface treating the material to suppress the spreading of the drops on the substrate [69]. This is in many cases sufficient for IC contacts and printed circuit board (PCB) wiring purposes. Murata et al. [70] developed an inkjet system which allows arrangements of dots with a submicron minimum size. Using an ultra-fine silver paste with a particle size of around 5 nm, ultrafine traces of only a few micrometres in width could be achieved without any pre-patterning treatment of the substrate. Park et al. [71] employed electrohydrodynamic liquid

ejection in an inkjet process to achieve a sub-micrometre printing resolution, which has potential applications in high-resolution printed electronics.

2.4.2 Control of spreading

To control the droplet spreading, two main categories of techniques have been developed. One category is altering the surface condition of the substrates, which can consequently lead to a reduced feature size under steady state condition. InSon et al.'s study [72], SAMs (Self-Assembled Monolayers) have been adopted to treat the surface of the glass substrate to control the contact angle of ink droplet. Hutt et al. [73] have identified a method for depositing SAMs of octadecanethiol onto copper surfaces leading to freshly prepared materials with no detectable oxygen inclusion, which has also proved effective in altering the wettability of the copper surface by fluids.

The other category is accelerating the drying or solidification speed of droplets to suppress the spreading process. Kang et al. [74] have varied the substrate temperature from room temperature to 75 °C and found that the printed line width tends to decrease as the substrate temperature increases due to the enhanced evaporation rate of the solvent. Inkjet technology has also been assisted with radiation curing to reduce the feature size. Radiation curing technology has been used in the graphics arts industry for more than 20 years. The most commonly used radiation sources include ultraviolet (UV), laser and electron beams (EB) [53, 75, 76].

Chapter 3 Experimental Methods

The aim of this chapter is to provide a detailed description of the equipment and materials utilized in this study, as well as the procedures of sample preparation and characterisation methods.

3.1 Inkjet printers

Three representative DOD inkjet printers were employed in this study. The Microfab Jetlab®4 inkjet printer is a standard printer for experimental use. The requirement of this printer on the properties of inks is not as strict as commercial inkjet printers, and the single nozzle makes it more convenient to control and observe the printing process. Therefore it can be used in the investigation of printing basic patterns. Different from the Microfab Jetlab®4 inkjet printer, the IIA-1501 inkjet printer uses multi-nozzle printheads which are widely used in commercial inkjet printers. Hence it has advantages in investigating the formulation of inkjet inks which can be commercially applied. The laser assisted inkjet (LIJ) printer is a special printer in which a laser emitting device is incorporated. This LIJ printer can be employed to study the effect of laser radiation on the printing of patterns, aiming to achieve narrow tracks with high aspect ratios.

3.1.1 Principle of inkjet printer

Although the three printers were supplied by different manufacturers, they are based on the same working principle and consist of three sub-systems: dispensing system, computer control system and mechanical motion system. A schematic diagram of these inkjet printers is given in Figure 0.1.

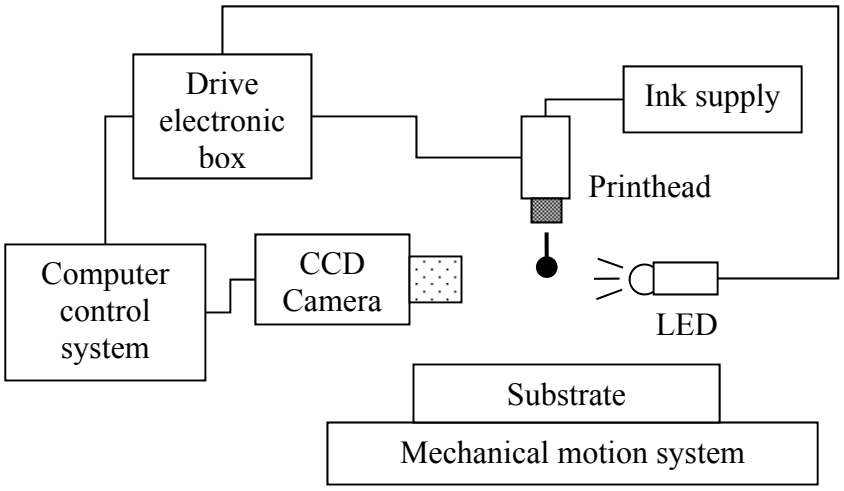

Figure 0.1 Schematic diagram of principle of DOD inkjet printer

The droplets are formed by the pressure pulse resulting from the motion of the piezoelectric crystal in the printhead. The piezoelectric motion is controlled by a signal output from the computer control system. During the ink jetting process, substrates on which the inks will be deposited are placed on a stage which is usually driven by electrical motors and able to move in a plane (the X-Y plane) orthogonal to the jetting direction. The light-emitting diode (LED) is used to illuminate the droplets and is strobed in synchronisation with the signals sent to the piezoelectric crystal, as such images of the droplets generated from the nozzle can be captured by the charge-coupled device (CCD) camera and then further analysed using the supporting software.

3.1.2 Jetlab®4 inkjet printer

Microfab Jetlab®4 inkjet printer (Figure 0.2) was employed in the printing of silver nanoparticle inks and PEDOT:PSS inks (Chapter 4 and Chapter 5).

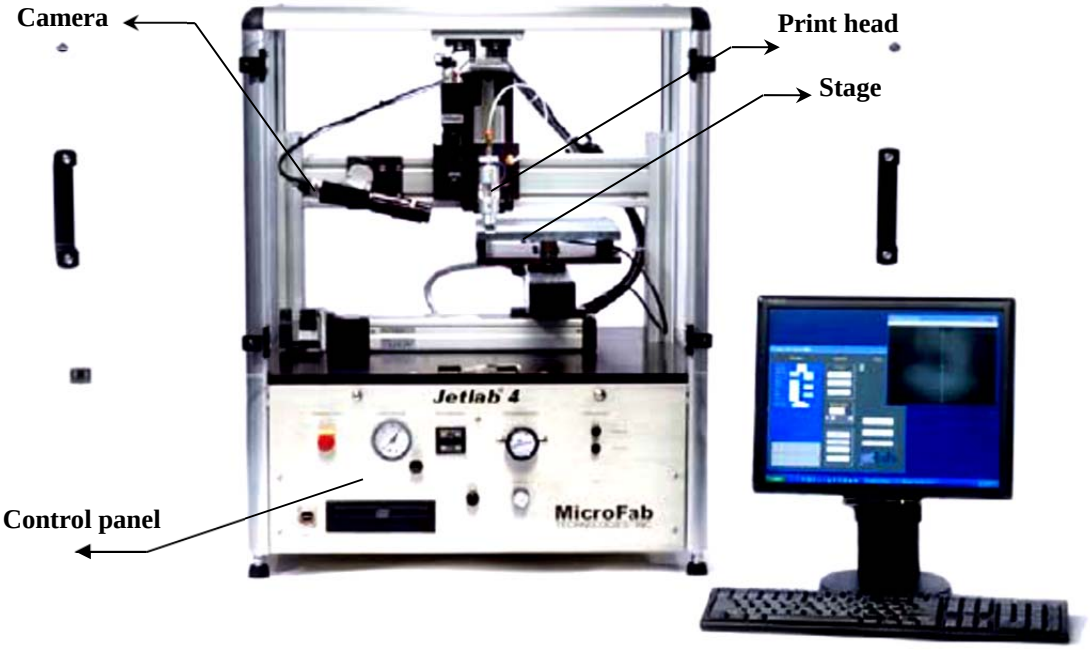

Figure 0.2 Microfab Jetlab® 4 inkjet printer

3.1.2.1 Dispensing system

Figure 0.3 shows a schematic illustration of the dispensing printhead of the Jetlab® 4 inkjet printer. The whole printhead assembly is comprised of a reservoir mount, a fluid reservoir and a micro dispensing device. The reservoir mount provides mechanical support to the dispensing device while the latter is in charge of jetting droplets. Dispensing devices with orifice diameters of 20 μm, 40 μm or 60 μm are available. A 60 μm orifice dispensing device was utilised in this study, as inks containing particles were involved and blockages occur less easily for larger orifices.

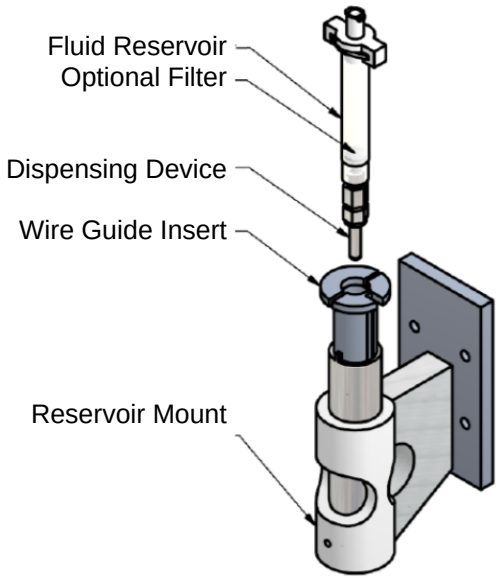

Figure 0.3 Schematic illustration of dispensing printhead of jetlab® 4 printer [77]

3.1.2.2 Computer control system

The Jetlab® 4 printer waveform is determined by parameters including rise time, dwell time, fall time, echo time, final rise time and voltage, as shown in Figure 0.4. These parameters need to be optimised for each specific ink to achieve droplets with the best morphology. The value of these parameters can be set on the relevant window of the supporting software. In this study, both rise time and fall time were fixed at 3 µs. The major adjustments for optimisation of parameters were primarily related to the voltage and dwell time. Normally, the recommended dwell time should be larger than 15 µs, otherwise the droplets can easily become unstable. A back pressure is provided at the top of the fluid reservoir to prevent the ink from dripping out of the nozzle spontaneously. The value of the back pressure is typically set between -2.0 and -0.6 Pa.

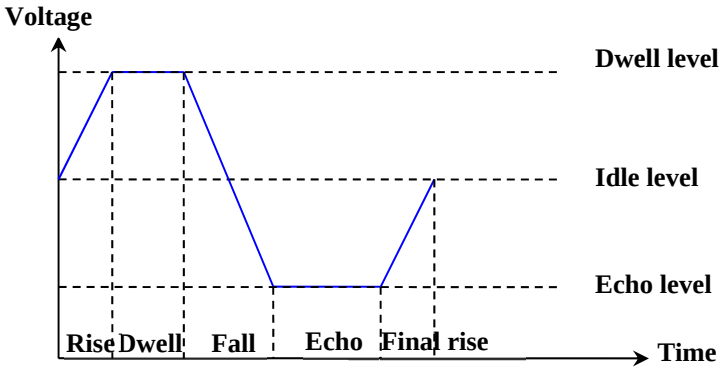

Figure 0.4 Waveform of jetlab® 4 printer

3.1.2.3 Mechanical motion system

The printing area of the Jetlab® 4 inkjet printer used is 160×120 mm^2. The stage can be moved in the *X*-*Y* plane controlled by a pre-designed programme and can be heated up to 100 °C. The distance between the nozzle of the printhead and the stage can be adjusted by shifting the position of the printhead in the *Z* axis to suit substrates with different thicknesses [78] .

3.1.3 Fanjet IIA-1501 inkjet printer

A IIA-1501 inkjet printer from Fanjet Co., Ltd. (Figure 0.5) was employed in the printing trials for inks containing silver nanoparticle doped with PEDOT:PSS (Chapter 5) and for semi-transparent silver thin films (Chapter 7).

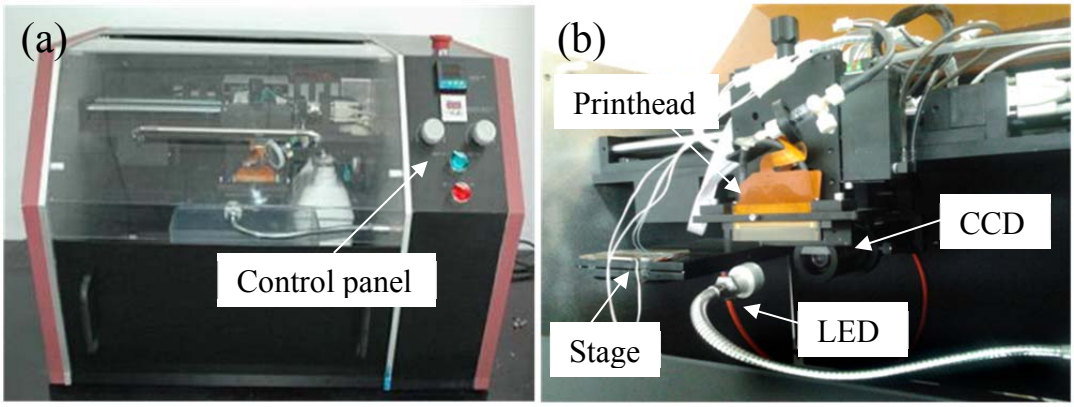

Figure 0.5 Fanjet IIA-1501 inkjet system (a) and partial enlarged detail (b)

3.1.3.1 Fanjet Dispensing system

A Nova-Q JA128/80 AQ printhead from Spectra Co. Ltd. is integrated within the IIA-1501 inkjet printer. An exploded view of the printhead is shown in Figure 0.6. The printhead provides 128 inline, individually addressable nozzles generating a typical droplet size of 80 pL under optimal conditions. This printhead is suitable for jetting inks with a surface tension of 20~40 dynes/cm and a viscosity of 5~35 mPas [79].

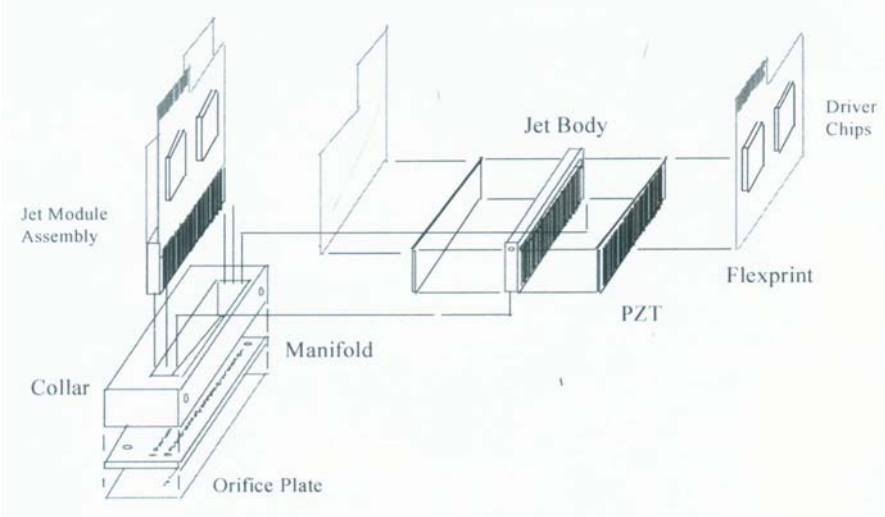

Figure 0.6 Exploded view of Nova-Q JA128/80 AQ [80]

3.1.3.2 Computer control system

The waveform and printing frequency can be controlled through the computer control software. The waveform of IIA-1501 inkjet printer is similar to the Jetlab® 4 printer. The frequency range is from 100 Hz to 45 KHz. The software contains a real time observation function which can help to analyse the velocity and volume of the droplets with a measuring accuracy of 2%~5%. The format of images that can be recognized by the software and further implemented in printing includes BMP, JPG, GERBER, and AUTOCAD. A FB-36/7 oil-free air compressor is incorporated in the printer to provide back pressure.

3.1.3.3 Mechanical motion system

The printing area of the IIA-1501 inkjet printer is 100 × 100 mm^2. The printing resolution can be altered from 150 ×150 dpi (dots per inch) to 1200 ×1200 dpi (equivalent to≈ 35 to 2232 dots/mm^2). The stage can be heated up to 100 °C.

3.1.4 Laser assisted inkjet (LIJ) printer

A laser assisted inkjet (LIJ) printer (Figure 0.7) at the National Institute of Advanced Industrial Science and Technology (AIST) in Japan was employed in the printing of metal organic decomposition (MOD) ITO inks and ITO nanoparticle inks (Chapter 6). This system was built by the Manufacturing Machinery Division of the Manufacturing Systems Department at AIST. Beside the three main systems introduced in Section

3.1.1, a laser emitting system is incorporated to enable an *in-situ* preheating on the substrate.

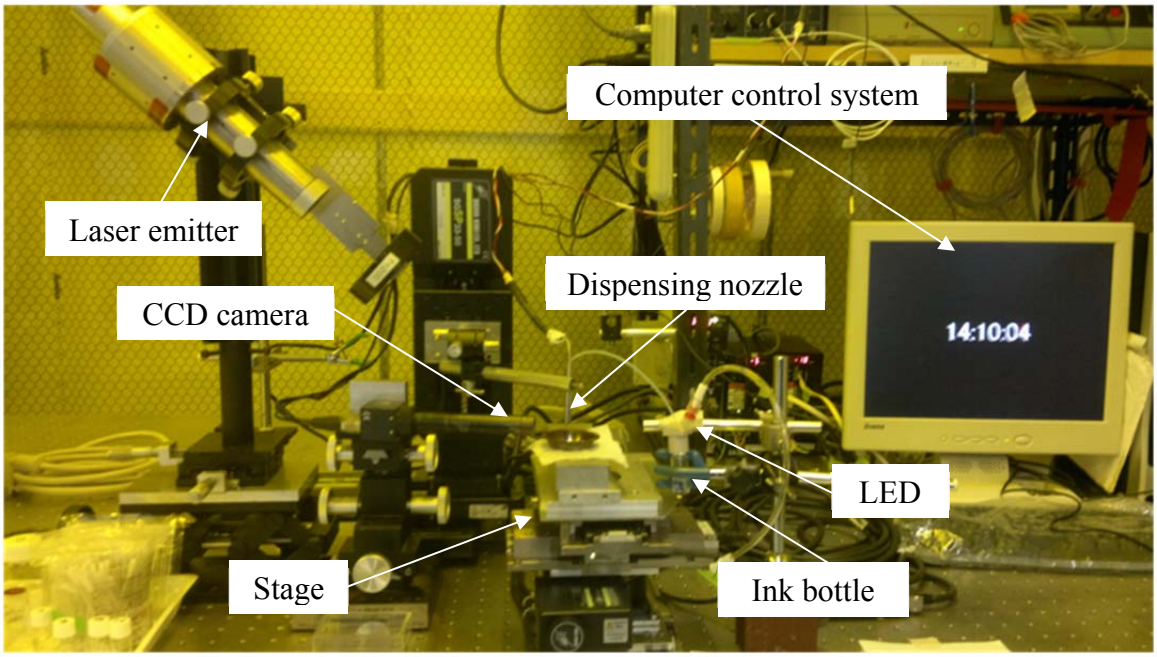

Figure 0.7 Laser assisted inkjet printer at AIST, Japan

3.1.4.1 Dispensing system

A Microjet IJHB printhead with an orifice diameter of 90 μm is utilized as the dispensing printhead. This printhead is designed for inks with high surface tension, i.e. up to 73 dynes/cm. Inks that the machine works with can range in viscosity from 0.5 to 10 mPas.

3.1.4.2 Computer control system

In the LIJ control system, only the printing frequency, voltage and dwell time can be manually adjusted through the supporting software. The ink bottle is connected to the atmosphere therefore no back pressure is induced.

3.1.4.3 Laser emitting system

The laser emitting system is integrated by Kantum Electronics Co., Ltd. including a CO_2 power supply from Synrad, Inc., a power controller, and the optical set. The maximum power the laser can supply is 10 W. The wavelength of the laser is 10.6 ± 0.03 μm. The laser energy distribution is approximately a Gaussian profile [81]. The diameter of the laser spot is 1mm.

3.2 Materials

3.2.1 Inks & precursors

3.2.1.1 PEDOT:PSS

The PEDOT:PSS solution utilized in this study was purchased from Sigma-Aldrich co. Ltd. The composition and concentration of the solution and the band gap and conductivity of the resulting PEDOT:PSS layer are given in Table 3.1.

Table 0.1 Properties of PEDOT:PSS solution from sigma-aldrich [40]

Composition	PEDOT, 0.5 wt. %
	PSS, 0.8 wt. %
Concentration	1.3 wt. % dispersion in H_2O
Band gap	1.6 eV
Conductivity	1 S/cm

3.2.1.2 Silver nanoparticles ink

The silver nanoparticle ink utilised in this study was SunTronic U5603, purchased from SunJet. This silver suspension ink is based on organic solvents, i.e. ethanediol and ethanol. The properties of the ink are given in Table 3.2.

Table 0.2 Properties of SunTronic U5603 silver ink from Sunjet

Appearance	Liquid
Odour	Odour of alcohol
Volatility description	Highly volatile
Boiling point	60~90 °C @ 760 mm Hg
Relative density	0.80 @ 25 °C
Viscosity	7~14 cps @ 25 °C
Solubility value	80 g/100g H_2O @ 20 °C

3.2.1.3 Metal Organic Decomposition (MOD) ITO ink

The metal organic decomposition (MOD) ITO ink is from Kojyundo Chemical Laboratory Co., Ltd. The components of the ink are given in Table 3.3.

Table 0.3 Components and their concentration of MOD ITO ink

Component	Concentration (wt. %)
In_2O_3	4~6
SnO_2	0.2~0.4
Ethylhexoic acid ($C_4H_9CH(C_2H_5)COOH$)	16~21
Organic additive	4~6
Butyle Acetate ($CH_3COOC_4H_9$)	69~74

In the MOD ITO ink, the indium oxide and tin oxide are combined with the 2-Ethylhexoic acid, forming a structure of *M(COOR)n* which can be dissolved in the organic solvent (butyle acetate). After deposition, the patterns printed with MOD ITO ink need to be baked first in air at 550 °C for 30 min and then in vacuum at 550 °C for 30 min to enable the decomposition of the metal organic material:

$$M(COOR)n \rightarrow MxOy + H_2O + CO_2 \quad (3.1)$$

3.2.1.4 ITO nanoparticle ink

The ITO nanoparticle ink was sourced from ULVAC, Inc. Some properties are given in Table 3.4.

Table 0.4 Properties of ITO nanoparticle ink

Concentration	20 wt.%
Average particle size	4 nm
Solvent	Cyclododecene
Viscosity	5~10 mPas

After deposition, the patterns printed with this ITO nanoparticle ink had to be baked first in vacuum at 230 °C for 60 min and then in air at 230 °C for 60 min.

3.2.2 Additives

In this study, various additives were necessary to functionalise the inks so that they are more inkjettable. These additives utilized in the formulation of inks and their suppliers are given in Table 3.5.

Table 0.5 Chemicals utilized in ink formulation and the sources

	Chapter 4	Chapter 5	Chapter 6	Chapter 7
Glycerol	Sinopharm Chemical Reagent Co., Ltd.	Sigma-Aldrich Co. LLC. (5.2) Sinopharm Chemical Reagent Co., Ltd. (5.3)	-	Sinopharm Chemical Reagent Co., Ltd.
Sodium Dodecyl Benzene Sulfonate (SDBS)	Sinopharm Chemical Reagent Co., Ltd.	-	-	Sinopharm Chemical Reagent Co., Ltd.
Poly(vinylpyrrolidone) PVP	Sinopharm Chemical Reagent Co., Ltd.	-	-	-
JC-601 (a commercial surfactant)	Guangdong Cosmic Digital Technology Co., Ltd.	Guangdong Cosmic Digital Technology Co., Ltd.	-	Guangdong Cosmic Digital Technology Co., Ltd.
Ethanol	Sinopharm Chemical Reagent Co., Ltd.	Sinopharm Chemical Reagent Co., Ltd.	-	Sinopharm Chemical Reagent Co., Ltd.
Tetradecane	-	-	Kojyundo Chemical Laboratory Co., Ltd.	-
Toluene	-	-	Kojyundo Chemical Laboratory Co., Ltd.	-

3.2.3 Substrates

The inkjet printing trials have been implemented on various potential substrates that can be associated with different applications. The substrates utilized in this study and the sources are provided in Table 3.6.

Table 0.6 Substrates utilized in the printing and the sources

	Chapter 4	Chapter 5	Chapter 6	Chapter 7
Microscope slides	Fisher Scientific UK Ltd.	Fisher Scientific UK Ltd. (5.2) Mingquan instrument Co., Ltd. (5.3)	Muto Pure Chemicals Co., Ltd.	Mingquan instrument Co., Ltd.
HN Polyimide film	DuPont UK Ltd.	-	-	-
Hydrophobic paper	Reynolds®	-	-	-
FR-4 epoxy laminate sheet	P. W. Circuits Ltd.	-	-	-

Before printing, the substrates were normally cleansed by immersing in an ethanol filled ultrasonic bath for 5 min and then dried with an air blower.

3.3 Characterization and analysis

3.3.1 Measurement of conductivity

3.3.1.1 Conductivity of tracks

Microscope slides with a conductive pattern were prepared for the conductivity measurement of the printed tracks in this study, as shown in Figure 0.8. The patterns, which are composed of a 20 nm thick titanium layer covered by a 100 nm thick gold layer, were prepared through photo lithography and vapour deposition.

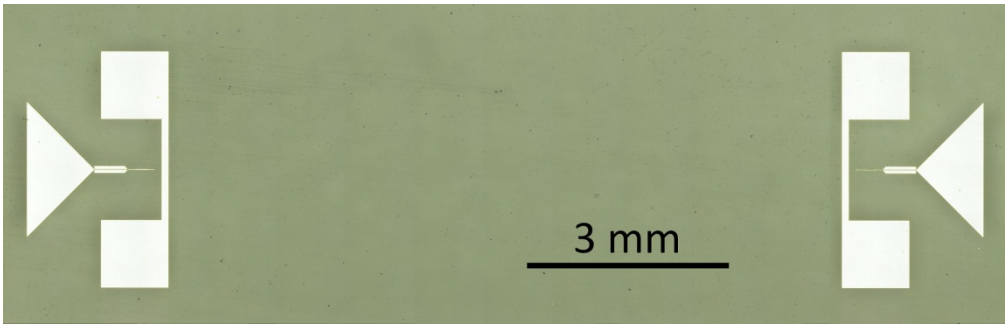

Figure 0.8 Patterns for conductivity measurement of tracks

In the printing of tracks, the deposition was started from one triangle pad and terminated at the other triangle pad, intersecting the lines connecting the square pads. The resistances, R, of the tracks were measured using either a multi-meter through two of the square pads or a four-point probing through the four square pads. Then the resistivity ρ is calculated using the following formula:

$$\rho = \frac{RA}{l} \tag{3.2}$$

Where *A* is the cross sectional area of the track (usually obtained from a measured cross sectional profile) and *l* is the length of the track which was fixed at 10 mm in this work. The conductivity *C* is the reciprocal of resistivity:

$$C = \frac{1}{\rho} \tag{3.3}$$

3.3.1.2 Conductivity of thin films

A Keighley Model 580 Micro-ohmmeter using four-point probing was employed to measure the sheet resistance of thin films deposited in this study. A schematic of a four-point probe arrangement is given in Figure 0.9. When a current is input through the two outer probes, the sheet resistance of the thin film can be calculated by measuring the voltage difference *V* between the inner probes. The distances between the probes *S1* = *S2* = *S3* = 1 mm. Assuming the film area is large enough to be treated as infinite, E is the electric field and j is the current density, the following equations can be deduced [82]:

$$E(x) = j(x)Rs \tag{3.4}$$

$$\mathrm{V} = \int_{S1}^{S1+S2} 2E(x)dx \tag{3.5}$$

$$j(x) = \frac{I}{2\pi x} \tag{3.6}$$

$$\mathrm{V} = \frac{R_S I}{\pi} \int_{S1}^{S1+S2} \frac{dx}{x} \tag{3.7}$$

$$\mathrm{V} = \frac{R_S I}{\pi} \ln {}^{S1+S2}_{S1} = R_s I \frac{\ln 2}{\pi} \tag{3.8}$$

$$R_s = \frac{\pi}{\ln 2} \frac{V}{I} \approx 4.53 \frac{V}{I} \tag{3.9}$$

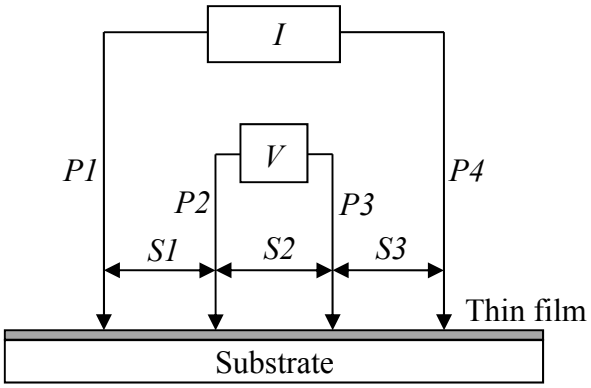

Figure 0.9 Schematic structure of four-point probe measurement of sheet resistance

In the measurements for this study, the input current was fixed at I = 4.5320 μA. This fixed value can simplify the calculation as the value of the sheet resistance (kΩ/sq) will be numerically the same as the voltage difference V (mV). Five measurements were taken on each sample at different locations and then a mean value obtained. To calculate the conductivity C (S/cm), the following formula can be used:

$$C = \frac{1}{\rho} = \frac{1}{R_s h} \tag{3.10}$$

Where h is the thickness of the thin film.

3.3.2 Transparency

A Cary 50 spectrophotometer was employed to measure the transparency of the PEDOT:PSS thin films (section 5.3 in chapter 5). A Cary 5000 spectrophotometer was employed to measure the transparency of silver nanoparticle doped PEDOT:PSS thin film (section 5.2 in chapter 5) and silver thin films (chapter 7). A Model 1240 UV spectrophotometer from Shimadzu co. Ltd. was employed to measure the transparency of ITO thin films in chapter 6. All the measurements were carried out on the patterns together with the substrates. The transmittance of the substrates was also given in the testing results as a reference.

3.3.3 Surface profile

Ambios XP-2 and Zygo NewView 5000 surface profile meters were employed in the characterization of patterns printed with the Jetlab® 4 inkjet printer (Chapter 5), while

an ET 4000A Surfcoder was employed in the characterization of patterns printed with the LIJ system (Chapter 6). The measurement principles of these three profile meters are different. The Zygo NewView 5000 is based on the interference of light, while the other two equipments measure by contacting the object with a probe. The Zygo NewView 5000 is therefore more precise and with no damage to the samples. However the measurements carried out by the Ambios XP-2 and ET 4000A require less time and the operation is also more convenient. Considering these advantages and disadvantages, the Zygo Newview 5000 was mainly used to observe the surface profiles of the inkjet printed patterns, whereas the Ambios XP-2 and ET 4000A were used to measure the cross sectional profile of tracks and the thickness of thin films. The measuring resolution of the profile meters is nano meter scale.

3.3.4 AFM

A Dimension 3100 atomic force microscope (AFM) with sub-nm height-measurement capability was employed to analyse the microstructure of PEDOT:PSS (Chapter 5) and ITO (chapter 6). The AFM was switched to tapping mode in this study to achieve high resolution, with a scan rate fixed at 0.5 Hz. Both height imaging and phase imaging were utilised during the analysis. For the height imaging maps the dark and bright regions correspond to the valleys and hills of the surface respectively. The phase imaging maps can reveal different components within composite materials through monitoring the variations in surface properties such as elasticity, adhesion and friction.

3.3.5 SEM

Three scanning electron microscopes (SEM) were employed. The models and corresponding applications in this study are listed in Table 3.7.

Table 0.7 Model and corresponding application of SEM employed in this study

Model	Application
Carl Zeiss (Leo) 1530 VP	Observation of PEDOT:PSS thin films (Chapter 5)
JEOL JSM-6060A	Observation of ITO patterns printed with LIJ system (Chapter 6)
Quanta 200 (FEI)	Observation of in situ synthesised silver grids (Chapter 7)

3.3.6 TEM

A Tecnai G2 20 transmission electron microscope (TEM) from FEI was employed in the observation of silver nanoparticles (Chapter 5). To prepare the samples, the composites containing silver nanoparticles were dispersed into ethanol using an ultrasonicator, and a drop of each suspension was placed over a carbon coated microscopic copper grid. After testing, the obtained TEM images were analysed using Nano Measurer 1.2 software to investigate the size distribution of the nanoparticles. Nano Measurer 1.2 is able to generate statistical curves based on manually measured data.

3.3.7 XRD

X' Pert PRO X-ray diffraction (XRD) from PANalytical B. V. was employed to characterise the composition and morphology of the silver nanoparticles (Chapter 5). The Scherrer Equation [83] was used to calculate the theoretical diameter of the nanoparticles based on the obtained XRD patterns through diffraction line broadening analysis:

$$B(2\theta) = \frac{K\lambda}{L\cos\theta} \tag{3.11}$$

Where B is the mean size of the nanoparticles, K is the shape factor, λ is the X-ray wavelength, L is the line broadening at half of the maximum intensity in radians, and θ is the Bragg angle.

3.3.8 Viscosity

Viscosity is a measure of a fluid's resistance to flow. A Brookfield RVDV-II +Pro viscometer was employed to measure the fluid viscosity at the required shear rates. The principal of operation of the DV-II +Pro is to drive a spindle through a calibrated spring. The viscous drag of the fluid against the rotating spindle is measured by the spring deflection. Spring deflection is measured with a rotary transducer. The measurement range of a DV-II +Pro is determined by the rotational speed of the spindle, the size and shape of the spindle, the container the spindle is rotating in, and the full scale torque of the calibrated spring. As the viscosity of the liquids in this study is normally smaller

than 100 cps, spindle 1 was adopted in the measurements. The rotating speed of the spindle was set to 60 rpm.

3.3.9 Surface tension

3.3.9.1 Surface free energy of substrates

The surface free energy of the substrates was measured using a Dataphysics OCA 20 by measuring the contact angles of water and diiodomethane on the surface of the substrate. The surface free energy of the substrate was then calculated based on the obtained contact angle values.

3.3.9.2 Surface tension of liquids

A Phoenix Alpha surface tension meter was employed to measure the surface tensions of the liquids used in the jetting experiments. During the measurement, 1 mL liquid was injected to a syringe and a pressure was then applied on the plunger to form droplets at the end of the stainless steel needle. The surface tension of the liquid can be calculated through measuring the diameter of the droplets.

Chapter 4 Ink Formulation and Pattern Printing

This chapter focuses on the preparation of the inks for the next stage of the research. The study starts with ink formulation, so that the content of the inks can be freely modified in the future work. On the other hand, the functional inks developed in this work can also be adapted for use in different printers by changing the properties according to the formulating methods.

The formation of droplets from a commercial printer has been simulated with FLUENT to provide theoretical guidance for the ink formulation. The simulation was firstly calibrated referring to the experimental results and then used to predict the printing behaviour of inks with various properties after a good agreement had been obtained. The effects of surface tension and viscosity on the formation of droplets have been studied with the assistance of simulation.

After the ink formulation, printing of patterns (i.e. dots, tracks and films) is investigated. The four types of commonly used substrates listed in T3.6 were utilized to investigate the effect of preheating on dot printing. Optimal preheat temperature was researched for each substrate to minimize the feature size. A mathematical model has been established to analyse the most critical factors in this process. During the track printing stage, the degree of overlap between successive dots and multi-layer printing were studied to ascertain their benefits in achieving continuous and homogenous tracks. Two methods for the control of film thickness are discussed in the printing of films.

4.1 Ink formulation

4.1.1 Introduction

The major components of the inks developed in this work as well as their effect on the main properties of the inks are shown in Figure 0.1. Deionized water was adopted as the solvent to carry soluble functional materials, metal nanoparticles or the mixture thereof. Surfactant was added to reduce the surface tension of the ink, while glycerol was used to adjust the viscosity. Ethanol served as a co-solvent which can further reduce the surface tension of the ink and, at the same time, facilitates the evaporation of solvent. Dispersants can play a role in stabilising the inks that contain nanoparticles. However, they were not included in this work as the inks prepared are relatively stable.

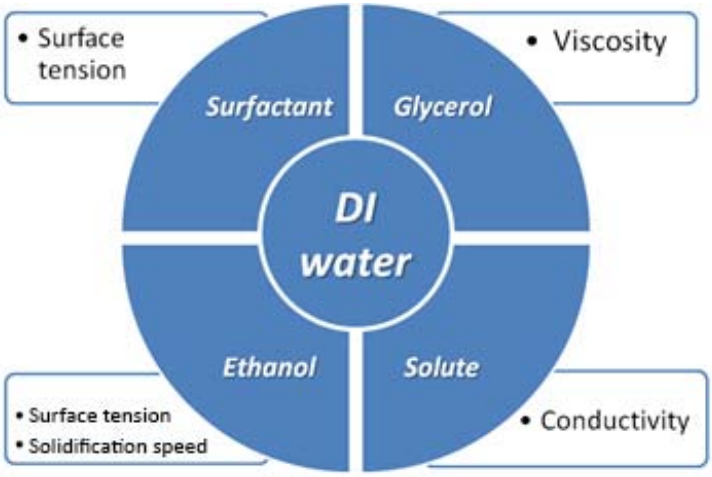

Figure 0.1 Components of self-developed water based inkjet ink and their properties that can affect characteristics of inks

4.1.2 Properties optimisation

4.1.2.1 Viscosity

The viscosity of a liquid mixture can be predicted using a three-step procedure [84]. The first step is to calculate the Viscosity Blending Index (VBI) of each component using the *Refutas* equation:

$$VBI = 14.534 \times \ln[\ln(v + 0.8)] + 10.975 \quad (4.1)$$

Where v is the viscosity in centipoise (cps). Then the VBI of the blend is calculated using the blending equation:

$$VBI\ (blend) = [wA \times VBIA] + [wB \times VBIB] + \cdots + [wX \times VBIX] \quad (4.2)$$

Where *w* is the weight fraction. It is necessary that all the viscosities are determined at the same temperature when using the above blending equation. Finally, the viscosity of the blend can be obtained using the following invert of equation (4.1):

$$v = \left(e^{e^{(VBI-10.975)}} \div 14.534\right) - 0.8 \quad (4.3)$$

The viscosity of water and glycerol at 20 °C are 1 cps and 1412 cps respectively, according to [85] and [86]. As water and glycerol are both Newtonian [87], the theoretical viscosity of the mixture of water and glycerol was calculated based on the above formulas and given in Figure 4.2. To verify the applicability of the formulas for this study, mixtures containing water and glycerol (weight percentage various from 0%-70% with a gap of 10%) were formulated and the viscosity of which was measured at 20 °C (given as asterisk in Figure 4.2). The theoretical viscosity curve matches well with the measuring results, which verifies the applicability of the formulas in the ink formulation.

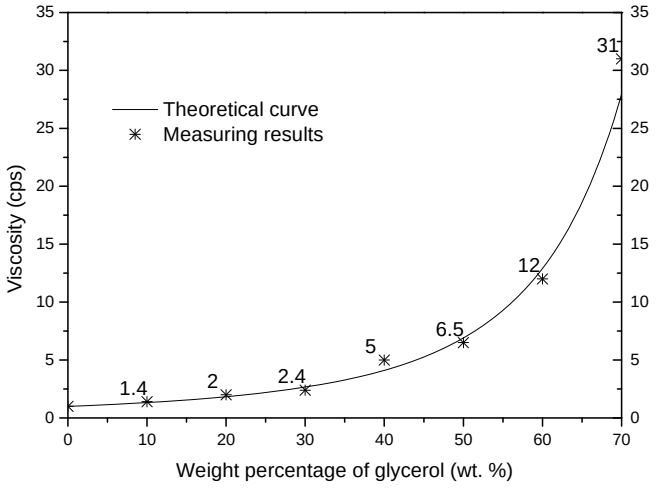

Figure 0.2 Theoretical prediction of the viscosities of water mixed with glycerol compared with experimental data obtained at 20 °C

However, the viscosity of the inks can be significantly affected by temperature. Five mixtures of water and glycerol, of which the viscosities are measured as 5.3, 10.6, 14.9, 20.1 and 25.7 cps at 20 °C, respectively, were compared with the results obtained under temperatures varying from 10 °C to 35 °C with an interval of 5 °C in Figure 0.3.

Accordingly, the viscosity of the inks can be adjusted by simply immersing the ink cartridge into a water bath, instead of altering the ink composition from time to time if needed in the applications.

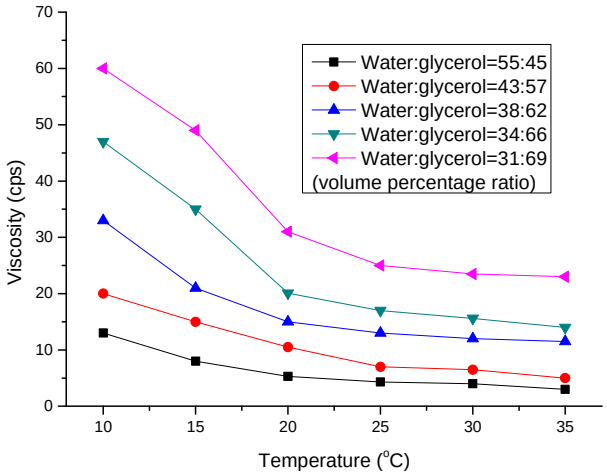

Figure 0.3 Viscosities of five mixtures of water and glycerol at temperatures from 10 °C to 35 °C

4.1.2.2 Surface tension

Surface tensions of the inks can be primarily adjusted by adding surfactants. Sodium dodecyl benzene sulfonate (SDBS), poly(vinylpyrrolidone) (PVP) and JC-601 were applied and tested and the results are given in Figure 0.4. From this result, one can see both SDBS and JC-601 can efficiently reduce the surface tension of water from ~70 dynes/cm to ~30 dynes/cm, while the addition of PVP has no obvious effect. Interestingly, the ability of the surfactants to change surface tension does not necessarily depend on their concentration, as the surface tension of water doped with SDBS was the same when the weight percentage of SDBS varied from 0.05% to 1%.

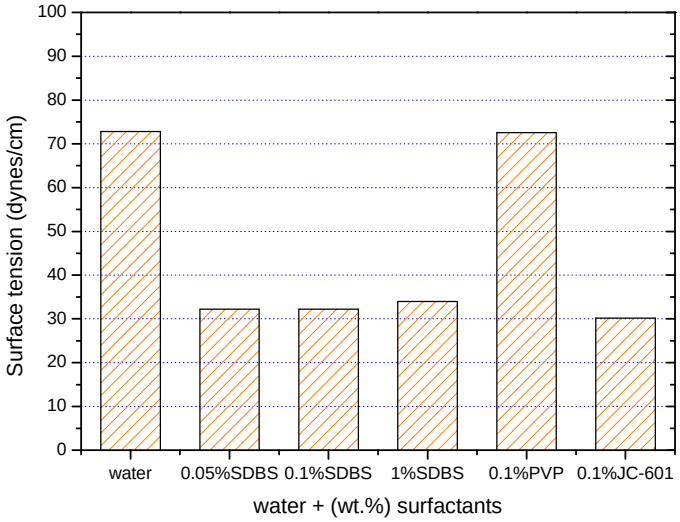

Figure 0.4 Surface tension of water and water mixed with different surfactants

The addition of ethanol and glycerol can also affect the surface tension. The efficiency of ethanol in reducing the surface tension of water is not as high as surfactants. A surface tension of 36 dynes/cm can be achieved with the addition of 17 wt.% ethanol, meanwhile further addition of ethanol has no more obvious effect (Figure 0.5). The addition of ethanol can facilitate the evaporation of the solvent in the droplets as the boiling point of ethanol is lower than water, which may consequently reduce the time of the solidification and thereby suppress the spreading of the droplets after landing on the substrate.

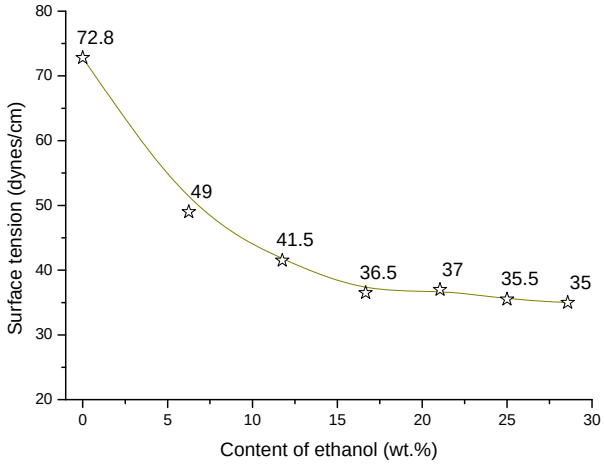

Figure 0.5 Surface tension of water mixed with ethanol

Although glycerol can increase the viscosity of the inks, it has a side-effect of also altering the surface tension. According to the results presented in Figure 0.6, an addition of 50 wt.% glycerol has increased the ink surface tension by around 10 dynes/cm. Therefore, the effects of glycerol on viscosity and surface tension must be considered during the ink formulation to obtain a compromise if necessary.

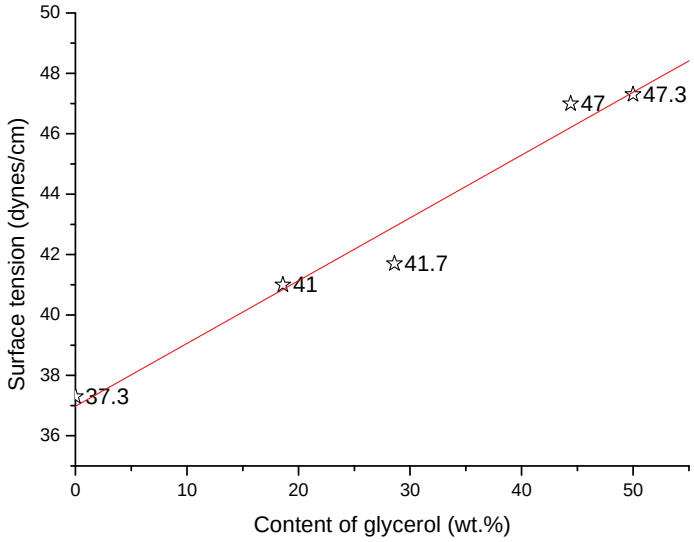

Figure 0.6 Surface tension of 85 wt.% water + 15 wt.% ethanol mixed with glycerol obtained at 20 °C

4.1.3 Prevention of nozzle blocking

Blocking of the nozzles in the printhead can happen during the inkjet printing process, which can be categorized as hard blocking and soft blocking. Hard blocking is normally caused by large particles or aggregation of material in the ink. To avoid this type of blocking, a filtering process after the ink formulation is essential.

Soft blocking is also a very common type of blocking caused by micro bubbles in the inks. The micro bubbles can be easily generated during the ink formulation which accompanies dissolution and dispersion. Therefore, ultrasonic processing has been employed in this study to eliminate the micro bubbles.

4.2 Simulation of droplet formation

4.2.1 Simulation procedures

A simulation of droplet formation in inkjet printing using the SE-128 printhead has been implemented. The flow chart of the simulation procedures is shown in Figure 0.7. A geometric model was firstly established and meshed into grids using GAMBIT (a program used to generate the grid or mesh for computational fluid dynamics solvers). The model was then imported into FLUENT (a computational fluid dynamics solver). After setting up the physical model, boundary conditions and material properties, the calculations were conducted, which was followed by a post processing. Finally, the simulation results were compared with experimental data to verify their validity.

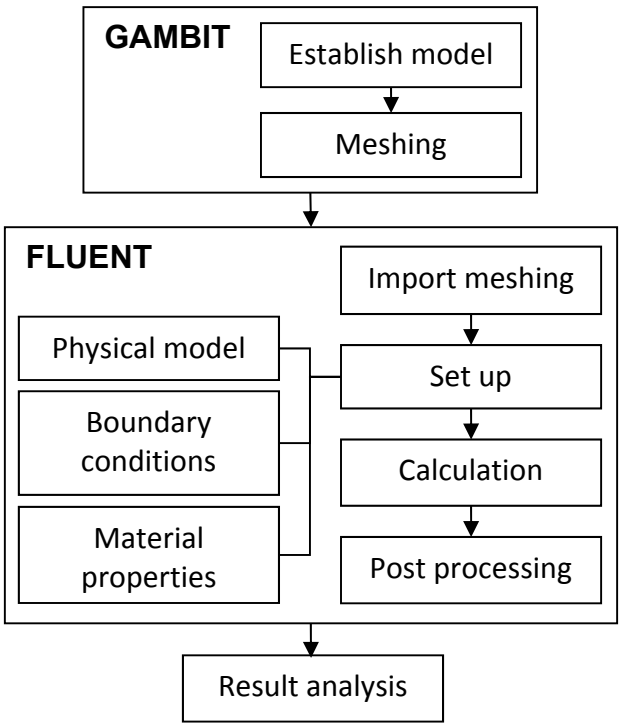

Figure 0.7 Flow chart of the simulation procedure for droplet formation in inkjet printing

4.2.1.1 Establishment of a geometrical model

The geometrical model was established based on the actual size of the nozzle. The flow behaviour of the inks in the chamber was not considered in this simulation. The model contained the orifice and flight area of the droplets under the orifice, as shown in Figure 0.8. A planar two-dimensional model was adopted to reduce the time required for the calculations Compared with a three dimensional model.

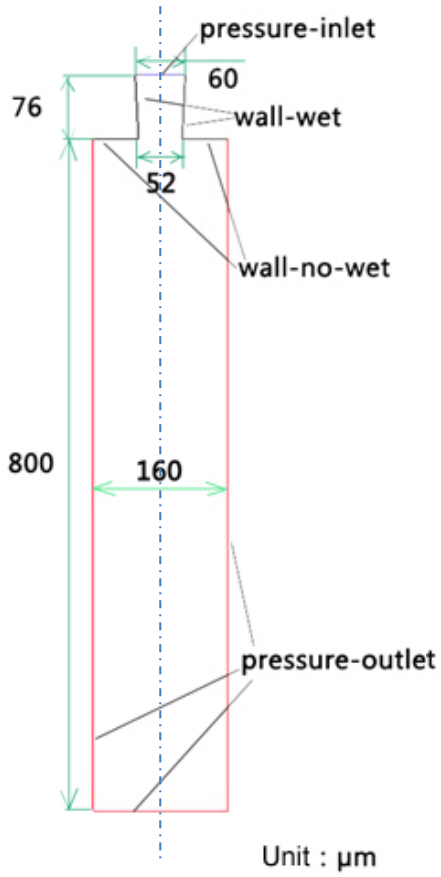

Figure 0.8 Geometrical model established by GAMBIT

4.2.1.2 Meshing

Quadrilateral meshes were generated using a division mode within GAMBIT referred to as 'Submap', which can divide an irregular region into numerous regular regions. After meshing, the model contained 34740 quadrilateral cells (control volumes into which domain is broken up), 68958 faces (cell boundaries) and 35263 nodes (grid points at cell vertices) (Figure 0.9).

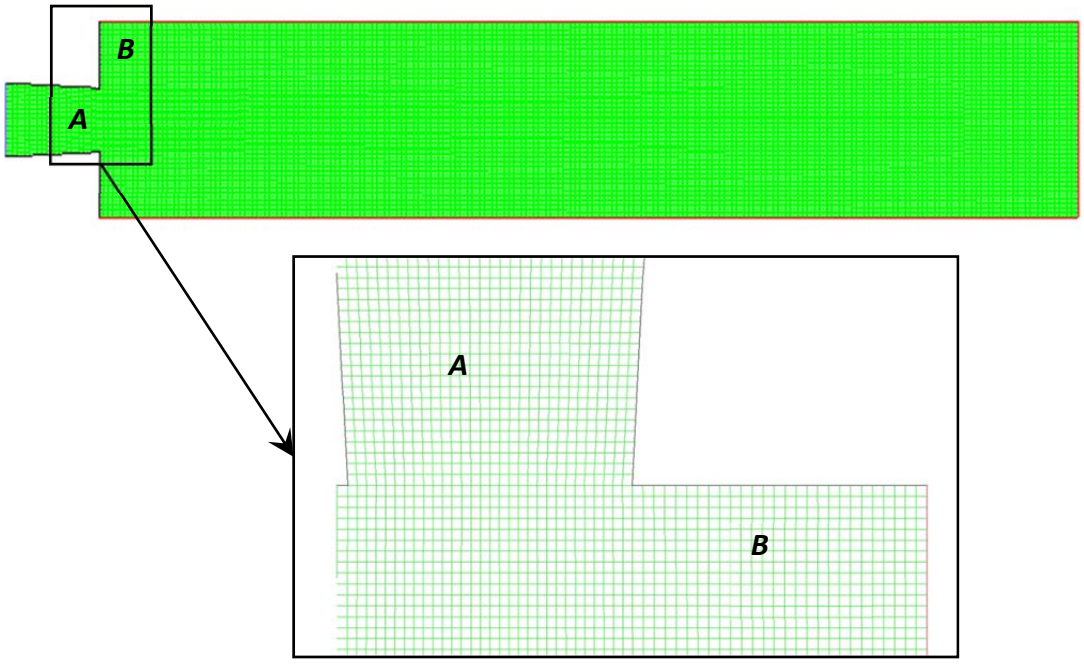

Figure 0.9 Meshed model and partial enlarged detail of the orifice

4.2.1.3 Setting up of the boundary conditions

After meshing, the boundary conditions were defined in GAMBIT. The entrance of the nozzle was defined as the pressure-inlet, with the three boundaries in the air area as the pressure-outlet. Considering the inner wall of the nozzle contacts with the ink, it was named as wall-wet. The outer wall of the nozzle was named as wall-no-wet, since it does not contact with the ink.

Ink jetting is a two phase process where a liquid moves through air. This can be described in FLUENT using a Volume of Fluid (VOF) model, a numerical technique for tracking and locating the free interface between the two phases. Therefore, a VOF model was chosen as the physical model, assuming the inks were an incompressible Newtonian fluid. In the VOF model, all the phases are mutually insoluble. A variable C is introduced for each cell after the addition of a new phase into the model. C is defined as the volume ratio of the fluid within the cell. The cell is empty when $C = 0$, and full of fluid when $C = 1$. Hence the movement of the fluid can be simulated by calculating the value of C for every cell. Then the geometry of the liquid surface can be estimated with high resolution by post processing algorithms which calculate the boundaries of the liquid [88].

It is reasonable to assume that the distribution of the pressure in the orifice can be regarded as homogeneous as the diameter of the orifice (52 μm) is far less than the diameter of the chamber (356 μm). According to Wu et al. [65], the pressure in a piezo-electric chamber approximates to a sinusoidal wave, as shown in Figure 0.10. The shape of the pressure wave is different from the waveform of the electrical signal due to the buffering effect of the fluids inside the chamber.

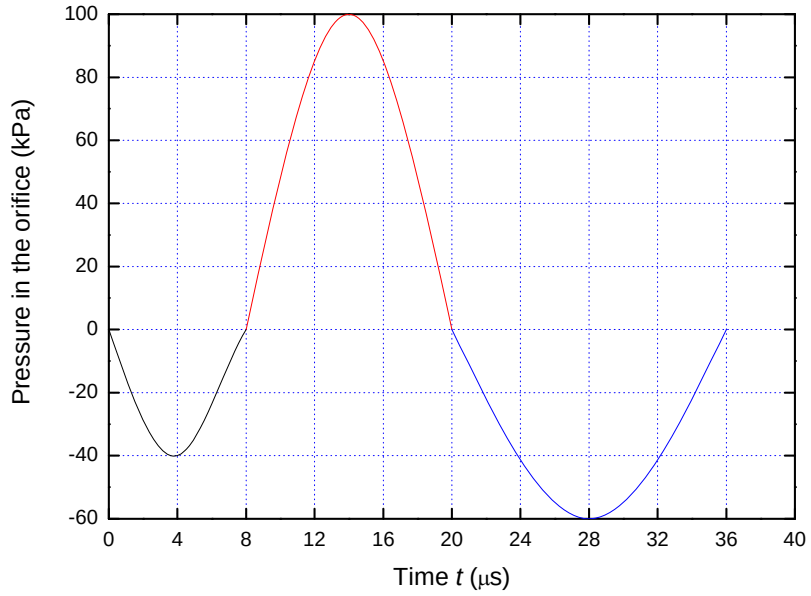

Figure 0.10 Typical variation predicted for the pressure in the orifice of the nozzle

As a controlling variable, the temporal variation of pressure cannot be directly set up in FLUENT. However, FLUENT has a UDF (User-Defined Function) facility which can be used to define the pressure using a library function written either in the language C or using the predefined macro language embedded in FLUENT. In this work, the condition of pressure varying with time in the pressure-inlet area was defined by a macro named DEFING-PROFILE. The source code for this program is attached in Appendix 1 and followed the time/pressure profile of Figure 4.10

4.2.2 Simulation and verification

The model and conditions must be set up before simulating the droplet formation in the inkjet printing. The effect of gravity was not considered in this simulation due to the low weight of droplet (~ 6×10^{-11} kg). Droplets with such small weights are observed to

have Brownian motion instead of freely falling body motion in the air because of the air resistance [89]. Throughout all of the simulations, the density of the fluid was set as 1 g/cm^3.

An initial simulation of droplet formation using the ink with defined properties was conducted. These properties include the viscosity, surface tension, and wetting angle of the inner wall which were set to be 1 cps (1 cps = 1 mPas), 40 dynes/cm and 30° respectively. The simulation was initiated from the commencement of the pressure pulse and completed after 130 µs with a fixed time step of 1×10^{-8} s. The obtained results are presented as images in Figure 0.11, where the red parts represent the liquid, and the blue strip represent the surrounding ambient condition (air). The times are chosen to show the representative morphology of the droplets during the whole jetting process.

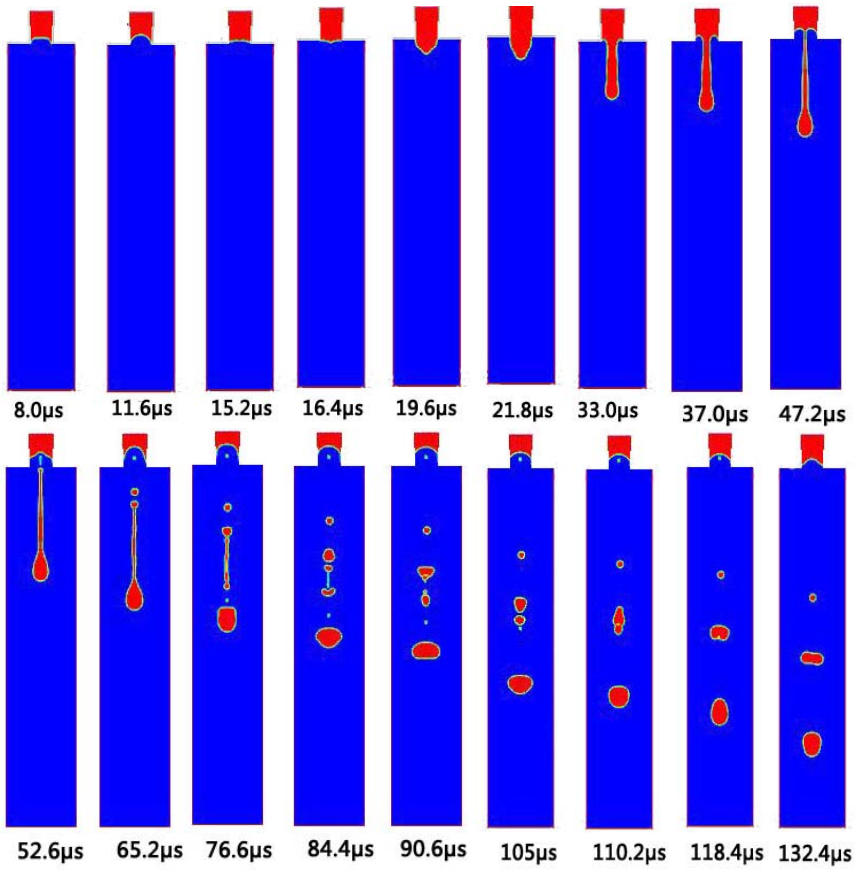

Figure 0.11 Simulation results of droplet formation from 8.0 µs to 132.4 µs from start of pressure pulse

The modelling results predict that, near the beginning of the jetting process (8.0 – 11.6 µs), a liquid meniscus of ink is induced by the combined action of negative pressure and wall adhesion. From 15.2 µs to 33.0 µs, the meniscus disappeared under the

positive pressure, instead, forming a liquid column with a prolonged spherical head from the orifice. As the length of the liquid column further increased, necking began to occur (47.2 μs) owing primarily to the delayed negative pressure reaching this position. After this, the column was broken from the orifice at 52.6 μs. Following this, the tail of the liquid column started to separate into several satellite droplets driven by Plateau-Rayleigh instability [90] (65.2 μs – 84.4 μs). However, these satellites may fly at different speeds following the breaking process, therefore it can be foreseen that the satellites with a relative higher speed can move faster merging those satellites moving at a lower speed, this leads to the formation of bigger satellites (90.6 μs – 110.2 μs). At the end, a main droplet accompanying two satellites was generated according to the simulation. The calculated velocity cloud picture (Figure 0.12) indicates that the main droplet, first satellite and second satellite have reached the velocities of 5.67 m/s, 5.38 m/s and 3.70 m/s, respectively, which meant no further merging could occur. The shape of the droplet was governed by a combined action of surface tension and inertia. The surface tension determined the formation of sphere which had the smallest surface area, while the inertia led to different speeds in different parts of the droplet. Under the combined effect of the two factors, the droplet shape changes between a longitudinal ellipse, a circle and a lateral ellipse repeatedly [65].

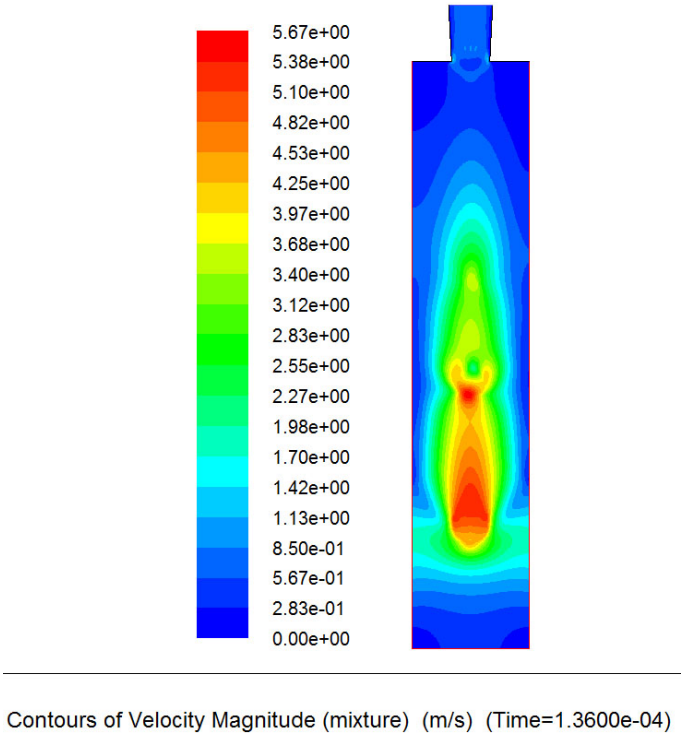

Figure 0.12 Velocity cloud picture of the droplets obtained at 136 μs

To verify the validity of the simulation, a water-based ink with a surface tension of 30 dynes/cm and a viscosity of 5 cps was developed and applied using the spectra SE-128 printhead. The values of these ink properties are different from those used in the simulation. This is because there are more factors influencing the formation of droplets in real situation which are hard to be considered in the simulation. The parameters had to be adjusted so that the simulation results can match the real situation. Therefore the analysis of simulation can only be qualitative but not quantitative. The jetting process captured by a CCD camera is shown in

Figure 0.13(a). Comparing the experimental data with the simulation results (

Figure 0.13(b)), the following conclusions can be drawn:

(1) The liquid column was generated due to the positive pressure which has been reflected in both experiment and simulation results. However, the head profiles of the liquid column were taking a slightly different shape or curvature. The simulated head was more spherical immediately after being jetted from the orifice, while the experiment showed a relative sharper tip formed at the start, which turned into a spherical profile eventually.

(2) The necking was clearly observed in both experiment and simulation study, with the similar main liquid body of droplets accompanying the satellite droplets induced at the end of the column. A drop with extremely small size can be observed between the liquid column and the orifice after the breaking of the neck. However, this satellite retracted back to the orifice in the experiment but fell off the orifice in the simulation.

(3) At the end of droplet formation, both experimental and modelling results showed a main droplet accompanied by two satellites. The main droplet has taken the substantial volume ratio of ink from the initial liquid column in comparison with the two satellites.

Overall, the simulation results have demonstrated its usefulness and ability to predict the droplet formation behaviour, providing a powerful tool to enable optimum design of the ink formulation which may lead to the high quality images to be printed. The simulation has been validated through the experimental work, in particular, the prediction of the final morphology of the droplets which has agreed very well with the simulation results.

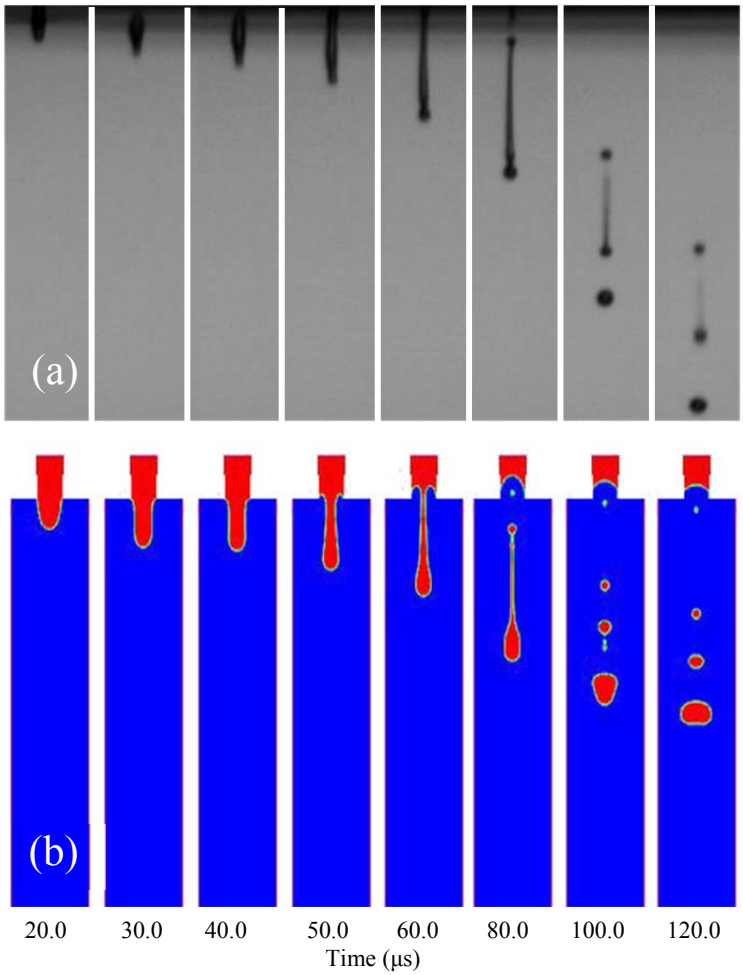

Figure 0.13 Experimental (ink properties: 5 cps, 30 dynes/cm) (a) and simulation (ink properties: 1 cps, 40 ynes/cm) (b) results of formation of droplets in the inkjet process

Surface tension and viscosity are important parameters among the ink properties for inkjet printing, which can significantly affect the formation of droplets as has been investigated by simulation. In this study, seven types of fluids with different properties were defined for use in the simulations, as given in Table 4.1. These properties cover the range of those required to suit the specifications of most commercial inkjet printhead. Fluids A, B, C and D had the same viscosity of 1 cps but different surface tensions varying from 20 dynes/cm to 50 dynes/cm. Fluids C, E, F and G had the same surface tension of 40 dynes/cm but with their viscosities varying from 1 cps to 10 cps.

Table 0.1 Ink properties used in the simulation

Liquid	Surface tension (dynes/cm)	Viscosity (cps)
A	20	1
B	30	1
C	40	1
D	50	1
E	40	2
F	40	5
G	40	10

The simulation results obtained for fluids A, B, C and D after the liquid was ejected from the nozzle for 33.0, 52.6, 90.6 and 118.4 μs are given in Figure 0.14. From Figure 0.14 (a) for 33 μs, the liquid columns formed at this stage are similar, as one can predict that the liquid of higher surface tension may result in a slightly shorter and thicker liquid column than the one of lower surface tension. The small difference can be caused by the higher attraction between the molecules of the liquid induced from surface tension. The attraction usually hinders the separation of the liquid from the orifice, leading to a lower growth speed of the liquid column. This elastic tendency can also prevent the liquid column from breaking into numerous droplets as happens in Figure 0.14 (c) and Figure 0.14 (d). Therefore high surface tension leads to less satellites but a lower speed of the droplets. However, during the necking, breaking of the column seemed to easily occur in the liquid with higher surface tension when the surface area of the column reaches a certain value (Figure 0.14 (b)), this can be attributed to the driving force provided by the higher surface tension that drives the reduction of surface area of the liquid so that lower surface free energy can be obtained.

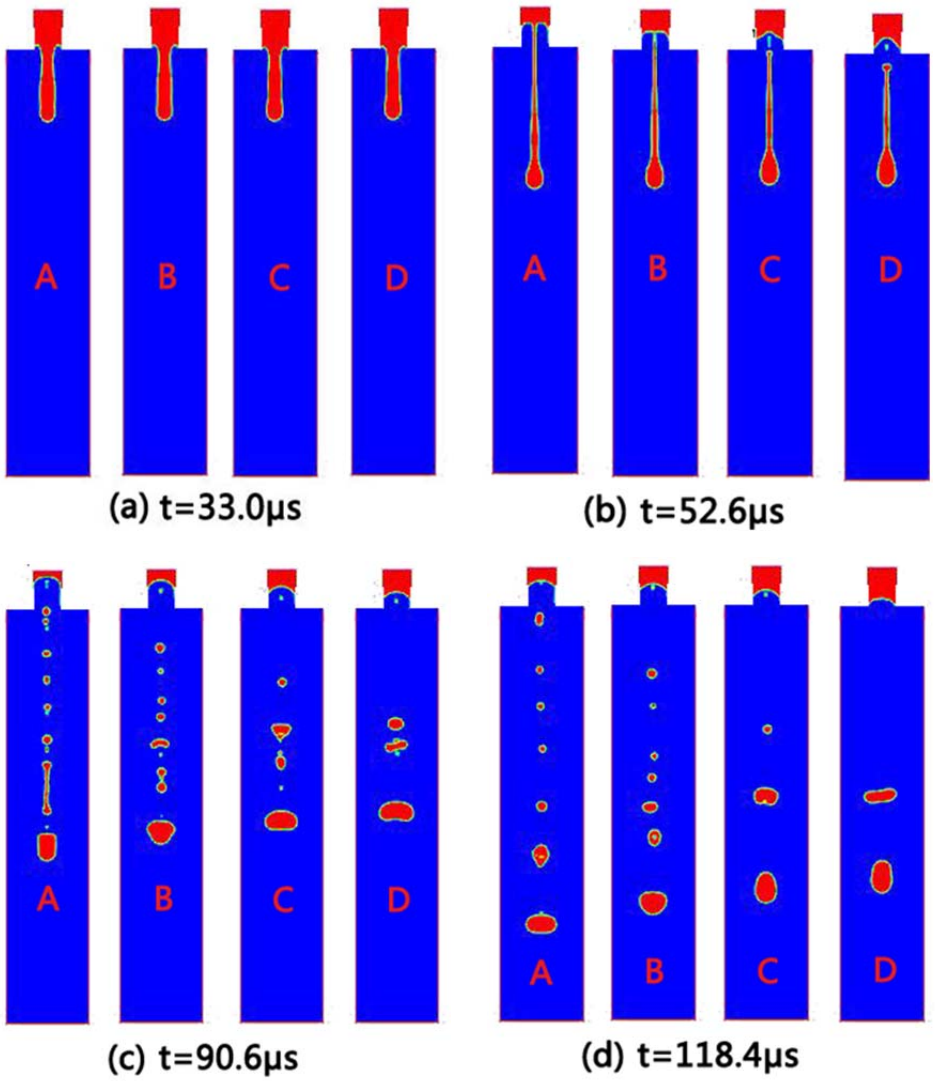

Figure 0.14 Simulation results for liquids A, B, C and D at 33.0 μs (a), 52.6 μs (b), 90.6 μs (c) and 118.4 μs (d)

The effect of viscosity on the formation of droplets was investigated by comparing the simulation results of fluids C, E, F and G. The results are given in Figure 0.15 (a) and Figure 0.15 (b), the length of the liquid column decreases with increasing viscosity. As the viscosity is a measure of the resistance to distortion of a fluid which is being deformed, the liquid with high viscosity tends to have less deformation. The internal friction also hinders the breaking of the liquid column. Therefore the viscosity had a similar effect to surface tension, which ultimately determines the formation of satellites and the speed of the droplets.

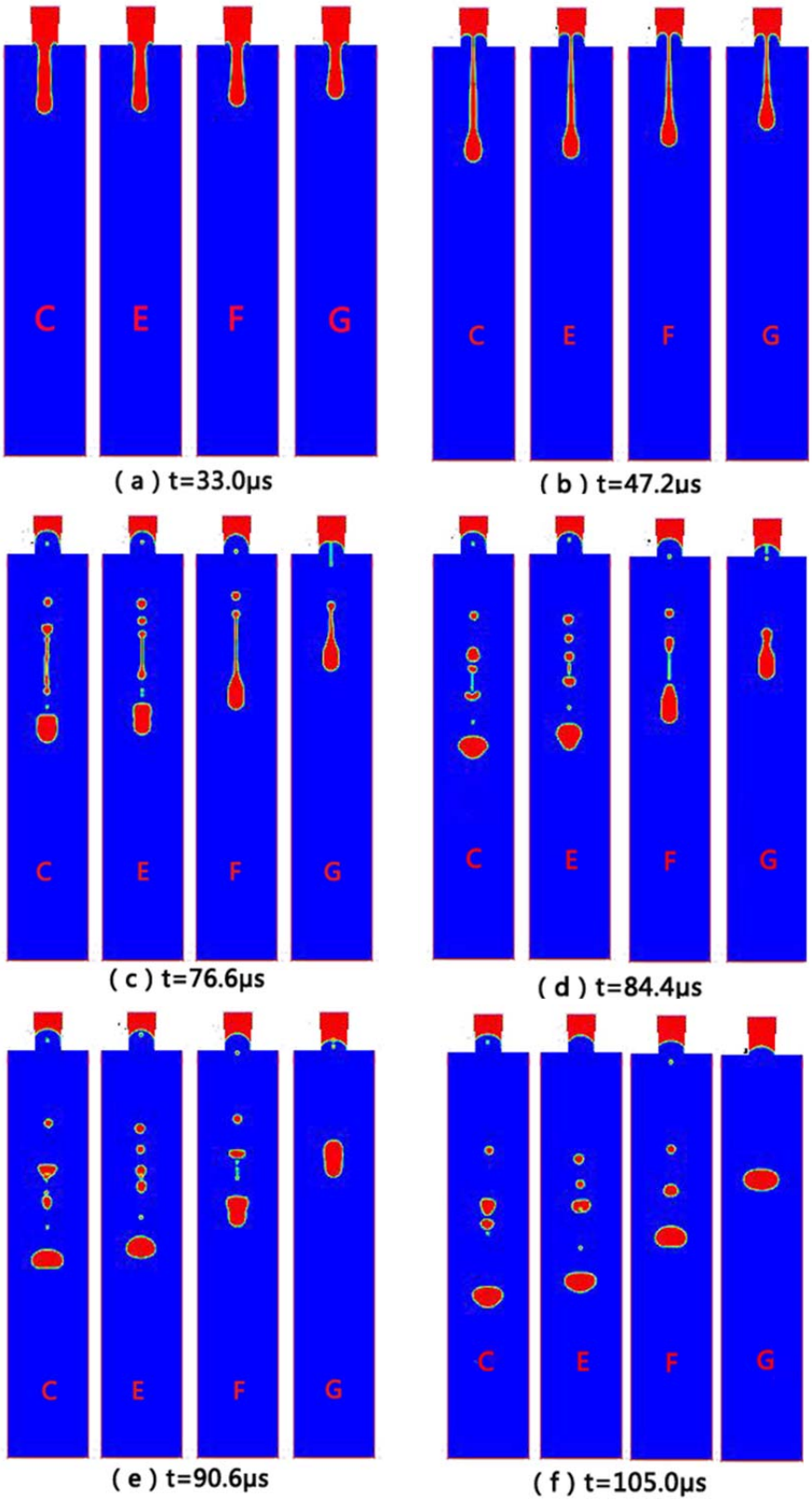

Figure 0.15 Simulation results for liquid C, E, F and G at 33.0 μs (a), 47.2 μs (b), 76.6 μs (c), 84.4 μs (d), 90.6 μs (e) and 105.0 μs (f)

The effects of surface tension and viscosity on the droplet velocity and number of satellites are summarised in Figure 0.16 and Figure 0.17. It can be observed that increasing surface tension can more effectively reduce the number of satellites, while viscosity has a more significant effect on the droplet velocity. This interpretation provides guidance for the adjustment of ink properties based on the morphology of obtained droplets. The numbers *Re*, *We*, *Oh* and *Z* (as introduced in Section 2.2) for liquids A-G calculated using the simulation results are given in Table 4.2. It can be concluded that the essential condition for inks which can be properly jetted by the Spectra printhead utilized in this study is $Z \approx 5$.

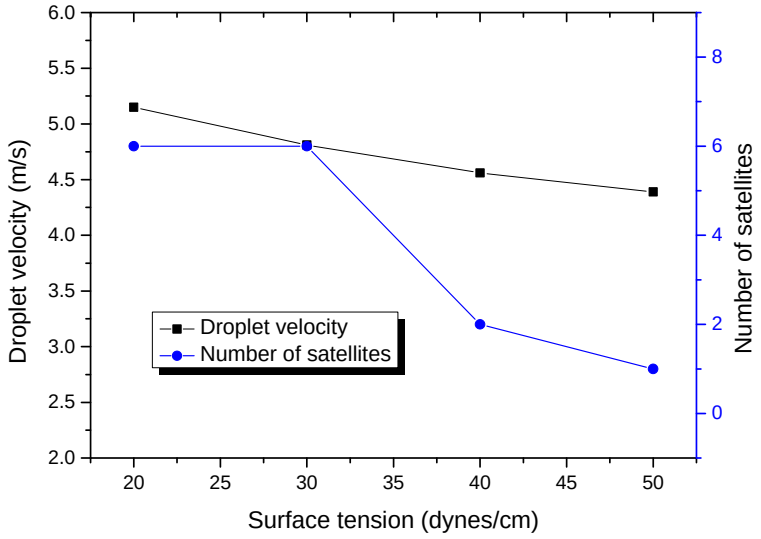

Figure 0.16 The predicted effect of surface tension on the droplet velocity and number of satellites

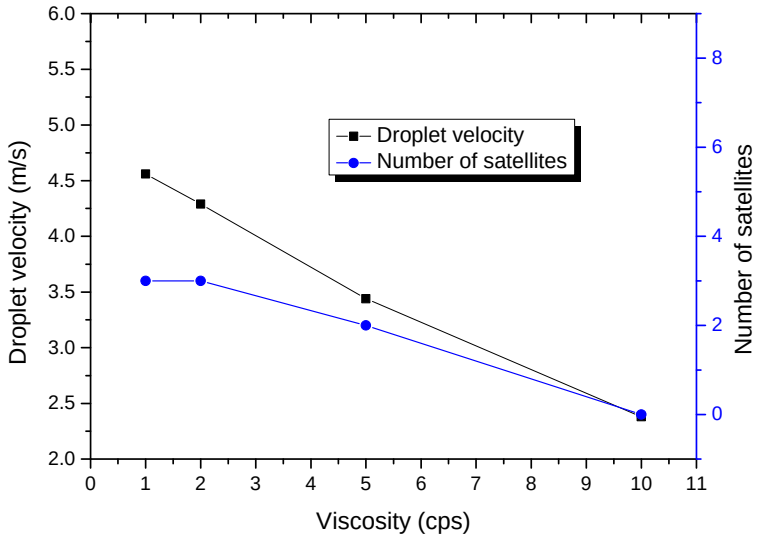

Figure 0.17 The predicted effect of viscosity on the droplet velocity and number of satellites

Table 0.2 The numbers *Re, We, Oh* and *Z* for liquid A-G calculated based on the simulation results

	Re	We	Oh	Z
A	267.8	68.9	0.031	32.2
B	250.1	40.1	0.025	39.5
C	237.1	27.0	0.022	45.6
D	228.3	20.0	0.019	51.0
E	111.5	23.9	0.044	22.8
F	35.8	15.4	0.109	9.1
G	12.4	7.4	0.219	4.6

4.2.4 Failure analysis

4.2.4.1 Retraction

The retraction of the droplet back to the chamber was often observed in the inkjet experiments, which led to printing failure. Figure 0.18 shows the whole process of retraction captured with the CCD camera during the inkjet printing trials. A short liquid column can be observed at the beginning of jetting. After that, a droplet was formed and drew back to the nozzle.

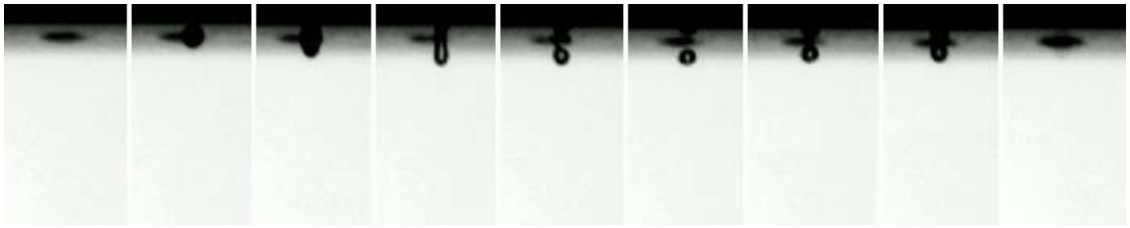

Figure 0.18 Retraction captured with CCD camera as the order of time (from left to right)

As it is not possible to observe the behaviour of liquid inside the nozzle, it can be difficult to understand retraction through interpreting the images obtained. For this reason, simulation is recognised to be a possible approach for developing such understanding, and thus was employed in this study to provide a qualitative explanation. As for the initial simulations a fluid with a surface tension of 40 dynes/cm and a viscosity of 1 cps was used to undertake the simulation. The shape of the pressure curve was the same as in Section 4.2.1.3, with a lower pressure peak of 60 kPa, and all the curve had been scaled by 60%. The simulation results are presented in Figure 0.19.

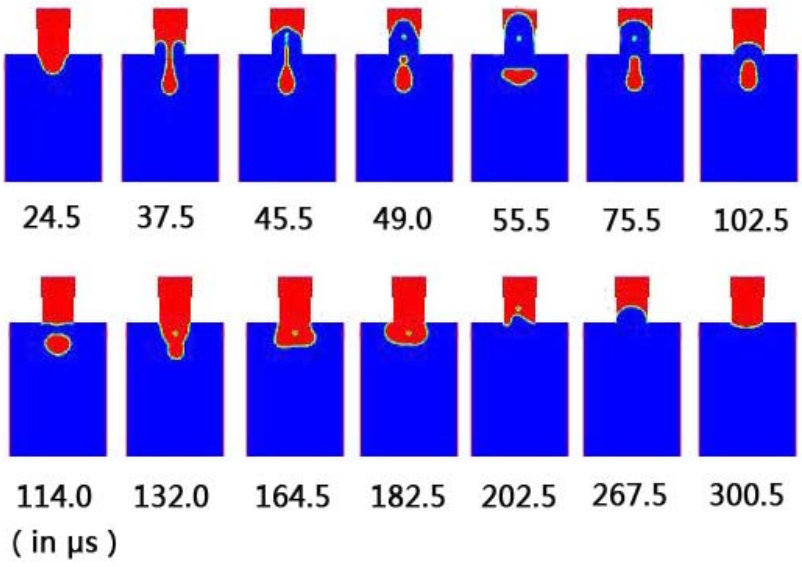

Figure 0.19 Simulation of the jetting process with a reduced pressure pluse magnitude

Both the formation of a liquid column and the necking process can be observed in the simulation results. However, the liquid column had obtained an upward velocity when breaking from the orifice, due to the atrraction caused by surface tension. As a result, the formed droplet moved upward, merging with the liquid inside the nozzle, and then was retracted back by the negative pressure.

It can be concluded that the direct cause of the retraction can be attributed to the upward velocity of the droplet. In the experimental tests, the drag force applied for the droplet is often higher than the one in simulation, for instance, due to the friction between the liquid and the inner wall. Besides, the interaction between the liquid and the outer wall of the nozzle, which may affect the formation of droplet in actual applications, was not considered in the simulation. Hence, the inks with high surface tension and viscosity are conventionally prohibited as they are not suitable for the jetting process. When retraction happens, increasing the positive pressure can be an alternative solution to obtain droplets with better morphology leading to successful droplet deposition.

4.2.4.2 Deviation

Another common failure in the inkjet printing process is the deviation of the flying pathway of droplets from the perpendicular direction. According to Lee [91], deviation is normally caused by an abnormal shape of meniscus. Hence a model of asymmetric meniscus has been established as shown in Figure 0.20, which contains a convex semi-circle and concave semi-circle. The surface tension and viscosity of the liquid chosen for the simulation was defined as 40 dynes/cm and 10 cps, respectively.

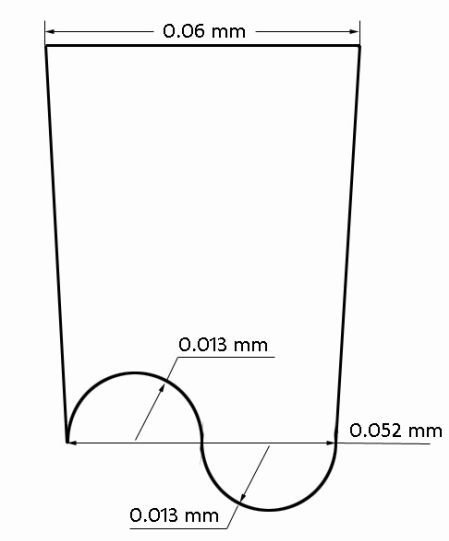

Figure 0.20 Model of sine-shaped meniscus

The result of the simulation using the above meniscus as the initial condition is shown in Figure 0.21. It can be observed that more volume of liquid was jetted through the concave side at the beginning of droplet formation. This is primarily attributed to the attraction caused by surface tension in the concave side which can be much smaller

than the one in the convex side. Hence the tip of the liquid column induced a horizontal velocity component, resulting in the inclining of the liquid column toward the concave side. Consequently, after the break of the liquid column, the formed droplet deviated from the perpendicular direction.

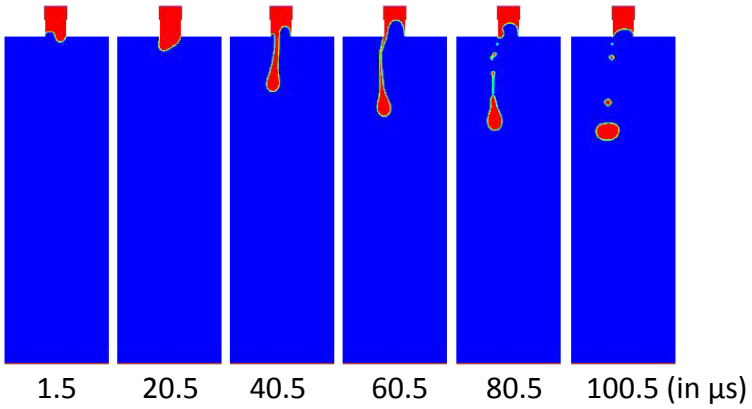

Figure 0.21 Simulation of the jetting process for sine-shaped meniscus

The meniscus model used to describe the jetting process best reflects the asymmetrical wetting behaviour of the liquid when interacting with the inner wall, which can result from any contamination of the nozzle. Therefore, to avoid such deviation, the nozzle must be cleaned before the jetting process is initiated. In this study, it has also been observed that cleaning of the nozzle can effectively eliminate deviation of the droplets.

4.3 Initial pattern printing

As all patterns no matter how complicated are composed of basic elements, the printing of single dots, straight tracks and rectangular film areas has been investigated in this section. The results are intended as a means to build a foundation for the printing of specific patterns, and also provide a guide for the latter studies presented within this thesis.

4.3.1 Methodology

The Microfab Jetlab® 4 inkjet system was employed in pattern printing. Silver nanoparticle ink and PEDOT:PSS solution were adopted as the printing material. Silver nanoparticle ink with a silver content of 20 wt.% was used in dot printing and for some of the track printing experiments. Patterns printed with the silver ink appeared as a white area as observed under the optical microscope. The PEDOT:PSS solution can be

directly jetted by the Jetlab 4 inkjet system without any modification of its properties. The PEDOT:PSS solution was used in film printing and for the remainder of the track printing experiments. Patterns printed with PEDOT:PSS solution appeared to be transparent with a colour slightly darker than the substrate.

In dot printing and track printing of Silver nanoparticle ink, four types of substrates commonly used in the industrial applications, i.e. glass, FR4 glass cloth reinforced Epoxy, polyimide (PI) and hydrophobic paper were utilised to investigate the droplet/substrate interactions and the spreading behaviour of ink droplets on substrates with different surface conditions. Prior to printing, the substrates were preheated to a temperature ranging from 20°C to 80°C. The printed deposits were then baked at 200°C for 20 min.

In film printing, 0.2%, 0.5%, 0.8%, 1.0% and 1.3% PEDOT:PSS solutions were formulated and then printed on glass substrates with a fixed dot spacing of 50 μm to investigate the relationship between the film thickness and solute concentration. The method of film printing using Jetlab 4 inkjet system is depicted in Figure 0.22. The films were composed of single dots which were printed one track by one track. Every two neighbouring tracks had a gap of 50 μm between them and had converse printing directions. Material enrichment occurred at the two edges of the film due to the deceleration of the nozzle during the change of printing direction (shown in Figure 0.23).

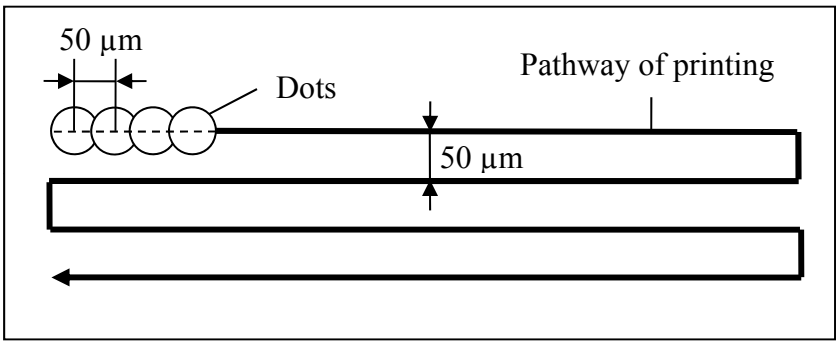

Figure 0.22 Pathway of nozzle in film printing

Figure 0.23 PEDOT:PSS film printed on glass substrate

4.3.2 Dot printing

Dots are basic element that is utilised to form various patterns using inkjet printing. The attainable feature size of a component fabricated using inkjet printing is directly determined by the dot size that can be achieved [43]. Dot size is determined by the droplet size generated from the nozzle and the subsequent interaction between droplet and substrate. The diameter of the nozzle was fixed at 60 μm in this study, therefore the droplet size cannot be adjusted. Instead, the effect of surface condition of the substrate on the dot size was investigated. Preheating was applied for the four types of substrate to study the optimal substrate temperature for each substrate.

4.3.2.1 Effect of substrate temperature

The optical top views and cross section profiles of the dots formed on a glass substrate with different preheated temperatures are shown in Figure 0.24. It is obvious that as the substrate temperature increases, the diameter of the dots was reduced, and the round shape became more regular. Since the surface of the glass was not perfectly smooth and homogeneous, irregular boundaries of the dots can be observed, which may be caused by the interaction and spreading of the liquid droplets on the surface after landing, but before reaching a steady state. However, as can be predicted, the increase of substrate temperature leads to a higher evaporation speed, resulting in suppression of spreading. The evaporation rate of a water based droplet can be calculated as following [92]:

$$M = \frac{A(m+nv_a)(P_w - P_a)}{H_v} \tag{4.4}$$

Where A is the surface area, m and n are constants, v_a is the air velocity over the ink surface which is zero in this study, P_w is the saturation vapour pressure at present

temperature, P_a is the saturation vapour pressure of air dew point, and H_v is the latent heat of vaporization of water.

Considering that the time from the beginning of the surface energy driven stage (introduced in Section 2.3.3) to the end of spreading (t_0) is often longer than the time to evaporate *t,* in practical situation for inks with low boiling point solvent (e.g. water, ethanol), the droplet can be assumed to keep spreading during the whole evaporation process. Thus the spreading time will be:

$$t_0 = t = \frac{Q_0}{M} = \frac{Q_0 H_v}{mA(P_w - P_a)} \tag{4.5}$$

Where Q_0 is the total mass of the solvent and according to Antoine formula [93]:

$$P_w = e^{A_1 - \frac{B_1}{T + C_1}} \tag{4.6}$$

It can be concluded that the spreading time decreases as the temperature rises, which is independent of the property of substrate. In addition, interestingly, the boundary of the dots printed on a higher substrate temperature e.g. 80 °C was found to be a darker line with a clear contrast from the optical observation (Figure 0.24). This is likely due to the coffee stain effect which causes a material enrichment on the edge of the dots, which was apparently accelerated at a higher substrate temperature [94].

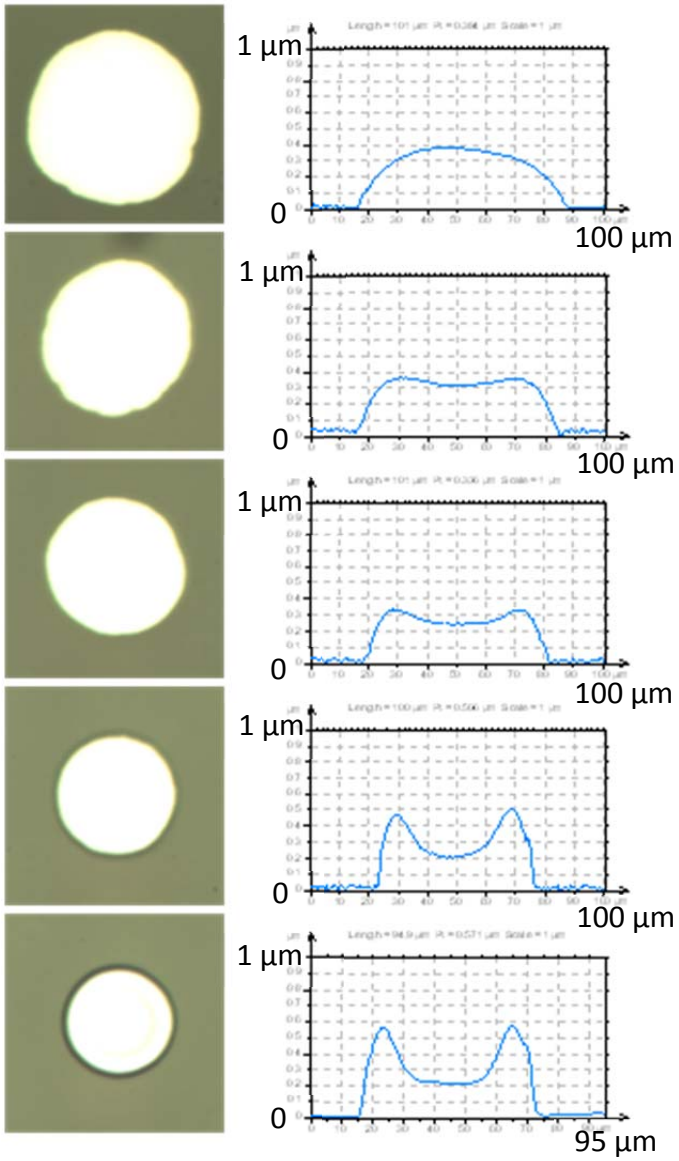

Figure 0.24 Top views obtained by optical microscopy and cross-section profiles obtained by Zygo of droplets on glass substrates preheated at different temperatures (top to bottom is 20°C, 35°C, 50°C, 65°C and 80°C)

4.3.2.2 Effect of substrate type

The substrates onto which the ink is deposited may have a significant effect on the formation of the dots. The top view of dots printed on the different substrates at 20 °C are given in Figure 0.25, which indicates that the outline shape of the dots can be significantly affected by the surface condition of the substrate. The diameters of the dots printed on the four substrates have been evaluated under different temperatures, the results are presented in Figure 0.26.

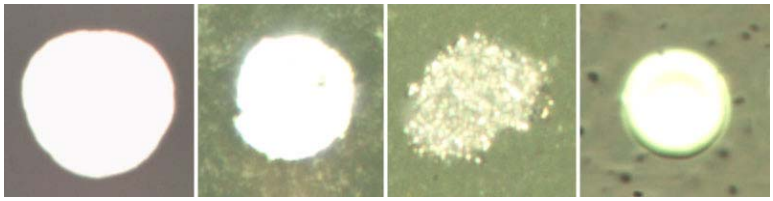

Figure 0.25 Optical top view of dots on (from left to right) glass, hydrophobic paper, FR4 and polyimide at 20°C

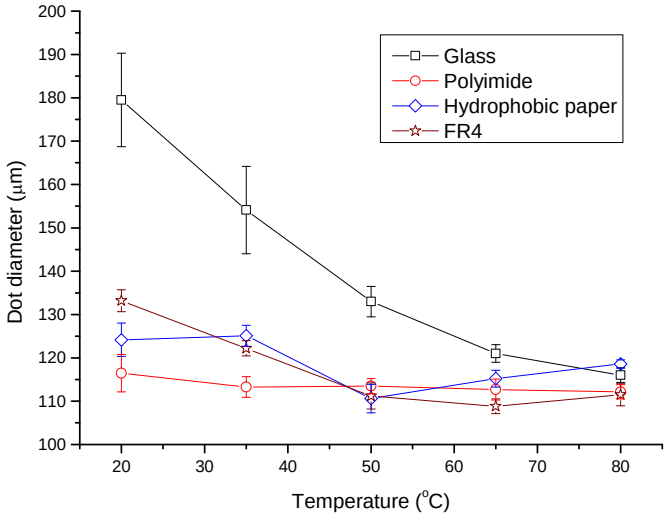

Figure 0.26 Diameters of dots printed on four substrates under different preheat temperatures (ambient temperature: 20°C)

As the experimental results in Figure 0.26 indicate, the size of the dots has been reduced to a certain degree due to the preheating of the substrate, which applies to each type of substrate. In particular, it had a drastic reduction of the dot diameter when printing on the glass substrate. However, it has appeared that the preheating did not affect the dot size significantly on the polyimide substrate. It is understood that each substrate may represent different properties, e.g. surface chemistry or energy which can considerably govern the impact and interaction of the droplets when they land on the surface, especially their wetting and evaporation behaviour. Therefore, both substrate temperature and types of substrate materials should be considered when aiming to achieve higher printing resolution (i.e. reducing the dot size). For instance, according to the trend of the curves, it can be roughly predicted that the optimal preheating temperature for glass in this experiment should be higher than 80 °C, in the range of 30-40 °C for polyimide, 60-70 °C for FR4 and 50-60 °C for hydrophobic paper. For all

substrates, the variation of dot diameters became smaller as the temperature increased, indicating that more uniform dot size has been obtained.

The final dot diameter can be qualitatively analysed using a mathematical model, as schematically illustrated in Figure 0.27. Assuming the diameter of the contact area between droplet and substrate after impact phase is D_0, the spreading speed of the contact line is v and the spreading time is t_0, the dot diameter after spreading will be:

$$D = D_0 + 2\int_0^{t_0} v dt \tag{4.7}$$

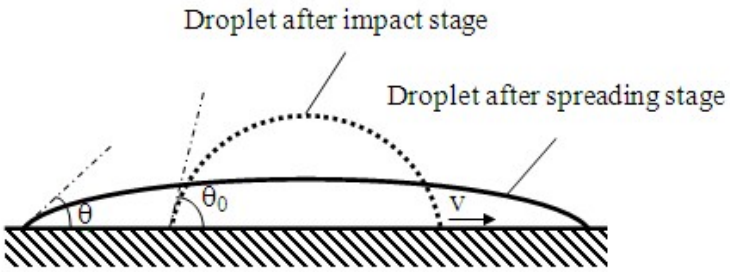

Figure 0.27 Schematic model of droplet spreading process

The instantaneous spreading velocity of the contact line is [95]:

$$v = 2K^0\lambda\sinh[\frac{\gamma_{LV}(\cos\theta_0-\cos\theta)}{2nk_BT}] \tag{4.8}$$

Where K^0 is the frequency of molecular displacements, λ is their average length, γ_{LV} is the surface tension of the liquid, θ_0 is the present contact angle, θ is the contact angle of steady state, n is the number of adsorption sites per unit area, k_B is Boltzmann's constant and T is the temperature. According to Ruijter [96], formula 4.8 can be simplified to:

$$v = \frac{1}{\zeta_0}\gamma_{LV}(\cos\theta_0 - \cos\theta) \tag{4.9}$$

Where ζ_0 is a friction coefficient per length of the contact line and γ_{LV} can be estimated using the Eotvos rule:

$$\gamma V^{2/3} = k(T_c - T) \tag{4.10}$$

Where V is the molar volume of substance. T_c is the critical temperature and k is a constant valid for almost all substances. Using the Gibbs adsorption isotherm,

thermodynamics and a molecular interaction model, the contact angle of steady state can be described as [97]:

$$\cos\theta = 1 + C(T_c - T)^{a/(b-a)} \tag{4.11}$$

Where C is an integration constant, and a and b are temperature-independent constants from a balance of intermolecular forces. The model predicts the general experimental trends of θ with respect to T. Based on formula (4.10) and (4.11), both the surface tension of the droplet and the steady state contact angle decrease when the temperature rises. However, the decrease of the contact angle can lead to an increasing spreading speed, while the decrease of droplet surface tension presents a negative effect. Since a, b and C are related to the substrate properties (e.g. surface energy and surface roughness), temperature influences the spreading speed of contact line in different ways according to the substrate type.

Table 0.3 Contact angle and surface energy of the substrates used in this study

Substrate	Contact angle (°)		Dispersive (J/m^2)	Polar (J/m^2)	Total (J/m^2)
	Water	Diiodomethane			
Glass	35.7	61.0	14.42	46.37	60.79
Hydrophobic paper	77.4	40.3	39.45	4.40	43.85
FR-4	122.7	80.3	19.77	0.75	20.52
Polyimide	80.4	31.9	40.59	2.14	42.73

In this study, without preheating the substrate, the diameter of dots printed on glass, hydrophobic paper and polyimide is approximately proportional to the surface energy of the substrate (shown in Table 4.3). However, the size of the dots on FR4, which should be the smallest in theory, is second to the one on glass. This is because, instead of a static situation, the droplets impact the substrates with a speed close to 2 m/s during the inkjet process. As stated in Section 2.3.3, the droplets experience receding in the impact phase [65]. Nevertheless, the contraction of the dots on FR4 may be hindered owning to the high surface roughness, resulting in an irregular outline shown in Figure 0.25.

As for the glass substrate, the acceleration of the solvent's evaporation significantly contributes to the decrease of dot size when it was heated. However, small range of spreading occurred while the droplets were landing on polyimide, as such, the dot size was slightly decreased at the early stage of preheating. When the substrate was heated

up to around 35 °C, a balance generated between the evaporation of the solvent and the increasing spreading speed kept the dot size staying at the same size. For FR4 and hydrophobic paper, minimal dot size can be achieved through preheating in a certain range of temperature. Above certain temperatures, the increase of spreading speed became dominant and the dot size increases.

4.3.3 Track printing

4.3.3.1 Study of dot spacing

In many application lines or tracks need to be printed to form functional components. Tracks are conventionally printed through a series overlapped dots, thereby dot spacing (the centre to centre distance of adjacent dots) is an important parameter in determining the quality of the printed tracks. Continuous track can only be obtained with suitable dot spacing value. The optimal dot spacing is dependent on the conditions of ink and substrate surface properties. The results from the dot spacing study on glass at room temperature (20 °C) are shown in Figure 0.28. According to the figure, an overlap rate (the ratio of overlap distance to the dot diameter, the overlap distance is calculated by subtracting the dot spacing from the dot diameter) of 27% is comparatively suitable in this process, where a continuous track with smooth edge can be obtained. For polyimide, FR4 and hydrophobic paper, the optimal overlap rate was also determined using the same method, and they are 32%, 33% and 28% respectively. When the dot spacing is too big, discontinuous track is inevitable. When the dot spacing is too small, on the other hand, the contact angle of the liquid with the substrate is greater than the advancing contact angle, which can ultimately lead to the formation of bulges [98].

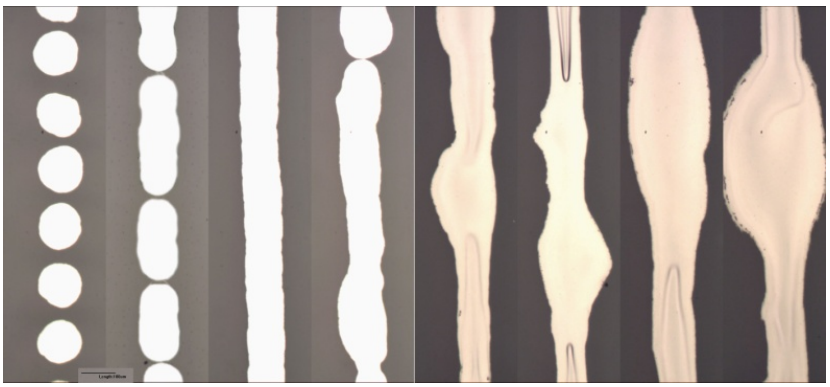

Figure 0.28 Printed silver tracks with different dot spacing values (from left to right: 170 µm, 125 µm, 110 µm, 100 µm, 80 µm, 70 µm, 60 µm and 50 µm. The average dot diameter is approximately 150 µm)

Error! Reference source not found. provides a correlation between the dot diameters and the track width which is printed, as well as a comparison between the four different substrates. Accordingly, the widths of the tracks are normally smaller than the corresponding dot diameters. This can be explained using a model illustrated in Figure 0.30. When the droplet landed on the substrate in the printing of a track, the spreading behaviour of the droplet is different from the situation in printing single dot. The liquid of the droplet firstly flowed to the indentation at the interface of adjacent droplets to form a uniform liquid surface. As a result, the contact angle between droplet and substrate at the interface of two droplets (broken line A in Figure 0.30) was larger than the one of other areas, leading to a preferential spreading in the grey area. Thus relatively regular track outline can be finally obtained.

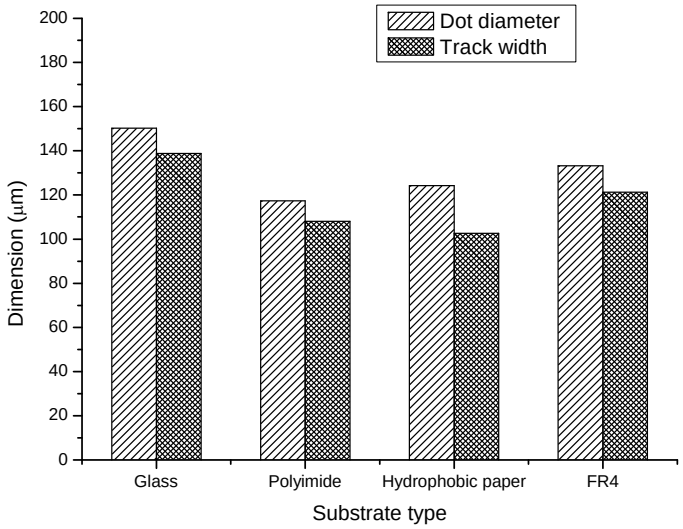

Figure 0.29 Average dot diameters, track width of one layer on different substrates (move down)

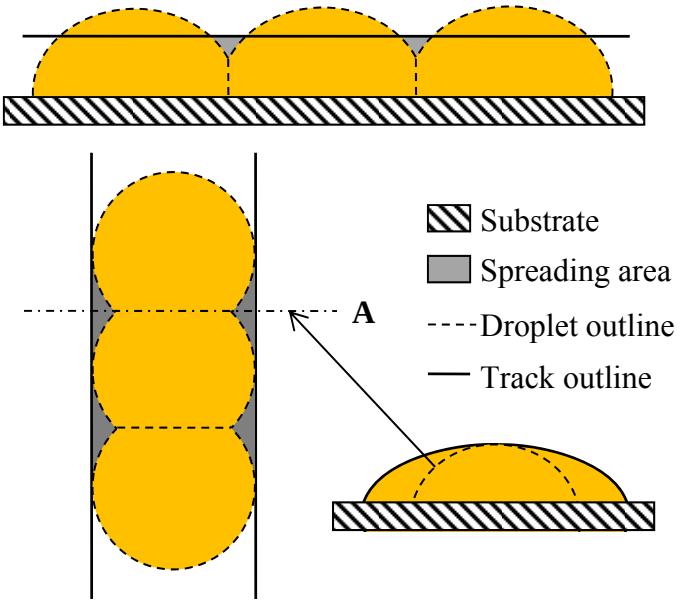

Figure 0.30 schematic illustration of droplet spreading

4.3.3.2 Multi-layer printing

Multi-layer tracks have been printed by repeating the printing process for a single track at the same position for number of times. The width and thickness of the tracks are shown in Figure 0.31. Both width and thickness increased with the increase of the number of layers. The morphology of the track (profile of the cross section perpendicular to the printing direction) is mainly determined by the combined action of surface tension and gravity. Before drying, the surface tension of the liquid prevents it from spreading on the substrate, while gravity contributes to the spreading. As the number of layers increases, the effect of gravity becomes more obvious due to the increased amount of material, resulting in smaller increases in the average track thickness. Meanwhile, the relationship between track width and number of layers becomes more linear. The deviation of the track width decreased as the increase of layers, which demonstrated that multi-layer printing can lead to more uniform tracks, as shown by the error bars in Figure 4.31.

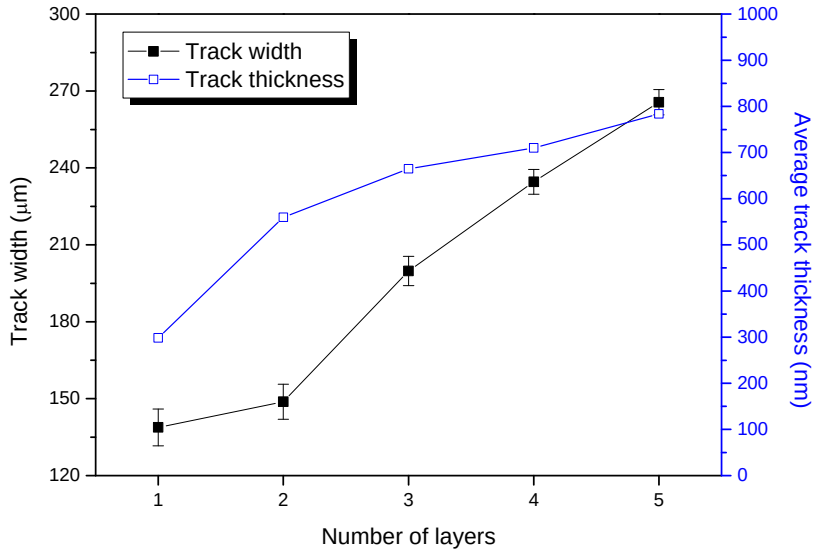

Figure 0.31 Width and thickness of tracks through multiple printing

4.3.4 Film printing

4.3.4.1 Thickness control

One of the most important advantages of inkjet printing is that the amount of deposited material can be precisely controlled. Hence the thickness of films printed with inkjet can be altered by adjusting the printing parameters. To obtain an understanding of printing PEDOT:PSS films with desired thickness, films were printed using PEDOT:PSS solutions of different concentrations. The relationship between film thickness and concentration of PEDOT:PSS solution is given in Figure 0.32, which exhibits an approximate linear relation. This demonstrates that film thickness can be controlled by the loading of inks.

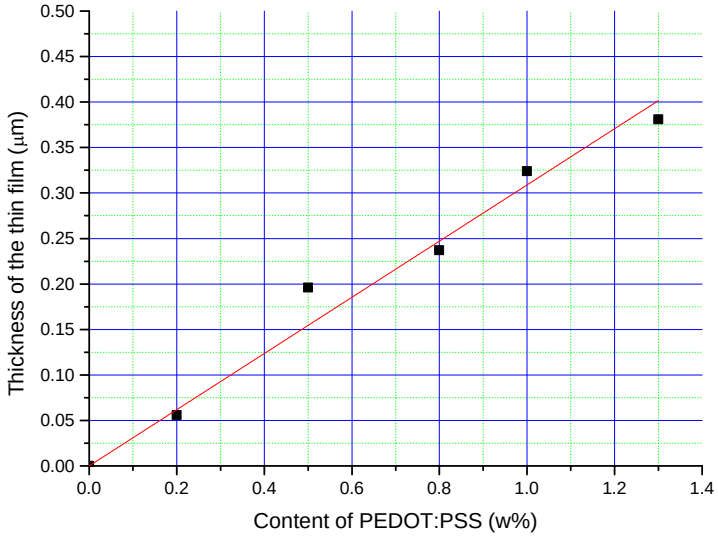

Figure 0.32 Relationship between the film thickness and the content of PEDOT: PSS in the ink

In fact, the purpose of altering the concentration of PEDOT:PSS is to change the amount of deposited material. Alternatively, by changing the printing dot spacing which determines the volume of ink deposited in a unit area the thickness of the printed films can be altered. The relationship can be calculated based on the results from Figure 0.32. The volume of a *Φ*60 μm single droplet is:

$$V_0 = \frac{4}{3}\pi r^3 = 1.1 \times 10^{-4}\, mm^3 \tag{4.12}$$

Since the dot spacing adopted in the thickness study is 50 μm, 400 droplets were contained in 1 mm^2 area and the total volume is:

$$V = 400 \times \frac{4}{3}\pi r^3 = 0.044\, mm^3 \tag{4.13}$$

Therefore the thickness of solution should be:

$$h_0 = 44\mu m \tag{4.14}$$

As the density of the solution is about 1.0 g/mm^3, the content of PEDOT:PSS is:

$$m = 0.044g \times 1.3\% = 5.72 \times 10^{-4} g \tag{4.15}$$

The density of PEDOT:PSS is:

$$\rho = \frac{m}{V} = \frac{5.72\times10^{-4}g}{4\times10^{-4}\ mm^3} = 1.43g/mm^3 \quad (4.16)$$

When the dot spacing is *s* μm, the thickness should be:

$$h = \frac{(\frac{1000}{s})^2\times V_0\times 1.3\%}{\rho} = \frac{1}{s^2}mm \quad (4.17)$$

Therefore, using 1.3 wt. % PEDOT:PSS solution to print film with a thickness of *h* mm, the dot spacing should be set as:

$$s = \sqrt{\frac{1}{h}}\ \mu m \quad (4.18)$$

4.4 Conclusions

(1) In the formulation and preparation of water-based ink, various methods to control ink properties have been investigated. Glycerol and surfactants have been used which are able to adjust the viscosity and surface tension respectively. The addition of ethanol also has certain impact on the surface tension. The relationship between viscosity and temperature has been established so that the viscosity of ink can be controlled by altering temperature without changing the components in the ink. After the formulation, filtering and ultrasonic processing are essential to avoid blocking of nozzle in the printhead.

(2) The droplet formation from a commercial printhead has been simulated using FLUENT. The simulation results suggest that both high surface tension and high viscosity can lead to less satellites and lower velocity of the droplets. However, retraction can occur when the droplet obtains an upward velocity. In addition, deviation of the droplets can likely be caused by the contaminated inner wall of the printhead.

(3) In dot printing, evaporation of the droplets can be accelerated by preheating, resulting in a more obvious coffee stain effect and more regular dot morphology. However, preheating is not always leading to smaller feature size. Although preheating can diminish the time of spreading, the upgraded wetting property can increase the spreading speed of the contact line at the same time. According to the experimental results of this study, to achieve the smallest feature size, it is predicted that the optimal preheat temperature of substrate in this experiment should be greater than 80 °C for

glass, but in a range of 30-40 °C for polyimide, 60-70 °C for FR4 and 50-60 °C for hydrophobic paper. The results are useful to provide a general guidance to the practice of inkjet printing industry. A mathematical model has been developed to explain the roles of surface tension and temperature in this process. In the printing of tracks, the optimal overlap rate for the four substrates has been tested and was found to be 27%, 32%, 33% and 28%, respectively. The width of the track is normally smaller than feature size due to the non-uniform spreading of inks in different direction of the printed droplets. For film printing, the thickness of films printed with PEDOT:PSS solutions with different concentration has been investigated. A relationship between the film thickness and printing resolution has also been established.

Chapter 5 Inkjet Printing of PEDOT:PSS Thin Film and Optimisation

In this chapter, deposition of PEDOT:PSS thin films using inkjet printing as well as their optimisation through modification of the inks are described. PEDOT:PSS is a prevalent conductive polymer, which has been widely used in the integration of electronic devices. It is also considered to be a competitive alternative to transparent conductive oxides (TCOs). Numerous methods have been developed to improve the electric conductivity of PEDOT:PSS. According to the mechanism of enhancement of electrical conductivity, these methods can be divided into two categories: i) altering the internal distribution of the conductive components, and ii) doping with additional conductive materials. This work aim to incorporating the two methods in the trials of inkjet printing of PEDOT:PSS thin films.

Section 5.1 is an introduction of the polymer blend PEDOT:PSS. The application of inkjet technology in printing PEDOT:PSS thin films and the optimisation of the printed PEDOT:PSS are also reviewed in this section. Altering internal distribution of conductive components and addition of doping with additional conductors into the matrix to improve the electrical conductivity of the inkjet printed PEDOT:PSS thin films are elaborated in section 5.2 and 5.3, respectively. The last section, 5.4, provides a conclusion of the results presented this chapter.

5.1 Introduction

5.1.1 Introduction of PEDOT:PSS

Poly(3,4-ethylenedioxythiophene):poly(styrenesulfonic acid) (PEDOT:PSS) is a polymer blend consisting of a polymeric form of ethylenedioxythiophene (PEDOT) and a polyelectrolyte sulfoxide (PSS) (Figure 0.1). PEDOT is unstable in its pH-neutral state which oxidizes rapidly in the air and insoluble in many common solvents. Therefore, PSS is added to improve the stability and solubility of PEDOT, allowing the formation of an aqueous dispersion of PEDOT:PSS, where PEDOT is in its oxidized state.

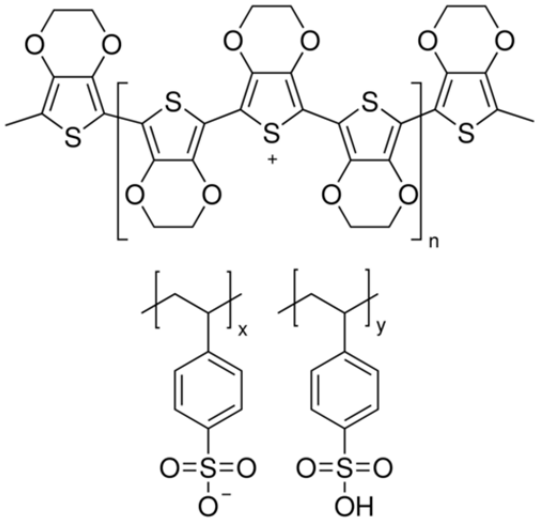

Figure 0.1 Chemical formula of PEDOT (top) and PSS (bottom) [40]

Numerous schematic models of the microstructure of PEDOT:PSS have been proposed. For instance, the PEDOT oligomers are considered as an attachment to the PSS chains [99], as shown in Figure **0.2**. However, Nardes [100] proposed a cross-sectional schematic morphological model of PEDOT:PSS (Figure 0.3). In this model, PEDOT:PSS is composed of pancake-like PEDOT-rich clusters (dark area) separated by PSS lamellas (bright area). The typical diameter of the clusters is in a range of 20-25 nm with a height of about 5-6 nm.

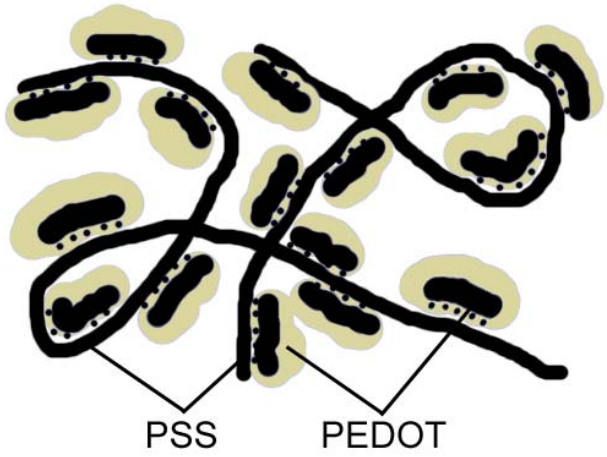

Figure 0.2 **Schematic structure of PEDOT:PSS (after ref. [92])**

Figure 0.3 Cross-sectional view of the schematic morphological model for PEDOT:PSS thin films derived from combined STM and X-AFM measurements [83]

PEDOT:PSS is a very promising material due to its excellent electrical and optical properties [101]. PEDOT has a low band gap of 1.5~1.6 eV, which is believed to originate from the influence of the electron-donor ethylene dioxy groups on the energies of the frontier levels of the π system. After doping with PSS, PEDOT exhibits reduced absorption in the visible and the oscillator strength shifts to below 1 eV in the metallic state. Hence it shows a high electrical conductivity up to 550 S/cm [102].

PEDOT:PSS has been widely used as an antistatic coating material, as electrodes for capacitors or photodiodes, and as a hole transport layer in organic LEDs during the last decade [103-107]. In polymer solar cell systems, it is often inserted as a sandwich structure between the TCO layer and the active layer to reduce the roughness of TCO, thereby reduces the possibility of shorts between the bottom and the top electrodes. Besides, PEDOT has a work function of 5.2 eV, further bridging the gap between the work function of ITO and the highest occupied molecular orbital (HOMO) level of Poly(3-hexylthiophene-2,5-diyl) (P3HT) donor material [108], which is beneficial for the transport of carriers.

PEDOT:PSS is also a promising candidate to replace ITO as an electrode in optoelectronic devices. As indium is a scarce and expensive material, there has been an imminent need to find new transparent conductive materials to replace ITO [109]. Furthermore, PEDOT:PSS exhibits high mechanical flexibility in contrast with the fragility of ITO, which enables various applications in flexible electronics. Kim et al. [36] fabricated TCO-free solar cells with a modified PEDOT:PSS layer as the anode. Such solar cells achieved the power conversion efficiency (PCE) as high as ITO-based organic solar cells. Yang et al. [110] used a PEDOT:PSS/Ag/PEDOT:PSS multilayer structure as the anode of the polymer solar cell and obtained a PCE of 2.99%. A large number of similar work [38, 111, 112] have increasingly demonstrated that PEDOT:PSS can act as a robust alternative option to replace ITO.

5.1.2 Inkjet printing of PEDOT:PSS thin film

As PEDOT:PSS is soluble in water, its solution can be deposited in principle by all techniques that are suitable for the deposition of waterborne coatings. The common deposition techniques include spin coating, drop casting, screen printing, doctor blading, inkjet printing and spraying. In recent years, deposition of PEDOT:PSS using inkjet printing has gained more and more interest and attention due to its agile data driven approach, and potential low material and energy consumption.

In Eom et al.'s study [27], a reliable solar cell with a PCE of 3.16% has been fabricated based on an inkjet-printed PEDOT:PSS layer. Ballarin et al. [28] printed thin films of PEDOT: PSS with inkjet printing and compared the properties with thin films prepared with spin coating. It has been found that no appreciable differences were noticed in terms of their electrochemical behaviour in the cells, which indicated that inkjet printing can be a good alternative for the thin film deposition of conjugated polymers. In Steirer et al.'s study [29], the standard bulk heterojunction (BHJ) devices containing PEDOT:PSS thin films prepared through spin coating, ultrasonic spray and inkjet printing as the buffer layer has achieved PCEs of 3.6%, 3.5%, and 3.3% respectively. The similar efficiencies also indicated that inkjet printing is a viable manufacturing route competing with spin coating for deposition of thin films in organic photovoltaic devices (OPV) applications.

As the properties of commercial aqueous PEDOT:PSS solutions (~1.2 mPas, ~72 dynes/cm) are not designed for inkjet printing, co-solvent with high viscosity and surfactants need be added into the PEDOT:PSS solution to adjust the jetting properties according to the requirements of specific inkjet printers [113, 114].

5.1.3 Optimisation of PEDOT:PSS

Numerous methods have been reported to improve the electrical conductivity of PEDOT:PSS. These methods can be divided into two categories: altering the internal distribution of PEDOT, and doping additional conductors.

5.1.3.1 Altering internal distribution of PEDOT

As introduced in Section 5.1.1, PEDOT:PSS is composed of conductive PEDOT islands surrounded by insulating PSS lamellas. Therefore, it can be deduced that the electrical conductivity of PEDOT:PSS will be influenced by the distribution of the PEDOT islands and PSS chains. Some related research works on this topic from the literature are summarized in Table 5.1. Dobbelin et al. [115] found that the addition of ionic liquids can swell the PSS domains inducing phase separation domain with an excess of insulating PSS surrounded by a phase of merged conducting PEDOT grains; a three-dimensional conducting network can thereby be formed. Ouyang et al. [116] emphasised that the conductivity of PEDOT:PSS can be enhanced by treating with a co-solvent which leads to the preferential arrangement of the PEDOT and PSS chains, resulting in phase separation of PSS-H chains from the PEDOT:PSS film and the conformational changes of the PEDOT chains. Xia et al. [117] reported similar results and expanded the range of co-solvent materials to demonstrate their effect on the thin film deposition. Reyes et al. [118] enhanced the conductivity of PEDOT:PSS films by adding a small amount of dimethyl sulphate (DMS), and found that the SO_4^{-2} anionic sulphates in DMS can partially replace the PSS^- segments and increase the bipolaron population by an ion exchange process. Huang et al. [119] revealed that high boiling point solvent can also improve the conductivity of PEDOT:PSS thin films as the added solvent leading to larger grain sizes and lower inter-grain hopping barriers. Fan et al. [120] proposed that the addition of anionic surfactants and salts can enhance the conductivity of PEDOT:PSS base on a different mechanism. The effect of anionic surfactant is due to the anion exchange between the surfactants and PEDOT:PSS in

solution, and the effect of salt is attributed to the PSS loss from the PEDOT:PSS film and the conformational change of PEDOT.

Table 0.1 Summary of research works of improving the conductivity of PEDOT:PSS by altering distribution

Additive	content (solution)	Conductivity (S/cm)		Author
		Pristine	Improved	
Ionic liquid (BF_4^-)	1.5 wt.%	14	136	Dobbelin [115]
Ethylene glycol	-	0.4	200	Ouyang [116]
DMSO			143	
NMP			46	
N,N-dimethylacetomide			37	
4-Methoxyphenol			20	
Methanol	70-80 vol.%	0.2	69.7	Xia [117]
Ethanol			72.7	
IPA			42	
ACN			78.9	
Acetone			47.1	
THF			40.9	
Dimethyl sulfate	4 wt.%	0.07	132	Reyes [118]
Sorbitol	5 wt.%	0.05	4	Huang [119]
Glycerol			0.6	
SDS	6 wt.%	0.16	80	Fan [120]
POETE	8 wt.%	0.16	4	
CuCl3	1 mol/L	0.2	144	

5.1.3.2 Doping with additional conductive materials

Metal nanoparticles (NPs) have been used to enhance the conductivity of conductive polymers (e.g. polyaniline [121, 122]) since 2002. Subsequently researchers utilised this method to enhance the conductivity of PEDOT:PSS, and the related work has been summarised in Table 5.2. The purpose of doping with additional conductors is to provide more conductive connections between the PEDOT islands which are separated by the insulating PSS lamellas. Melendez et al. [123] synthesised the Ag NPs in the presence of PEDOT:PSS to obtain Ag(PEDOT:PSS) composites. The films deposited using the composites exhibited conductivity three orders of magnitude higher than pristine PEDOT:PSS. Similar results have been reported in Moreno et al.'s work [124]. Moreover, PEDOT:PSS films doped with metal nanoparticles are able to sense biologically important compounds such as dopamine and uric acid in presence of excess ascorbic acid, with superior selectivity and sensitivity when compared to the polymer film alone [125]. Other conductors, such as graphene [126], ZnO [127] and

carbon nanotubes (CNT) [128, 129], have also been incorporated into PEDOT:PSS to improve the electrical properties.

Table 0.2 Summary of research works in improving the conductivity of PEDOT:PSS by doping with additional conductors

Conductor	Conductivity		Transparency	Author
	Pristine	Improved		
Ag	5.24×10^{-4} S/cm	1.63 S/cm	-	Melendez [124]
Graphene	10^{-5}-10^{-6} S/cm	0.2 S/cm	> 80 %	Xu [126]
ZnO	~168 S/cm	~300 S/cm	-	Semaltianos [127]
CNT	> 4 kΩ/sq	~400 Ω/sq	-	Denneulin [129]
CNT	10^4 kΩ/sq	~1 kΩ/sq	~70%	Mustonen [128]

5.2 Solvent & thermal annealing

In this section, solvent annealing and thermal annealing are incorporated in the inkjet printing of PEDOT:PSS thin films. The effect of the annealing processes on the microstructure and properties of the PEDOT:PSS are discussed.

5.2.1 Solvent annealing

5.2.1.1 Experimental procedures

The PEDOT:PSS solution was modified to reach a jettable viscosity by doping glycerol and deionized (DI) water. The viscosities of the mixture liquid with different contents of the components are shown in Figure 0.4. The prepared ink was then jetted on the glass substrate at room temperature using the Microfab Jetlab® 4 inkjet system. Droplets with a diameter of 60 µm were obtained without satellite. Dot spacing was fixed at 50 µm. After printing, the samples were baked in an oven at 100°C, 150°C and 200°C for 20 min, respectively.

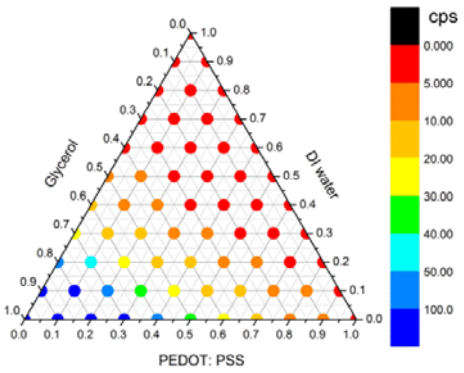

Figure 0.4 Viscosity distribution mapping of the mixture of glycerol, PEDOT: PSS and DI water

5.2.1.2 Effect of doping content

5.2.1.2.1 Morphology

From Figure 0.5, interestingly, the addition of glycerol has exhibited an opposite effect on the surface roughness of the thin films (baked at 100 °C) at macro scale (250×250 μm^2) in comparison with micro scale (1×1 μm^2). At the macroscopic scale, the surface of inkjet printed thin films is not as uniform as the films deposited by other printing methods, e.g. spin coating. This is primarily attributed to the "coffee stain effect" that has occurred in the inkjet printing on the bases of individual single dots forming a continuous film. As a high boiling point solvent, glycerol in this case can assist to reduce the evaporation rate of the droplets, thereby the formation of "coffee ring" can be hindered resulting in a relatively flatter surface [130]. However, at the microscopic level, the aggregation of PEDOT-rich particles which have been generated due to the addition of glycerol can result in an increased roughness on the film surface. Such aggregations have been observed on an area of 1×1 μm^2 using AFM analysis.

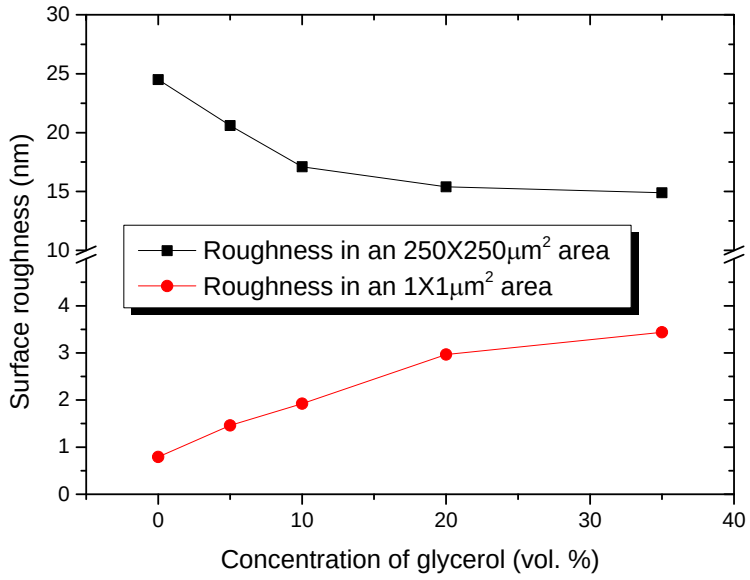

Figure 0.5 Surface roughness of PEDOT:PSS thin films vs. addition of glycerol (deposited at room temperature)

As shown in the images in Figure 0.6, no obvious particles can be found in the thin films prepared with pristine PEDOT:PSS with 5% glycerol. However, the surface morphology of the glycerol doped PEDOT:PSS became more inhomogeneous than the pristine PEDOT:PSS. When doped with 10% glycerol, the topography of the thin films

displayed elliptic particles in a preferential direction, as been reported in Nardes et al.'s study [131]. The alignment of such particles can be explained by referring to the model Vitoratos has established [99]. Accordingly, the ionic bonds between PEDOT and PSS chains are firstly broken by the addition of glycerol [117]. The negative charges on the PSS chains then repulse each other to form a better organized alignment. As the content of glycerol increases to 20%, the elliptic particles become round shape and bigger, which indicates a significant concentration of PEDOT caused by the repulsion. A further increase in the content of glycerol makes the particles much easier to be identified, exhibiting more significant aggregation.

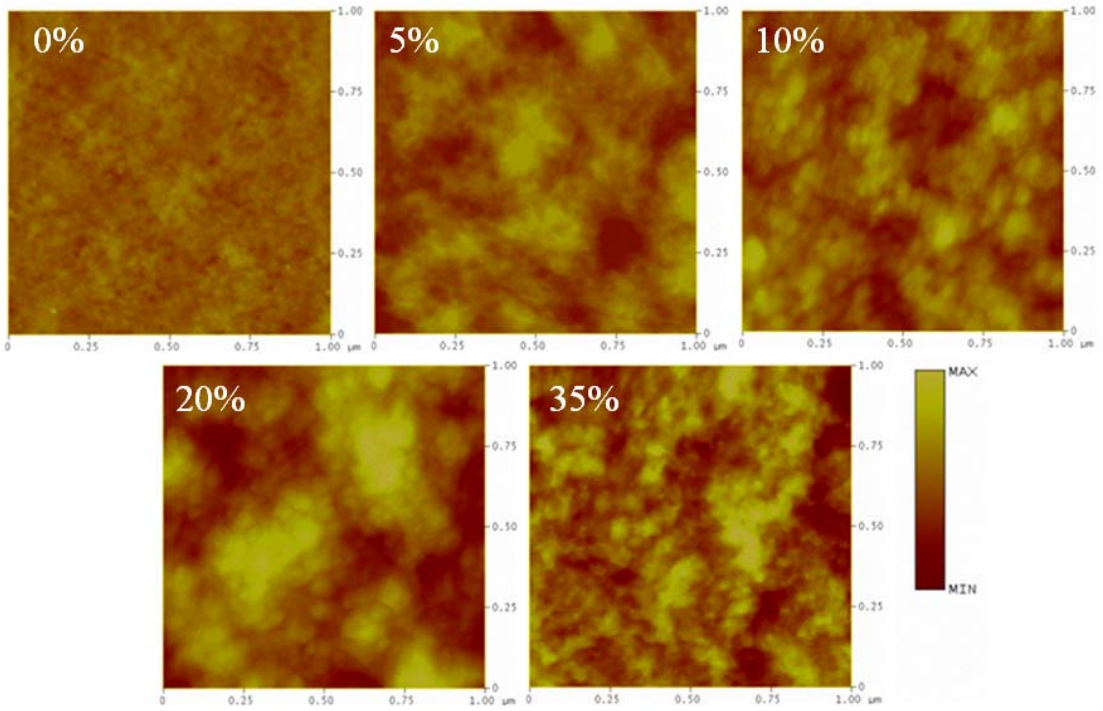

Figure 0.6 AFM images on an area of 1 × 1 μm^2 of thin films prepared with pristine PEDOT:PSS and PEDOT:PSS doped with 5%, 10%, 20% and 35% glycerol

5.2.1.2.2 Conductivity

Figure 0.7 shows the conductivity of the thin films prepared with glycerol doped PEDOT:PSS inks. Clearly, the conductivity of the thin film increases rapidly with the content of glycerol. With the addition of 5% glycerol, the conductivity is enhanced for over 20 times, close to the 12 times of Huang's work [119]. With the content of glycerol 35%, the conductivity is increased approximately 300 times. Despite the significant improvement in film conductivity, further addition of glycerol to the ink led to a high viscosity which ultimately reduces its jetting ability as seen in Figure 0.4. It is

reported that the electrical conductivity of PEDOT:PSS thin films depends strongly on the extent of aggregation of the constituent polymer nanoparticles [39, 132]. Therefore, the addition of glycerol in the inks can improve the conductivity of the thin films drastically.

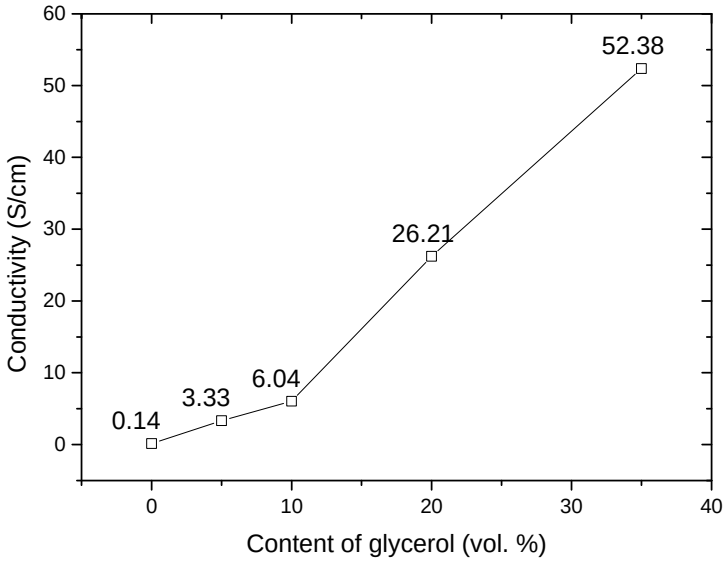

Figure 0.7 Conductivity of PEDOT:PSS thin films vs. addition of glycerol

5.2.1.3 Effect of baking temperature

5.2.1.3.1 Morphology

The thickness and surface roughness of the PEDOT:PSS thin films baked at different temperatures are shown in Figure 0.8. The concentration of PEDOT:PSS in the doped inks was reduced due to the addition of glycerol, resulting in a much thinner film. However, Baking at 150 °C and 200 °C, has led to a reduction of the thickness of the thin films by approximately 50 nm compared with the ones baked at 100 °C. Since 150 °C is lower than the degradation temperature (~200 °C) of both PEDOT and PSS, the shrinkage induced from this process is probably due to the evaporation of the residual glycerol.

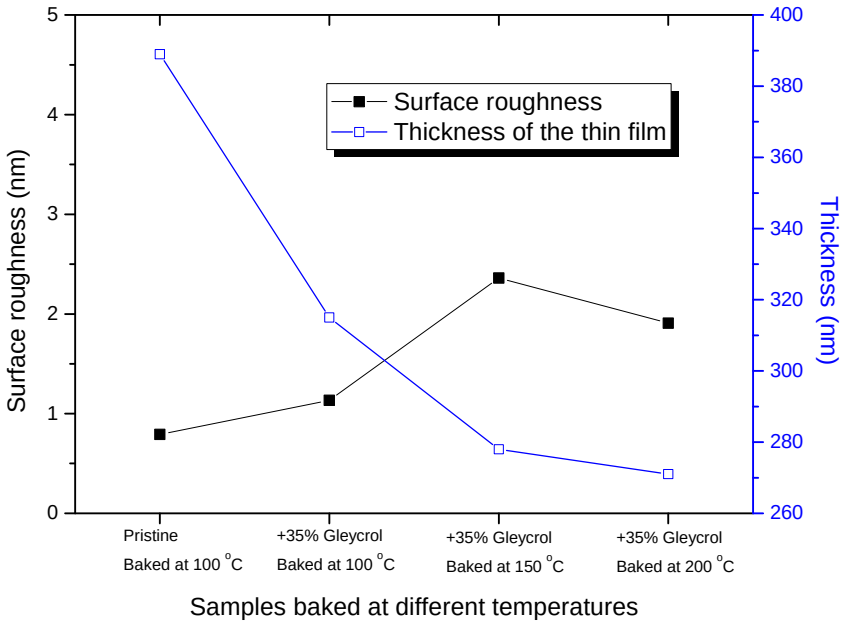

Figure 0.8 Thickness and surface roughness of PEDOT:PSS thin film under different baking conditions

The surface profile of the thin films was affected by such shrinkage, as shown in Figure 0.9. It is reported [133] that the PEDOT and PSS chains can be reorganised and stabilised during subsequent thermal annealing by a plasticizing effect with the existence of glycerol.

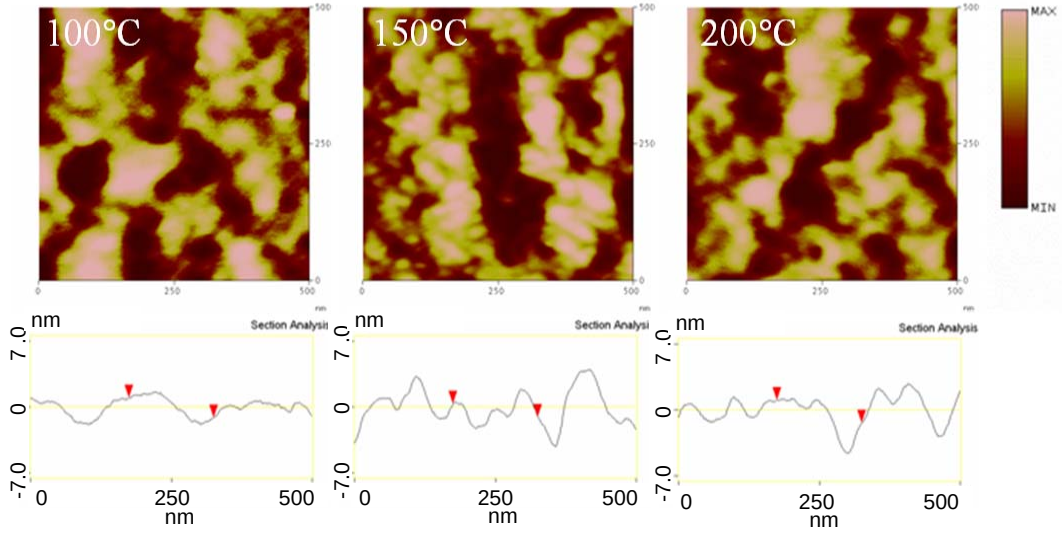

Figure 0.9 AFM images (500 × 500 nm^2) and cross section profiles of PEDOT:PSS thin films baked at 100°C, 150°C and 200°C

5.2.1.3.2 Conductivity

Further improvement in the conductivity of the thin films was found after annealing as shown in Figure 0.10. The measured conductivity of the thin films was 82.5 S/cm after baking at 150 °C, in comparison with 52.4 S/cm obtained by baking at 100 °C. However, no further significant improvement in conductivity has been observed when baking at 200 °C. This might be caused by the reorganization and stabilization of the PEDOT and PSS chains during subsequent thermal annealing.

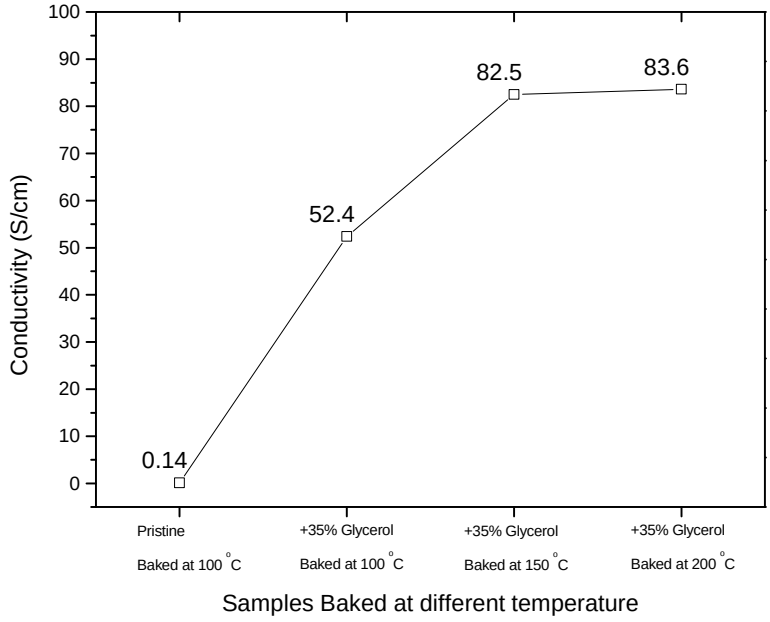

Figure 0.10 Conductivity of PEDOT:PSS thin film under different baking conditions

5.2.1.3.3 Transparency

The transmittance of the thin films (including the substrate) prepared with pristine and glycerol doped PEDOT:PSS inks are shown in Figure 0.11. Comparing the films with and without doping, it can be concluded that the addition of glycerol is beneficial to transparency. As above mentioned, glycerol can facilitate the formation of large PEDOT-rich particles, therefore, the number of interfaces between PEDOT-rich particles and PSS lamellas can be reduced, contributing to the reduction of absorbance of light. Moreover, the loss of transmittance of glycerol doped PEDOT:PSS is not as significant as the pristine PEDOT:PSS after baking above 150 °C, which suggests that the existence of glycerol may also help to restrain the degradation of PEDOT.

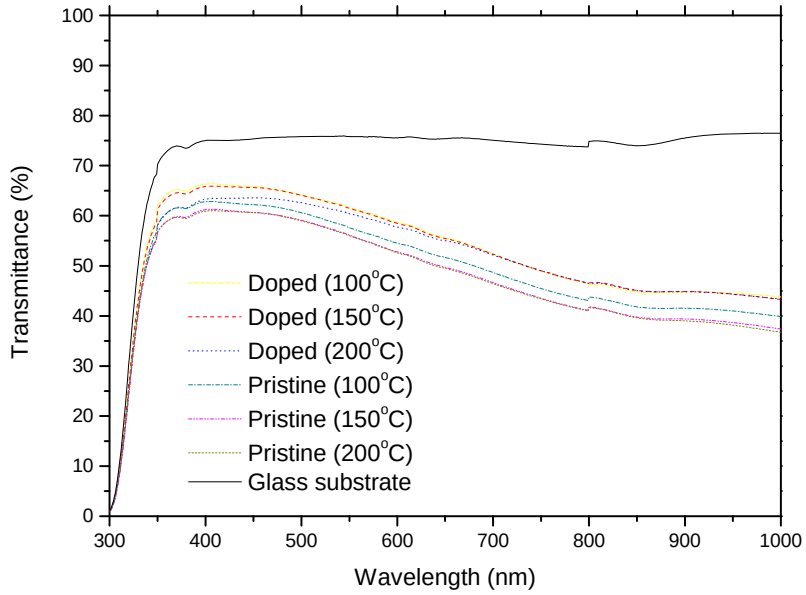

Figure 0.11 Transmittance of glass substrate, pristine and glycerol doped PEDOT:PSS thin films with substrate

5.2.2 Thermal annealing

5.2.2.1 Experimental procedures

The inkjet printing was carried out using the Microfab Jetlab® 4 inkjet system. During the thin film printing, droplets with a diameter of 60 μm were firstly optimised to eliminate any satellite. Thin films of an area of 6 mm × 55 mm were then printed on prewashed glass substrates with a fixed dot spacing of 50 μm. Pristine 1.3 wt.% PEDOT:PSS solution was printed and then baked at temperatures of 100 °C, 150 °C, 200 °C, 225 °C, 250 °C, 275 °C, and 300 °C for 20 min.

5.2.2.2 Effect of baking temperature

5.2.2.2.1 Morphology

The appearances of baked PEDOT:PSS thin films obtained from optical microscope are given in Figure 0.12. Accordingly, the colour of the thin films is found to become darker with the increase of baking temperature. The difference is particularly obvious between 250 °C and 275 °C. This indicates the possible effect on the transmittance of the thin films deposited.

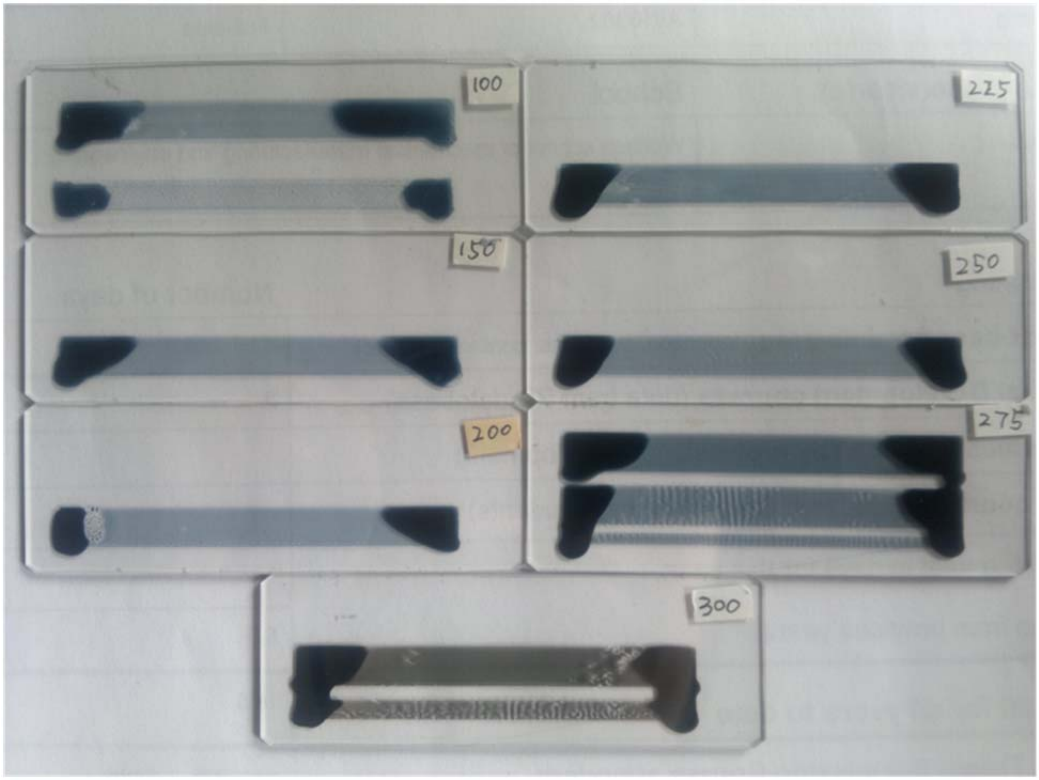

Figure 0.12 The appearance of PEDOT:PSS films after baking at different temperatures

Figure 0.13 shows the thickness and surface roughness of these PEDOT:PSS thin films baked under different temperatures. When the baking temperature is below 275 °C, both thickness and surface roughness remain nearly constant. However, after baking at 300 °C, an obvious decrease in the thickness can be observed, with an increase in the surface roughness. This indicates that the film has been damaged at such high temperature.

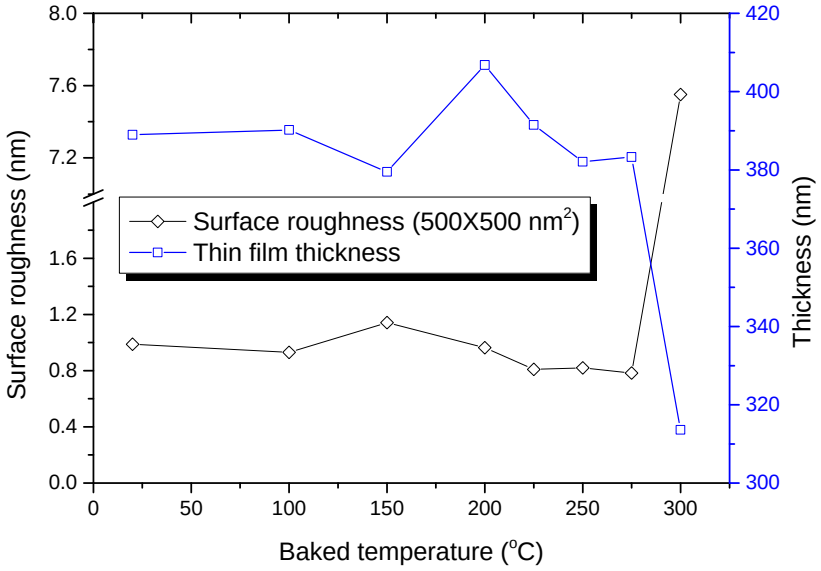

Figure 0.13 Thickness and surface roughness of the PEDOT:PSS thin films baked at different temperatures

According to the AFM height images and phase images (PEDOT and PSS can be distinguished by colour) derived simultaneously from the thin films after baking and presented in Figure 0.14 and Figure 0.15, it is indicative that the microstructure has changed due to the baking at 225 °C or higher. In particular, the size of PEDOT-rich particles seemed to have increased which was accompanied by a decrease in surface roughness. It is recognised that the increase of the PEDOT-rich particle size is attributed to following two effects: i) aggregation of PEDOT [99], ii) degradation of PSS chains (especially when baking above 250 °C) [134]. Severe degradation of the surface of the thin film after baking at 300 °C has been observed (Figure 0.14 and Figure 0.15).

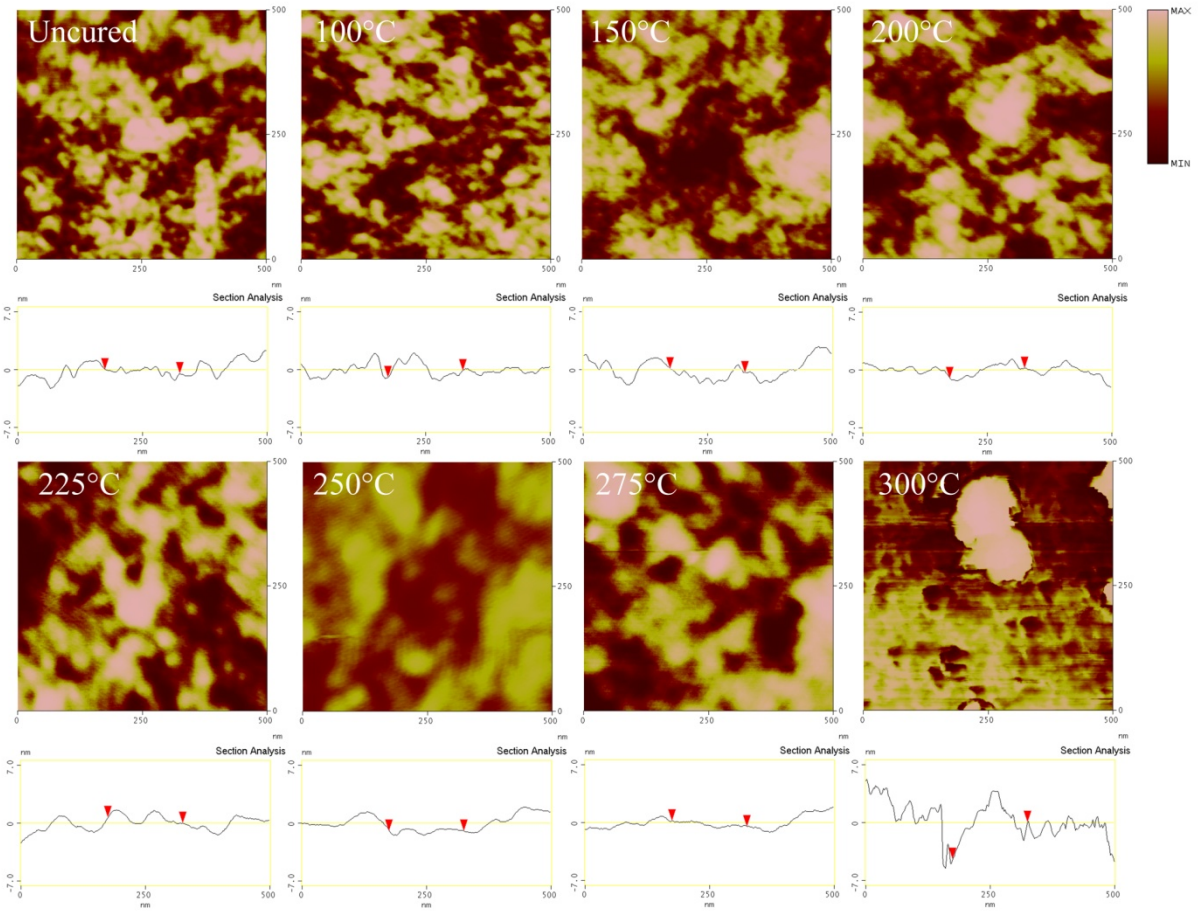

Figure 0.14 AFM images and cross section profiles of PEDOT:PSS thin films: affect of thermal annealing

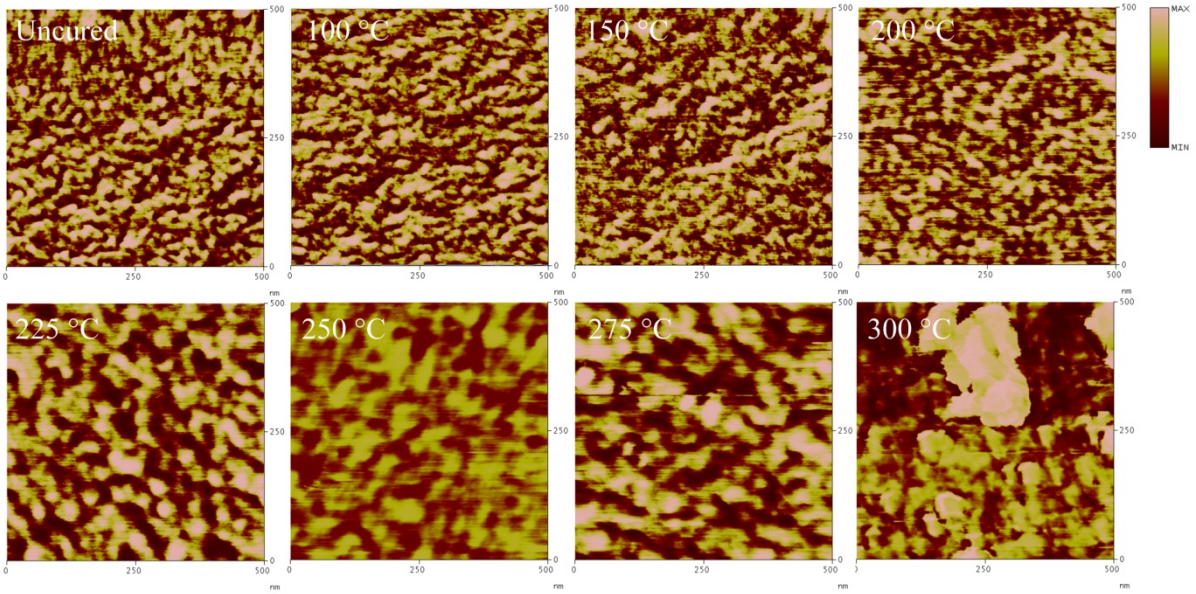

Figure 0.15 Phase images of PEDOT:PSS thin films due to thermal annealing

5.2.2.2.2 Conductivity

Figure 0.16 shows the results from the measurements of conductivity. Thermal annealing did not significantly reduce the electrical resistivity of the PEDOT:PSS thin films, which somewhat disagrees to what have been reported in the literature [35, 135]. Indeed, when baking below 250 °C, the conductivities remain almost constant, with a slight rise. An obvious decrease in conductivity of the thin film when baking at 275 °C has occurred. However, very poor conductivity was observed for films baked at 300 °C, which is out of the range of the micro-ohmmeter. According to the morphology obtained *via* AFM, the relationship between conductivity and microstructure of the thin films can be established. Although the aggregation of PEDOT is beneficial to the electric conductivity of the thin film, the electric conductivity was still reduced, which is primarily attributed to the weakened connection between PEDOT-rich particles because of the loss of PSS.

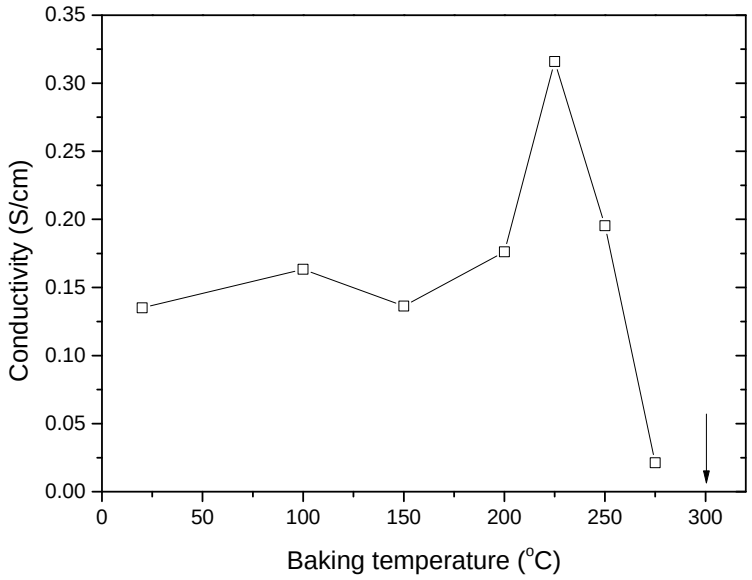

Figure 0.16 Conductivity of the PEDOT:PSS thin films after baking at different temperatures

Such negative effect of baking on the electrical conductivity of thin films does not necessarily present a problem when used in actual devices, as such thermal annealing may still be beneficial for the connection between the thin films and other parts of the devices [136]. Based on the experimental results in this study, it is recommended that the thermal annealing temperature should not be higher than 250 °C.

5.2.2.2.3 Transparency

Figure 0.17 presents the effect of baking on transmittance. The transmittance of the thin films decreases with the increase of baking temperature. This is particularly when the baking above 250 °C, which is in agreement with the colour change shown in Figure 0.12. Baking at 300 °C seemed to result in a rather different behaviour in light absorption, which indicates a dramatic change in the components of the thin film.

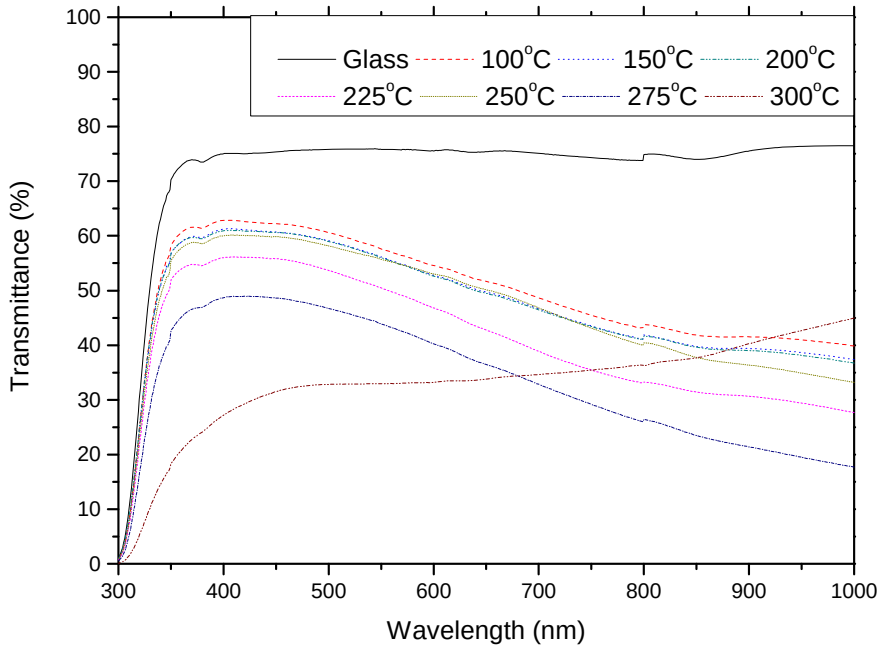

Figure 0.17 Transmittance of bare glass and PEDOT:PSS thin films with glass substrate after baking at different temperatures

5.3 Conductor doped PEDOT:PSS

This section verifies the applicability of doping with additional conductive materials in the inkjet printing of PEDOT:PSS patterns.

5.3.1 Silver nanoparticle (Ag NPs) doped PEDOT:PSS

5.3.1.1 Experimental procedures

5.3.1.1.1 Ink preparation

To investigate the formation of Ag NPs doped PEDOT:PSS, two methods have been used in the study.

In the first method, seven equal volume solutions of reactants for composite solutions I-VII were prepared by dissolving silver nitrate in deionized water, then mixing with PEDOT:PSS solution (1.3 wt.%). After being homogeneously mixed by ultrasonicator, the mixture was stirred vigorously in a heated water bath to induce a reaction between silver nitrate and PEDOT:PSS. The formulation, reaction time and temperature to prepare composites I-VII are listed in Table 5.3. Following this, 0.5 wt.% JC-601, 1 wt.% glycerol and 5 wt.% ethanol were added into these to form Inks A-G using the readily prepared composites I-VII respectively. The viscosity and surface tension of the inks were adjusted to 5 cps and 35 dynes/cm respectively prior to the inkjet printing trials.

Table 0.3 Preparation and reaction parameters of Ag-PEDOT:PSS composite solutions and mass of filtered Ag particles

Composites	$AgNO_3$ (g)	PEDOT:PSS solution (g)	DI water (g)	Reaction time (h)	Temperature (°C)	Mass of filtered Ag NPs (g)
I	0. 16	10	90	1	60	0.075
II	0.16	10	90	2	60	0.079
III	0.16	10	90	3	60	0.081
IV	1.6	10	90	3	60	0.843
V	0.016	10	90	3	60	0.004
VI	0.16	10	90	3	40	0.081
VII	0.16	10	90	3	80	0.083

In the second method, the same group of composite solutions I-VII shown in the Table 5.3 were also prepared following the same procedures, but they were subsequently centrifugally rotated (4000 r/min, 10 min) for several times to enable the separation and filtration of the pure Ag NPs from solvent. The mass of the filtered Ag NPs from each composite solutions (I-VII) is given in the Table 1, which indicates a collection rate was close to 80% of the theoretical masses which are approximately 0.1 g from composites I, II, III, VI and VII, 1 g from IV and 0.01 g from V. The composite V represents an abnormal low collection rate as the particle size is too small to be separated at a high rate. The similar collection rate from different samples indicates the complete reduction reaction for all the samples. Once the silver particles were obtained

from the filtration, they were subsequently ultrasonically dispersed into a solution of 10 g PEDOT:PSS solution (1.3 wt.%) then dissolved in 90 g DI water. Ultrasonic cavitation generates high shear that can break particle agglomerates into single dispersed particles and therefore is suitable for the dispersion of Ag NPs in this study. Such prepared mixtures were then thoroughly blended with 0.5 wt.% JC-601, 1 wt.% glycerol and 5 wt.% ethanol to form the Ag-PEDOT:PSS inks a-g with respect to the initial composite solutions I-VII, which can be readily utilized for inkjet printing trials.

In both methods, the contents of PEDOT:PSS were 0.12 wt.% in all inks, so that it is possible to investigate the effect of silver content and silver nanoparticle size. The contents of silver in different inks are listed in Table 5.4. The materials and contents of the other components in inks A-G and a-g were kept the same and less critical, therefore they were not included. No sedimentation was observed in the inks after standing for 24 h. However, few micro scale black particles can be found on the bottom and side of the container after standing for 72 h, which means the stability of the inks needs to be further improved. Hence the printing works in this study were carried out in 24 h after the formulation of inks.

Table 0.4 Contents of silver in Inks A-G and a-g

Ink	Silver content (g)	Ink	Silver content (g)
A	0.1	a	0.075
B	0.1	b	0.079
C	0.1	c	0.081
D	1	d	0.843
E	0.01	e	0.004
F	0.1	f	0.081
G	0.1	g	0.083

5.3.1.1.2 Inkjet printing of thin films

The inks were jetted using model Spectra SE-128 printhead with a printing frequency of 2000 Hz. The droplet size was ~50 μm and the subsequent dot size ranged from 120 to 150 μm. Areas of 10 mm × 10 mm squares were printed on prewashed glass substrates and then dried at 50 °C in dry chamber for 1 h. The printing resolution was fixed at 500 × 500 dpi, so that thin films with a thickness around 300 nm after drying can be obtained.

5.3.1.2 Synthesis of Ag NPs

5.3.1.2.1 XRD patterns

The XRD patterns shown in Figure 0.18 confirmed the formation of Ag NPs. The peaks in the spectra matched very well with the standard cubic silver particles. The line broadening (~0.0134 rad) indicates that the obtained silver in the solutions are nano-sized particles.

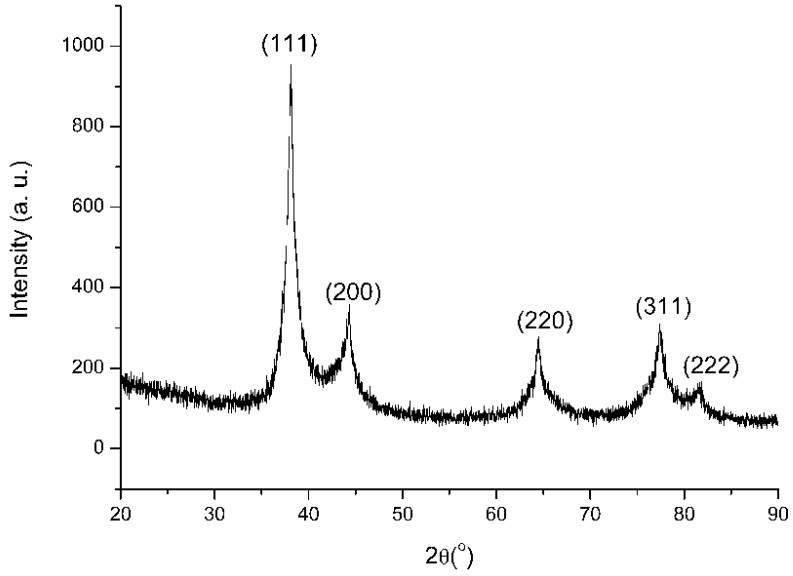

Figure 0.18 XRD patterns of silver lattice structure from the obtained Ag NPs for the ink formulation

5.3.1.2.2 TEM

The interpretation has been verified in Figure 0.19 which shows the TEM images of composite III (Figure 0.19 (a)) and silver particles separated from composite III (Figure 0.19 (b)). Before the separation of PEDOT:PSS and silver nanoparticles (Figure 0.19 (a)), most of the nanoparticles are attached to PEDOT:PSS pieces which appears as a gray area which is slightly darker than the background in the image. Only a few particles with extreme small size were spread apart from the polymer islands. After the centrifugal separation and cleansing (Figure 0.19 (b)), no obvious gray clusters can be observed, indicating that the polymer is thoroughly removed from the silver nanoparticles. In addition, the nanoparticles are well dispersed in ethanol due to the low concentration and deagglomeration effect of ultrasonic.

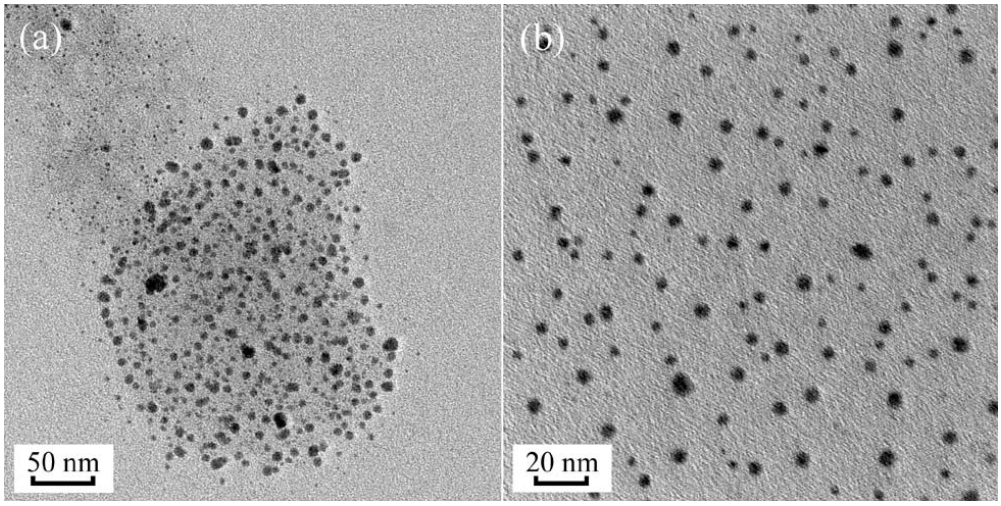

Figure 0.19 TEM images of silver NPs before (a) and after (b) separation from PEDOT:PSS

Based on the measurement results of Nano Measurer 1.2, the optimised B-splines of size distribution of the nano particles are shown in Figure 0.21, Figure 0.22, and Figure 0.21. The statistical results indicate that reaction time, reaction temperature and reactant ratio have had certain effects on the size of silver nano particles. Extending the reaction time from 1 hour to 2 hours has slightly increased the average size of silver NPs by 1 nm. However, no obvious further increase of the particle size was observed during the reaction for another hour (Figure 0.20). The concentration of silver ions has a distinct impact on the particle size. When the content of silver was 1 wt.%, the average size reached 11 nm with a broadened peak which suggests a heterogeneous size distribution. At 0.01 wt.% silver content, the average size was only 4.5 nm due to the low concentration of silver ion which limited the growth of the particles (Figure 0.21). By comparing composites VI, I and VII, their average size of particles was 5 nm, 6 nm and 8.5 nm respectively. It can therefore be concluded that the particle size increased with the increase of reaction temperature, indicating that the higher reaction temperature leads to fast growth of Ag NPs [137] (Figure 0.22). Moreover, according to the measuring results, the uniformity of the particle diameter, which can be inferred by the width of B-splines, is inversely proportional to the average particle size.

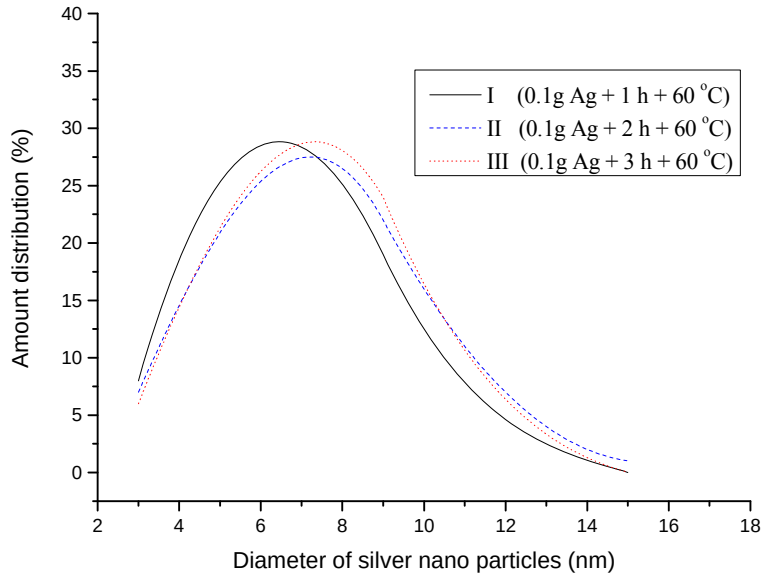

Figure 0.20 B-splines of size distribution of the silver NPs of composites I, II, and III

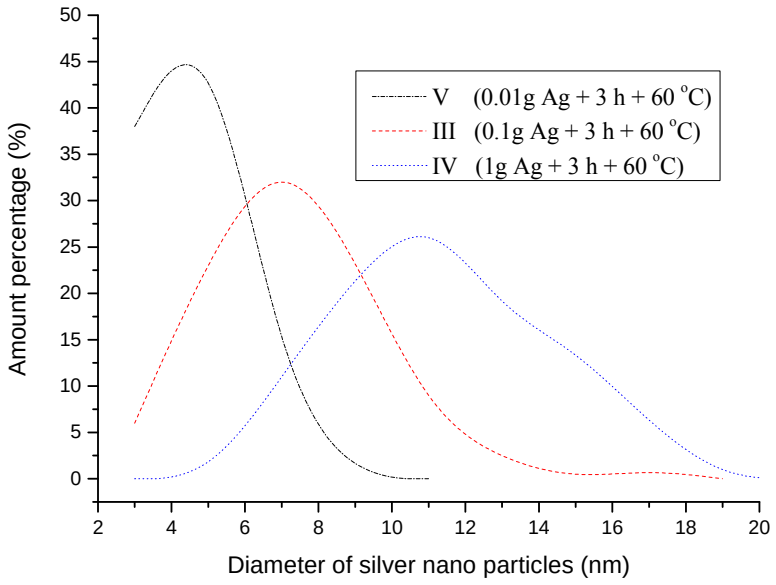

Figure 0.21 B-splines of size distribution of the silver NPs of composites V, III, and IV

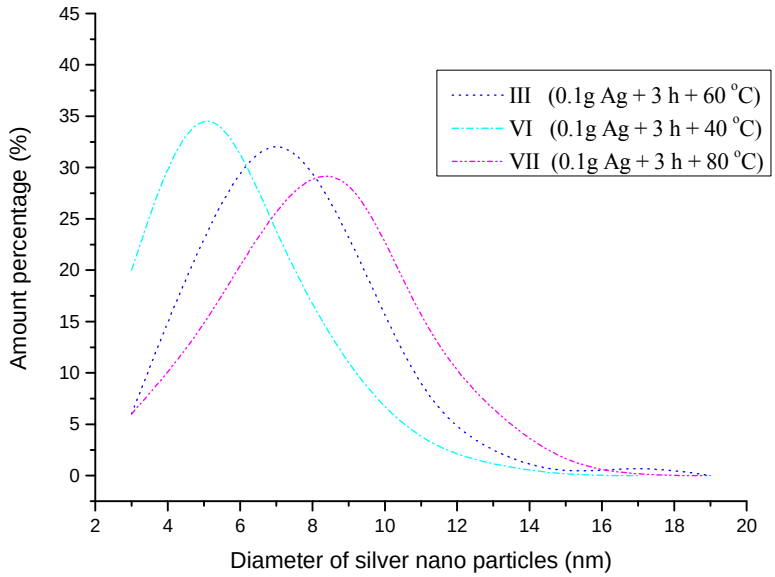

Figure 0.22 B-splines of size distribution of the silver NPs of composites III, VI, and VII

5.3.1.3 Thin film printing and characterisation

5.3.1.3.1 Electric conductivity

The conductivity of thin films printed with pristine PEDOT:PSS, Inks A-G and a-g are measured and given in Figure 0.23, as well as the calculated weight percentage of silver in the dried films. Interestingly, the thin films printed with *in situ* synthesised Ag-PEDOT:PSS composite inks (Inks A-G) were not enhanced as expected. However, reductions of conductivity are observed in thin films printed with A, B, C and F. The reaction between PEDOT:PSS and silver ion is predicted to be as follows [138]:

$$\mathrm{PEDOT{:}\,PSS} + \mathrm{Ag^{+}} + \mathrm{e^{-}} \leftrightarrow \mathrm{PEDOT} + \mathrm{Ag{:}\,PSS} \qquad (5.1)$$

It can be deduced that the electrostatic interaction between PEDOT and PSS was inhibited by the formation of Ag NPs and Ag:PSS bonds [139]. Although the obtained Ag NPs increased the percolation of PEDOT-rich islands [128], which can potentially enhance the thin film conductivity, the inhibited bonds between PEDOT and PSS have a more pronounced opposite effect. These two concurrent processes had taken place simultaneously, leading to unpredictable results in conductivity of the deposited films.

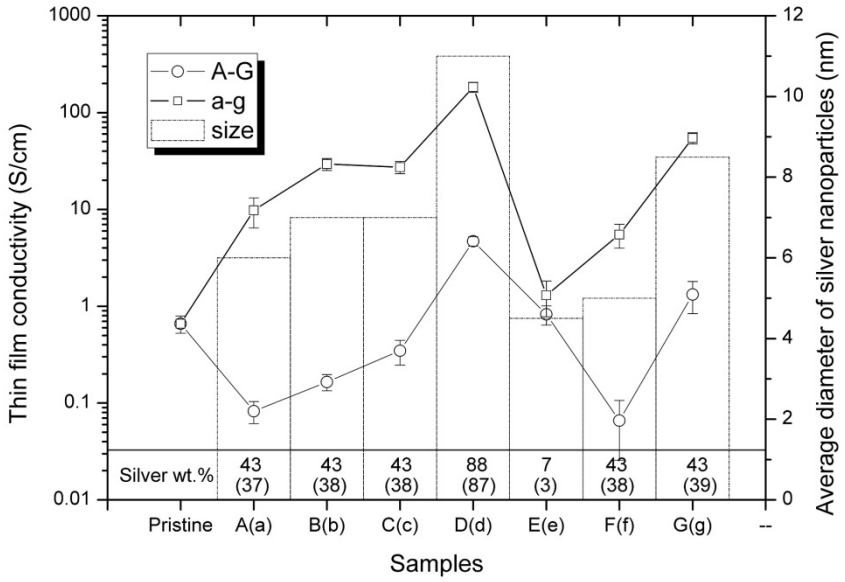

Figure 0.23 Conductivity of thin film prepared by ink-jetting the pristine PEDOT:PSS, Inks A-G and a-g, and the average size of the Ag NPs in them.

However, the conductivity of thin films printed with Inks a-d, f and g had been significantly enhanced. Without the reaction between PEDOT:PSS and silver ions, the enhancement was no longer hindered by the negative effect which occurred in Inks A-G. The content of silver has a significant influence on the degree of such enhancement. The conductivity of the thin films has been drastically improved, for instance, by adding 0.1 wt.% silver it can be 15-80 times higher than the films without addition of silver particles (48 kΩ/sq), the sheet measured resistance can reach approximately 609~3400 Ω/sq. If more silver being added, the sheet conductivity can even be as 280 times higher, e.g. 182 Ω/sq by adding 1 wt.% silver. No obvious change in conductivity has been observed for thin films printed with Inks E and e (0.01 wt.% silver), as the content of silver in them is too low to make any major effect on the thin film properties. By comparing thin films printed with Inks a, b, c, f and g, which have the same silver content, it can be concluded that the larger size of Ag NPs has had a more obvious improvement of conductivity. Similar conclusion has been reported in Rebeca G. Melendez et al.'s work [116]. The effect of particle size on the conductivity can be understood with the assistance of schematic illustration established based on the model Nardes proposed [93] (Figure 0.24). Compared with small Ag NPs, large Ag NPs are more easily to contact with more than one PEDOT islands simultaneously and thereby bridge the gap of insulating PSS between different PEDOT islands. Meanwhile larger contact surface area between PEDOT and the bridging Ag NPs (yellow area in

Figure 0.24) will be formed. As the work functions of silver and PEDOT:PSS are close to each other [140], more effective conducting networks can be obtained with large Ag NPs, leading to higher conductivity of the thin films.

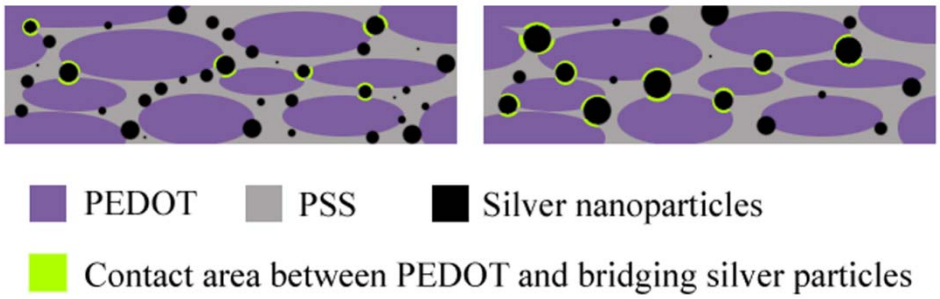

Figure 0.24 Schematic illustration of the proposed structure of the films formed by ink-jet printing of Ag NPs doped PEDOT:PSS

5.3.1.3.2 Transparency

The UV-Vis spectrum of thin films printed with pristine PEDOT:PSS, Inks E, C, D and c are shown in Figure 0.25. Thin films printed with Inks A, B, F and G are not listed in the figure as they have very similar curves with Ink C. Due to the low content of silver nitrate, the transmittance of thin film printed with Ink E (~94.7%, absorbance: 0.024) is close to pristine PEDOT:PSS (~95.1%). The average transmittances of thin films printed with Inks C, D, c are 82.5% (absorbance: 0.084), 74.5% (absorbance: 0.128) and 82.4%, respectively. Apparently, the absorbance of the films increases with the concentration of silver nanoparticles. As the weight percentage of silver in films printed with Inks E, C and D are 7%, 43% and 88%, a quasi linear relationship between the absorbance and silver content can be fit, which accords with Beer's Law [141]. A formula is therefore deduced to roughly predict the average transmittance of the Ag-PEDOT:PSS films:

$$T\% = 10^{1.98-0.1273\times x} \tag{5.2}$$

Where $T\%$ is the average transmittance and x is the weight percentage of silver. It is noticed that, with the same content of Ag, thin films printed with Ink C and Ink c have slight difference in the shape of transmittance curves, where the absorbance near 400 nm of thin film printed with Ink C is more significant. When doping with PSS, PEDOT is in its oxidized state which presents quasi-transparency; in the undoped state, PEDOT presents blue colour and therefore exhibits a higher absorbance in the blue light region

[142, 143]. Therefore the dedoping of PSS from PEDOT after the reaction between silver ion and PEDOT:PSS is confirmed.

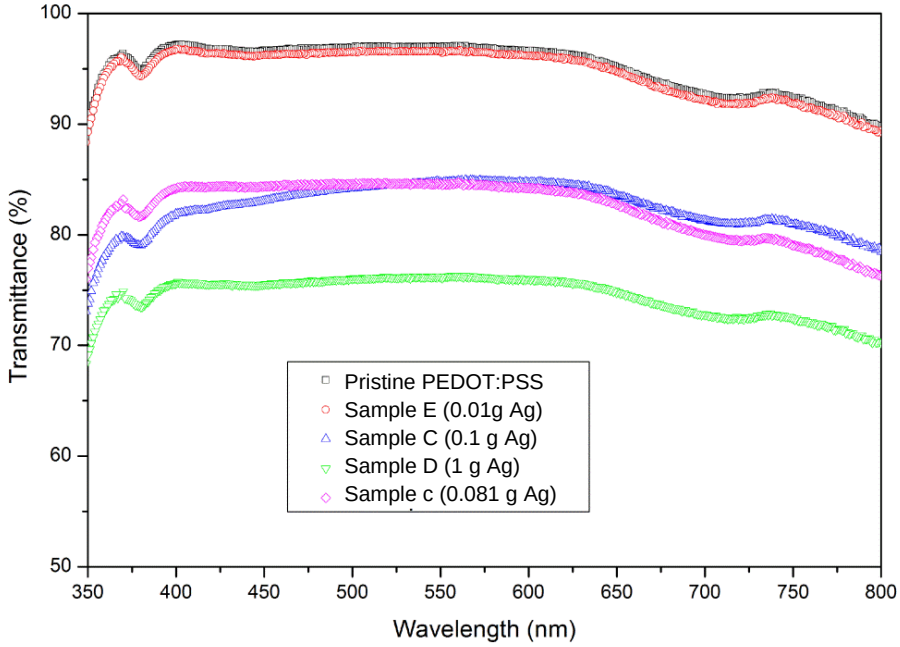

Figure 0.25 UV-Vis spectrum of thin films printed with pristine PEDOT:PSS, Inks E, C, D and c

5.3.1.3.3 AFM

The AFM height images of thin films printed with pristine PEDOT:PSS, Inks D and d are shown in Figure 0.26. The RMS (Root Mean Square) surface roughness of thin films printed with Inks D and d are 1.339 nm and 1.266 nm respectively, this was slightly higher than the roughness of the thin films of pristine PEDOT:PSS, which is 0.817 nm. Nanometre-sized bumps can be observed in thin films printed with Inks D and d, which have been caused by the Ag NPs incorporated in the inks. Interestingly, the average bump size of thin film printed with Ink D is slightly larger than the one of Ink d. Considering the Ag NPs in these two thin films are identical, it can be deduced that the Ag NPs in thin films printed with Ink D were encapsulated with a layer of PSS-rich polymer (according to the reaction) during the *in situ* synthesis, leading to larger size of bumps. However, in the preparation of Ink d, the encapsulating polymer was cleansed away and the subsequent ultrasonic dispersion process was not able to provide such firm adhesion between Ag NPs and the polymer. Therefore less amount of polymer was contained in the bumps of thin film printed with Ink d, resulting in smaller sized bumps.

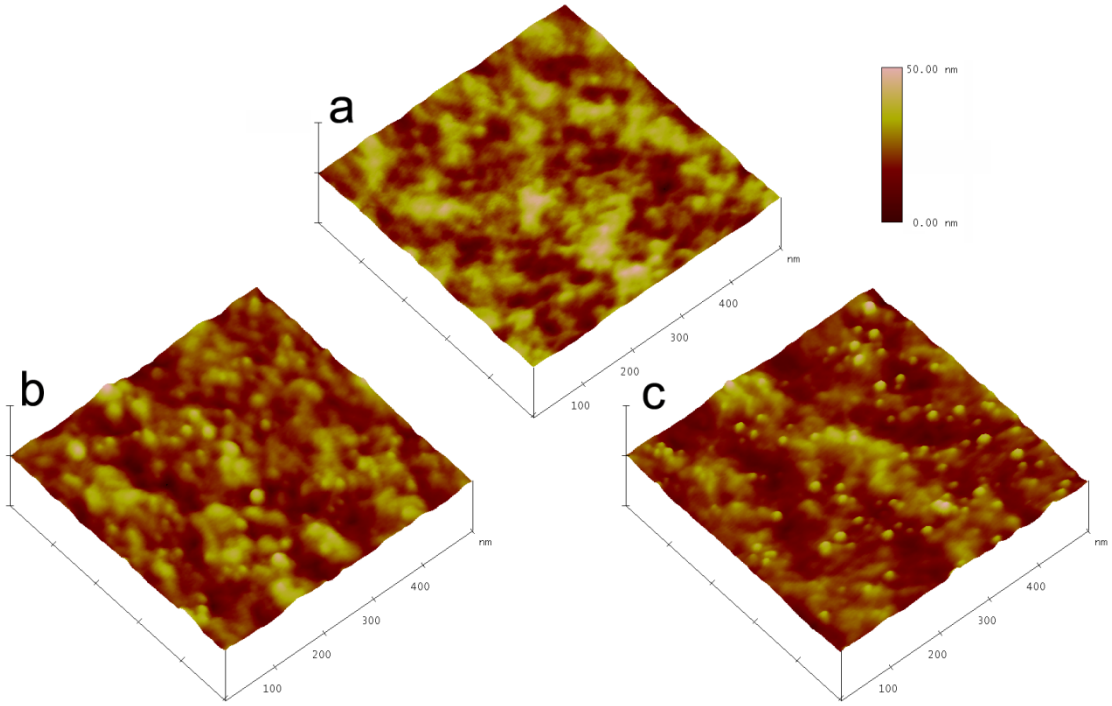

Figure 0.26 AFM height images of thin films printed with pristine PEDOT:PSS (a), Ink D (b) and Ink d (c) with a vertical scale of 50 nm

5.3.1.3.4 SEM

The SEM images of thin films printed with pristine PEDOT:PSS and Ag-PEDOT:PSS are shown in Figure 0.27. Irregular shapes of islands are found on the surface of pristine PEDOT:PSS thin films. Such islands are reported in [106] as oxide inclusions formed by reaction between PEDOT:PSS and oxygen in the air. However, the oxide on the surface of Ag-PEDOT:PSS thin films are observed as dispersion of numerous particulates of tiny size but in a higher density. This may be attributed to the high surface free energy at the interface of PEDOT:PSS and silver, which leads to high tendency of oxidation reaction. Such refined dispersion of oxides are considered to be beneficial to the lifetime of devices in which the PEDOT:PSS thin film is integrated [106].

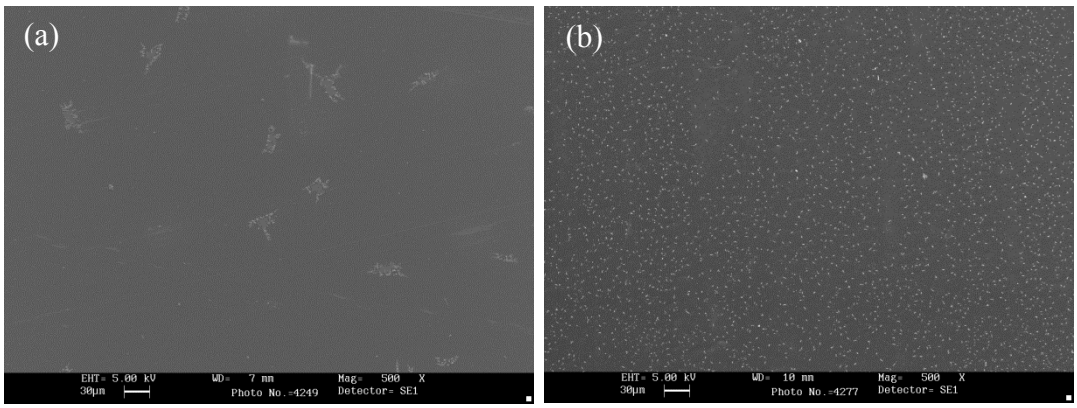

Figure 0.27 SEM images of pristine PEDOT:PSS thin film (a) and Ag-PEDOT:PSS thin film (b)

5.3.2 Effect of substrate temperature

When the PEDOT:PSS solution is doped with conductors, the solution becomes a mixture of a solid phase and a liquid phase. As a result the structure and properties of patterns prepared using the conductors doped PEDOT:PSS can be affected by the printing condition (e.g. substrate temperature) due to the coffee stain effect that may occur during the printing process. In this section, the effect of substrate temperature on the properties of thin films printed with Ag NPs doped PEDOT:PSS solution is investigated.

5.3.2.1 Experimental procedures

To formulate the Ag NPs doped PEDOT:PSS ink, the 1.3 wt.% PEDOT:PSS solution was mixed with Sun Tronic silver ink (10 wt.%) using Misonix Sonicator 4000, at a mixing volume ratio of 9:1. The frequency and power of the sonicator are set as 22.5 kHz and 14 W, respectively. The mixing time was 10 min, which is relatively short as a longer time may induce heat which may affect the properties of the mixture. Afterward, the mixture was filtered with a 5 μm Millex® syringe driven filter to eliminate large particles and agglomerations. The formulated ink was then deposited on the glass substrate using Microfab jetlab®4 inkjet system. Droplets with an average size of 60 μm were generated by optimising their jetting waveform. The inks were printed onto prewashed 50 mm × 6 mm glass microscope slides, with a fixed dot spacing of 50 μm.

5.3.2.2 Morphology

The optical appearances of thin films with and without doping Ag NPs are presented in Figure 0.28. Figure 0.28 (a) and (b) are the films printed on substrate at a temperature

of 20 °C and (c) (d) are the films printed on the substrate which was preheated to 80 °C. As pristine PEDOT:PSS thin film is transparent, only defects on the glass can be observed from Figure 0.28 (a). However, numerous inclusions as groups of nano particles can be observed in the thin films printed with Ag NPs doped PEDOT:PSS ink, as shown in Figure 0.28(b). Considering Ag NPs are theoretically invisible under such magnification, the particles are believed to be agglomerations of Ag NPs formed after deposition. The outlines of the printed tracks are distinct in Figure 0.28 (c) and (d), due to the high drying rate of the deposited patterns caused by the high temperature of substrate. The surface profile of Ag-PEDOT:PSS films printed on substrates with different temperatures shown in Figure 0.29 indicates that the preheating of substrate can lead to coarse and roughening morphology of the printed film.

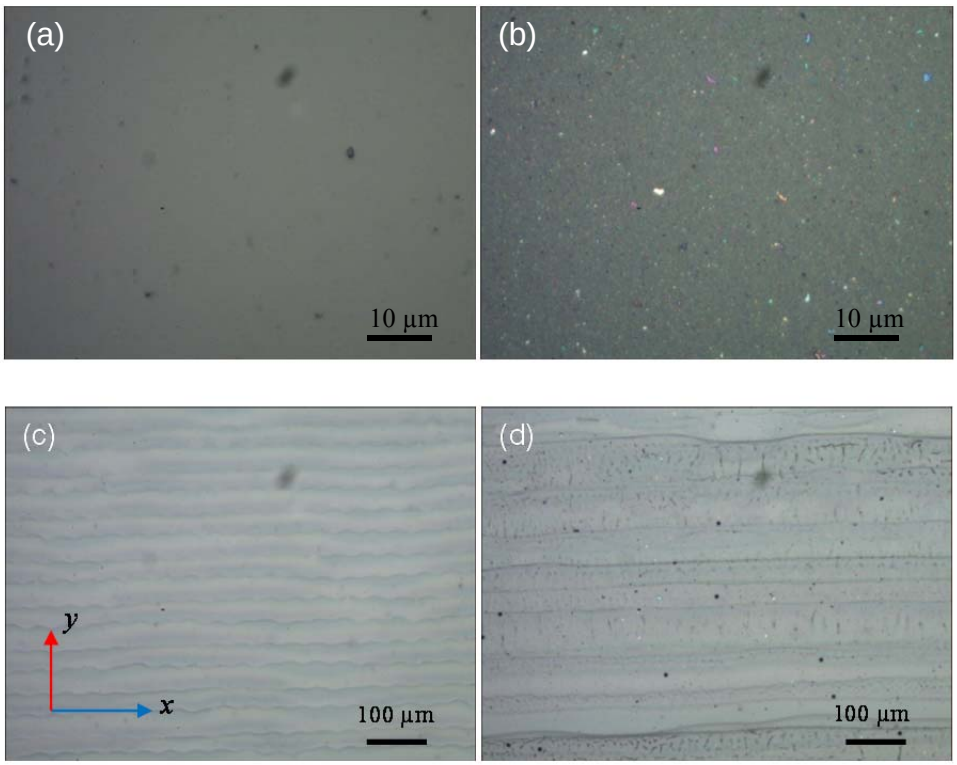

Figure 0.28 Pristine PEDOT:PSS thin films printed on glass substrate preheated to 20°C (a) and 80°C (c), and Ag NP doped PEDOT:PSS thin films printed on glass substrate preheated to 20°C (b) and 80°C (d).

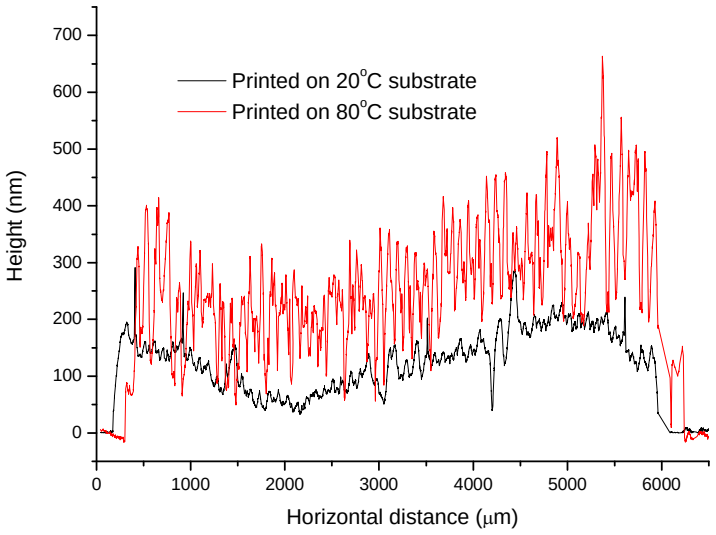

Figure 0.29 Surface profiles taken in the y direction of Ag-PEDOT:PSS thin film printed on substrates at different temperatures

5.3.2.3 Electrical conductivity

5.3.2.3.1 Effect of substrate temperature

The conductivity of the thin films printed with pristine PEDOT:PSS and Ag-PEDOT:PSS on substrates with different substrate temperatures are presented in Figure 0.30. Interestingly, for films printed with pristine PEDOT:PSS ink, the preheating of substrate has led to a significant reduction in film conductivity along both *x* and *y* directions, which is attributed to the poor morphology of the films caused by the high temperature substrates. However, preheating has a rather opposite effect on the film conductivity when the films were deposited using Ag-PEDOT:PSS ink. For the films printed on 20 °C substrate, the conductivity along the two directions is 17.3 S/cm and 18.2 S/cm, where no significant difference can be observed. However, the film printed on 80 °C substrate exhibited an anisotropic conductivity in *x* and *y* direction. The conductivity along printing direction (*x* axis) reaches 50.8 S/cm, which is nearly 3 times higher than the film printed on 20 °C substrate. However, conductivity along the cross direction (*y* axis) is only slightly increased to 23.2 S/cm. This anisotropic nature of conductivity is caused by the inhomogeneous distribution of Ag NPs. Due to the coffee stain effect, an accumulation of Ag NPs occurred at the edge of each track when printed on preheated substrate, which led to the high conductivity along the printing direction. The anisotropic conductivity was only observed in this section.

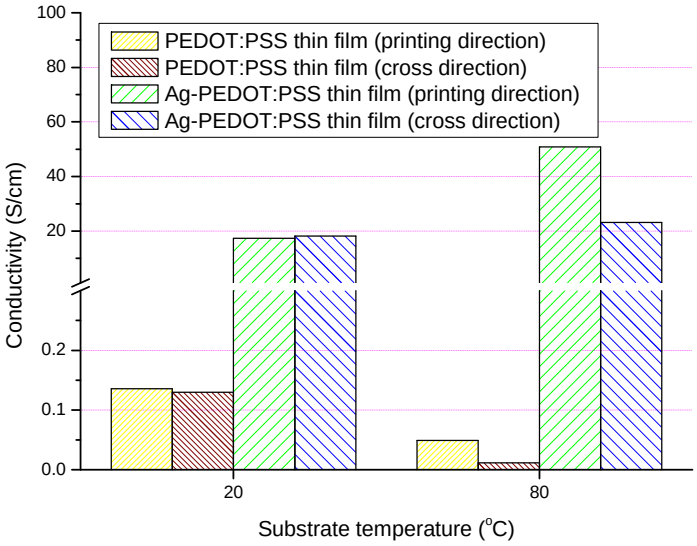

Figure 0.30 Conductivity of thin films prepared with pristine and Ag NP doped PEDOT:PSS vs. preheating temperature

5.3.2.3.2 Effect of final baking

Figure 0.31 shows the effect of post baking at 200 °C for 20 min on the conductivity of the deposited films. The conductivity of films printed with pristine PEDOT:PSS was not significantly affected by the baking. However, the conductivity of the thin films printed with Ag-PEDOT:PSS was almost reduced by half. This reduction is speculated to be attributed to the weakened connection between Ag NPs and PEDOT:PSS caused by the expansion and contraction during the baking process.

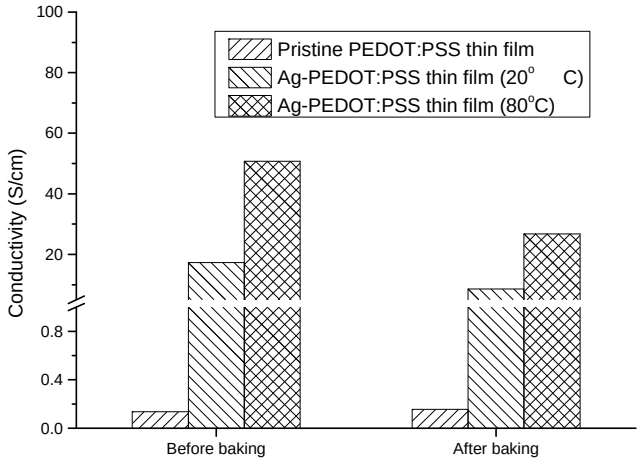

Figure 0.31 Conductivity of pristine PEDOT:PSS and Ag-PEDOT:PSS thin films after baking at 200 °C

5.4 Conclusion

In this chapter, inkjet printing has been applied in the preparation of PEDOT:PSS thin films. PEDOT:PSS solutions modified by adding a co-solvent and doping with additional conductors have been utilised to form inkjettable inks and then successfully deposited thin films using the inkjet printer. Both categories of methods that can improve the electrical conductivity of PEDOT:PSS thin films have been proved to be applicable in the trials of inkjet printing. The effect of further thermal baking on the conductivity and transparency of the deposited films has also been investigated.

In solvent annealing, the addition of glycerol not only makes the inks more suitable for jetting in terms of the change of viscosity, but also improves the conductivity of the films by over 300 times. The transmittance and surface evenness at macro scale of the PEDOT:PSS films can also be improved by solvent annealing. However, the surface roughness at micro scale has been slightly increased due to the doping of glycerol, which is primarily attributed to the aggregation of PEDOT-rich particles. Subsequent thermal annealing has been found to be able to further improve the conductivity of glycerol doped PEDOT:PSS thin films.

The results of thermal annealing study show that the colour of the thin film becomes darker with the increase of baking temperature, due to the degradation of PEDOT and PSS. Although aggregation of PEDOT can be observed when the film was baked at 225 °C, the aggregation has not led to increase in the conductivity of the films. In addition, the transmittance of the films decreases due to the degradation of PEDOT and PSS. If baking is conducted at or above 300 °C, which can easily damage the surface evenness and the conductivity of the thin films.

Ag NPs have been synthesised by adopting silver nitrate as the precursor, which can be subsequently used to form inkjet inks for the enhancement of conductivity of inkjet-printed PEDOT:PSS thin films. The size of the Ag NPs increases with the increase of reaction time, reaction temperature and concentration of silver ion in the synthesis of Ag NPs, which will ultimately govern the electrical properties of the thin films deposited by inkjet printing. The dedoping of PSS from PEDOT during the reaction between silver nitrate and PEDOT:PSS has appeared to be detrimental to the electrostatic interaction between PEDOT and PSS, leading to a reduction in the

conductivity of deposited Ag-PEDOT:PSS thin films. The thin film conductivity has been improved by dispersing the obtained Ag NPs into pristine PEDOT:PSS solution. Higher content or larger size of Ag NPs can more effectively improve the conductivity of the thin films. A mechanism is therefore proposed to provide an insight into the fundamental reasons that are responsible for the enhancement of conductivity of the thin films in the case of more and larger nanoparticles involved in the deposition of the thin films. The addition of Ag NPs has also caused definite reduction in the surface evenness and transparency of the composite thin films. Thin films deposited with *in situ* synthesised Ag-PEDOT:PSS inks exhibited higher absorbance in the blue light region due to the dedoping of PSS from PEDOT.

Temperature of substrate on which the films were deposited is found to have a strong influence on the surface morphology of the printed films. The Ag-PEDOT:PSS thin films printed on preheated substrate exhibited anisotropic conductivity in the printing direction and cross direction. The conductivity of Ag-PEDOT:PSS thin films along the printing direction has been improved by three times when the temperature of the substrate increased from 20 °C to 80 °C, which is mainly attributed to the accumulation of Ag NPs caused by coffee stain effect. The addition of Ag NPs has also affected the formation of oxide on the surface of PEDOT:PSS thin films, they take the irregular shaped islands in the films and homogenously dispersed particles in the films without and with Ag NPs, respectively. The conductivity of Ag-PEDOT:PSS thin film was reduced by post baking at 200 °C. As expected, greater transmittance loss has been observed in the Ag-PEDOT:PSS thin films printed on the preheated substrate.

Chapter 6 Laser Assisted Inkjet Printing of Indium Tin Oxide

In this chapter, laser assisted inkjet (LIJ) technology is for the first time applied in the printing of indium tin oxide (ITO) patterns. Metal organic decomposition (MOD) ITO ink and ITO nanoparticle ink are used in the printing trials of thin films and tracks. In the printing of thin films, the critical thicknesses that may induce cracks, as well as the electrical and optical properties of the printed films are investigated. In the printing of tracks, the position of laser radiation around the droplet depositing point is optimised to obtain uniform tracks with fine track width. The effect of laser power on the morphology of tracks and the subsequent influence on the conductivity are also studied respectively using two types of inks: MOD ITO ink and ITO nanoparticle ink. The experimental results indicate that the critical thickness causing the cracks in the printed tracks is larger than the one in the printed films; the fundamental reasons for this phenomenon are therefore discussed with the assistance of an established mathematical model.

6.1 Introduction

6.1.1 Indium tin oxide (ITO)

Indium tin oxide (ITO, or tin-doped indium oxide) is a solid solution of indium (III) oxide (In_2O_3) and tin (IV) oxide (SnO_2), typically consisting of 90% In_2O_3 and 10% SnO_2 by weight [144]. It has been widely used in numerous applications such as touch panels, displays, OLED, sensors and photovoltaics due to the excellent electrical conductivity and optical transparency [145].

ITO patterns are commonly fabricated by physical vapour deposition (PVD) methods such as sputtering and thermal evaporation [146, 147]. However, these PVD methods are expensive since vacuum processing is often required. Another type of fabrication method is wet chemical deposition, implemented by either nanoparticle dispersion or sol-gel process, which has gained much attention in recent years. The inks applied in wet chemical deposition can be deposited by various printing processes (e.g. inkjet printing, spin coating, gravure printing). A summary of such printing work is given in Table 6.1.

Table 0.1 Summary of research into preparation of ITO patterns using wet chemical deposition

	Wt. %	Particle size (nm)	Sintering Temp. (°C)	Film thickness (nm)	Resistance (kΩ/sq)	Trans. (%)	Printing method	Author
1	30%	<10	350-600	~1000	2.19	78.6	inkjet	Hong [30]
2	20%*	10-20	130	100	0.8	85	spin	Maksimenko [148]
3	50%	20-30	120, 180	710	1.3-1.5	>80	gravure	Heusing [149]
4	30%	~25	450	750	202.7	86.66	inkjet	Jeong [31]
5	15%	~25	400	580	517	87	inkjet	Hwang [32]
6	10%	precursor	600	220	0.11	>95	Spin inkjet	Hoffmann [33]
7	20%	~5.9	-	100	4.11	93	inkjet	Hong [34]

***with addition of PEDOT:PSS.**

Although wet chemical deposition is more convenient and less expensive, the conductivity of ITO films that can be achieved by wet chemical deposition is much lower than the conventional vacuum processes, normally by two to three orders in magnitude [150]. In addition, a subsequent sintering process at high temperature (>

200 °C) is essential for the wet chemical deposition, which limits the application of this method on polymer substrates. Therefore, organic additives (e.g. polyvinyl derivatives and PEDOT:PSS) [151-153] have been added into the ITO inks to enable sintering at low temperature. The ITO films have also been combined with the silver grids to achieve better conductivity [32].

6.1.2 Laser assisted inkjet (LIJ) process

Laser assisted inkjet (LIJ) process is a method where the ink solvent is evaporated and dried very quickly by input of heat, through radiation of a focused laser beam on the droplet and the substrate while the droplet ejected from the inkjet head lands onto the glass substrate (Figure 0.1) [154]. Connecting tracks with high aspect ratio and improved adhesion have been achieved by LIJ process. In addition, the LIJ process makes it possible to deposit patterns on 3D such as uneven, stepped and rough-surface substrates.

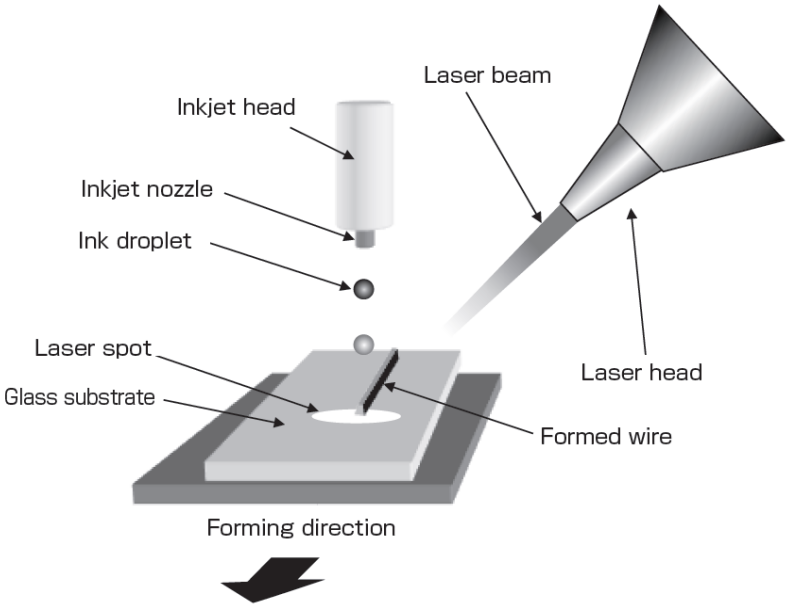

Figure 0.1 Schematic illustration of laser assisted inkjet process

As a newly developed technology, LIJ has only been applied in the printing of silver inks [76, 154]. It has been demonstrated to be an effective method to improve the resolution of printed patterns through the experimental trials. Since high density interconnect (HDI) has become the major trend of electronic packaging, it is very imperative to expand the application of the LIJ process in the printing of more types of functional materials to enable printed patterns with high resolution.

6.2 Experimental procedures

Commercially available metal organic decomposition (MOD) ITO and ITO nanoparticle inks were adopted in the LIJ printing trials. The laser assisted inkjet system built in house at AIST was employed as the printing system. Both inks were modified with solvents to obtain better jettability in the course of ink formulation. The MOD ITO ink was mixed with tetradecane at a weight ratio of 9:1, while the ITO nanoparticle ink was mixed with toluene at a weight ratio of 1:4. The properties of the modified inks and the diameter and velocity of the stable droplets that can be achieved in the printing trials are listed in Table 6.2.

Table 0.2 Properties of modified ITO inks and the diameter and velocity of the obtained droplets

Raw material	Modification solvent	Ink properties			Droplets
		Wt. % of solute	Surface tension (dynes/cm)	Viscosity (cps)	
MOD ITO ink (5 wt.%)	Tetradecane	4.5	24	1.9	• 120 μm, 1.7 m/s • 80 μm, 2.25 m/s
ITO nanoparticle ink (20 wt.%)	Toluene	4.0	26	2.0	• 110 μm, 1.5 m/s • 70 μm, 2.5 m/s

The inkjet printing was carried out to deposit thin films and tracks on the glass substrate. In printing of films, the diameters of the droplets of the two inks were adjusted to 120 μm and 110 μm respectively. 10 mm × 10 mm sized films were printed on glass substrate for each ink, with dot matrix (number of droplets in row × number of droplets in column) of 250 × 20, 250 × 25, 250 × 33, 250 × 50, and 250 × 100. The amount of material per unit area that were deposited can thereby be calculated, which is 45.2 nL/mm^2, 56.5 nL/mm^2, 74.6 nL/mm^2, 113 nL/mm^2, and 226 nL/mm^2 for MOD ITO ink, and 34.8 nL/mm^2, 43.5 nL/mm^2, 57.4 nL/mm^2, 87 nL/mm^2, and 174 nL/mm^2 for ITO nanoparticle ink. In track printing, CO_2 laser was induced to assist the printing process. The printing frequency and speed were set as 100 Hz and 5 mm/s, respectively. The locations of laser radiation were optimised to achieve fine ITO tracks with good morphology, using the MOD ITO ink only. Then the effect of laser power on the morphology and conductivity of the printed patterns were also investigated using both MOD ITO and ITO nanoparticle inks. The patterns printed with the two ITO inks were then baked under their specific required sintering conditions (given in Section 3.2.1).

6.3 ITO thin film printing

6.3.1 Morphology

The relationship between thickness and deposited amount of ink per unit area of the films printed with MOD ITO ink and ITO nanoparticle ink is shown in Figure **0.2**. The black dots are the results measured from experimental trials, and the red lines are derived from the theoretical value calculated based on the volume of deposited ink. It can be concluded that the test results are in good agreement with the theoretical value when the film is thinner than 100 nm. However, when the film is thicker than 100 nm, the results from the measurements are smaller than the theoretical value and the differences between them increase with the increase of film thickness. This is primarily due to the coffee stain effect which led to the enrichment of material at the edge of the films during the drying process.

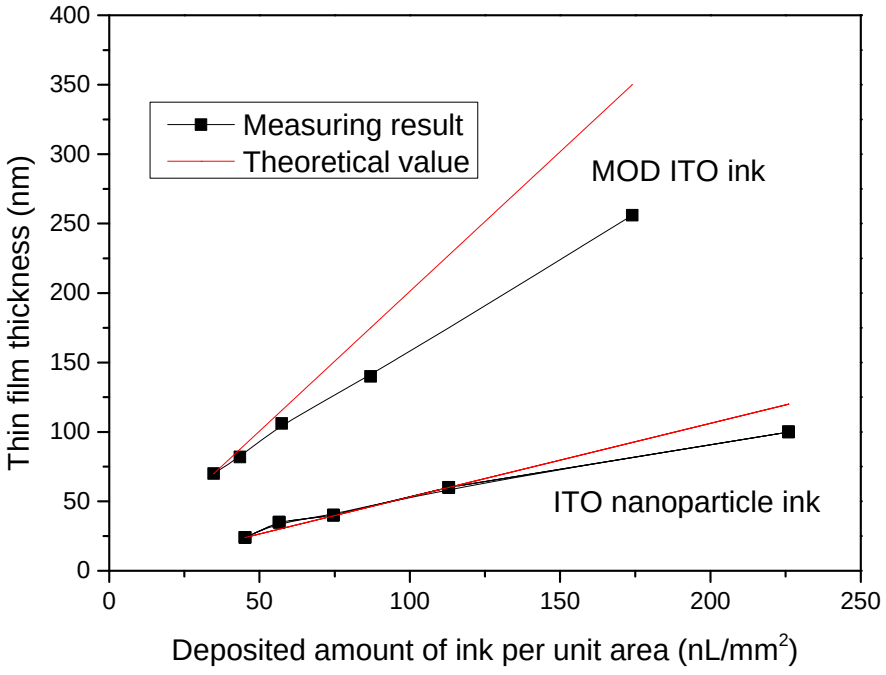

Figure 0.2 **Thickness vs. deposited amount of ink per unit area of the films printed with MOD ITO ink and ITO nanoparticle ink**

According to the optical observation, the initial cracks in both films printed with MOD ITO ink (Figure 0.3 (a)) and ITO nanoparticle ink (Figure 0.3 (b)) start as the printing dot matrix increased to 250 × 50. It has been found that the internal stress in the thin

film was induced by sintering process which may subsequently lead to cracks. The internal stress increases with the increase of film thickness, therefore a critical thickness that may cause a significant internal stress thus cracking has been determined to describe the value of thickness of the film that may not result in any cracks in the films [155]. Cracking is usually not initiated below this critical value of thickness even for layers of hard particles. In this work, it has been possible to determine the critical thickness which is ~60 nm for MOD ITO ink and ~140 nm for ITO nanoparticle ink.

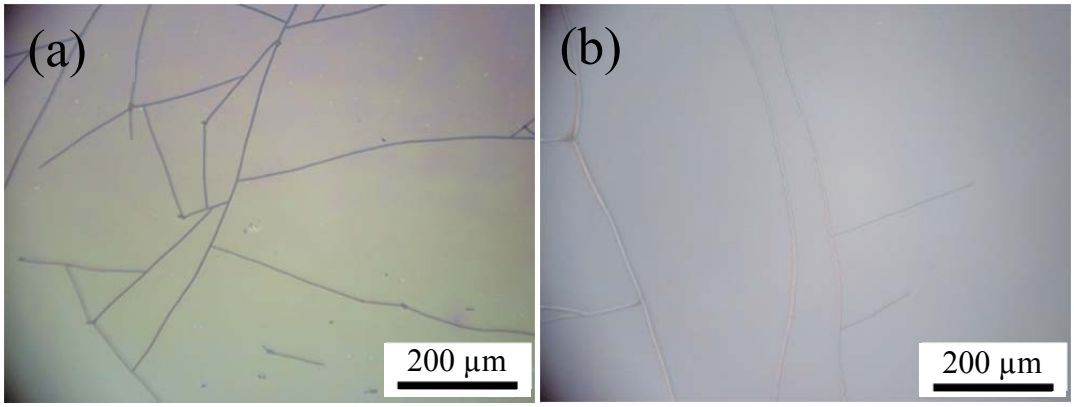

Figure 0.3 Cracks on the films printed with MOD ITO ink (a) and ITO nanoparticle ink (b)

The height image and phase image (500 nm × 500 nm) of ITO films printed with MOD ITO ink have been obtained from AFM testing, as given in Figure 0.4. It can be concluded that the films are composed of nano-sized grains after the decomposition. However, the size of the grains is significantly affected by the thickness of the films, the thicker films the larger grains.

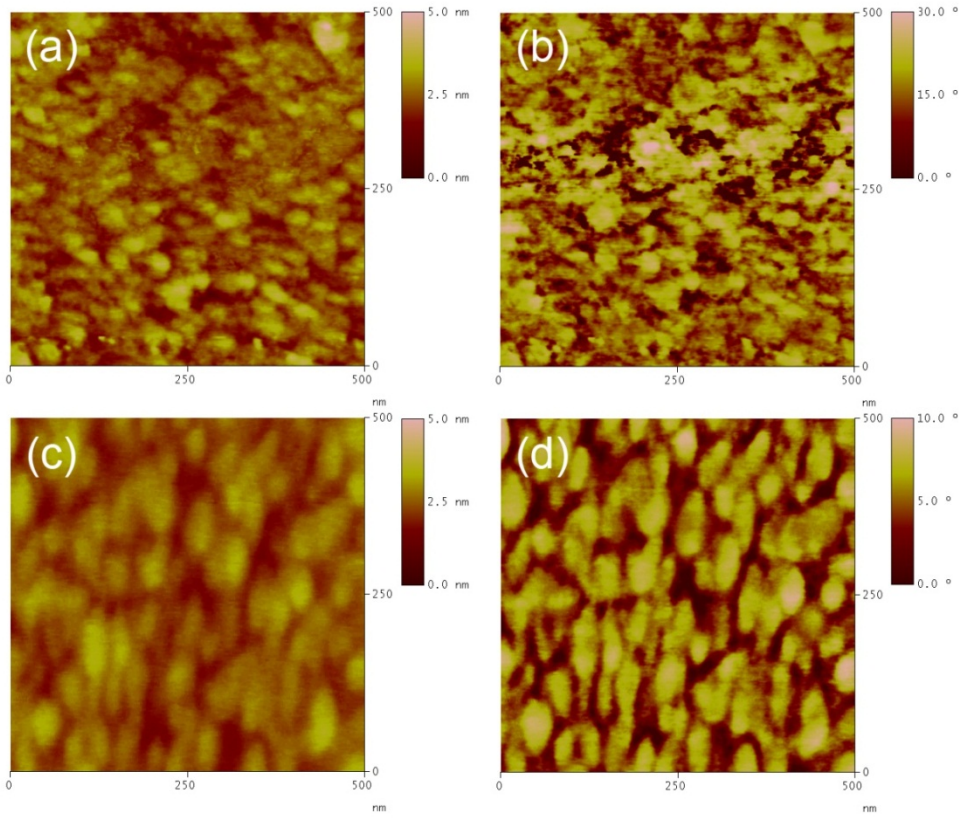

Figure 0.4 Height image ((a) and (c)) and phase image ((b) and (d)) of ITO films printed with MOD ITO ink under dot matrix of 250×20 ((a) and (b)) and 250×100 ((c) and (d))

Interestingly, the microstructure of films printed with ITO nanoparticle ink (Figure 0.5) is very different from the one printed with MOD ITO ink. Firstly, the size of the grains in the films printed with ITO nanoparticle ink is larger than that with MOD ITO ink, probably due to the high sintering temperature (550 °C). Secondly, the grain size seems to be independent of the thickness of the films.

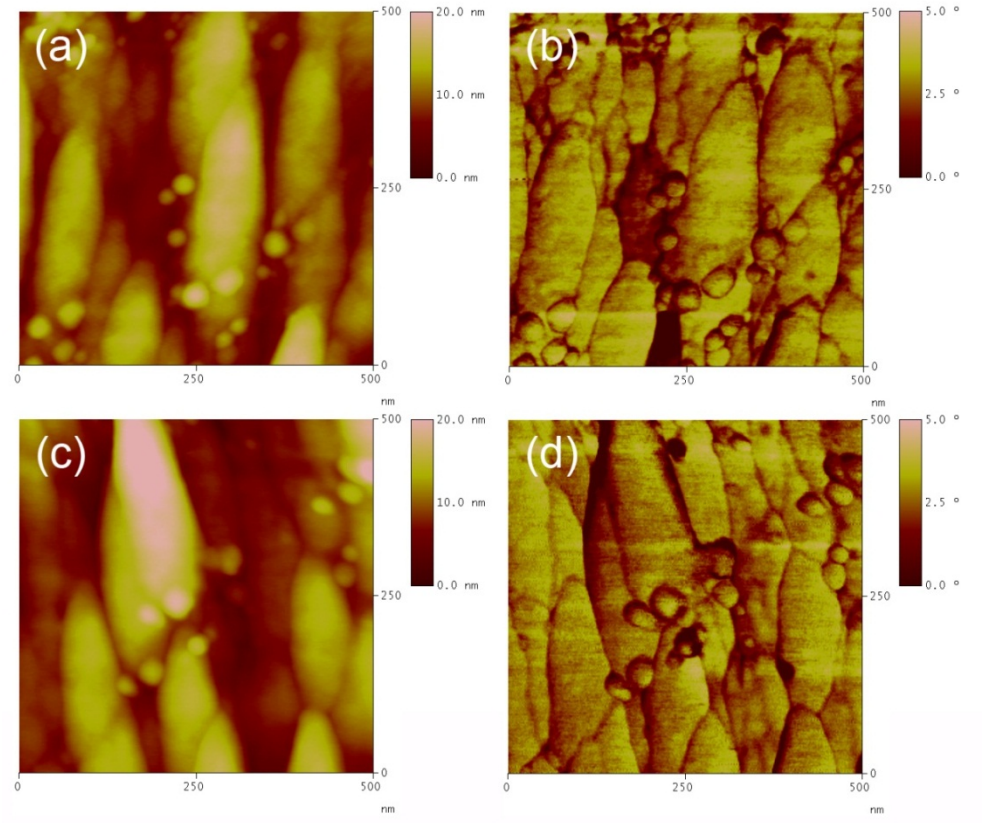

Figure 0.5 Height image ((a) and (c)) and phase image ((b) and (d)) of ITO films printed with ITO nanoparticle ink under dot matrix of 250×20 ((a) and (b)) and 250×100 ((c) and (d))

6.3.2 Conductivity

The sheet resistances of the films printed with MOD ITO ink and ITO nanoparticle ink under different printing dot matrix are shown in Figure 0.6. Theoretically, the sheet resistance is inversely proportional to the film thickness. However, this relationship is not observed in the films printed with MOD ITO ink. Benoy et al. [156] suggested that unstable conductivity of ITO films can be caused by the discontinuous nature of the film when the thickness of the film is less than 150 nm, which may explain the unpredictable conductivity of ITO films printed with MOD ITO ink in this study. When the thickness increased to 100 nm, an obvious rise can be found in the sheet resistance which is most likely caused by the cracks. The sheet resistance of the films printed with ITO nanoparticle ink decreases with the increase of film thickness as expected until crack occurs under the thickness of 140 nm. The large deviation of measuring results at thickness of 140 nm indicates that cracks have led to heterogeneous conductivity of the ITO films.

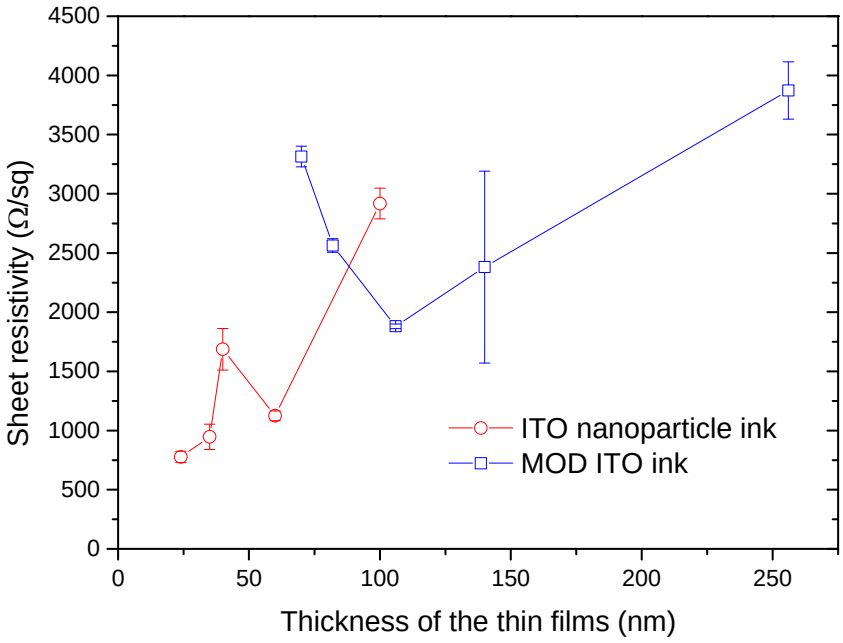

Figure 0.6 Sheet resistance of the films printed with MOD ITO ink and ITO nanoparticle ink at different thicknesses

6.3.3 Transmittance

The optical transmittance of glass substrate and ITO films printed at a dot matrix of 250×33 are shown in Figure 0.7. The average transmittance (wavelength between 380 nm and 800 nm) of ITO films printed with MOD ITO ink and ITO nanoparticle ink are ~85.9% and ~87.3%, respectively, which are comparable to the ITO thin films fabricated with conventional vacuum process [157].

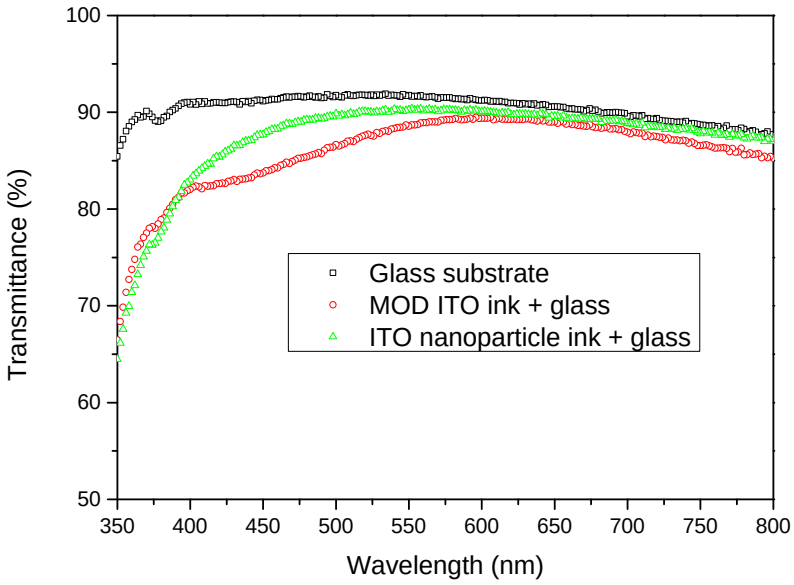

Figure 0.7 Transmittance of glass substrate and ITO films

6.4 ITO track printing

In the printing of ITO tracks, the CO_2 laser was introduced to locally preheat the substrate. The high temperature of the substrate can accelerate the evaporation speed of the solvents in droplets and consequently suppress the spreading of droplets on substrate to form fine tracks. As the morphology of the tracks can be significantly affected by the distribution of temperature on the substrate, the effects of laser position and laser power which determine the distribution of temperature were investigated.

6.4.1 Effect of laser position

The effect of laser position of radiation on the morphology of printed tracks has been studied by applying laser at one of the eight spots A-H (yellow areas in Figure 0.8) individually. Seven spots A-G are located along the printing trail with an equal distance of 10 μm between every two adjacent spots, while the spot D coincides with the landing position of droplets. Another spot H is at one side of the printing trail with a perpendicular distance of 300 μm from the printing trail.

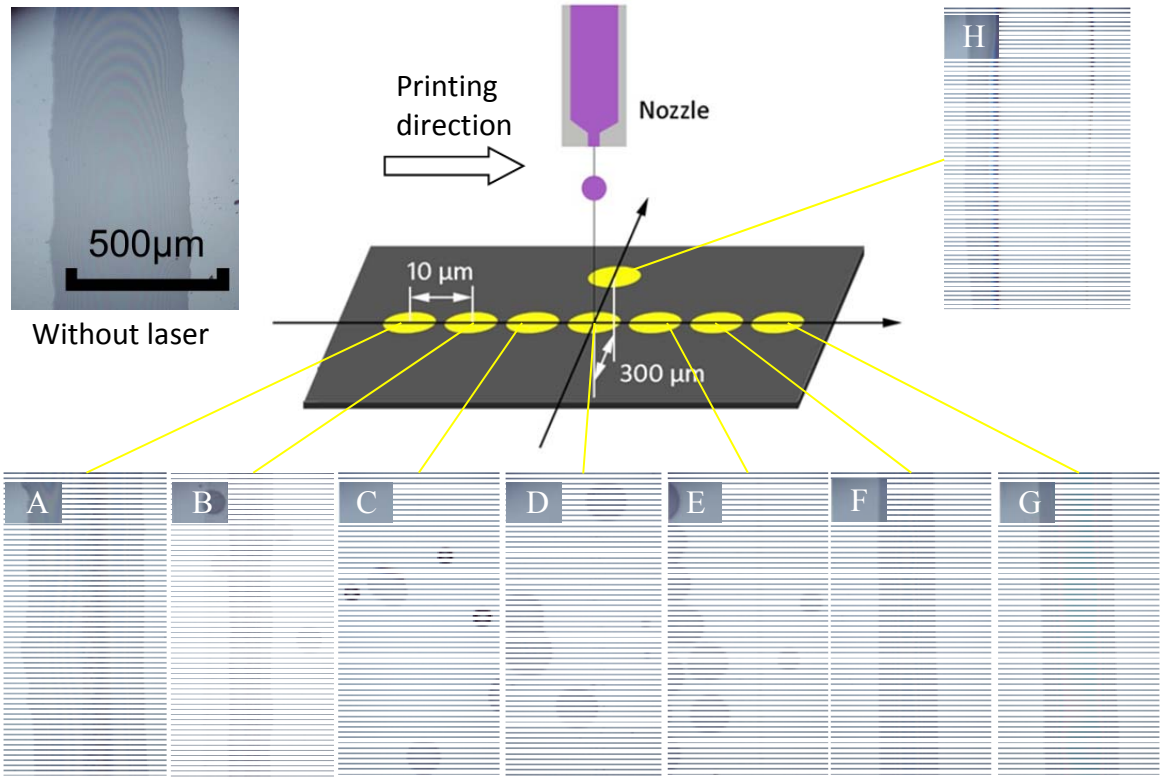

Figure 0.8 Position of laser radiations (yellow dots) in the inkjet printing and the corresponding top view of the obtained tracks

According to the top view images obtained from the optical microscope, the morphology of tracks printed with LIJ is significantly influenced by the position of laser radiation. Without the assistance of the laser, a continuous track with a width close to 500 μm was obtained.

When the laser was applied at the position of A and B, the tracks were firstly printed on the substrate and then scanned by the laser beam. Although the tracks have been narrowed down in some degree as a result of the laser heating, the edge of the tracks was irregular due to the spreading of the droplets. In addition, according to the cross sectional profile obtained through Zygo surface profiling, as shown in Figure 0.9, the application of laser has induced displacement of the inks before drying fully, this has resulted in a local enrichment of ink material at the edges of the track, e.g. when laser positions to point A, as well as a deviation, thus an uneven deposited track when laser radiates at point B. It is also noticed that some small bumps on the substrate can be formed within the tracks predominantly due to the laser localised heating (Figure 0.9, A, B, and C), which is believed to be the deformation of the substrate caused by the radiation of laser.

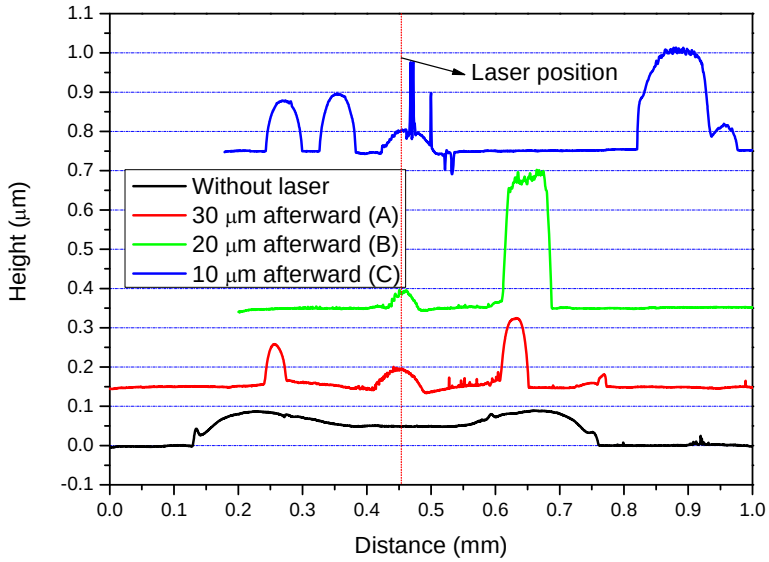

Figure 0.9 Cross sectional profile of tracks printed with laser applied at A, B, C and without laser

When the laser was applied very close to the landing position of droplet (position C-E), only randomly distributed dots can be observed, which indicates a failure of forming continuous tracks and one possible explanation can be the Marangoni effect described in Figure 0.10. When the substrate is irradiated by laser, a temperature gradient can be generated on the surface of substrate. As the surface energy can be affected by temperature, which has been explained in Section 4.3.2.2, a gradient of interfacial tension between the solid surface and the vapour (Γ_{SG}) is consequently formed. When the laser radiation is very close to the landing position of droplet, the gradient of Γ_{SG} in the cross section becomes big enough to cause fragments of the droplets into many small satellites and draw them alongside to the sides of the tracks, as observed in the experimental trials when laser was applied at position C-E. Another possible explanation is that when the droplets land on the substrate, the high temperature of the substrate causes intense evaporation of the solvent inside the droplet and creates steam explosion, resulting in fragments.

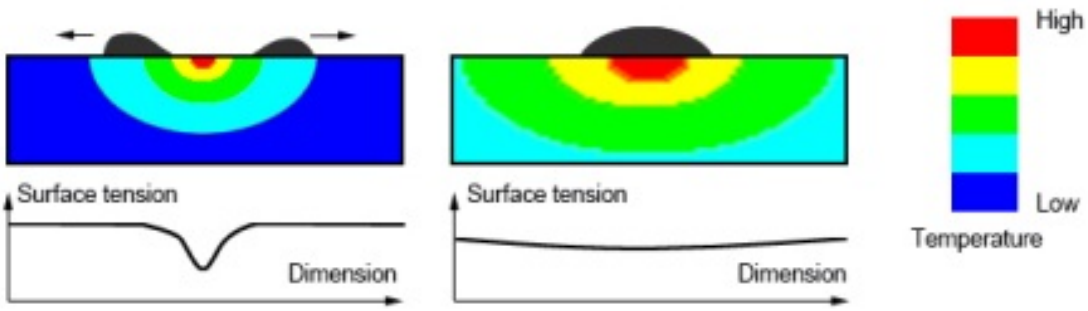

Figure 0.10 Schematic illustration of Marangoni effect

When laser was applied at point F and G, both the top view and the cross section profiles (Figure 0.11) have been found to be improved. The spreading of the ink has been efficiently suppressed, resulting in reduced track width and smoother track edges. The track with the optimal morphology was obtained when the laser radiation was applied at position F, where a track width of approximately 200 μm has been achieved. Therefore the optimum position of the laser is 20 μm ahead of the landing position of droplet in this study. This is very much associated with the local pre-heating through laser radiation prior to the disposition of ink droplets.

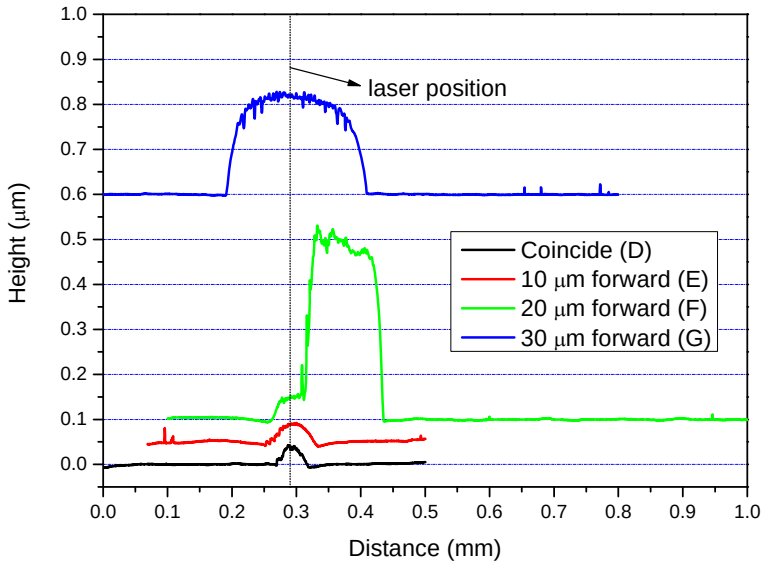

Figure 0.11 Cross sectional profile of tracks printed with laser applied at D, E, F, and G

When the laser radiates along the side of landing point of droplet (position H in Figure 0.8), by comparing with the cross sectional profile of the track obtained (Figure 0.12), the track exhibited an extremely uneven surface. By doing so, a pattern

with high aspect ratio can be formed due to the rapid evaporation of the solvent along the side (near position H) where the laser radiation is more effective. However, the substrate temperature in the other side was not high enough to induce rapid evaporation, but still can cause an increase of surface energy on the substrate, resulting in a large area of spreading of the ink (Figure 0.12).

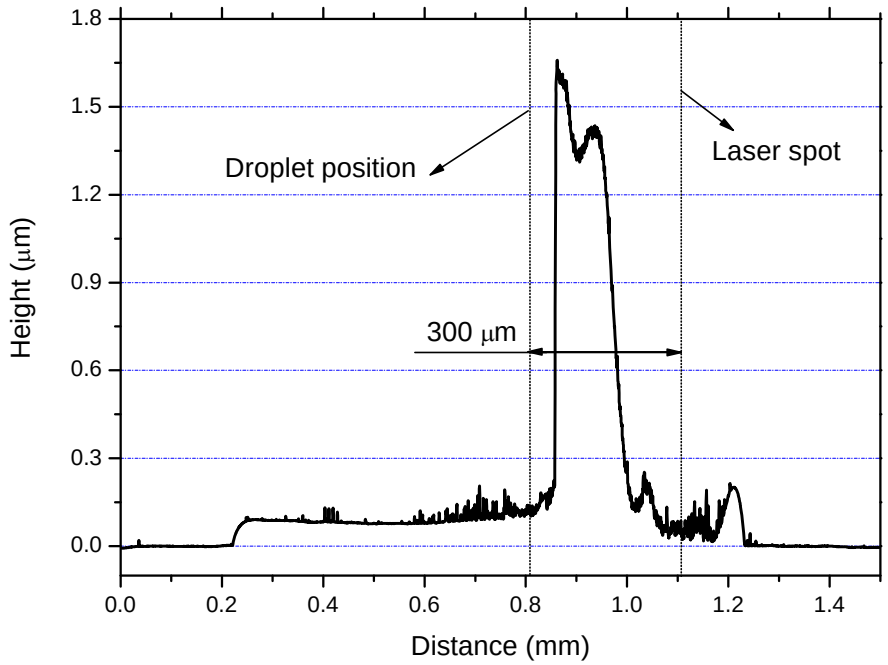

Figure 0.12 Cross sectional profile of track printed with laser radiation applied at point H

6.4.2 Effect of laser power

As the formulation of MOD ITO ink and ITO nanoparticle ink are different, the laser may influence the deposition of tracks in different ways, therefore, the effects of laser power on the deposition of the two inks through ink-jet printing were investigated separately. The laser was applied in the optimal position determined in the previous section.

6.4.2.1 MOD ITO ink

6.4.2.1.1 Morphology

The optical top view of the ITO tracks printed with LIJ under different laser power is given in Figure 0.13. Combined with the measured results of track width (Figure 0.14),

it can be concluded that the irradiation of laser is efficient in reducing track width. Without the assistance of laser, the track width can reach 250 μm, in comparison with the track of 100 μm when a 0.8 W laser radiation was applied. When the laser power was lower than 0.8 W, the track width decreased gradually with the increase of laser power. Relatively smooth track edge can be achieved as a result of the laser treatment. However, further increase of the laser power (> 0.8 W) led to very limited reduction in the track width, instead it has resulted in poorer morphology with irregular track edges. This is attributed to the more intense vaporization caused by the high temperature of the substrate when such high power laser was applied. The formation of the track was affected by the vaporization, leading to tortuous edge, in particular for the laser power of 1.7 W (Figure 0.13).

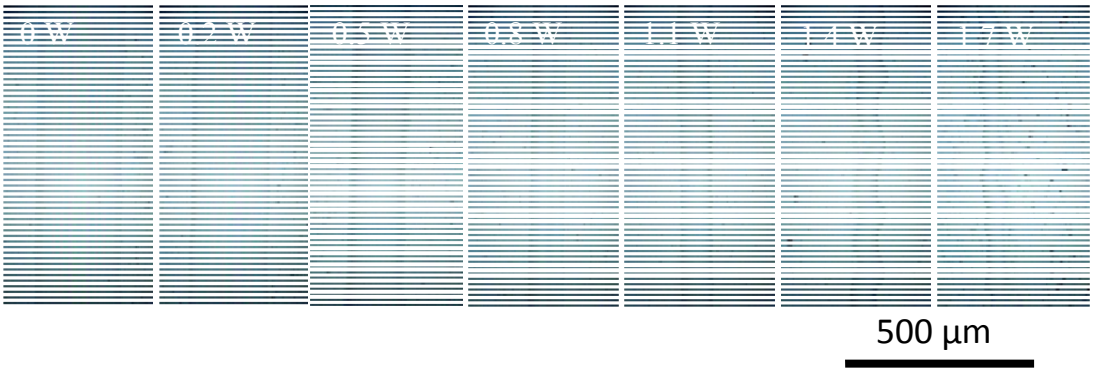

Figure 0.13 Optical top view of ITO tracks printed with MOD ITO ink under different laser powers

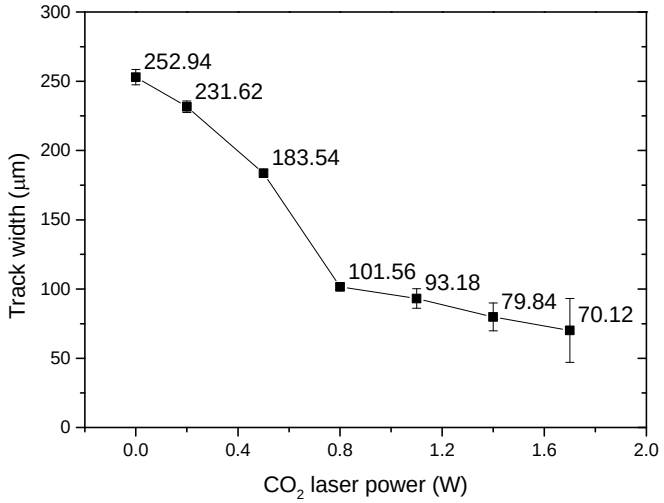

Figure 0.14 Width of tracks printed with MOD ITO ink vs. laser power

In general, preheating of substrate leads to more obvious coffee ring effect, as the high temperature speeds up the evaporation of solvent near the contact line, resulting in a greater transfer of solute to its edge [94], as observed in Section 4.3.2. However, in the printing of MOD ITO track, the coffee ring effect was diminished when the laser power of 1.1 W was utilised (Figure 0.15). This is attributed to Marangoni flow generated by the temperature gradient at the interface between droplet and air, which has reversed the coffee ring effect, thereby brought the solute to the centre of the droplet rather than spreading them toward the edge of tracks [158, 159].

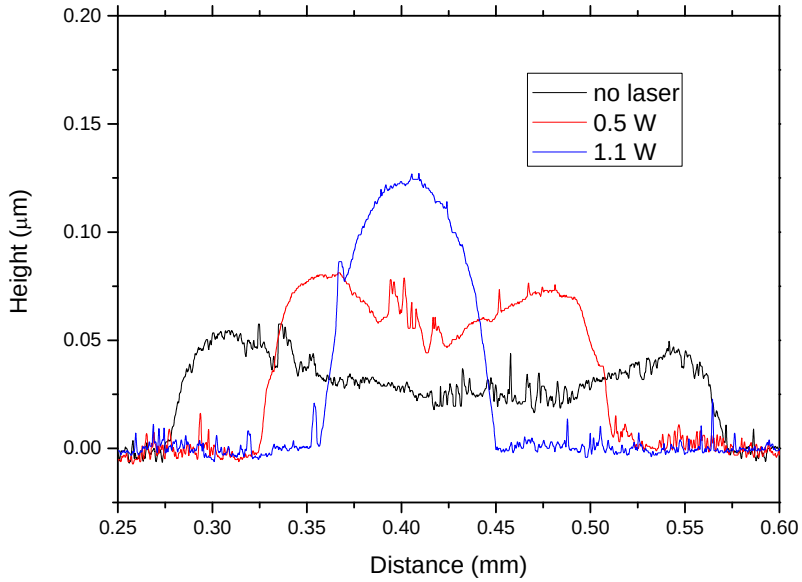

Figure 0.15 Cross sectional profile of ITO tracks printed with MOD ITO ink under different laser power

6.4.2.1.2 Conductivity

The conductivity of the ITO tracks printed with MOD ITO ink is given in Figure 0.16. It can be found that the conductivity of the tracks was not significantly affected by the morphology change when the power of the applied laser was lower than 1.1 W. However, as the size of grains in the ITO film printed with MOD ITO ink increases with the increase of film thickness (Figure 0.4), a lower density of grain boundaries as predicted may behave as traps for free carriers and barriers for carrier transport in the film as expected in thicker films [160-162]. Therefore, the conductivity of ITO tracks should increase with the increase of thickness. The cause of this contradiction between theoretical interpretation and experiment results requires further investigation and testing on the structure of materials that compose the ITO film. When the laser power

was higher than 1.1 W, the morphology of the tracks were no longer homogeneous along the printing direction, leading to lower conductivity and larger deviation of the testing results.

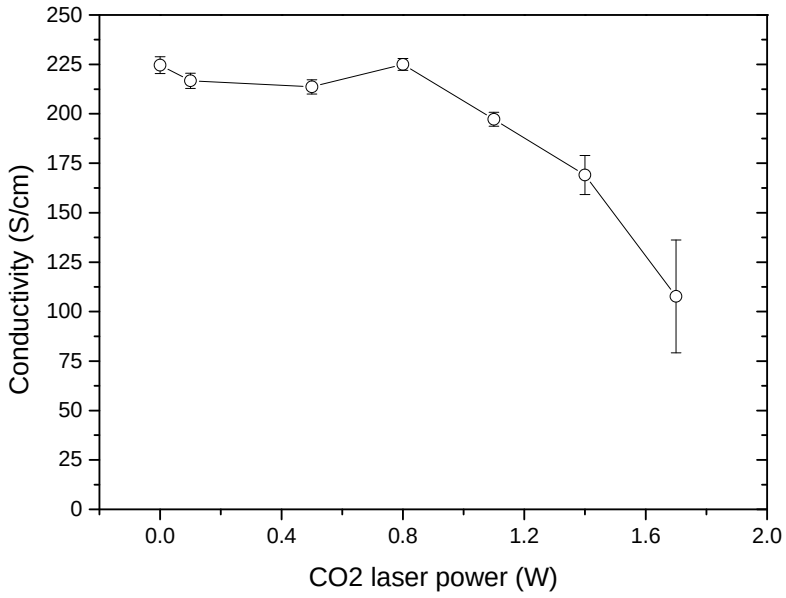

Figure 0.16 Conductivity measurements of tracks printed with MOD ITO ink vs. laser power

6.4.2.2 ITO nanoparticle ink

6.4.2.2.1 Morphology

The morphology of the tracks printed with ITO nanoparticle inks has been improved by the assistance of laser as shown in Figure 0.17. However, compared with MOD ITO ink, the track width of ITO nanoparticle ink is more sensitive to the variation of laser power. A sudden drop from 450 μm to 150 μm in track width of the printed with ITO nanoparticle ink was observed when the laser power increased from 0.5 W to 0.6 W (Figure 0.18). This is attributed to the low boiling point of the solvent in ITO nanoparticle ink, which is very sensitive to the heat applied from laser. The region of overlap is easy to be distinguished in the tracks printed with the assistance of laser, indicating the rapid evaporation of solvent. Similar with MOD ITO ink, when the laser power is higher than a certain value, 0.6 W for this case, the track width almost stays unchanged. According to Section 2.1.4.3, the feature size of inkjet printing is determined by the impacting period and spreading period of projected ink droplets. Since the spreading of the droplets can be suppressed by the preheating of the substrate,

the feature size of patterns printed with LIJ is mainly determined by the impacting period. However, when the applied laser power is higher than 1 W, cracks were induced on the track.

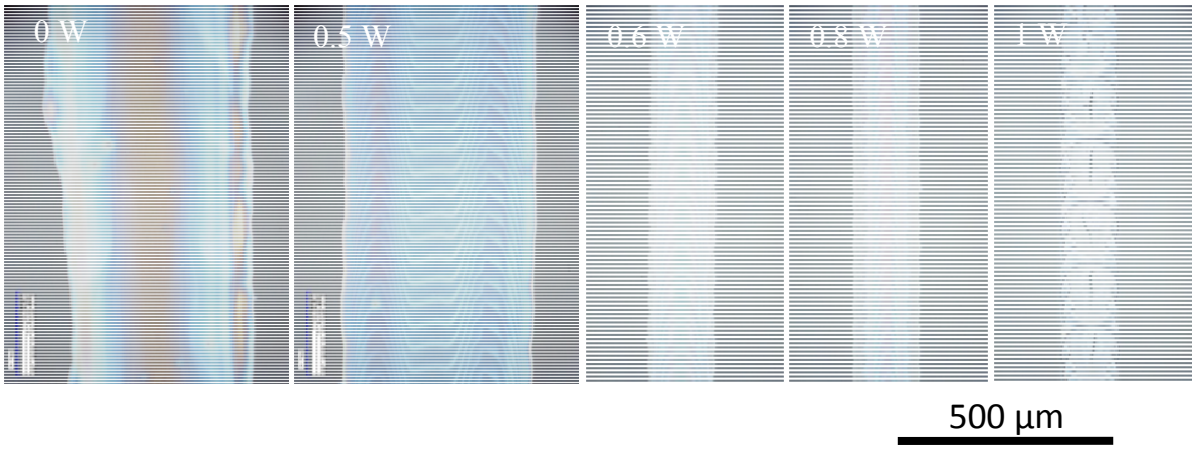

Figure 0.17 Optical top view of ITO tracks printed with ITO nanoparticle ink under different laser power

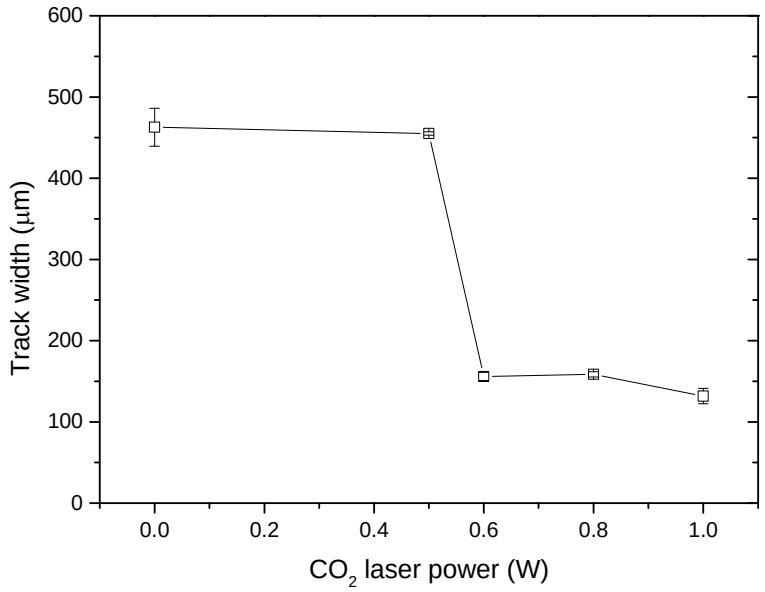

Figure 0.18 Width of tracks printed with ITO nanoparticle ink vs. laser power

The cross sectional profile of tracks printed with ITO nanoparticle ink is shown in Figure 0.19. Coffee ring effect has also been observed due to the applied laser. For the tracks printed with 1 W laser, two pairs of ring edges can be observed according to the view of the cross section which was primarily induced from two sets of droplets. The first droplet dried before the landing of the second droplet due to a time delay, and the

former has formed the outer edges, a lower coffee ring, followed by the latter droplet partially landed on the first droplet and formed the inner edges, a higher coffee ring. The bulge in the centre part of track indicates the Marangoni flow under such high substrate temperature.

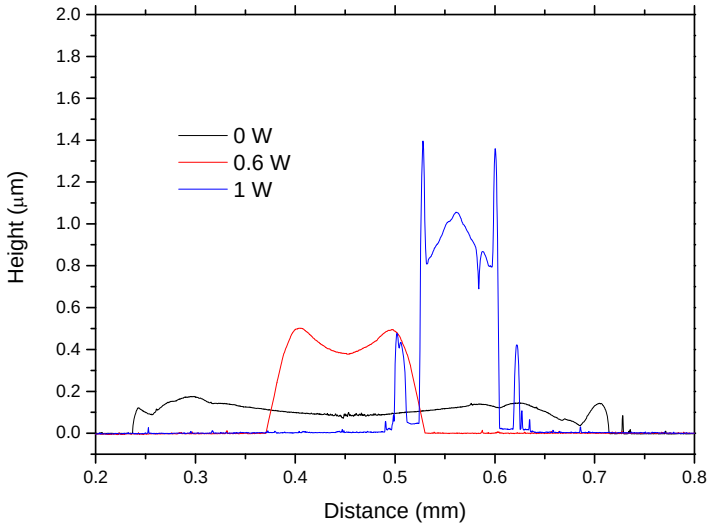

Figure 0.19 Cross sectional profile of ITO tracks printed with ITO nanoparticle ink under different laser power

6.4.2.2.2 Conductivity

The measured conductivity of the tracks printed with ITO nanoparticle ink in relation to CO_2 laser power applied is shown in Figure 0.20. The results indicate that the conductivity is significantly affected by the morphology of the tracks (Figure 0.17), which can be altered by the applied laser power. Without the irradiation of laser, the poor morphology of the printed track results in a relatively low conductivity as seen in Figure 0.20. When a power of 0.5 W laser was applied, the two edges of printed track became more regular or smoother, however a heterogeneous cross section profile along the printing direction has been induced due to the fast drying of solvents. Therefore, the conductivity is measured even lower than the one of track printed without laser. When the laser power is between 0.6~0.8 W, tracks with a uniform profile and morphology with a high aspect ratio have been achieved, which exhibited higher and more stable conductivity than the tracks produced with the lower power of laser. A further increase of laser power has led to reduced conductivity, which is likely to attribute to the initiation and propagation of cracks in the sintering process of the deposited inks.

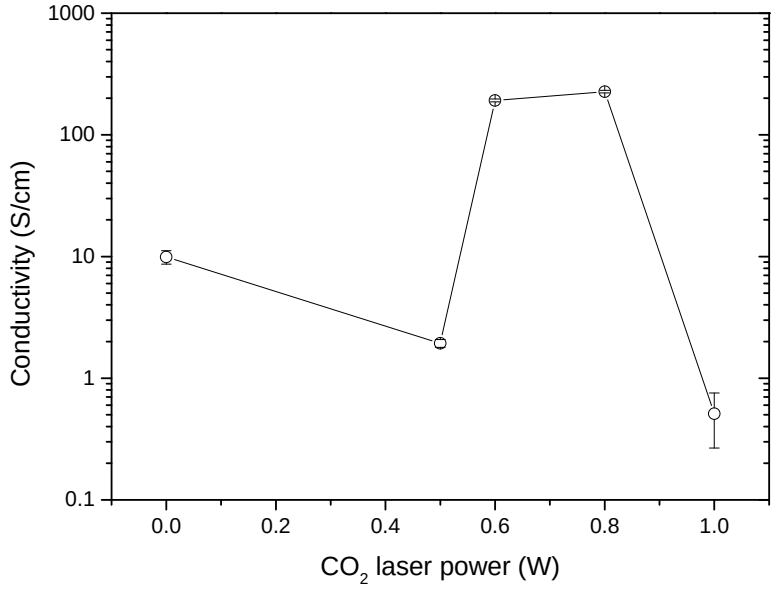

Figure 0.20 Conductivity of tracks printed with ITO nanoparticle ink vs. laser power

6.4.3 Critical thickness of track

It is interesting to observe that the critical thickness of tracks is larger than the one of thin films which has been identified previously (Section 6.3.1). For the thin films that were printed with MOD ITO or ITO nanoparticle ink, the critical thicknesses are found to be ~60 nm and ~140 nm, respectively. However, no cracks were visible in the printed tracks of 130 nm thick with MOD ITO ink, and it is even thicker up to approximate 500 nm in the tracks printed with ITO nanoparticle ink. To interpret such a finding and the difference of critical thickness between printed thin films and tracks, a mathematical model which can describe the internal stresses in tracks and films are established to simulate the mechanics and mechanical behaviour of the thin films or tracks.

In this study, the growth of cracks was observed during the sintering process. Sintering is the process through which a porous powder compact is to transform into a denser material with the application of heat. In the solidification stage the powder particles in the body of a mixture of solvent and various chemicals fuse together to form a denser solid structure. During the sintering process, the neck curvature produces a chemical potential gradient which causes material to flow from the grain boundary to the neck [163]. The reduction of the free energy of the system by the replacement of solid-

vapour interfaces with solid-solid interfaces generates a sintering driving force which causes the material to shrink [164]. Under a free sintering condition, the total volume of the material will decrease and the internal stresses will be released, as shown in Figure 0.21 (b). However, if the material is constrained to the surface of a rigid substrate Figure 0.21 (c), the stress remains and may lead to cracks or fractures in the structure, which explains the fundamentals of the cracking in the structures deposited by inkjet printing.

(a) Initial (b) Free (c) Constrained

Figure 0.21 Schematic illustration of microstructures of initial ink material deposited (a), sintered under a free flow condition (b), and sintered under a constrained condition (c) [165]

According to the SEM image of initial cracks on the film printed with MOD ITO ink (Figure 0.22), the growth of cracks were accompanied by the separation of two adjacent ITO particles as well as interface debonding between the ITO particle and substrate. As illustrated in Figure 0.23, the interface between adjacent ITO particles mainly bears the pulling force along the horizontal directions which can be decomposed as F_x and F_y, while at the interface between ITO particle and substrate there exists a pulling force F_z. In this study the ITO film was constrained on the substrate during the sintering process, thus the shear force between the ITO particle and substrate is not considered.

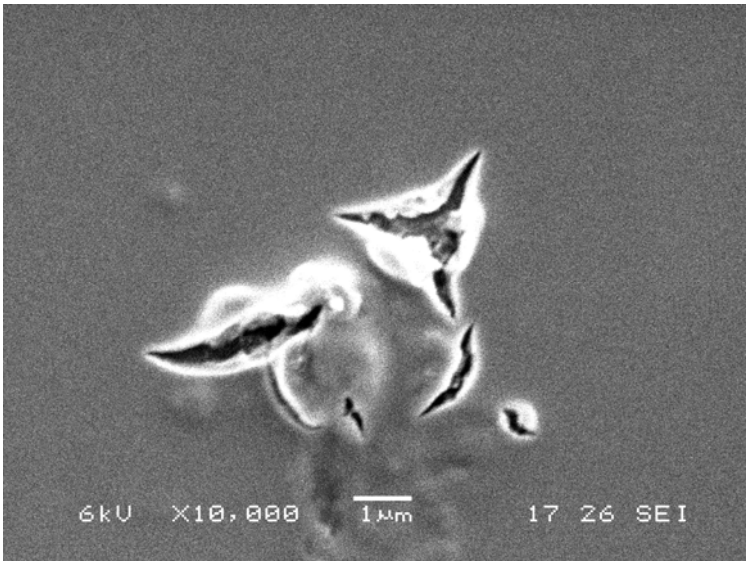

Figure 0.22 SEM image of initial cracks on ITO thin film

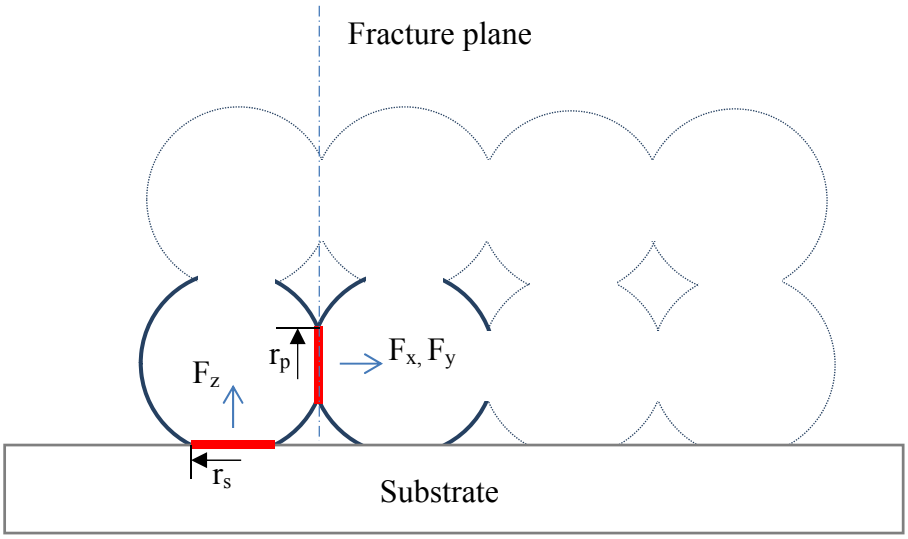

Figure 0.23 Schematic drawing of pulling forces between particles and at the interfaces

The pulling force on a specific interface is the results of accumulation of the applied force of every single point of the material matrix. If we set the coordinate of the interface to *(0, 0, 0)*, the pulling force from a point *(x, y, z)* can be described as $F_{(x, y, z)}$. Due to the elastic deformation of the particles, the value of $F_{(x, y, z)}$ decreases as the increase of the distance between this specific interface and the point. The pulling force can be deconvoluted into forces in three directions, F_x, F_y, and F_z, as shown in Figure 0.24.

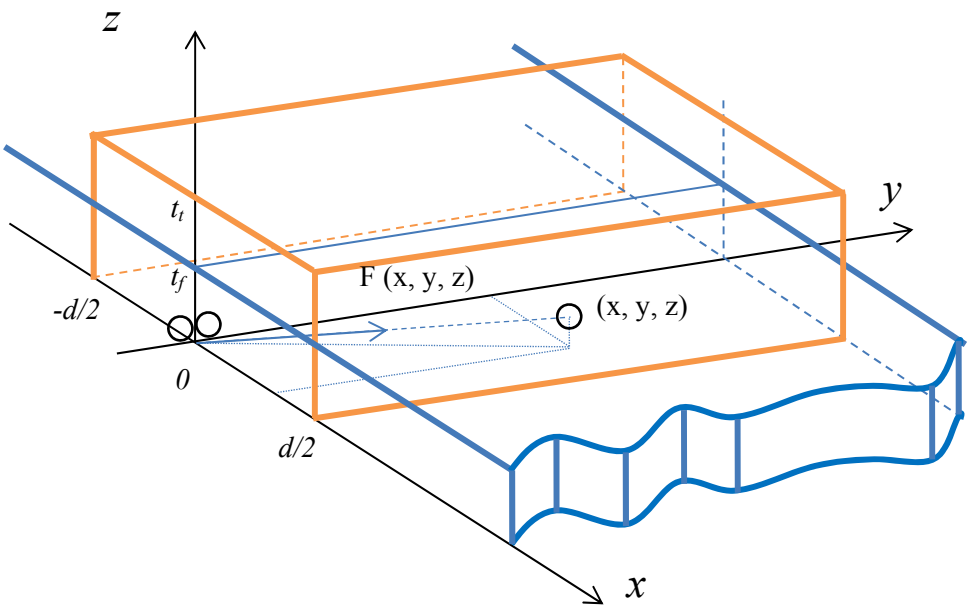

Figure 0.24 Schematic drawing of force F(x,y,z) exerted in the ITO track and film due to sintering

On the interface between particles, the equilibrium equation is:

$$\sigma_{x,y} = \frac{F_{x,y}}{2\pi {r_p}^2} = b_p \tag{6.1}$$

where r_p is the diameter of contact area of two particles, and b_p represents the effective body force [166]. When $\sigma_{x,y} > b_p$, the sintering neck between two particles breaks. For an infinite thin film, the stresses along the x direction and y direction are equal, therefore:

$$\sigma_{fx} = \frac{1}{2\pi {r_p}^2} \int_0^{t_f} \int_{-\infty}^{+\infty} \int_0^{+\infty} \frac{xF(x,y,z)}{\sqrt{x^2+y^2+z^2}} dxdydz \tag{6.2}$$

$$\sigma_{fy} = \frac{1}{2\pi {r_p}^2} \int_0^{t_f} \int_0^{+\infty} \int_{-\infty}^{+\infty} \frac{yF(x,y,z)}{\sqrt{x^2+y^2+z^2}} dxdydz \tag{6.3}$$

$$\sigma_{fx} = \sigma_{fy} \tag{6.4}$$

Considering the thickness of thin film is very small when compared to the area of thin film coverage, the pulling force from layers at the different heights can be approximately regarded as identical. Therefore the critical thickness for the fracture for thin film t_{fcb} is:

$$t_{fcb} = \frac{2\pi {r_p}^2 b_p}{\int_{-\infty}^{+\infty}\int_{0}^{+\infty}\frac{xF(x,y,z)}{\sqrt{x^2+y^2+z^2}}dxdy} = \frac{2\pi {r_p}^2 b_p}{\int_{0}^{+\infty}\int_{-\infty}^{+\infty}\frac{yF(x,y,z)}{\sqrt{x^2+y^2+z^2}}dxdy} \tag{6.5}$$

For a track with a width of *d*, the stresses along *x* direction and *y* direction are different due to the asymmetric geometry. In addition, certain shrinkage along the *x* direction is allowed at the top section of the track. This deformation can release an internal force F_d.

$$\sigma_{tx} = \frac{1}{2\pi {r_p}^2}\left(\int_0^{t_t}\int_{-\infty}^{+\infty}\int_0^{\frac{d}{2}}\frac{xF(x,y,z)}{\sqrt{x^2+y^2+z^2}}dxdydz - F_d\right) \tag{6.6}$$

$$\sigma_{ty} = \frac{1}{2\pi {r_p}^2}\int_0^{t_t}\int_0^{+\infty}\int_{-\frac{d}{2}}^{\frac{d}{2}}\frac{yF(x,y,z)}{\sqrt{x^2+y^2+z^2}}dxdydz \tag{6.7}$$

$$\sigma_{tx} < \sigma_{ty} \tag{6.8}$$

Therefore cracks tend to occur along the *x* direction, and the critical thickness of fracture for track t_{tcb} is:

$$t_{tcb} = \frac{2\pi {r_p}^2 b_p}{\int_0^{+\infty}\int_{-\frac{d}{2}}^{\frac{d}{2}}\frac{yF(x,y,z)}{\sqrt{x^2+y^2+z^2}}dxdy} \tag{6.9}$$

As

$$\int_0^{+\infty}\int_{-\infty}^{+\infty}\frac{yF(x,y,z)}{\sqrt{x^2+y^2+z^2}}dxdy = \int_0^{+\infty}\int_{-\infty}^{-\frac{d}{2}}\frac{yF(x,y,z)}{\sqrt{x^2+y^2+z^2}}dxdy + \int_0^{+\infty}\int_{-\frac{d}{2}}^{\frac{d}{2}}\frac{yF(x,y,z)}{\sqrt{x^2+y^2+z^2}}dxdy + \int_0^{+\infty}\int_{\frac{d}{2}}^{+\infty}\frac{yF(x,y,z)}{\sqrt{x^2+y^2+z^2}}dxdy \tag{6.10}$$

Thus

$$\int_0^{+\infty}\int_{-\infty}^{+\infty}\frac{yF(x,y,z)}{\sqrt{x^2+y^2+z^2}}dxdy > \int_0^{+\infty}\int_{-\frac{d}{2}}^{\frac{d}{2}}\frac{yF(x,y,z)}{\sqrt{x^2+y^2+z^2}}dxdy \tag{6.11}$$

$$t_{tcb} > t_{fcb} \tag{6.12}$$

In a similar way, at the interface between particle and substrate, the equilibrium equation is:

$$\sigma_z = \frac{F_z}{2\pi {r_s}^2} = b_s \tag{6.13}$$

Where r_s is the diameter of contact area between particle and substrate, and b_s represents the combination force. When $\sigma_z > b_s$, the particle debonds from the substrate. Assuming the critical thickness of debonding for thin film and track are t_{fcd} and t_{tcd}, respectively, then:

$$2\pi {r_s}^2 b_s = \int_0^{t_{fcd}} \int_{-\infty}^{+\infty} \int_{-\infty}^{+\infty} \frac{zF(x,y,z)}{\sqrt{x^2+y^2+z^2}} dxdydz = \int_0^{t_{tcd}} \int_{-\infty}^{+\infty} \int_{-\frac{d}{2}}^{\frac{d}{2}} \frac{zF(x,y,z)}{\sqrt{x^2+y^2+z^2}} dxdydz \tag{6.14}$$

As $F(x,y,z) > 0$,

$$t_{tcd} > t_{fcd} \tag{6.15}$$

In summary, both the critical thicknesses for cracking between particles and debonding from substrates of tracks are higher than the ones of films. This explains the experimental results that the tracks can achieve higher thickness without inducing cracks. Moreover, the t_{tcb} and t_{tcd} are inversely proportional to the track width d, which means thicker crack-free tracks can be obtained by reducing the track width. As LIJ printing is an effective way to reduce the track width, thick ITO patterns can thereby be achieved through such an innovative approach.

6.5 Conclusion

ITO thin films are firstly deposited via inkjet technology using both MOD ITO ink and ITO nanoparticle ink. The thickness of the thin films is found to be thinner than the theoretical value when the printed films are thicker than 100 nm, primarily due to the coffee stain effect. The critical thickness with respect to the emerging of cracks in the deposited structures is identified to be ~60 nm for the printed thin films with MOD ITO ink, and ~140 nm when using ITO nanoparticle ink. The generation of crack decreases the conductivity of the thin films as well as the morphology of the printed structures. The average transmittance of ITO films printed with MOD ITO ink and ITO nanoparticle ink were determined and they are ~85.9% and ~87.3%, respectively, which are comparable to the ITO thin films fabricated through conventional vacuum process.

In the printing of tracks, laser is applied during the inkjet process which can allow producing fine patterns. The optimal position of laser radiation is found to be 20 μm ahead of the landing position of the inkjetted droplet. Laser power also has a significant impact on the morphology of printed tracks. With optimum set of a value of laser power, the track width can be reduced by 3/5 with MOD ITO ink and 2/3 with ITO nanoparticle ink in comparison with non-laser assistance. The conductivity of tracks printed with MOD ITO ink is not influenced by the laser treatments. However, for tracks printed with ITO nanoparticle ink, the improved conductivity can only be achieved through the reinforcement of morphology as well as a high aspect ratio.

It is also found that the critical thickness of tracks without inducing any cracks in the deposited structures is greater than the one for the printed thin films. No cracks were observed in the track thinner than 130 nm printed with MOD ITO ink, and it can reach 500 nm thick track printed with ITO nanoparticle ink without cracking. Hence a model to simulate the internal stresses in tracks and films are established and mathematically analysed. The model suggests LIJ printing can be an effective way in fabricating thick ITO patterns with a high aspect ratio.

Chapter 7 Self-assembly Synthesis of Silver Thin Film *via* Inkjet Printing

In this chapter, a novel process which is able to fabricate transparent and conductive silver thin film is developed. This process utilises a unique approach to integration of conductive silver networks using a layer of precursor materials which can be pre-deposited on the substrate, instead of the conventional one-by-one printed silver grids. Inkjet printing is employed to print the precursor layer as it can precisely control the volume of deposited materials and directly print the designed patterns. The printed layer is then cured to enable *in-situ* synthesis of a thin film of silver on the substrate. The experimental results from this study have demonstrated that the microstructure of such thin films is determined by the amount of ink materials deposited; as such conductive transparent silver thin film can be produced under sufficient printing resolution.

7.1 Introduction

Metal grids are considered to be an alternative transparent conducting pattern which may replace ITO as the electrode in photovoltaic devices. Metals are good conductors, while the gaps or spaces between the grids can provide sufficient transparency to allow the light transmission as shown in Figure 0.1. It is particularly attractive that the metal grids are compatible with flexible substrates if the patterns may be deposited onto such flex materials.

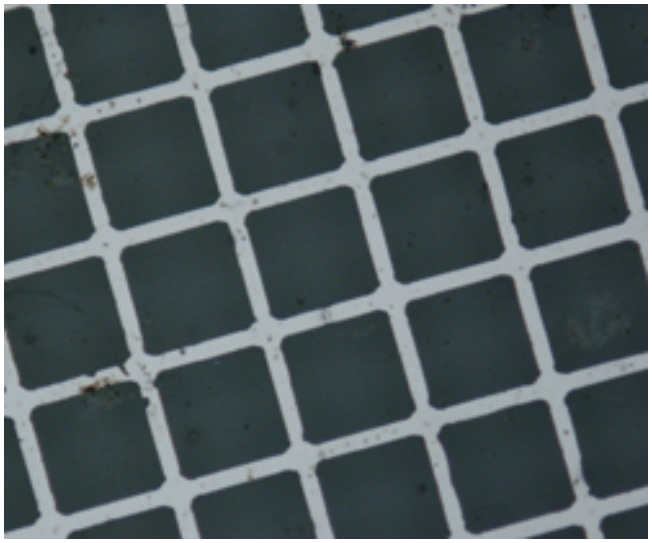

Figure 0.1 Fine metal grids with a track width of 5 μm [167]

Metal grids have been fabricated by using numerous printing methods, e. g. screen printing, imprint, flexographic and inkjet printing [168][169][170]. Nano-scale tracks can also be achieved in the metal grids prepared using nano imprint, which helps to enable high transparency of the metal grids [17]. However, the procedures of imprint are complicated and the cost is extremely high. In contrast, screen printing and inkjet printing are relatively simple and cost-effective, but the patterns printed with these two processes cannot achieve as high resolution as imprint. The track width in the metal grids prepared using screen printing is often larger than 100 μm [171, 172], and normally ranges from 60 to 200 μm using inkjet printing [37, 173, 174]. One exception is reported by Conductive Inkjet Technology [175] which has fabricated a silver grid composed of 5 μm wide tracks, with an effective conductivity of 2 Ω/square and an optical transmission of 95%.

In the conventional inkjet printing of forming metal grids, the inks containing metal nanoparticles are usually deposited onto substrate surfaces through multiple intersected tracks perpendicularly arranged. The track width is strictly limited by the size of jetted droplets and the interaction between the droplets and the substrate, thereby it is extremely challenging to reduce the size of the grids due to the restricted limit of the resolution of the prints. In this study, we have developed a novel method to fabricate silver grids by inkjet printing a precursor layer which is then cured to form silver films with extremely refined microstructure of nano-scale patterns. The silver films that were obtained are composed of 10 μm wide tracks, and the density of the tracks can be altered by changing the printing parameters. Silver nitrate and glycerol were added as the main components of the precursor material, as they have been demonstrated to be suitable for the synthesis of silver nanoparticles [176-178].

7.2 Experimental procedures

7.2.1 Ink formulation

To formulate the precursor ink used in this work, silver nitrate and glycerol were firstly dissolved in deionized water to form a composite solution. The weight ratio of silver nitrate, glycerol and deionized water was 1:1:100. SDBS and JC-601 have been added into two separate sets of composite solution to serve as surfactants. The pristine composite solution, SDBS doped composite solution and JC-601 doped composite solution were stood for 24 hours to investigate the effect of the surfactants on the reaction between silver nitrate and glycerol, and the appearances of the solutions before and after standing are shown in Figure 0.2. All the three composite solutions appeared to be transparent right after formulating. After standing for 24 hours, black deposits could be observed at the bottom of the container for the pristine composite solution, which indicates the occurrence of reaction. The colour change of the solutions with surfactants (Figure 0.2 (e) and Figure 0.2 (f)) suggested that the reaction between silver nitrate and glycerol could be affected by the addition of SDBS and JC-601. It can be further concluded that SDBS can more effectively facilitate the formation of silver nanoparticles, as a darker colour of the solution has been incurred. However, the reaction is supposed to commence after the solution is deposited on substrate. In contrast with SDBS, JC-601 is more beneficial for the stability of the composite solution, therefore was adopted as the surfactant at a concentration of 0.05 wt.%. In

addition, 5 wt.% ethanol was added into the solution to adjust the surface tension of the solution to 38 dynes/cm. The mixture was blended using an ultrasonicator for 5 min to form a bubble-free homogenous ink which is readily for jetting.

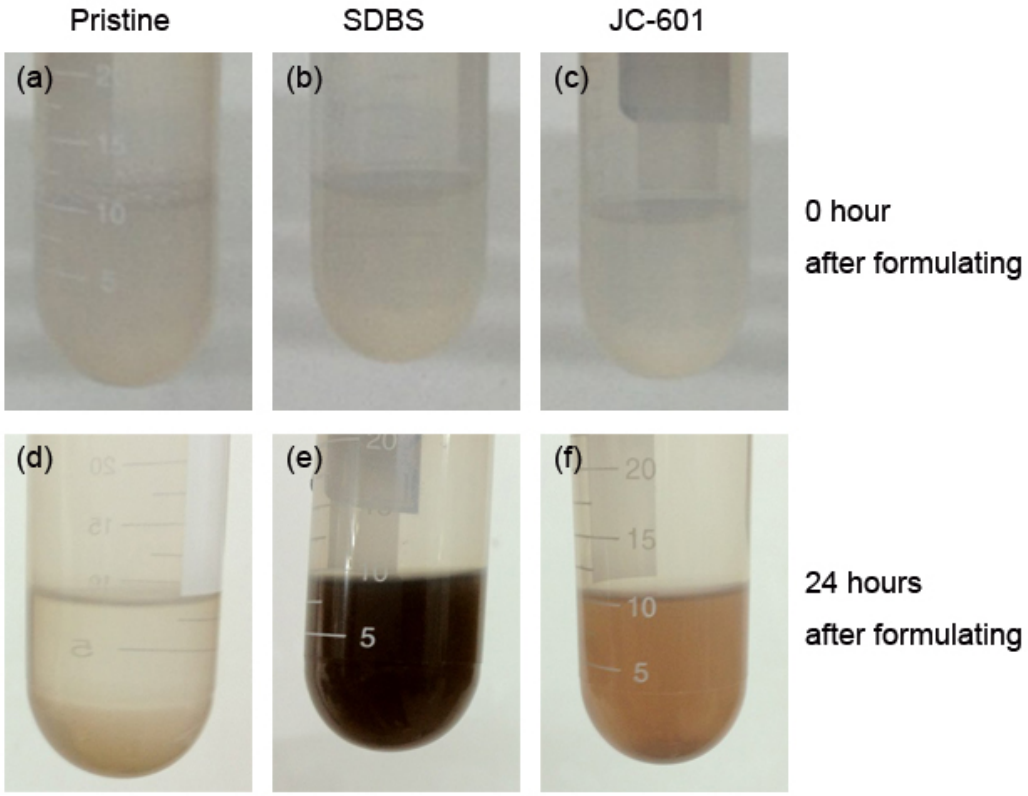

Figure 0.2 Appearances of pristine composite solution (a) (d), SDBS doped composite solution (b) (e) and JC-601 doped composite solution (c) (f) right after formulating (a) (b) (c) and 24 hours after formulating (d) (e) (f)

7.2.2 Thin film deposition

IIA-1501 inkjet printer supplied by Fanjet electronic technology co., Ltd was utilised for the deposition. Droplets with a diameter of 50 μm were obtained using the ink prepared in Section 7.2.1 and the dot array printed is shown in Figure 0.3. The diameter of the dots ranges from 150 to 180 μm. 10 mm × 10 mm square films were printed on prewashed glass substrates at the resolution of 300 × 300, 600 × 600, 900 × 900 and 1200 × 1200 dpi (dot per inch, equivalent to 140, 560, 1260 and 2240 dots/mm^2), which enables different volumes of ink material per unit area to be deposited. The corresponding weight of silver per unit area is 56.7 mg/m^2, 113.5 mg/m^2, 170.2 mg/m^2, and 226.9 mg/m^2. The printed films were then baked at 150 °C for 1 hour to accelerate the reduction reaction between silver nitrate and glycerol [176]; this can also allow the excess glycerol and some of the resultants to be evaporated. After baking, optical

microscope and SEM were employed to observe the structure of the obtained films. The electric and optical properties of the films were also characterised.

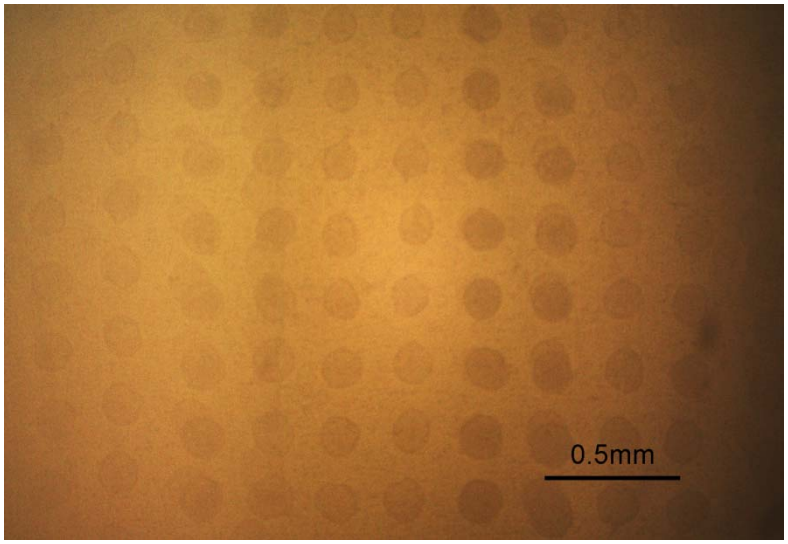

Figure 0.3 Dot array printed with self-developed ink

7.3 Effect of printing resolution

7.3.1 Morphology

The images obtained from the optical microscope in Figure 0.4 revealed that the thin films contain interconnected networks consisting of numerous dendritic micro-branches (i.e. the arms of dendrites,) with varying density and width, which are clearly associated with the volume of deposited material under the different printing resolutions. It is interesting to observe the 60 ° intersection angle between the stem and individual branches [179] (i.e. arms). At the printing resolution of 300 × 300 dpi (Figure 0.4(a)), the branches are randomly arranged and disordered with some significant spacing between dendritic arms. At the 600 × 600 dpi printing resolution (Figure 0.4(b)), the increased amount of precursors enabled further growth of the branches, resulting in a well-organized and homogenous dendritic structure with varying spaces between branches. Further increase of the printing resolution led to a denser packing of branches in the saturated dendritic structure, but the spaces between branches have drastically reduced (Figure 0.4(c)), and as can be seen, the complete coverage of substrate surfaces by the very refined densely packed networks has taken place when using 1200 × 1200 dpi printing resolution (Figure 0.4(d)).

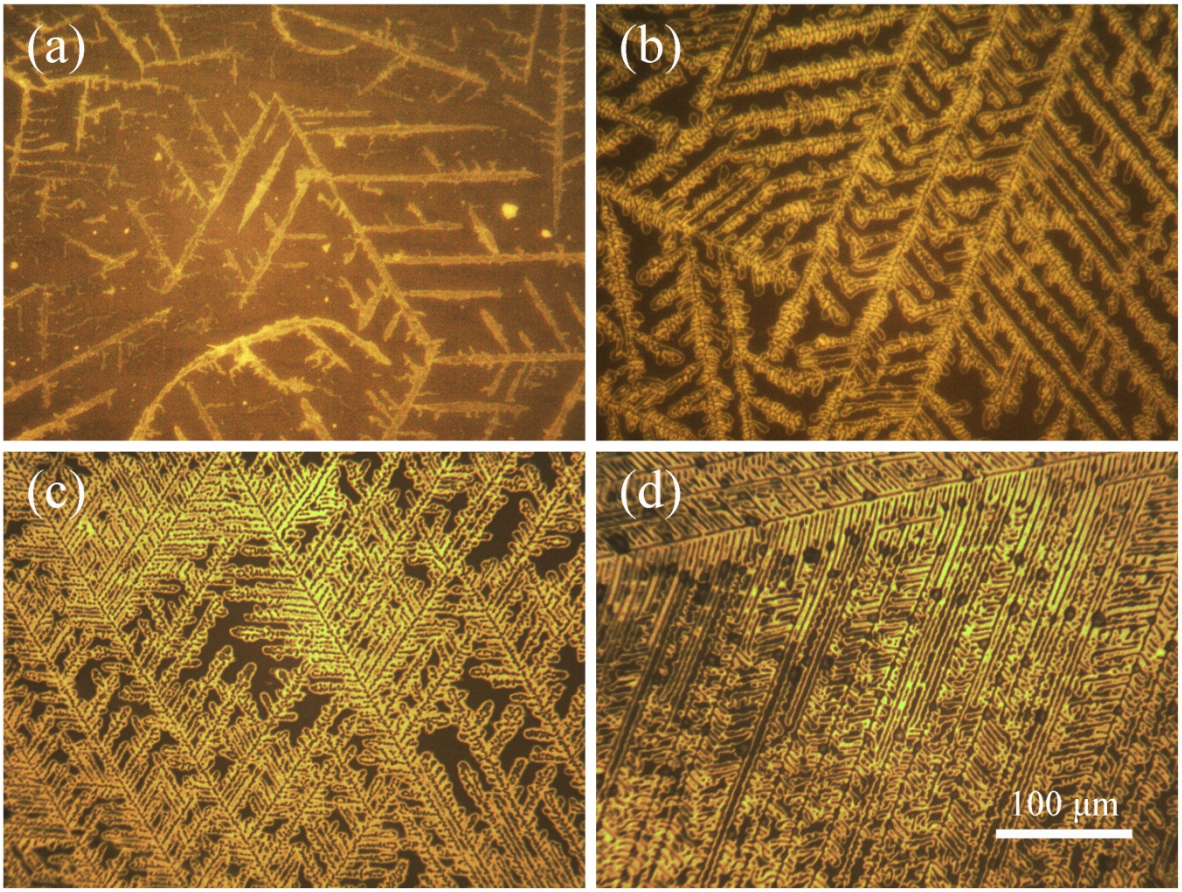

Figure 0.4 Optical observation of thin films printed under resolutions of 300 × 300 (a), 600 × 600 (b), 900 × 900 (c) and 1200 × 1200 (d) dpi after baking under 150 °C for 1 hour

According to the SEM image of top view (given in Figure 0.5 (a)) and cross section (given in Figure 0.5 (b)) of the deposited films, the branches are composed of nano-scale silver grains, with the majority of them being smaller than 300 nm. After baking at 150 °C for 1 hour, sintering necks can be observed between the nano grains. The formation of such unique silver dendritic structure can be explained through the following steps, with the assistance of schematic illustration given in Figure 0.6.

1) With the increase of temperature, numerous silver crystal nuclei formed (Figure 0.6 (a)) through the oxidation reduction reaction in the composite ink as following: [180]

$CH_2OH\text{-}CH(OH)\text{-}CH_2OH \rightarrow CH_2OH\text{-}CH(OH)\text{-}CHO + H_2$,

$CH_2OH\text{-}CH(OH)\text{-}CH_2OH \rightarrow CH_2OH\text{-}CO\text{-}CH_2OH + H_2$,

$CH_2OH\text{-}CH(OH)\text{-}CHO + 2AgOH \rightarrow 2\ Ag + H_2O + 2CH_2OH\text{-}CH(OH)\text{-}COOH$,

$CH_2OH\text{-}CH(OH)\text{-}CHO + 2AgOH \rightarrow 2\ Ag + CH_2OH\text{-}CO\text{-}COOH + H_2O + H_2$.

2) The crystal nucleus grew and became numerous grains (Figure 0.6 (b)). The grains could migrate freely in the solution as a result of Brownian motion due to their small size, and collisions between different grains occurred. When the grains made contact in a parallel lattice orientation, which could lead to the reduction of total energy, metallic bonds between atoms were formed so as to achieve a full coordination. Therefore, the silver grains spontaneously aggregated along crystallographically special directions. This oriented attachment-based aggregation has also been described in Banfield et al. and Lu et al.'s study [181, 182]. As the silver grains formed in this study have a hexagonal structure as observed in Figure 0.5, a hierarchical dendritic pattern was obtained (Figure 0.6 (c)).

3) Silver grains were continuously formed and precipitated following the previous pattern until silver nitrate was completely consumed. Sintering necks were formed between attached silver grains under such temperature, and an effectively connected network was thereby obtained (Figure 0.6 (d)).

4) The remaining glycerol and the volatile resultants were evaporated. The network composed of silver dendritic pattern remained on the glass substrate (Figure 0.6 (e)).

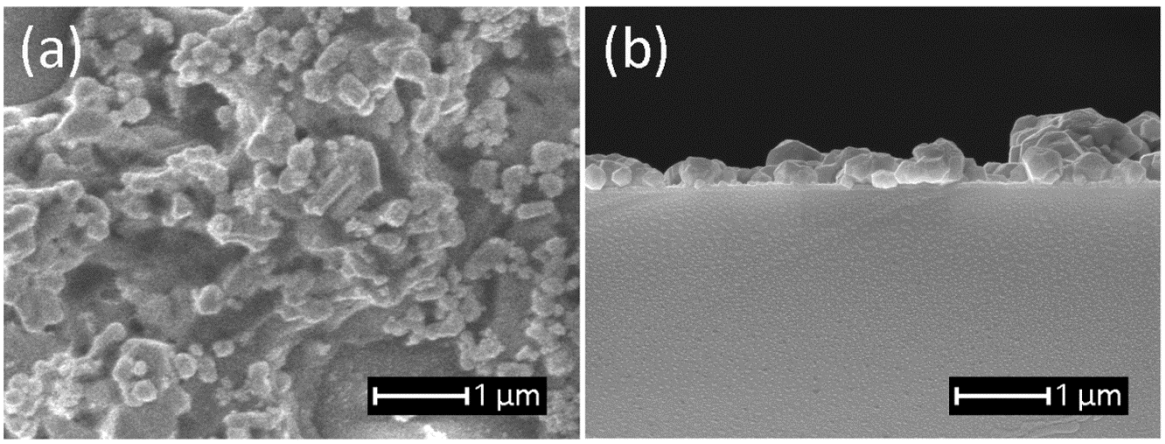

Figure 0.5 SEM images of top view (a) and cross section profile (b) of the thin films

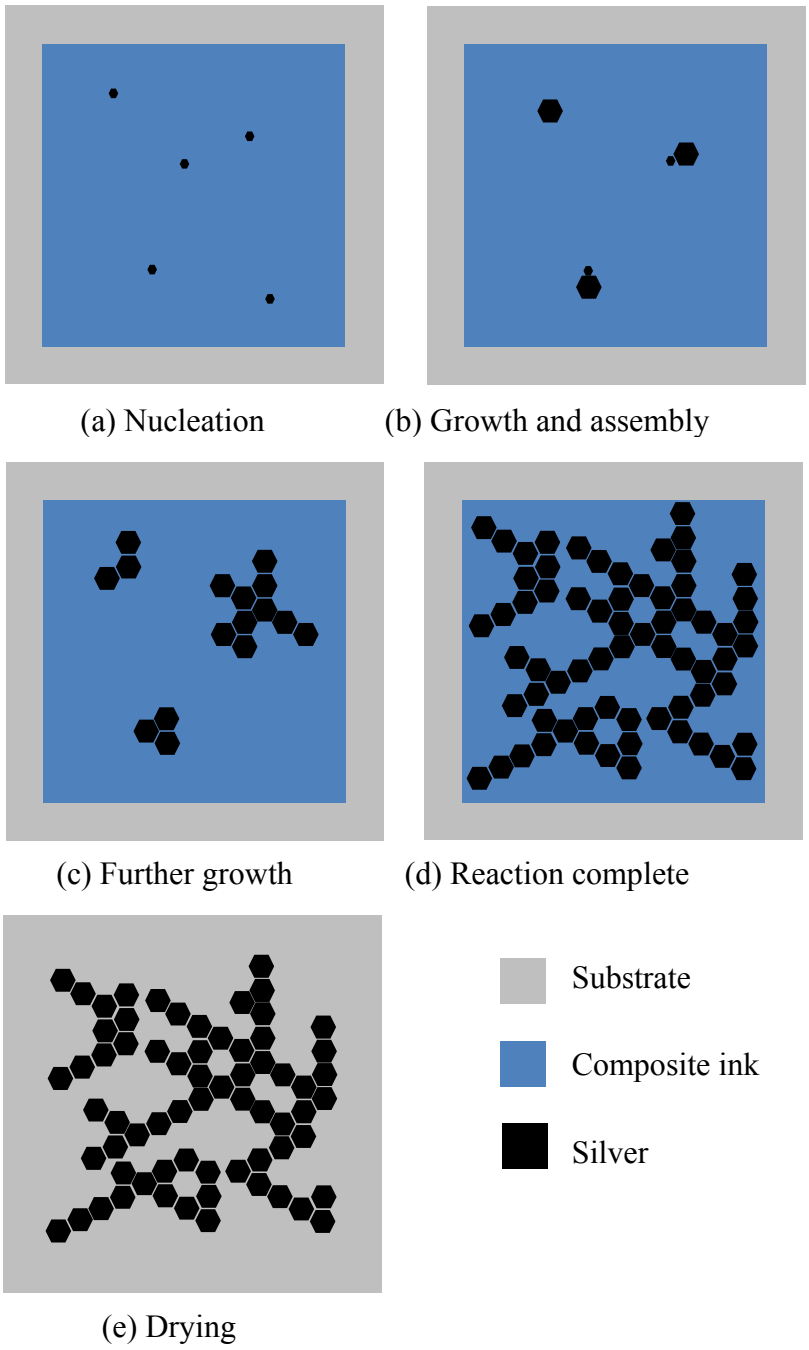

Figure 0.6 Schematic illustration of the *in-situ* formation of silver grids

7.3.2 Conductivity

The measured sheet resistance of the printed thin films is presented in Figure 0.7. A significant reduction of resistivity was observed when the printing resolution increased from 300 × 300 dpi to 600 × 600 dpi. According to the microscopic image of the printed thin film at the resolution of 300 × 300 dpi (Figure 0.4(a)), most of the branches

or arms in the silver networks were disconnected and away from the main branches, which has resulted in a very low conductivity of the printed thin films. However, most of the branches at the 600 × 600 dpi print resolution are interconnected (Figure 0.4(b)) forming effectively various electrical paths throughout the entire network in the printed thin films. It is interesting to observe that further increase of the printing resolution can continue to reduce the sheet resistance of the thin films, but relatively less significant.

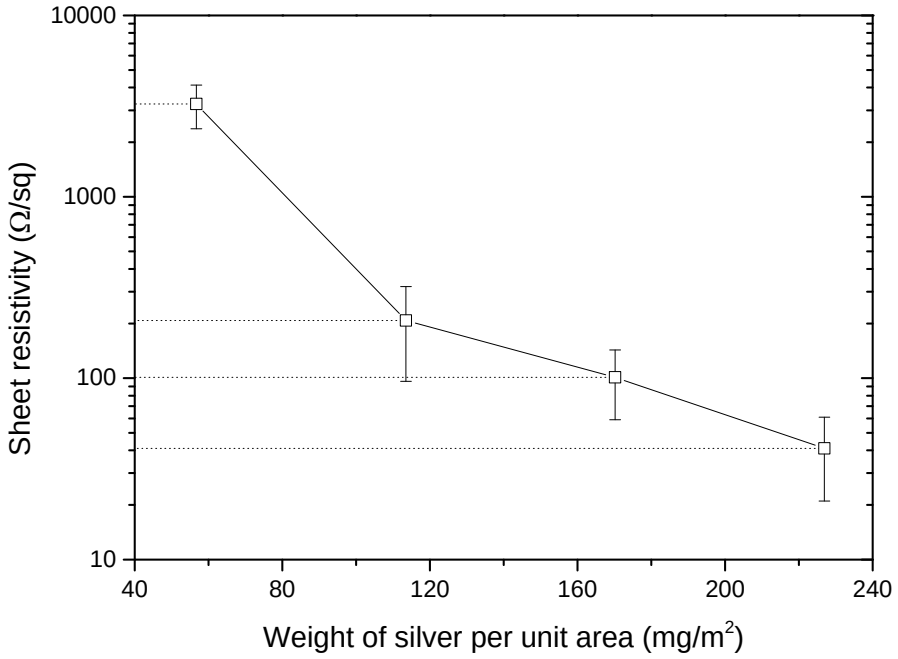

Figure 0.7 Measurement of sheet resistance of the printed silver thin films

7.3.3 Transparency

As can be predicted, the decrease or loss of transparency of the films may be inevitable as the films became denser by increasing the print resolution which can be confirmed by the measurement of transmittance of these films, and results are given in Figure 0.8. Indeed, the transmittance of the films decreases rapidly with the increase of printing resolution. The average transmittances of the films are 91.2%, 73.0%, 60.8% and 19.1%, successively. From Figure 0.8, an absorption peak ranging from 420 nm to 450 nm appears in each UV-Vis spectrum. Although the peak is slightly different than the reported absorption peak of nano silver (390 nm), [183] it is still well within the range of values that has been identified for nano silver in Ref. [184]. It is understood that the red shift of these peaks as the result of increasing printing resolution was caused by the

agglomeration of the silver nanoparticles, which indicates that a larger volume of precursor material can lead to a higher aggregation level of the resultant during the formation of the films.

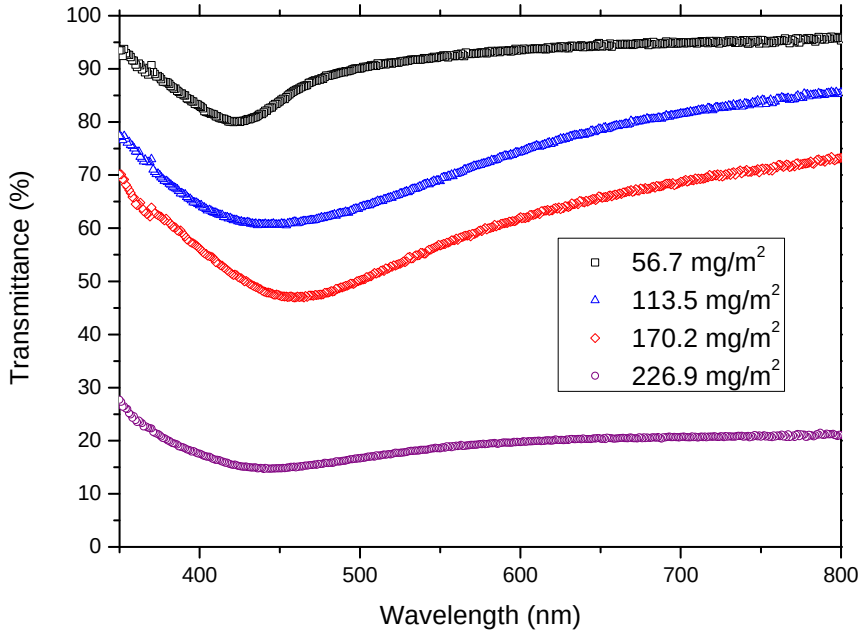

Figure 0.8 UV-Vis spectrum of printed silver thin films

7.4 Conclusion

In summary, an *in-situ* synthetic process of fabricating transparent conductive silver thin films using inkjet printing has been developed, by which the silver micro-networks as the deposited films containing dendritic silver branches were formed. The mechanism of the *in-situ* formation of such dendritic structure has been discussed with the assistance of a schematic illustration. The results indicate that the density of the films which can be controlled through altering the packing of dendritic silver branches using different printing resolution will ultimately determine the conductivity and transmittance of the films. At a printing resolution of 600 × 600 dpi, thin films with a sheet resistivity of 200 Ω/sq and a transmittance ~73.0% have been obtained, which demonstrates the feasibility of the process.

Chapter 8 Conclusions and Future Work

8.1 Main conclusions

This thesis has been focused on the preparation and optimisation of transparent conducting patterns by the inkjet printing process, targeting potential applications of the fabrication of photovoltaic devices. At the initial stage, the formulation of inkjettable inks and inkjet printing deposition of basic patterns were exercised to gain the underpinned fundamental knowledge for the subsequent stages of further investigations on the feasibility of inkjet printing of various TCPs using the prepared inks for each application. Three types of ink materials for printing transparent conducting patterns, i.e. PEDOT:PSS, ITO, and silver were selected for the ink formulation and tested in the inkjet printing trials. In the printing of PEDOT:PSS thin films, with an intention of further enhancing the electrical conductivity of the printed films, the work applied thermal annealing, solvent annealing as well as doping with nano-particulate conductors and their effects on the electric conductivity and optical transparency of the obtained PEDOT:PSS films have been investigated, which has indicated the increase of the conductivity. In the deposition of ITO thin films and tracks, MOD ITO inks and ITO nanoparticle inks have been for the first time developed and printed onto substrates using laser assisted inkjet printing. The locations and power of the laser radiation applied have been optimised during the printing process to obtain patterns with smoother morphology and high aspect ratio. A novel method which is capable of depositing semi-transparent thin films with uniformly distributed silver-grid patterns through self-assembly synthesis has been identified, thus the deposited microstructure was characterised in terms of electrical and optical properties. The primary scientific and technological findings can therefore be summarised as follows:

1. The sheet resistivity and transmittance of the thin films prepared in this study, as well as the inkjet printed thin films that have been reported, are summarised in Figure 0.1. It can be concluded that both solvent annealing and doping conductor nano particulates can be incorporated in the inkjet printing of PEDOT:PSS patterns. Through the optimisations in this study, the functionality of the PEDOT:PSS thin films even achieved the same level of inkjet printed ITO thin films. However, in

contrast with solvent annealing, doping conductor nano particulates is less efficient in improving the electrical conductivity of PEDOT:PSS and also causes inevitable reduction in transmittance. Although inkjet printing is proved to be an alternative method to prepare ITO patterns, the sheet resistivity of ITO thin films prepared with inkjet printing is nearly two orders of magnitude higher than the ones prepared using traditional vacuum processes. The newly developed process of fabricating silver thin films in this study still needs to be optimised to produce silver thin films with lower sheet resistivity and higher transparency.

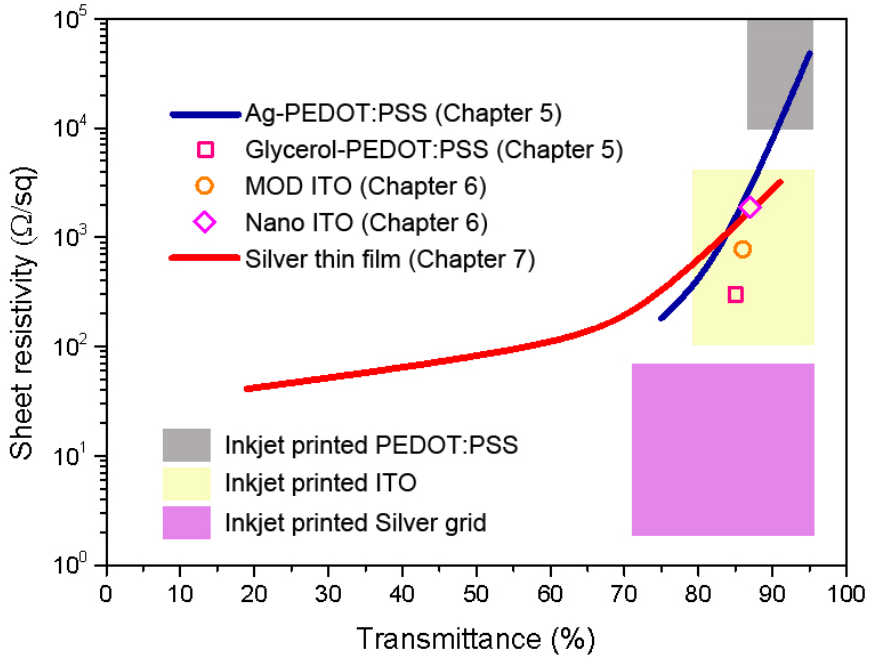

Figure 0.1 Sheet resistivity and transmittance of reported inkjet printed thin films (coloured rectangular blocks) and thin films prepared in this study (coloured curves and dots)

2. In the formulation of water-based inkjet inks, the addition of glycerol leads to the increase of viscosity, as well as a slight increase in the surface tension. Changing the temperature of the inks in the printing trials is also an effective method to alter the viscosity of inks. SDBS and JC-601 are identified as the suitable surfactants in reducing the surface tension of the inks. Post treatments of the inks, e.g. filtering and ultrasonic processing are essential to ensure the fluent and efficient printing.
3. The simulation results generated from software FLUENT suggest that both surface tension and viscosity can significantly affect the formation of droplets. It has been found that the number of satellites that were formed can be effectively reduced by increasing surface tension of the inks, whilst viscosity of the inks exhibited a significant effect on the velocity of droplets that can be induced during inkjet

printing. The simulations have been validated through experimental printing trials. Such simulation are proven to be able to accurately predict the behaviour of the droplet formation, providing a useful guidance to further adjustment and refinement of ink properties based on the morphology of obtained droplets and behaviour of the inks in the inkjet printing. For the Spectra SE-128 printhead which has been used in the inkjet printing systems, the essential inkjettable condition, which can be measured using the parameter Z for the inks, must be $Z \approx 5$.

4. The retraction of droplet toward the chamber or jetting device is attributed to the upward velocity of droplets that can be induced when the droplets are formed by breaking from the orifice. The upward velocity has been usually caused by an excessive viscosity of the ink or an insufficient positive pressure of the applied waveform. The deviation of the flying pathway of droplets from the perpendicular direction is attributed to a horizontal velocity of the droplet which is normally induced by the heterogeneous surface condition of the inner wall of the nozzle. All these factors are vital in the inkjet printing to ultimately determine the final landing locations of the droplets onto the substrate surfaces, the experimental trials have been carried out to understand their effects as such the optimisation may be possible for properly control of printing process.
5. The evaporation of the solvent liquid in the formed droplets can be significantly accelerated due to the preheat applied to the substrate after the droplets land on the surface, resulting in more obvious coffee stain effect and more regular dot outline. However, preheating cannot always lead to high resolution of the print as the increased wetting property of droplets caused by preheating can increase the spreading speed of the droplets at the same time. The optimal preheating temperatures that can assist to achieve the smallest size of features of the prints has been found to be greater than 80 °C for glass, but in a range of 30-40 °C for polyimide, 60-70 °C for FR4 and 50-60 °C for hydrophobic paper substrates.
6. The optimal overlapping rates of neighbouring dots that can form continuous tracks with refined and smooth morphology for glass, polyimide, FR4 and hydrophobic paper are identified through the printing trials, and they are 27%, 32%, 33% and 28%, respectively. The width of the track is normally smaller than droplet size due to the non-uniform spreading of inks at different directions after landed onto the surfaces. The thickness of thin films deposited by inkjet printing is dependent on

both the concentration of the solute in the inks and the value of dot spacing during the printing.

7. The transmittance and surface uniformity at macro scale of the PEDOT:PSS films deposited by inkjet printing can be optimised by solvent annealing. The aggregation of PEDOT-rich particles has been observed in the PEDOT:PSS thin films, which is induced by the addition of glycerol in the PEDOT:PSS inks. This aggregation has led to an increase in conductivity of the films up to 300 times higher than that without aggregation, and an increase in the surface roughness at micro scale. The conductivity of the thin films printed with glycerol doped PEDOT:PSS inks can be further improved by post baking process.
8. Thermal annealing of the thin films printed with pristine PEDOT:PSS ink leads to the degradation of PEDOT and PSS, resulting in a darker colour of the thin films, thus less transmittance to the light. Baking at 225 °C induces the aggregation of PEDOT-rich particles; nevertheless, the conductivity of the thin films is not improved by such aggregation as the connection between different PEDOT-rich particles is weakened by the degradation of PSS. It is highly recommended that the baking should be conducted below 300 °C, otherwise, the thin films may be susceptible to a damage the surface profile of the deposited thin films.
9. PEDOT:PSS can be served as a reducing agent in the reduction reaction of silver nitrate, *in-situ* forming a mixture of Ag nanoparticles (NPs) and PEDOT:PSS solution. The size of the Ag NPs increases with the increase of reaction time, reaction temperature and concentration of silver ion. The dedoping of PSS from PEDOT during the reaction between silver nitrate and PEDOT:PSS is detrimental to the electrostatic interaction between PEDOT and PSS, leading to a reduction in the conductivity of the thin films deposited with inkjet ink developed from the *in-situ* synthesised mixture.
10. The conductivity of thin films printed with the inks formulated by dispersing Ag NPs into pristine PEDOT:PSS solution can be improved in comparison with pristine PEDOT:PSS thin films since the Ag NPs can bridge different PEDOT-rich particles providing more paths thus better electric connections. The lager the size and/or the higher content of Ag NPs are added, the more effective the increase of the conductivity of printed thin films. This is attributed to the increased surface areas of contact between PEDOT and the bridging Ag NPs through the increased

number of such connections. The addition of Ag NPs also causes certain reduction in the surface evenness of the deposited thin films.

11. The light absorbance of the thin films printed with Ag NPs doped PEDOT:PSS inks is associated with the concentration of Ag NPs, following a quasi linear relationship. The addition of Ag NPs also affects the formation of oxide on the surface of PEDOT:PSS thin films, by forming the irregular islands in the films, and homogenously dispersed particles in the films without and with Ag NPs, respectively.
12. The temperature of substrate has a strong influence on the morphology and properties of patterns deposited by inkjet printing using inks containing suspended solid particles. The conductivity of Ag NPs doped PEDOT:PSS thin films along the printing direction can be improved by three times if the temperature of the substrate increased from 20 °C to 80 °C by preheating, which is mainly attributed to the accumulation of Ag NPs during the ink drying process which can consequently cause the coffee stain effect.
13. The critical thickness with respect to the emerging of cracks in the deposited ITO structures has been identified, and they are ~60 nm for the printed thin films with MOD ITO ink, and ~140 nm when using ITO nanoparticle ink. The average transmittance of ITO films printed with MOD ITO ink and ITO nanoparticle ink are ~85.9% and ~87.3%, respectively, which are comparable to the ITO thin films fabricated through conventional vacuum process. However, the sheet resistivity of the printed ITO films ranges from 1000 to 3000 ohm/sq, which is higher than the ITO thin films fabricated through conventional vacuum process.
14. The optimal location of *in-situ* laser radiation is identified which should be 20 μm ahead of the landing point of the inkjetted droplet during the laser assisted inkjet printing of ITO tracks. With optimum set of parameters of laser power, the track width can be reduced by 3/5 with MOD ITO ink, and 2/3 with ITO nanoparticle ink in comparison without laser radiation. The conductivity of tracks printed with MOD ITO ink is not significantly influenced by the laser treatments. However, for tracks printed with ITO nanoparticle ink, the improved conductivity can only be achieved through the reinforcement of morphology as well as a high aspect ratio.
15. The critical thickness for not causing cracking tracks is identified to be below 130 nm for the ITO tracks printed with MOD ITO ink, and 500 nm for the ITO tracks printed with ITO nanoparticle ink, which both are higher than the critical thickness

for the printed films, indicating the possibility to fabricate thick ITO patterns through laser assisted inkjet printing, especially with the inks formulated with ITO nanoparticles.

16. Semi-transparent silver thin films containing dendritic silver braches have been incidentally obtained by inkjet printing a layer of self-developed precursor ink followed by a baking process. The density of the films which can be controlled through altering the packing of dendritic silver branches using different printing resolution will ultimately determine the conductivity and transmittance of the films. Silver thin films with a sheet resistivity of 200 Ω/sq and a transmittance ~73.0% can be obtained, which demonstrated the feasibility of the *in-situ* synthesis process.

8.2 Recommendation for future work

Due to the constraints of research facilities and time of undertaking this research, a number of areas have not been fully investigated. The following recommendations for future work can be outlined:

1. The further characterisation in terms of stability of the formulated inks can be carried out to ensure the jettability of the developed inks for various applications. As aggregation of solid particles as well as existing agglomerated deposits inside the inks can potentially cause severe blocking of jetting devices during the jetting process, thereby the stability of an ink can be critical in determining the quality of prints, especially for the inks which may contain some suspended particles. However, long term ink stability or shelf life in terms of use of ink has not been concerned in this study, as all the inkjet printing in the experiments was implemented using the formulated inks within a short period of time of exposure to the ambient after filtering. According to the observation of the inks, sediments have been found in the Ag NPs doped PEDOT:PSS ink (Chapter 5) and precursor ink made of silver nitrate and glycerol (Chapter 7) after several days of standing. For this reason, the suitable dispersants are demanded for different types of inks to improve their shelf life or stability, thereby ensure the success of deposition of the inks in practical printing works if it needs a longer lead time.
2. The impact of an ink droplet and interaction with substrate under various conditions in the inkjet printing can be very important and determine the morphology of final printed structures deposited by inkjet printing. This has been

investigated to certain degree in this study, but still demands further significant understanding. Although numerous formulas have been employed to understand the spreading behaviour of the droplets on substrates. Ultimately, a relationship should be established to calculate the diameter of obtained dots based on given ink properties (i.e. density, viscosity, surface tension) and substrate surface conditions (i.e. roughness, surface tension, temperature). This work can be further extended by adding a dimension of modelling or simulation which can assist an estimation or prediction of the formation of an ink droplet and its interactions with the substrate surfaces.

3. It has been identified that glycerol can be used as the co-solvent in the solvent annealing of PEDOT:PSS, as such the results from the printing trials indicate that the conductivity of glycerol doped PEDOT:PSS has been significantly enhanced due to the increase of the content of glycerol. However, it has been found that, owing to the solubility limitation of the developed inkjet inks, the content of glycerol that can be added to the ink cannot succeed 35%. Therefore, it will be beneficial if any other types of co-solvent with lower viscosity (e.g. glycol) can be identified and considered as the additive components during the solvent annealing of PEDOT:PSS inkjet inks in future trials, which may enable the expansion of the properties of the inks.
4. The experimental results from this work has indicated that the electric conductivity of PEDOT:PSS films can be enhanced by doping Ag NPs. However, the mechanism of the enhancement is mostly based on deduction and conjecture as have been proposed; this was not fully validated, therefore more experimental evidence may assist the elaboration of the detailed underlying mechanisms. One viable approach to this is to utilise a conductive AFM system and perform a scan across the cross section of Ag NPs doped PEDOT:PSS film. By doing so, it may be possible to identify a more effective conducting network which can be detected in contrast with pristine PEDOT:PSS films.
5. In the deposition of ITO patterns using LIJ printing, it has been concluded that the critical thickness of crack for tracks is higher than the one for the films, and this is attributed to the change of geometry. It would be more beneficial to the industry if a quantitative relationship between the critical thickness and track width can be established using an appropriate mathematic model, which can also be verified through experimental study. This established relationship may allow predicting the

critical thickness of inkjet printed patterns based on given track widths in association with the specific applications.

6. The initial experimental trials have demonstrated the feasibility of synthesising semi-transparent conducting silver thin film by depositing a layer of precursor material on substrate using inkjet printing. Although this novel approach can simplify the fabrication process and obtain finer structure, the electric and optical properties of the silver film are not fully satisfactory when compared with silver grids prepared using conventional methods. Therefore, there exists a further opportunity of exploring the mechanism of the formation of the films to enable an optimum process in terms of how the formulation of precursor ink and baking condition which can affect the size and preferential growth of the silver nano grains. There is a potential need to further investigate the printed deposits for the optimisation of the microstructure and the improvement of optical and electric properties of the deposited silver thin films.
7. The multifunctional patterns prepared and investigated in this study can be integrated into photovoltaic devices (e.g. OLED, solar cells) to test the functionality. Therefore, if suitable equipment are available, and through collaborating with industry, a sets of specimens can be produced for various tests and trials to qualify the technologies that have been developed from this study.

References

[1] N. Sariciftci, A. Heeger, and H. Nalwa, Handbook of Organic Conductive Molecules and Polymers. *John Wiley and Sons Ltd*, 1997. 1: pp. 414.

[2] S. Roth and H.J. Park, Nanocarbonic transparent conductive films. *Chemical Society Reviews*, 2010. 39(7): pp. 2477-2483.

[3] W.Z. Cai and Xun, Progress and trend in study on the transparent conducting films. *Functional Materials*, 2004. 35: pp. 7.

[4] D.S. Hecht, L. Hu, and G. Irvin, Emerging transparent electrodes based on thin films of carbon nanotubes, graphene, and metallic nanostructures. *Advanced materials*, 2011. 23(13): pp. 1482-1513.

[5] Transparent conducting film. [cited 2013 8th March]; Available from: http://en.wikipedia.org/wiki/Transparent_conducting_film#References.

[6] T. Miyata, S. Suzuki, M. Ishii, and T. Minami, New transparent conducting thin films using multicomponent oxides composed of ZnO and V_2O_5 prepared by magnetron sputtering. *Thin Solid Films*, 2002. 411(1): pp. 76-81.

[7] T. Minami, T. Kakumu, K. Shimokawa, and S. Takata, New transparent conducting ZnO–In_2O_3–SnO_2 thin films prepared by magnetron sputtering. *Thin Solid Films*, 1998. 317(1): pp. 318-321.

[8] H. Mbarek, M. Saadoun, and B. Bessaïs, Screen-printed Tin-doped indium oxide (ITO) films for NH_3 gas sensing. *Materials Science and Engineering: C*, 2006. 26(2): pp. 500-504.

[9] C. O'Dwyer, M. Szachowicz, G. Visimberga, V. Lavayen, S. Newcomb, and C.S. Torres, Bottom-up growth of fully transparent contact layers of indium tin oxide nanowires for light-emitting devices. *Nature nanotechnology*, 2009. 4(4): pp. 239-244.

[10] K.A. Sierros, D.R. Cairns, J.S. Abell, and S.N. Kukureka, Pulsed laser deposition of indium tin oxide films on flexible polyethylene naphthalate display substrates at room temperature. *Thin Solid Films*, 2010. 518(10): pp. 2623-2627.

[11] H. Lin, J. Yu, N. Wang, S. Lou, and Y. Jiang, Fabrication and properties of DC magnetron sputtered indium tin oxide on flexible plastic substrate. *Journal of materials science & technology*, 2009. 25(1): pp. 119.

[12] T.A. Skotheim and J.R. Reynolds, Handbook of conducting polymers. Vol. 2. 2007: CRC Press LLC.

[13] Y. Xia, K. Sun, and J. Ouyang, Solution‐Processed Metallic Conducting Polymer Films as Transparent Electrode of Optoelectronic Devices. *Advanced materials*, 2012. 24(18): pp. 2436-2440.

[14] L. Groenendaal, F. Jonas, D. Freitag, H. Pielartzik, and J.R. Reynolds, Poly (3, 4‐ethylenedioxythiophene) and its derivatives: past, present, and future. *Advanced materials*, 2000. 12(7): pp. 481-494.

[15] A. Kumar and C. Zhou, The race to replace tin-doped indium oxide: which material will win? *ACS nano*, 2010. 4(1): pp. 11-14.

[16] D. Ghosh, L. Martinez, S. Giurgola, P. Vergani, and V. Pruneri, Widely transparent electrodes based on ultrathin metals. *Optics letters*, 2009. 34(3): pp. 325-327.

[17] M.G. Kang and L.J. Guo, Nanoimprinted Semitransparent Metal Electrodes and Their Application in Organic Light‐Emitting Diodes. *Advanced materials*, 2007. 19(10): pp. 1391-1396.

[18] D. Ghosh, T. Chen, and V. Pruneri, Ultrathin Cu-Ti bilayer transparent conductors with enhanced figure-of-merit and stability. *Applied Physics Letters*, 2010. 96(9): pp. 091106-091106-3.

[19] J. Xu, C. Zhong, and C. Fu, Illumination & Displays Novel method for printing high-quality metal wires. *Spie Newsroom. 2007.*

[20] R. Elmqvist. Measuring instrument of the recording type. *U.S. Patent*. 2566443. 1951.

[21] D. Wallace, P. Cooley, B. Antohe, D. Hayes, and T. Chen. Ink jet technology for manufacturing and instrument applications. in *Proceedings, 20th workshop on micromachining, micromechanics and microsystems, Toulouse, France*. 2009.

[22] T. Boland, T. Xu, B. Damon, and X. Cui, Application of inkjet printing to tissue engineering. *Biotechnology journal*, 2006. 1(9): pp. 910-917.

[23] A.V. Lemmo, D.J. Rose, and T.C. Tisone, Inkjet dispensing technology: applications in drug discovery. *Current opinion in biotechnology*, 1998. 9(6): pp. 615-617.

[24] M. Singh, H.M. Haverinen, P. Dhagat, and G.E. Jabbour, Inkjet printing—process and its applications. *Advanced materials*, 2010. 22(6): pp. 673-685.

[25] P. Calvert, Inkjet printing for materials and devices. *Chemistry of Materials*, 2001. 13(10): pp. 3299-3305.

[26] Inkjet head business. [cited 2013 04.12]; Available from: http://www.toshibatec.co.jp/en/corporate/inkjet/.

[27] S.H. Eom, S. Senthilarasu, P. Uthirakumar, S.C. Yoon, J. Lim, C. Lee, H.S. Lim, J. Lee, and S.-H. Lee, Polymer solar cells based on inkjet-printed PEDOT:PSS layer. *Organic Electronics*, 2009. 10(3): pp. 536-542.

[28] B. Ballarin, A. Fraleoni-Morgera, D. Frascaro, S. Marazzita, C. Piana, and L. Setti, Thermal inkjet microdeposition of PEDOT:PSS on ITO-coated glass and characterization of the obtained film. *Synthetic Metals*, 2004. 146(2): pp. 201-205.

[29] K.X. Steirer, J.J. Berry, M.O. Reese, M.F.A.M. van Hest, A. Miedaner, M.W. Liberatore, R.T. Collins, and D.S. Ginley, Ultrasonically sprayed and inkjet printed thin film electrodes for organic solar cells. *Thin Solid Films*, 2009. 517(8): pp. 2781-2786.

[30] S.-J. Hong, J.-W. Kim, J.-W. Lim, G.-S. Choi, and M. Isshiki, Characteristics of printed thin films using indium tin oxide (ITO) ink. *Materials transactions*, 2010. 51(10): pp. 1905-1908.

[31] J.-A. Jeong and H.-K. Kim, Characteristics of inkjet-printed nano indium tin oxide particles for transparent conducting electrodes. *Current Applied Physics*, 2010. 10(4): pp. e105-e108.

[32] M.-s. Hwang, B.-y. Jeong, J. Moon, S.-K. Chun, and J. Kim, Inkjet-printing of indium tin oxide (ITO) films for transparent conducting electrodes. *Materials Science and Engineering: B*, 2011. 176(14): pp. 1128-1131.

[33] R.C. Hoffmann, S. Dilfer, and J.J. Schneider, Transparent indium tin oxide as inkjet‐printed thin film electrodes for organic field‐effect transistors. *physica status solidi (a)*, 2011. 208(12): pp. 2920-2925.

[34] J.W.C. S. J. Hong, J. I. Han, Effect of heat treatment on the characteristics of ITO nanoparticles for inkjet printing. *Journal of the Korean Physical Society*, 2008. 53(5): pp. 4.

[35] G.P. Kushto, W. Kim, and Z.H. Kafafi, Flexible organic photovoltaics using conducting polymer electrodes. *Applied Physics Letters*, 2005. 86(9): pp. 093502-093502-3.

[36] J.-R. Kim, J.H. Jung, W.S. Shin, W.-W. So, and S.-J. Moon, Efficient TCO-Free Organic Solar Cells with Modified Poly (3, 4-Ethylenedioxythiophene): Poly (Styrenesulfonate) Anodes. *Journal of Nanoscience and Nanotechnology*, 2011. 11(1): pp. 326-330.

[37] M. Neophytou, F. Hermerschmidt, A. Savva, E. Georgiou, and S.A. Choulis, Highly efficient indium tin oxide-free organic photovoltaics using inkjet-printed silver nanoparticle current collecting grids. *Applied Physics Letters*, 2012. 101(19): pp. 193302-193302-4.

[38] Z.A. Rahman, K. Sulaiman, A. Shuhaimi, and M. Rusop, PEDOT: PSS Thin Film as Transparent Electrode in ITO-Free Organic Solar Cell. *Advanced Materials Research*, 2012. 501: pp. 252-256.

[39] F. Zhang, M. Johansson, M.R. Andersson, J.C. Hummelen, and O. Inganas, Polymer photovoltaic cells with conducting polymer anodes. *Advanced materials*, 2002. 14(9): pp. 662-665.

[40] [cited 2013 14th March]; Available from: http://www.agfa.com/sp/global/en/internet/main/solutions/orgacon_electronic_materials/index.jsp.

[41] [cited 2013 14th March]; Available from: http://www.ulvac.com/specialty-materials-services/ITO_Series.cfm.

[42] [cited 2013 18th March]; Available from: http://www.ossila.com/support/FAQs_pedot_pss_inkjet.php.

[43] J. Stringer and B. Derby, Limits to feature size and resolution in ink jet printing. *Journal of the European Ceramic Society*, 2009. 29(5): pp. 913-918.

[44] M.L. Chabinyc. Inkjet printing in macroelectronics. Available from: http://people.ccmr.cornell.edu/~cober/mse542/page2/files/chabinyc-inkjet-f.pdf.

[45] W. Buehner, J. Hill, T. Williams, and J. Woods, Application of ink jet technology to a word processing output printer. *IBM Journal of research and development*, 1977. 21(1): pp. 2-9.

[46] E.L. Kyser and S.B. Sears, Method and apparatus for recording with writing fluids and drop projection means therefor, US patent 3946398, 1976.

[47] S.I. Zoltan, Pulsed droplet ejecting system, US patent 3683212, 1972.

[48] E. Tekin, P.J. Smith, and U.S. Schubert, Inkjet printing as a deposition and patterning tool for polymers and inorganic particles. *Soft Matter*, 2008. 4(4): pp. 703-713.

[49] L. Hakola, Benefits of inkjet printing for printed electronics. *Pira Printed Electronics*, 2005. 14(9.2005).

[50] Industrial inkjet printing. [cited 2013 3rd April]; Available from: http://www.xennia.com/knowledgecentre/industrial-inkjet-printing.asp.

[51] H.P. Le, Progress and trends in ink-jet printing technology. *The Journal of imaging science and technology*, 1998. 42(1): pp. 49-62.

[52] A. Hudd, Inkjet printing technologies. *The Chemistry of Inkjet Inks. World Scientific: New Jersey-London-Singapore*, 2010: pp. 3-18.

[53] A. Hancock and L. Lin, Challenges of UV curable ink-jet printing inks–a formulator's perspective. *Pigment & resin technology*, 2004. 33(5): pp. 280-286.

[54] High-viscous material inkjet printer. [cited 2013 18th March] Available from: http://www.tno.nl/.

[55] J.S. Miller, Ink jet printing of printed circuit boards, US patent 4668533, 1987.

[56] V. Bergeron, D. Bonn, J.Y. Martin, and L. Vovelle, Controlling droplet deposition with polymer additives. *Nature*, 2000. 405(6788): pp. 772-775.

[57] J. Fromm, Numerical calculation of the fluid dynamics of drop-on-demand jets. *IBM Journal of research and development*, 1984. 28(3): pp. 322-333.

[58] N. Reis and B. Derby. Ink jet deposition of ceramic suspensions: modeling and experiments of droplet formation. in *MRS proceedings*. 2000. Cambridge Univ Press.

[59] D. Jang, D. Kim, and J. Moon, Influence of fluid physical properties on ink-jet printability. *Langmuir*, 2009. 25(5): pp. 2629-2635.

[60] E. Özkol, J. Ebert, and R. Telle, An experimental analysis of the influence of the ink properties on the drop formation for direct thermal inkjet printing of high solid content aqueous 3Y-TZP suspensions. *Journal of the European Ceramic Society*, 2010. 30(7): pp. 1669-1678.

[61] Q. Xu and O.A. Basaran, Computational analysis of drop-on-demand drop formation. *Physics of Fluids*, 2007. 19: pp. 102111.

[62] J.Q. Feng, A general fluid dynamic analysis of drop ejection in drop-on-demand ink jet devices. *Journal of Imaging Science and Technology*, 2002. 46(5): pp. 398-408.

[63] A. Asai, Three-dimensional calculation of bubble growth and drop ejection in a bubble jet printer. *Transaction-American Society of Mechanical Engineers Journal of Fluids Engineering*, 1992. 114: pp. 638-638.

[64] H. Dong, W.W. Carr, and J.F. Morris, An experimental study of drop-on-demand drop formation. *Physics of Fluids*, 2006. 18: pp. 072102.

[65] H. C. Wu, W. S. Hwang, and H. J. Lin, Development of a three-dimensional simulation system for micro-inkjet and its experimental verification. *Materials Science and Engineering: A*, 2004. 373(1): pp. 268-278.

[66] R. Rioboo, M. Marengo, and C. Tropea, Time evolution of liquid drop impact onto solid, dry surfaces. *Experiments in Fluids*, 2002. 33(1): pp. 112-124.

[67] S. Schiaffino, A. A. Sonin, Molten droplet deposition and solidification at low Weber nujmbers. *Physics of Fluids*, 1997. 9: pp. 3174.

[68] L. H. Tanner, The spreading of silicone oil drops on horizontal surfaces. *Journal of Physics D: Applied Physics*, 1979. 12.

[69] M. Mantysalo and P. Mansikkamaki. Inkjet-deposited interconnections for electronic packaging. in *International Conference on Digital Printing Technologies*. 2007.

[70] K. Murata, J. Matsumoto, A. Tezuka, Y. Matsuba, and H. Yokoyama, Super-fine ink-jet printing: toward the minimal manufacturing system. *Microsystem technologies*, 2005. 12(1-2): pp. 2-7.

[71] J. Park, M. Hardy, S, Kang et al., Hihg-resolution electrohydrodynamic jet printing. *Nature Materials*, 2007. 6: pp. 782-789.

[72] Y. Son and C. Kim, Spreading of inkjet droplet of non-Newtonian fluid on solid surface with controlled contact angle at low Weber and Reynolds numbers. *Journal of Non-Newtonian Fluid Mechanics*, 2009. 162(1): pp. 78-87.

[73] D.A. Hutt and C. Liu, Oxidation protection of copper surfaces using self-assembled monolayers of octadecanethiol. *Applied surface science*, 2005. 252(2): pp. 400-411.

[74] B.J. Kang and J.H. Oh, Geometrical characterization of inkjet-printed conductive lines of nanosilver suspensions on a polymer substrate. *Thin Solid Films*, 2010. 518(10): pp. 2890-2896.

[75] N.B. Cho, T.H. Lim, Y.M. Jeon, and M.-S. Gong, Inkjet printing of polymeric resistance humidity sensor using UV-curable electrolyte inks. *Macromolecular Research*, 2008. 16(2): pp. 149-154.

[76] Laser-assisted ink-jet technology for high-speed printing of fine wiring. [cited 2013 27th March] Available from: http://www.aist.go.jp/.

[77] Cartridge style low temperature printhead. [cited 2013 27th March] Available from: http://www.microfab.com/images/pdfs/ph-41_mf4.

[78] Jetlab 4 - Tabletop printing platform. [cited 2013 27th March] Available from: http://www.microfab.com/index.php?option=com_content&view=article&id=41&Itemid=88.

[79] Spectra printhead mannual. [cited 2013 18th December]; Available from: http://www.fujifilmusa.com/shared/bin/PDS00024.pdf.

[80] I. Spectra, Confidential Information Nova/Nova-Q Jetting Assembly Product Manual.

[81] Laser operator's manual M version. [cited 2013 18th December]; Available from: http://www.synrad.com/Manuals/48SeriesM_v8.1.pdf.

[82] M. G. Buehler and W. R. Thurber, An experimental study of various cross sheet resistor test structures. Journal of the Electrochemical Society, 1978. 125: pp. 645-650.

[83] P. Scherrer, Bestimmung der Grösse und der inneren Struktur von Kolloidteilchen mittels Röntgenstrahlen. *Göttingen*, 1918. 26: pp. 3.

[84] Available from: http://profmaster.blogspot.jp/2007/12/how-to-calculate-viscosity-of-liquid.html.

[85] R. A. Serway, Physics for Scientist & Engineers (4thed). *Saunders College Publishing*, 1996. ISBN 0-03-005932-1.

[86] J. B. Segur, H. E. Oberstar, Viscosity of glycerol and its aqueous solutions. *Industrial & Engineering Chemistry*, 1951. 43(9): pp.2117.

[87] S.R. Wickramasinghe, C.M. Kahr, and B. Han, Mass transfer in blood oxygenators using blood analogue fluids. *Biotechnology progress*, 2002. 18(4): pp. 867-873.

[88] F. Jiang and P. Huang, Advanced Applications and Example Analysis on Fluent, 2008, Tsinghua University Press.

[89] N.F. Morrison and O.G. Harlen, Viscoelasticity in inkjet printing. *Rheologica acta*, 2010. 49(6): pp. 619-632.

[90] D. T. Papageorgiou, On the breakup of viscous liquid threads. *Physics of Fluids*, 1995. 7: pp. 1521-1529.

[91] E.R. Lee, Microdrop generation. Vol. 5. 2010: CRC press.

[92] C.C. Smith, G. Löf, and R. Jones, Measurement and analysis of evaporation from an inactive outdoor swimming pool. *Solar Energy*, 1994. 53(1): pp. 3-7.

[93] G.W. Thomson, The Antoine Equation for Vapor-pressure Data. *Chemical Reviews*, 1946. 38(1): pp. 1-39.

[94] D. Soltman and V. Subramanian, Inkjet-printed line morphologies and temperature control of the coffee ring effect. *Langmuir*, 2008. 24(5): pp. 2224-2231.

[95] T. Blake, A. Clarke, J. De Coninck, and M.J. De Ruijter, Contact angle relaxation during droplet spreading: Comparison between molecular kinetic theory and molecular dynamics. *Langmuir*, 1997. 13(7): pp. 2164-2166.

[96] M.J. De Ruijter, T. Blake, and J. De Coninck, Dynamic wetting studied by molecular modeling simulations of droplet spreading. *Langmuir*, 1999. 15(22): pp. 7836-7847.

[97] A.W. Adamson, Potential distortion model for contact angle and spreading. II. Temperature dependent effects. *Journal of Colloid and Interface Science*, 1973. 44(2): pp. 273-281.

[98] P. Duineveld, The stability of ink-jet printed lines of liquid with zero receding contact angle on a homogeneous substrate. *Journal of Fluid Mechanics*, 2003. 477(1): pp. 175-200.

[99] E. Vitoratos, S. Sakkopoulos, E. Dalas, N. Paliatsas, D. Karageorgopoulos, F. Petraki, S. Kennou, and S.A. Choulis, Thermal degradation mechanisms of PEDOT: PSS. *Organic Electronics*, 2009. 10(1): pp. 61-66.

[100] A.M. Nardes, On the conductivity of PEDOT: PSS thin films. PhD thesis, *Technische Universiteit Eindhoven*, 2007.

[101] T.M. Schweizer, Electrical characterization and investigation of the piezoresistive effect of PEDOT: PSS thin films, 2005, Georgia Institute of Technology.

[102] Y. Wang. Research progress on a novel conductive polymer–poly (3, 4-ethylenedioxythiophene)(PEDOT). in *Journal of Physics: Conference Series*. 2009. IOP Publishing.

[103] C. Plesse, F. Vidal, H. Randriamahazaka, D. Teyssié, and C. Chevrot, Synthesis and characterization of conducting interpenetrating polymer networks for new actuators. *Polymer*, 2005. 46(18): pp. 7771-7778.

[104] K. Liu, Z. Hu, R. Xue, J. Zhang, and J. Zhu, Electropolymerization of high stable poly (3, 4-ethylenedioxythiophene) in ionic liquids and its potential applications in electrochemical capacitor. *Journal of Power Sources*, 2008. 179(2): pp. 858-862.

[105] M. Biancardo, K. West, and F.C. Krebs, Quasi-solid-state dye-sensitized solar cells: Pt and PEDOT:PSS counter electrodes applied to gel electrolyte assemblies. *Journal of Photochemistry and Photobiology A: Chemistry*, 2007. 187(2): pp. 395-401.

[106] Y.f. Zhou, Y.b. Yuan, L.f. Cao, J. Zhang, H.-q. Pang, J.-r. Lian, and X. Zhou, Improved stability of OLEDs with mild oxygen plasma treated PEDOT: PSS. *Journal of luminescence*, 2007. 122: pp. 602-604.

[107] Z. Mousavi, J. Bobacka, A. Lewenstam, and A. Ivaska, Response mechanism of potentiometric Ag^+ sensor based on poly (3, 4-ethylenedioxythiophene) doped with silver hexabromocarborane. *Journal of Electroanalytical Chemistry*, 2006. 593(1): pp. 219-226.

[108] P. Vanlaeke, A. Swinnen, I. Haeldermans, G. Vanhoyland, T. Aernouts, D. Cheyns, C. Deibel, J. D'Haen, P. Heremans, and J. Poortmans, P3HT/PCBM bulk

heterojunction solar cells: Relation between morphology and electro-optical characteristics. *Solar energy materials and solar cells*, 2006. 90(14): pp. 2150-2158.

[109] A. Chipman, A Commodity no more, the flat-screen television boom has materials scientists scrambling to replace the valuable metal oxide that coats the screens. *Nature*, 2007. 449(13).

[110] H. Yang, B. Qu, S. Ma, Z. Chen, L. Xiao, and Q. Gong, Indium tin oxide-free polymer solar cells using a PEDOT: PSS/Ag/PEDOT: PSS multilayer as a transparent anode. *Journal of Physics D: Applied Physics*, 2012. 45(42): pp. 425102.

[111] Y. Zhou, H. Cheun, S. Choi, W.J. Potscavage Jr, C. Fuentes-Hernandez, and B. Kippelen, Indium tin oxide-free and metal-free semitransparent organic solar cells. *Applied Physics Letters*, 2010. 97: pp. 153304.

[112] Y.H. Kim, C. Sachse, M.L. Machala, C. May, L. Müller‐Meskamp, and K. Leo, Highly Conductive PEDOT: PSS Electrode with Optimized Solvent and Thermal Post‐Treatment for ITO‐Free Organic Solar Cells. *Advanced Functional Materials*, 2011. 21(6): pp. 1076-1081.

[113] F. Ely, C.O. Avellaneda, P. Paredez, V. Nogueira, T. Santos, V. Mammana, C. Molina, J. Brug, G. Gibson, and L. Zhao, Patterning quality control of inkjet printed PEDOT: PSS films by wetting properties. *Synthetic Metals*, 2011. 161(19): pp. 2129-2134.

[114] S.D. Hoath, S. Jung, W.K. Hsiao, and I.M. Hutchings, How PEDOT: PSS solutions produce satellite-free inkjets. *Organic Electronics*, 2012.

[115] M. Döbbelin, R. Marcilla, M. Salsamendi, C. Pozo-Gonzalo, P.M. Carrasco, J.A. Pomposo, and D. Mecerreyes, Influence of ionic liquids on the electrical conductivity and morphology of PEDOT: PSS films. *Chemistry of Materials*, 2007. 19(9): pp. 2147-2149.

[116] J. Ouyang, Q. Xu, C.W. Chu, Y. Yang, G. Li, and J. Shinar, On the mechanism of conductivity enhancement in poly (3, 4-ethylenedioxythiophene): poly (styrene sulfonate) film through solvent treatment. *Polymer*, 2004. 45(25): pp. 8443-8450.

[117] Y.Xia and J. Ouyang, PEDOT:PSS films with significantly enhanced conductivities induced by preferential salvation with cosolvents and their application in polymer photovoltaic cells. *J. Mater. Chem.*, 2011. 21: pp. 8.

[118] M. Reyes-Reyes, I. Cruz-Cruz, and R.N. López-Sandoval, Enhancement of the electrical conductivity in PEDOT: PSS films by the addition of dimethyl sulfate. *The Journal of Physical Chemistry C*, 2010. 114(47): pp. 20220-20224.

[119] J. Huang, P.F. Miller, J.S. Wilson, A.J. de Mello, J.C. de Mello, and D.D. Bradley, Investigation of the Effects of Doping and Post‐Deposition Treatments on the Conductivity, Morphology, and Work Function of Poly (3, 4‐ethylenedioxythiophene)/Poly (styrene sulfonate) Films. *Advanced Functional Materials*, 2005. 15(2): pp. 290-296.

[120] B. Fan, Y. Xia, and J. Ouyang. Novel ways to significantly enhance the conductivity of transparent PEDOT: PSS. in *Proc. of SPIE Vol*. 2009.

[121] T. KumaráSarma, Synthesis of Au nanoparticle–conductive polyaniline composite using H_2O_2 as oxidising as well as reducing agent. *Chemical communications*, 2002(10): pp. 1048-1049.

[122] S.K. Pillalamarri, F.D. Blum, A.T. Tokuhiro, and M.F. Bertino, One-pot synthesis of polyaniline-metal nanocomposites. *Chemistry of Materials*, 2005. 17(24): pp. 5941-5944.

[123] I. Moggio, E. Arias, K.J. Moreno, A. Ponce, R.G. Melendez, I. Llanera, and S.E. Moya. On the Influence of Silver Nanoparticles Size in the Electrical Conductivity of PEDOT: PSS. in *Materials Science Forum*. 2010. Trans Tech Publ.

[124] K.J. Moreno, I. Moggio, E. Arias, I. Llarena, S.E. Moya, R.F. Ziolo, and H. Barrientos, Silver nanoparticles functionalized in situ with the conjugated polymer (PEDOT: PSS). *Journal of Nanoscience and Nanotechnology*, 2009. 9(6): pp. 3987-3992.

[125] A. Nagata, T. Oku, T. Akiyama, A. Suzuki, Y. Yamasaki, and T. Mori, Effects of Au Nanoparticle Addition to Hole Transfer Layer in Organic Photovoltaic Cells Based on Phthalocyanines and Fullerene. *Journal of Nanotechnology*, 2011.

[126] Y. Xu, Y. Wang, J. Liang, Y. Huang, Y. Ma, X. Wan, and Y. Chen, A hybrid material of graphene and poly (3, 4-ethyldioxythiophene) with high conductivity, flexibility, and transparency. *Nano Research*, 2009. 2(4): pp. 343-348.

[127] N. Semaltianos, S. Logothetidis, N. Hastas, W. Perrie, S. Romani, R. Potter, G. Dearden, K. Watkins, P. French, and M. Sharp, Modification of the electrical properties of PEDOT: PSS by the incorporation of ZnO nanoparticles synthesized by laser ablation. *Chemical physics letters*, 2010. 484(4): pp. 283-289.

[128] T. Mustonen, K. Kordás, S. Saukko, G. Tóth, J.S. Penttilä, P. Helistö, H. Seppä, and H. Jantunen, Inkjet printing of transparent and conductive patterns of single‐walled carbon nanotubes and PEDOT‐PSS composites. *physica status solidi (b)*, 2007. 244(11): pp. 4336-4340.

[129] A. Denneulin, J. Bras, F. Carcone, C. Neuman, and A. Blayo, Impact of ink formulation on carbon nanotube network organization within inkjet printed conductive films. *Carbon*, 2011. 49(8): pp. 2603-2614.

[130] E. Tekin, B.-J. de Gans, and U.S. Schubert, Ink-jet printing of polymers–from single dots to thin film libraries. *Journal of Materials Chemistry*, 2004. 14(17): pp. 2627-2632.

[131] A.M. Nardes, R.A. Janssen, and M. Kemerink, A Morphological Model for the Solvent‐Enhanced Conductivity of PEDOT: PSS Thin Films. *Advanced Functional Materials*, 2008. 18(6): pp. 865-871.

[132] C.S. Sangeeth, M. Jaiswal, and R. Menon, Correlation of morphology and charge transport in poly (3, 4-ethylenedioxythiophene)–polystyrenesulfonic acid (PEDOT–PSS) films. *Journal of Physics: Condensed Matter*, 2009. 21(7): pp. 072101.

[133] A.M. Nardes, M. Kemerink, R.A. Janssen, J.A. Bastiaansen, N.M. Kiggen, B.M. Langeveld, A.J. van Breemen, and M.M. de Kok, Microscopic understanding of the anisotropic conductivity of PEDOT: PSS thin films. *Advanced materials*, 2007. 19(9): pp. 1196-1200.

[134] G. Greczynski, T. Kugler, and W. Salaneck, Characterization of the PEDOT-PSS system by means of X-ray and ultraviolet photoelectron spectroscopy. *Thin Solid Films*, 1999. 354(1): pp. 129-135.

[135] B. Friedel, P.E. Keivanidis, T.J. Brenner, A. Abrusci, C.R. McNeill, R.H. Friend, and N.C. Greenham, Effects of layer thickness and annealing of PEDOT: PSS layers in organic photodetectors. *Macromolecules*, 2009. 42(17): pp. 6741-6747.

[136] G. Li, V. Shrotriya, Y. Yao, and Y. Yang, Investigation of annealing effects and film thickness dependence of polymer solar cells based on poly (3-hexylthiophene). *Journal of Applied Physics*, 2005. 98(4): pp. 043704-043704-5.

[137] X. Jiang, W. Chen, C. Chen, S. Xiong, and A. Yu, Role of temperature in the growth of silver nanoparticles through a synergetic reduction approach. *Nanoscale Research Letter*, 2011. 6: pp. 32-40.

[138] A. Elschner, S. Kirchmeyer, W. Lovenich, U. Merker, and K. Reuter, PEDOT: principles and applications of an intrinsically conductive polymer2010: CRC Press.

[139] S.-J. Wang, Y.-J. Choi, and H.-H. Park, Investigation of Ag-poly (3, 4-ethylenedioxythiophene): polystyrene sulfonate nanocomposite films prepared by a one-step aqueous method. *Journal of Applied Physics*, 2011. 109(12): pp. 124902-124902-4.

[140] J. Weickert, H. Sun, C. Palumbiny, H.C. Hesse, and L. Schmidt-Mende, Spray-deposited PEDOT: PSS for inverted organic solar cells. *Solar energy materials and solar cells*, 2010. 94(12): pp. 2371-2374.

[141] J.D. Ingle Jr and S.R. Crouch, Spectrochemical analysis. 1988.

[142] H.W. Heuer, R. Wehrmann, and S. Kirchmeyer, Electrochromic Window Based on Conducting Poly (3, 4 - ethylenedioxythiophene) - Poly (styrene sulfonate). *Advanced Functional Materials*, 2002. 12(2): pp. 89-94.

[143] X. Crispin, S. Marciniak, W. Osikowicz, G. Zotti, A. van der Gon, F. Louwet, M. Fahlman, L. Groenendaal, F. De Schryver, and W.R. Salaneck, Conductivity, morphology, interfacial chemistry, and stability of poly (3, 4 - ethylene

dioxythiophene) – poly (styrene sulfonate): A photoelectron spectroscopy study. *Journal of polymer science Part B: Polymer physics*, 2003. 41(21): pp. 2561-2583.

[144] Indium tin oxide. [cited 2013 17th April] Available from: http://en.wikipedia.org/wiki/Indium_tin_oxide.

[145] Indium Tin Oxide (ITO) – Properties and Applications. [cited 2013 17th April] Available from: http://www.azom.com/article.aspx?ArticleID=2349.

[146] T.J. Coutts, D.L. Young, and X. Li. Fundamental Advances in Transparent Conducting Oxides. in *Materials Research Society Symposium Proceedings*. 2000. Cambridge Univ Press.

[147] J. Chang, H.-L. Wang, and M.-H. Hon, Studying of transparent conductive ZnO: Al thin films by RF reactive magnetron sputtering. *Journal of Crystal Growth*, 2000. 211(1): pp. 93-97.

[148] I. Maksimenko, D. Kilian, C. Mehringer, M. Voigt, W. Peukert, and P.J. Wellmann, Fabrication, charge carrier transport, and application of printable nanocomposites based on indium tin oxide nanoparticles and conducting polymer 3, 4-ethylenedioxythiophene/polystyrene sulfonic acid. *Journal of Applied Physics*, 2011. 110(10): pp. 104301-104301-8.

[149] S. Heusing, P. Oliveira, E. Kraker, A. Haase, C. Palfinger, and M. Veith. Development of printed ITO coatings on PET and PEN foil for flexible organic photodiodes. in *Photonics Europe*. 2008. International Society for Optics and Photonics.

[150] M. Ali, K. Ibrahim, O.S. Hamad, M. Eisa, M. Faraj, and F. Azhari, Deposited indium tin oxide (ITO) thin films by dc-magnetron sputtering on polyethylene terephthalate substrate (PET). *Rom J Phys*, 2011. 56: pp. 730-741.

[151] I. Maksimenko, M. Gross, T. Königer, H. Münstedt, and P.J. Wellmann, Conductivity and adhesion enhancement in low-temperature processed indium tin oxide/polymer nanocomposites. *Thin Solid Films*, 2010. 518(10): pp. 2910-2915.

[152] I. Maksimenko and P.J. Wellmann, Low-temperature processing of transparent conductive indium tin oxide nanocomposites using polyvinyl derivatives. *Thin Solid Films*, 2011. 520(4): pp. 1341-1347.

[153] I. Maksimenko and P. Wellmann, Low temperature processing of hybrid nanoparticulate Indium Tin Oxide (ITO) polymer layers and application in large scale lighting devices. *Thin Solid Films*, 2011. 519(17): pp. 5744-5747.

[154] A.E. and J. Akedo, Development of laser-assisted inkjet printing technology. *Synthesiology*, 2011. 4: pp. 10.

[155] M.S. Tirumkudulu and W.B. Russel, Cracking in drying latex films. *Langmuir*, 2005. 21(11): pp. 4938-4948.

[156] M. Benoy, E. Mohammed, M. Suresh Babu, P. Binu, and B. Pradeep, Thickness dependence of the properties of indium tin oxide (ITO) films prepared by activated reactive evaporation. *Brazilian Journal of Physics*, 2009. 39(4): pp. 629-632.

[157] Y. Hu, X. Diao, C. Wang, W. Hao, and T. Wang, Effects of heat treatment on properties of ITO films prepared by rf magnetron sputtering. *Vacuum*, 2004. 75(2): pp. 183-188.

[158] H. Hu and R.G. Larson, Marangoni effect reverses coffee-ring depositions. *The Journal of Physical Chemistry B*, 2006. 110(14): pp. 7090-7094.

[159] T. Still, P.J. Yunker, and A.G. Yodh, Surfactant-induced Marangoni eddies alter the coffee-rings of evaporating colloidal drops. *Langmuir*, 2012. 28(11): pp. 4984-4988.

[160] H. Kim, J. Horwitz, G. Kushto, A. Pique, Z. Kafafi, C. Gilmore, and D. Chrisey, Effect of film thickness on the properties of indium tin oxide thin films. *Journal of Applied Physics*, 2000. 88(10): pp. 6021-6025.

[161] G. Mei-Zhen, R. Job, X. De-Sheng, and W. Fahrner, Thickness dependence of resistivity and optical reflectance of ITO films. *Chinese Physics Letters*, 2008. 25(4): pp. 1380.

[162] G.L. Ping and Z. Keran, Effect of the thickness of indium tin oxide (ITO) on its properties, [cited 2013 21st April], Available from:

http://staff.science.nus.edu.sg/~scilooe/srp2002/sci_paper/IMRE/research_paper/Gan%20Lee%20Ping1.pdf .

[163] P. J. Jorgensen, Final stage sintering and grain growth in oxides. *Battelle Institute Materials Sience Colloquia*, 1974. pp. 379-395.

[164] M.-Y. Chu, Sintering stress and microstructure in ceramic powder compacts, 1990, Lawrence Berkeley Lab., CA (USA).

[165] R. Bjørk, H.L. Frandsen, V. Tikare, and N. Pryds. Modeling the microstructural evolution during constrained sintering. in *Powder Metallurgy World Congress and Exhibition (PM 2012)*.

[166] R.K. Bordia and A. Jagota, Crack growth and damage in constrained sintering films. *Journal of the American Ceramic Society*, 1993. 76(10): pp. 2475-2485.

[167] S. Ver-Bruggen. Graphene-based transparent flexible electrodes from Rice University. [cited 2013 21st April] Available from: http://www.plusplasticelectronics.com/consumerelectronics/graphene-based-transparent-flexible-electrodes-from-rice-university-36399.aspx.

[168] W. Yin, D. H. Lee, J. Choi et al., Screen printing of silver nanoparticle suspension for metal interconnects. *Korean Journal of Chemical Engineering*, 2008. 25: pp. 1358-1361.

[169] J. Yu, I. Kim, J. Kim et al., Silver front electrode girds for ITO-free all printed polymer solar cells with embedded and raised topographies, prepared by thermal imprint, flexographic and inkjet roll-to-roll processes. *Nanoscale*, 2012. 4: pp. 6032-6040.

[170] C. E. Hendriks, P. J. Smith, J. Perelaer et al., “Invisible” silver tracks produced by combining hot-embossing and inkjet printing. *Advanced Functional Materials*, 2008. 18(7): pp. 1031-1038.

[171] E. Ramasamy, W.J. Lee, D.Y. Lee, and J.S. Song, Portable, parallel grid dye-sensitized solar cell module prepared by screen printing. *Journal of Power Sources*, 2007. 165(1): pp. 446-449.

[172] Y. Galagan, J.-E. JM Rubingh, R. Andriessen, C.-C. Fan, P. WM Blom, S. C Veenstra, and J. M Kroon, ITO-free flexible organic solar cells with printed current collecting grids. *Solar energy materials and solar cells*, 2011. 95(5): pp. 1339-1343.

[173] A. Ebong, I. Cooper, K. Tate, B. Rounsaville, F. Zimbardi, V. Upadhyaya, A. Rohatgi, M. Dovrat, E. Kritchman, and D. Brusilovsky. Implementing narrow front silver gridlines through ink jet machine for high quality contacts to silicon solar cells. in *Photovoltaic Specialists Conference (PVSC), 2011 37th IEEE*. 2011. IEEE.

[174] Y. Galagan, E.W. Coenen, S. Sabik, H.H. Gorter, M. Barink, S.C. Veenstra, J.M. Kroon, R. Andriessen, and P.W. Blom, Evaluation of ink-jet printed current collecting grids and busbars for ITO-free organic solar cells. *Solar energy materials and solar cells*, 2012. 104: pp. 32-38.

[175] Core applications & technologies. [cited 2013 22nd April] Available from: http://www.conductiveinkjet.com/~/media/Files/C/Conductive-Inkjet-Technology/pdfs/applications%20and%20technologies%20oct%202009.pdf.

[176] M. Valaskova, G. Simha Martynkova, J. Leskova, P. Capkova, V. Klemm, and D. Rafaja, Silver nanoparticles/montmorillonite composites prepared using nitrating reagent at water and glycerol. *Journal of Nanoscience and Nanotechnology*, 2008. 8(6): pp. 3050-3058.

[177] E. Nisaratanaporn and K. Wongsuwan, Preparation of ultrafine silver powder using glycerol as reducing agent. *Journal of Metals, Materials and Minerals*, 2008. 18(2): pp. 1-5.

[178] A. Sinha and B. Sharma, Preparation of silver powder through glycerol process. *Bulletin of Materials Science*, 2005. 28(3): pp. 213-217.

[179] Q. Zhou, S. Wang, N. Jia, L. Liu, J. Yang, and Z. Jiang, Synthesis of highly crystalline silver dendrites microscale nanostructures by electrodeposition. *Materials Letters*, 2006. 60(29): pp. 3789-3792.

[180] K. Patel, S. Kapoor, D. Dave, and T. Mukherjee, Synthesis of nanosized silver colloids by microwave dielectric heating. *Journal of Chemical Sciences*, 2005. 117(1): pp. 53-60.

[181] J.F. Banfield, S.A. Welch, H. Zhang, T.T. Ebert, and R.L. Penn, Aggregation-based crystal growth and microstructure development in natural iron oxyhydroxide biomineralization products. *Science*, 2000. 289(5480): pp. 751-754.

[182] L. Lu, A. Kobayashi, Y. Kikkawa, K. Tawa, and Y. Ozaki, Oriented attachment-based assembly of dendritic silver nanostructures at room temperature. *The Journal of Physical Chemistry B*, 2006. 110(46): pp. 23234-23241.

[183] L. Mo, L. Li, Y. Li, Y. Hao, T. Meng, and Y. Wang, Preparation and study on the spectra of conductive nano-silver film. *Guang pu xue yu guang pu fen xi, Guang pu*, 2007. 27(12): pp. 2502.

[184] G. Jiang, L. Wang, T. Chen, H. Yu, and J. Wang, Preparation and characterization of dendritic silver nanoparticles. *Journal of materials science*, 2005. 40(7): pp. 1681-1683.

Appendix

```
#include "udf.h"
#include "sg.h"
#include "sg_mphase.h"
#include "flow.h"

#define PI 3.141592654

DEFINE_PROFILE(membrane_pressure，          /* function name   */
            th   ，                  /* thread         */
            nv)                    /* variable number */
{
 face_t f;
 real x[ND_ND];
 real f_time = RP_Get_Real("flow-time");

 begin_f_loop (f，th)
   {
    F_CENTROID(x，f，th);
    if (f_time<=8e-6)
    {
            F_PROFILE(f，th，nv) = -40000*sin(PI*f_time/(8e-6));
   }
    else if(f_time>8e-6&&f_time<=20e-6)
    {
            F_PROFILE(f，th，nv) = 100000*sin(PI*(f_time-8e-6)/(12e-6));
    }
    else if(f_time>20e-6&&f_time<=36e-6)
    {
            F_PROFILE(f，th，nv) = -60000*sin(PI*(f_time-20e-6)/(16e-6));
    }
    else
     F_PROFILE(f，th，nv) = 0;
```

```
    }
  end_f_loop (f，th)
}
```